Laser-driven terahertz spin transport: driving force and applications

Dissertation

zur Erlangung des Grades eines
Doktors (Dr. rer. nat.)

am Fachbereich Physik
der Freien Universität Berlin

vorgelegt von

Seyed Mohammadreza Rouzegar

Berlin, October 2023

This work was done between January 2018 and October 2023 in the Terahertz Physics Group (Prof. Dr. Tobias Kampfrath) of the Department of Physics at the Freie Universität Berlin and at the Department of Physical Chemistry at the Fritz-Haber-Institute of the Max-Planck-Society.

Erstgutachter: Prof. Dr. Tobias Kampfrath

Zweitgutachter: Prof. Dr. Martin Wolf

Tag der Disputation: 18.04.2024

Abstract

The research field of spintronics emerges as a promising solution to address the core challenges posed by charge-based electronic information processing, aiming to reduce power dissipation while delivering lasting endurance and robust read and write capabilities. Spintronic circuits have already made their mark, finding practical applications in commercially accessible magnetic random-access memories. However, to effectively compete with future complementary metal–oxide–semiconductor (CMOS) and photonic technologies, fundamental spin operations speed should ideally extend to terahertz (THz) frequencies. In this respect, an exciting discovery is a new class of highly efficient and broadband THz emitters based on magnetic heterostructures, harnessing spintronic effects at terahertz frequencies.

This work is dedicated to addressing a series of fundamental questions, for example: What is the primary driving force for spin currents in spintronic THz emitters (STEs)? How do these spin currents relate to other processes such as ultrafast demagnetization dynamics? How do spin currents propagate through different material systems? What are the maximum speeds of spin current propagation? How can the spin conductance of various materials be quantified? Finally, how can the amplitude of the THz radiation from STEs be maximized to values exceeding 1 MV/cm?

First, we compare two central phenomena in femtomagnetism: ultrafast demagnetization and ultrafast spin currents in magnetic heterostructures. Strikingly, our findings unveil that both phenomena are driven by the same force, a generalized spin voltage, i.e., the excess of magnetization relative to equilibrium. We conclude that the spin voltage is genuinely ultrafast, and the decay of the spin voltage is predominantly due to spin-flip processes inside the ferromagnet, with only a minor fraction of spins contributing to the transport.

Subsequently, we explore spin current propagation in copper and MgO tunnel junctions. Our results reveal that spin currents in copper propagate at high speed, reaching the Fermi velocity $v_\mathrm{F} = 1.1$ nm/fs with velocity-relaxation time of of $\tau = 4 \pm 2$ fs, and we separate ballistic and diffusive modes of spin transport. Furthermore, we introduce the new concept of THz spin-conductance spectroscopy. We apply this method to measure the spin conductance of an MgO tunnel junction, allowing to separate different spin-transport contributions, including coherent tunneling and incoherent resonant spin tunneling mediated through MgO defects.

Finally, based on these findings, we significantly improve the STE performance by optimizing the heat management and maximizing the THz outcoupling. Our proposed Si-based STE design outperforms previous glass-based STEs by a factor of six, achieving a peak electric field of 1.7 MV/cm. Eventually, Si-STEs prove to be highly effective in inducing nonlinear effects such as the THz Kerr effect in diamond or Zeeman torque in magnets.

In conclusion, this work demonstrates the significant potential of terahertz spin transport that can shape the future of ultrafast circuits.

Kurzfassung

Das Forschungsfeld der Spintronik ist ein vielversprechender Ansatz für die zentralen Herausforderungen, die bei ladungsbasierten elektronischen Informationsverarbeitung auftreten. Sie zielt darauf ab, Wärmeverluste zu reduzieren und gleichzeitig eine dauerhafte Nutzung, sowie robuste Lese- und Schreibfähigkeiten zu bieten. Spintronische Schaltkreise haben bereits erste Erfolge erzielt und finden praktische Anwendung in kommerziell verfügbaren magnetischen Random-Access-Speichern. Um jedoch effektiv mit zukünftigen komplementären Metall-Oxid-Halbleiter- (CMOS) und photonischen Technologien konkurrieren zu können, sollte die Geschwindigkeit der fundamentalen Spinoperationen idealerweise in den Terahertz-Frequenzbereich ausgeweitet werden. Eine bedeutende Entdeckung ist eine neue Klasse hoch effizienter und breitbandiger THz-Strahler, die auf magnetischen Heterostrukturen basieren und spintronische Effekte bei Terahertz-Frequenzen nutzen.

Diese Arbeit widmet sich einer Reihe grundlegender Fragen, z.B.: Was ist die treibende Kraft von Spinströmen in spintronischen THz-Strahlern Emittern (STEn)? Wie korrelieren Spinströme mit dem zentralen Phänomen der ultraschnellen Entmagnetisierungs? Wie breiten sich Spinströme durch verschiedene Materialsysteme aus? Was sind die maximalen Geschwindigkeiten der Spinstrompropagation? Wie kann die Spinleitfähigkeit verschiedener Materialien quantifiziert werden? Und wie kann die Amplitude der THz-Strahlung von STEn optimiert werden, um nichtlineare Effekte anregen zu können?

Zunächst untersuchen wir zwei grundlegende Phänomenene des Femtomagnetismus: ultraschnelle Entmagnetisierung und ultraschnelle Spinströme in magnetischen Heterostrukturen. Bemerkenswerterweise zeigen unsere Ergebnisse, dass beide Phänomene von derselben Kraft angetrieben werden, nämlich von einer verallgemeinerten Spin-Spannung, d.h., dem Überschuss an Magnetisierung im Vergleich zur Gleichgewichtsmagnetisierung. Daraus folgt, dass diese Spin-Spannung tatsächlich auf ultraschnellen Zeitskalen operativ ist und ihre Relaxation hauptsächlich auf Spin-Flip-Streuung im Ferromagneten zurückzuführen ist, wobei nur ein kleiner Teil der Spins zum Transport beiträgt.

Anschließend erforschen wir die Ausbreitung von Spinströmen in Kupfer- und MgO-Tunnelbarrieren. Unsere Ergebnisse zeigen, dass Spinströme mit hoher Geschwindigkeit, nahe der Fermi-Geschwindigkeit $v_{\mathrm{F}} = 1.1$ nm/fs bei Streuzeiten von $\tau = 4 \pm 2$ fs, durch Kupfer propagieren. Dabei gelingt es uns, ballistische und diffuse Modi des Spintransports zu separieren. Darüber hinaus führen wir das Konzept der THz-Spinleitfähigkeitsspektroskopie ein. Wir verwenden diese Methode, um die Spinleitfähigkeit einer MgO-Tunnelbarriere zu messen und separieren verschiedene Spintransportbeiträge, einschließlich kohärentem und inkohärentem, resonantem Spin-Tunneln durch MgO-Defekte.

Basierend auf diesen Ergebnissen verbessen wir schließlich die Leistung des STEs signifikant, indem wir das Wärmemanagement und die Auskopplung der THz-Strahlung optimieren. Der vorgeschlagene Si-basierte STE übertrifft glas-basierte STE um einen Faktor 6 und erreicht eine Spitzenfeldstärke von 1.7 MV/cm. Dabei erweist sich der Si-STE als äußerst effektiv beim Anregen nichtlinearer Effekte wie dem Kerr-Effekt in Diamant.

Abschließend zeigt diese Arbeit das erhebliche Potenzial von Terahertz-Spintronik auf, die die Zukunft ultraschneller Schaltkreise gestalten kann.

Contents

1

Introduction

An important cornerstone of our society is the rapid development of digital communication. There is a permanent quest for high computational power, and faster, smaller and more efficient devices. The electron spin is envisioned to play a pivotal role to meet these growing demands.

1.1 Spintronics

Conventional electronics rely on encoding binary information (0/1) with the charge of electrons. However, we are approaching insurmountable physical limits in our capacity to further enhance the speed and miniaturization of these charge-based electronic devices without significant power dissipations due to the leakage current [152, 194, 263].

Spin-based electronics (spintronics) aims at extending electronic functionalities by incorporating the electron spin degree of freedom. Indeed, binary information (0/1) can be encoded to electron spin states (↑/↓) [11, 195, 211, 213]. Integrating spintronic circuits into existing electronic technology holds the key to future progress. At the least, three fundamental spin operations are essential for constructing spintronic circuits as shown in Fig.1.1: (1) writing information by reversing the spin direction (↑ to ↓), (2) transporting spin angular momentum through space, and (3) detecting the spin information [251, 285]. Each of these spin operations is elaborated further below.

(1) The electron spin can be turned around by applying a torque, which can be achieved through various means. Examples of spin torque sources include an external magnetic field via Zeeman torque, a spin-polarized current using the spin-transfer-torque (STT) [145, 257], or an electric field via spin-orbit torque (SOT) [194]. Indeed, STT is already utilized in magnetoresistive random-access memories (MRAM) to switch the spin orientation [112]. These STT-MRAMs are on the brink of commercial availability through companies such as Samsung or Everspin Technologies [194].

(2) Spin currents can be carried by spin-polarized conduction electrons or spin waves, also known as magnons [45]. They can be induced by gradients of spin voltage (i.e., an excess of spin), temperature or electrostatic potential. The gradient of spin voltage, also known as spin accumulation, is achieved in magnetic heterostructures, in which the inversion symmetry is broken either by the structure or by the light field [30, 43, 67]. Temperature-driven spin-transport effects were discovered only recently, including the spin Seebeck effect (SSE) [15, 218, 248], spin-dependent Seebeck effect (SDSE)[15, 232], anomalous Nernst effect (ANE) and others [15]. Moreover, a gradient in electrostatic potential induces a charge current, that is converted into a spin current via spin Hall effect (SHE) in materials

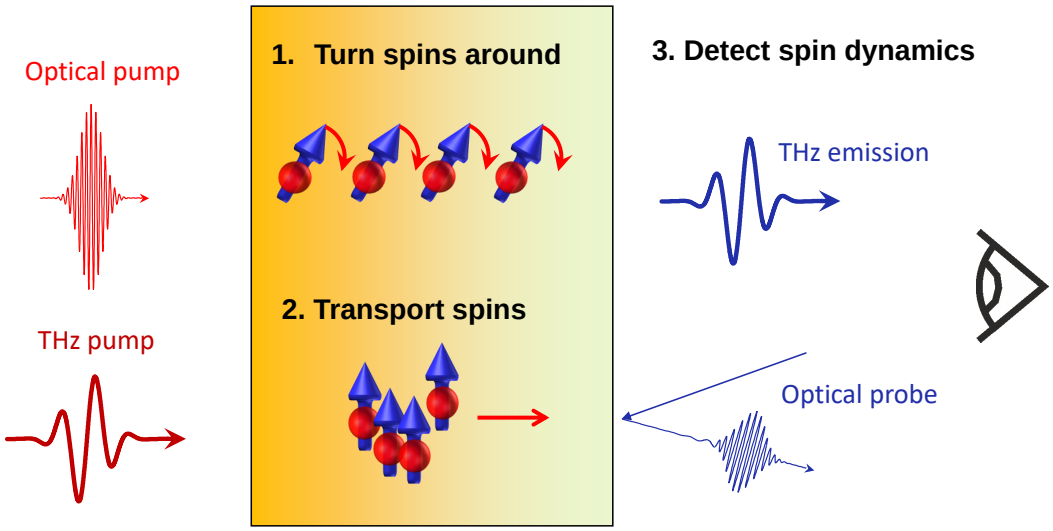

Figure 1.1. | Elementary spin operations. (1) Turning spin around using torque. (2) transport spin by inducing gradients of spin voltage, temperature, or electrostatic potential. (3) detecting spin operations. In ultrafast time scales, femtosecond laser pulses and THz electromagnetic pulses (0.1-30 THz) are used to drive and detect these spin dynamics. This figure is adapted from [120] with permission of Tobias Kampfrath.

with large spin-orbit coupling.

(3) Finally, spin currents can be detected by the torque they exert on magnetization through STT. This torque can be measured by various magneto-resistive and magneto-optical effects [183, 188, 190, 198]. More directly, spin currents can be detected via spin-to-charge conversion (SCC) either in a bulk material with large spin-orbit coupling via inverse spin Hall effect (ISHE) [119, 218] , or at an interface by inverse Rashba Edelstein effect (IREE) [156].

In order to make spintronic operations compatible and competitive with other information carriers such as electrons in field-effect transistors [51] and photons in optical fibers [90], it is essential to push their speed to femtosecond time scale and, thus, into the terahertz (THz) frequency range.

1.2 Implementing THz spintronics

Pushing spintronic operations to ultrafast time scales requires the development of specialized tools for achieving spin operations at THz frequencies and implementing fast detection techniques. Femtosecond (fs) laser pulses (visible to near-infrared) and THz electromagnetic pulses are used to drive and probe spin operations.

The terahertz spectral window ranges from 0.1-30 THz, which corresponds to an electro-

magnetic wave with wavelength of 10-3000 µm or photon energy range of 0.4-125 meV. The THz window fills the gap between frequencies (few 100 THz) of optical light sources and gigahertz (GHz) frequencies of typical electrical sources [29, 92] as shown in Fig. 1.2. THz electromagnetic fields are resonant with many fundamental modes of matter, for example, electronic intraband transport, magnons or phonons in solids [53, 276]. Moreover, typical spin-orbit interaction energies coincide with THz photon energies, suggesting the possibility that spin operations can be pushed to THz frequencies. Consequently, THz spectroscopy is a powerful probe of many fundamental processes in a wide range of materials [119, 141, 218].

A fs laser pulse can be used to deposit ultrafast heat in magnetic systems and drive numerous spin-caloric effects lying in THz frequencies. These ultrafast spin-caloric effects result in THz electromagnetic wave emission (see Fig. 1.1). The emitted THz pulse can be detected by time-domain THz spectroscopy (TDTS). The distinctive feature of TDTS lies in its capacity to simultaneously measure both the amplitude and phase of a coherent THz electric field, eliminating the requirement for phase retrieval through Kramers-Kronig relations [192]. Furthermore, this all-optical technique does not face the limitations of the narrow bandwidth found for electrical circuits.

Additionally, the THz pulse can be used to drive THz spin operations. In fact, the electric field of a THz pulse is used to generate ultrafast charge currents, which can subsequently be converted into a THz spin current via SHE and Rashba-Edelstein effect (REE) [111, 156, 183]. On the other hand, the magnetic field of a THz pulse can exert Zeeman torque on spins, allowing for manipulation of the magnetic order [37]. The development of high-amplitude THz sources allows pushing these spin operations to non-linear regimes [92, 102, 122, 178]. In current table-top setups, THz peak electric fields reach amplitudes around 1 MV/cm with a spectrum predominantly located at low THz frequencies ranging from 0.5-3 THz [54, 91].

Additionally, the THz radiation can be integrated to other well-stablished experimental probes such as angle-resolved photoelectron emission spectroscopy [201] and scanning tunneling microscopy [47, 273] to gain access to fundamental processes on ultrafast time scales.

THz radiation has extensive applications beyond spintronics in various industries owing to its exceptional selectivity and sensitivity. Notably, THz imaging serves an important role in quality control in manufacturing processes [59, 172], as well as in security applications such as at airports [85]. Furthermore, the imminent advent of 6G wireless telecommunication is based on harnessing THz frequencies [58, 135, 225], offering an enormous data transmission rate enabled by the abundant spectrum within the THz range. Simultaneously, the research field of THz radars is experiencing a fast development, driven by the manifold potential applications such as autonomous driving [46, 271]. Due to these impressive potential applications of THz radiation, a central focus of this thesis pertains to the development of a robust, efficient and broadband THz source.

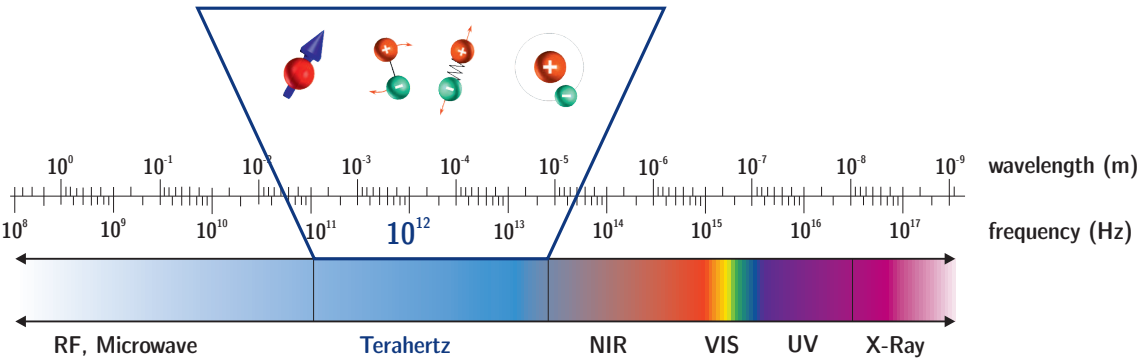

Figure 1.2. | Electromagnetic wave spectrum. The THz spectrum lies in between the microwave and the near-infrared (NIR) regime, covering the frequency range from 0.1 to 30 THz corresponding to wavelengths from 10 to 3000 µm. The THz photon energy (0.4 meV to 125 meV) is resonant with many fundamental modes of matter, such as manipulation of electron spin, electron-hole bound state (excitons), and electronic intraband transport. This figure is taken from [77] with permission from T. S. Seifert and O. Gückstock.

1.3 THz spintronics: relevance and status

The integration of spintronics with femtosecond laser pulses and THz radiation has yielded remarkable outcomes in recent years. Notably, THz pulses have been employed to apply THz spin torques (Zeeman, SOT, NSOT), enabling the fast switching of magnetic order. For instance, Jhuria et al. [108] effectively reversed the magnetic order in Co|Pt stacks via SOT by using a 6 ps THz pulse. More recently, Behovits et al. [20] used intense THz pulses to exert Neel spin-orbit torque (NSOT) to rotate the Neel vector in the antiferromagnet Mn_2Au by up to 30 degrees.

Additionally, THz transmission spectroscopy has been successfully employed to probe magnetoresisitive effects such as GMR [111], anisotropic magnetoresistance (AMR)[183] and anomalous Hall effect [223] at THz frequencies.

Moreover, laser-induced spin caloritronic effects has been demonstrated to operate at the THz frequency regime. Seifert et al. [222] measured the spin current generated by the spin Seebeck effect (SSE) in an insulating ferromagnet/metallic paramagnetic system, observing spin currents with speeds as fast as 1 THz. In metallic magnetic heterostructures, spin currents reached even faster speeds, up to 10 THz [119, 218]. More recently, it has been shown that the ANE is also active at THz frequencies [64].

A significant milestone emerged through the demonstration that spin Hall effect operates at THz frequencies, resulting in numerous new developments and functionalities [218]. In particular, the THz spin current generated by spin caloritronic effects can be converted into a THz charge current, emitting a measurable THz electromagnetic wave. This has led to the emergence of a novel class of spintronic THz emitters (STE) that combines many benefits of other THz sources [119, 218].

Ultrafast spin current generation and transport hold paramount importance in THz spintronics. There are still many fundamental open questions revolving around the driving force of THz spin current generation [19, 67, 170, 218], its relaxation [61, 239], and its

subsequent spin transport dynamics (ballistic, superdiffusive and diffusive) [14, 164, 283]. Form an applied point of view, STEs are routinely used in many laboratories [10, 96, 243, 255, 268] owing to multitude of advantages. However, it is noteworthy to mention that the peak of the THz electric so far has been limited to 0.3 MV/cm [219]. To effectively drive various non-linear phenomena, considerably higher field strengths are required [92]. Thus, a comprehensive study to optimize the amplitude of the THz spin current and THz electromagnetic field out-coupling to maximize the peak field in STE is highly desirable.

With the rapid development of THz spintronics, the need for novel techniques to characterize spin transport on ultrafast timescales in various material systems becomes more pronounced. Ultrafast electron transport is characterized by its conductance via THz transmission spectroscopy [111, 183, 224]. However, an equivalent approach to characterize spin transport in THz frequencies is missing, and thus needs to be developed.

1.4 This thesis

This thesis is motivated to address the above open questions regarding THz spin transport, while simultaneously exploring its potential for practical applications. The primary objectives of this thesis are i) gaining a more profound understanding of laser-induced THz spin transport, ii) developing new techniques to characterize ultrafast spin transport in various material systems by quantities that are as intrinsic as possible, and iii) employing the previous insights to optimize the THz emission from STEs. Ultrashort femtosecond laser pulses and ultrabroadband THz time-domain spectroscopy serves as the main tool to pursue these goals. The subsequent sections elaborate on each objective in more detail.

Chapter 2 is dedicated to providing the essential concepts and theoretical background required to understand the subsequent chapters of this thesis. It begins with an overview of electron and spin transport through metals, interfaces and tunnel barriers. Subsequently, a concise overview of the origin of itinerant magnetism in 3d transition metals is presented. Finally, electromagnetic wave generation and propagation are addressed.

In Chapter 3, all the necessary details on the experimental methods employed throughout this thesis are provided.

Chapter 4 is dedicated to a comprehensive understanding of the underlying driving force of the central phenomena of laser-induced terahertz spin transport (TST) and ultrafast demagnetization (UDM) in magnetic heterostructures. We reliably measure both processes in one setup using broadband terahertz emission spectroscopy. Intriguingly, our findings suggest that the rate of the UDM in a single ferromagnetic metal layer F follows the same time evolution as the TST from F into an adjacent normal-metal layer N such as Pt or W. This observation, combined with our modeling, leads to a remarkable conclusion: UDM in F and TST in F|N are both driven by a generalized spin voltage, i.e., an excess of magnetization, which is defined even for arbitrary, nonthermal electron distributions. These findings allow us to apply the extensive knowledge of UDM to TST to enhance spin-current amplitudes.

In chapters 5 and 6, we make first use of the spin-voltage concept and characterize the

spin current propagation in non-magnetic materials X. We consider two extreme choices of the intermediate layer X: a highly conductive metal X=Cu and insulating X=MgO. Spin transport through Cu and MgO covers an entirely different modes of spin propagation, band-like electron transport and tunneling, respectively. In particular, we investigate ultrafast spin transport within CoFeB (2nm)|$X(d)$|Pt(2nm) with X being either MgO or Cu as an intermediate layer.

More precisely, in chapter 5, the spin current $j_s^d(t)$ transmitted through a X= Cu(d) interlayer with thickness d is measured as a function of Cu thickness d. The spin current exhibits an increasing delay and stronger dispersion when d increases. By using both THz emission and transmission spectroscopy and an analytical dynamic-diffusion model, we can describe the spin current propagation for a spin velocity of 1.1 nm/fs, which agrees well with the Fermi velocity of Cu, and a electron scattering time of $\tau = 4 \pm 2$ fs. In the framework of our model, we can separate ballistic and diffusive components of the spin current. We conclude that, for thicknesses of $d > 2$ nm, the spin current is dominated by diffusive transport.

To characterize spin transport through X= MgO(d) tunnel barriers with thickness d (Chapter 6), we develop a new technique to obtain transport information independent of extrinsic experimental factors. We are able to retrieve the complex-valued spin conductance $\tilde{G}_d(\omega)$ of MgO layers (thickness $d = 0 - 6$ Å) over a wide frequency range (0.5-8 THz). We can explain the measured spin conductance by three different contributions: (i) spin transport through Pt pinholes in MgO, (ii) coherent spin tunneling and (iii) incoherent resonant spin tunneling through defect states in MgO. A remarkable signature of incoherent resonant tunneling is its relaxation time that grows monotonically with d to as much as 270 fs at $d = 6$ Å, in full agreement with an analytical model. We anticipate that the developed terahertz spin-conductance spectroscopy will yield new and relevant insights into ultrafast spin transport for a wide range of materials.

In Chapter 7, we turn to applications by building upon the insights gained in the previous chapters. More precisely, we improve the performance of spintronic terahertz emitters by a factor of up to six in field amplitude through an optimized photonic and thermal environment. We generate terahertz pulses with peak electric fields above 1.5 MV/cm, fluences of the order of 1 mJ/cm^2 and a spectrum covering the range 0.1-11 THz. Remarkably, the field and fluence values are comparable to those obtained from a state-of-the-art terahertz table-top high-field source based on tilted-pulse-front optical rectification in $LiNbO_3$. The optimized STE has all attractive features such as ease-of-use and the straightforward rotation of the terahertz polarization plane. Therefore, it opens up a promising pathway to nonlinear terahertz spectroscopy using STEs.

Finally, Chapter 8 summarizes the main results and findings of this thesis.

2

Conceptual background

This chapter provides the essential theoretical background to comprehend the following chapters of this thesis. It gives a short overview of electron dynamics under electromagnetic wave perturbations in transition metals. It also presents a simple model to understand itinerant magnetism in Fe, Co, and Ni transition metals. Furthermore, spin transport and related Hall effects in metallic heterostructures are discussed. Finally, THz generation and propagation are described in a didactical way.

2.1 Photoexcited electrons in a crystalline solid

Coupled subsystems

This thesis deals with ultrafast dynamics of photoexcited electrons in metallic magnetic heterostructures. To model these dynamics, we subdivide the system into three coupled baths: ionic lattice, electron orbitals and electron spin as shown in Fig. 2.1 [7, 150].

The ionic lattice includes positively charged nuclei and core electrons. The core electrons are bound to the nuclei and have less impact on material properties. These ions are arranged in a periodic structure called Bravais lattice, forming a crystalline structure. This periodic arrangement of ions has a significant impact on the electron dynamics. However, ions can move due to thermal excitations and, thus, perturb the discrete translational symmetry. The motion of ions in the lattice is described by the quasi-particles called phonons [7].

The rest of this Section focuses on electron orbital, while electron spin is discussed in Section 2.3.

2.1.1 Bloch electrons

The motion of electrons can be accurately described by a many-body Hamiltonian including all electrons and ions and their interactions such as the Coulomb interaction. In a system with a large number of electrons and ions, it is practically impossible to solve the underlying Schrödinger equation. Therefore, as a first approximation, we consider the so-called independent-electron approximation, which assumes that each electron moves in an effective single-electron potential $U(\boldsymbol{r})$ produced by the static lattice and other electrons [149]. In a crystal lattice with perfect periodicity, the potential $U(\boldsymbol{r})$ is also periodic, and therefore, it satisfies $U(\boldsymbol{r}+\boldsymbol{R}) = U(\boldsymbol{r})$, where $\boldsymbol{R}$ is Bravais lattice vector.

The wave function Ψ of a single electron in the periodic potential $U(r)$ fulfills the Bloch

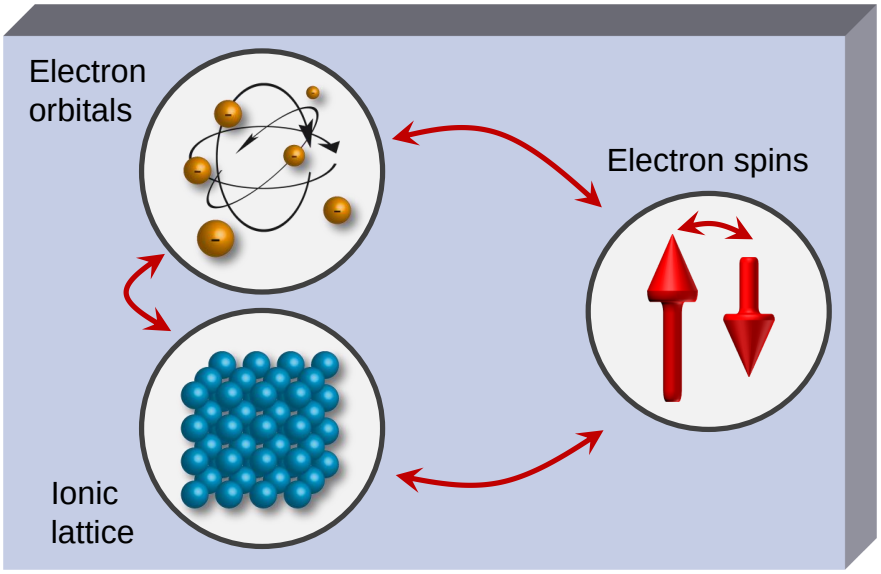

Figure 2.1. | Subsystems of condensed matter. Crystalline solids can be viewed as three bathes: electron orbitals, ionic lattice and electron spin. These subsystems interact with each other (shown here with red arrows). This figure is redrawn from [77] with the permission of Oliver Gückstock and Sebastian Mährlein.

theorem

$$\Psi_{b,\mathfrak{s},\boldsymbol{k}}(\boldsymbol{r}) = \mathrm{e}^{\mathrm{i}\boldsymbol{k}\cdot\boldsymbol{r}} u_{b,\mathfrak{s},\boldsymbol{k}}(\boldsymbol{r}), \tag{2.1}$$

where $\mathrm{e}^{\mathrm{i}\boldsymbol{k}\cdot\boldsymbol{r}}$ is a plane wave with wave vector $\boldsymbol{k}$, $u_{b,\mathfrak{s},\boldsymbol{k}}(\boldsymbol{r})$ is a lattice-periodic function that satisfies $u_{b,\mathfrak{s},\boldsymbol{k}}(\boldsymbol{r}) = u_{b,\mathfrak{s},\boldsymbol{k}}(\boldsymbol{r}+\boldsymbol{R})$ for all $\boldsymbol{R}$ in the Bravais lattice, b is the band index, and $\mathfrak{s} = \uparrow, \downarrow$ is the electron spin. The wavefunction $\Psi_{b,\mathfrak{s},\boldsymbol{k}}$ is called a Bloch wave, and the electrons are called Bloch electrons [7]. Note that the Bloch theorem implies that a single electron does not scatter from fixed ions in a perfect crystal [3]. However, deviations from perfect crystallinity, i.e. phonons and impurities, induce scattering between Bloch states [7].

There are two extreme cases of Bloch electrons: nearly free and tightly bound electrons. Examples of nearly free electrons include the conduction band of alkali metals like Na, and noble metals like Al and Cu. They experience a weak and almost constant potential, since core electrons screen the positively charged ions. Therefore, one can describe the motion of conduction electrons with plane waves of the form $\mathrm{e}^{\mathrm{i}\boldsymbol{k}\cdot\boldsymbol{r}}$ (similar to the Sommerfeld model of the free electron gas) that is modified by the presence of the weak potential [7].

In contrast, the tight-binding model is used to, e.g., describe the d-shells of transition metals where the periodic potential is strong, and electrons are almost bound to their ions.

Fermi-Dirac statistics.

Electrons are fermions and, thus, obey the Pauli exclusion principle, implying they cannot occupy the same Bloch state. A consequence of this fact is that the occupation number of

a given Bloch state $(b, \mathfrak{s}, \boldsymbol{k})$ follows Fermi-Dirac statistics according to [7]

$$n^f(\epsilon, \mu, T) = \frac{1}{1 + \exp[(\epsilon(\boldsymbol{k}) - \mu)/k_\mathrm{B}T]}. \tag{2.2}$$

Here ϵ is the electron energy with wave vector $\boldsymbol{k}$, μ is the chemical potential, $k_\mathrm{B} = 1.38 \times 10^{-23}$ J/K is known as Boltzmann constant, and T is the electronic temperature. At zero temperature $T = 0$ K, electrons fill the energy bands up to the Fermi energy ϵ_F. At higher temperatures, electrons in the energy range of $O(k_\mathrm{B}T)$ below ϵ_F, gain thermal energy and fill the states to an energy range $O(k_\mathrm{B}T)$ above ϵ_F [7]. Assuming the occupation of each Bloch state is fully given by its energy ϵ, the electronic spin-dependent energy density $u_\mathfrak{s}$ and the electron density $\mathcal{N}_\mathfrak{s}$ with spin $\mathfrak{s}$ are given by

$$u_\mathfrak{s} = \int \mathrm{d}\epsilon \; \epsilon \; D_\mathfrak{s}(\epsilon) \; n^f(\epsilon), \tag{2.3}$$

$$\mathcal{N}_\mathfrak{s} = \int \mathrm{d}\epsilon \; D_\mathfrak{s}(\epsilon) \; n^f(\epsilon), \tag{2.4}$$

where $D_\mathfrak{s}(\epsilon) = \sum_k \delta(\epsilon - \epsilon_{\mathfrak{s},\boldsymbol{k}})$ is the spin-dependent density of Bloch states [3,5].

Electron chemical potential.

The electron chemical potential represents the change in Helmholtz free energy, denoted as $F(N, V, T)$, when an electron is added or removed from the system [7]

$$\mu = F(N+1, V, T) - F(N, V, T), \tag{2.5}$$

where N is the number of electrons and V is the volume. The Helmholtz free energy is defined as $F = U - TS$, where U is the internal energy and S is the entropy. For large systems, one can show the chemical potential simplifies to

$$\mu = \frac{\partial \overline{F}(\mathcal{N}, T)}{\partial \mathcal{N}}, \tag{2.6}$$

where $\overline{F} = F(N, V, T)/V$. Importantly, the value of chemical potential determines the number of electrons in the system. Note that the electron chemical potential μ varies with temperature according to Eq. (2.6). This shift can be quantified by using Fermi-Dirac distribution in Eq. (2.2) and the Sommerfeld expansion [7], resulting in:

$$\mu = \epsilon_\mathrm{F} - \frac{\pi^2 k_\mathrm{B}^2}{6} \frac{D'(\epsilon_\mathrm{F})}{D(\epsilon_\mathrm{F})} T^2. \tag{2.7}$$

At $T = 0$ K, the chemical potential equals $\mu = \epsilon_\mathrm{F}$. However, at higher temperatures, chemical potential varies depending on the density of states D and its slope D' at ϵ_F [7].

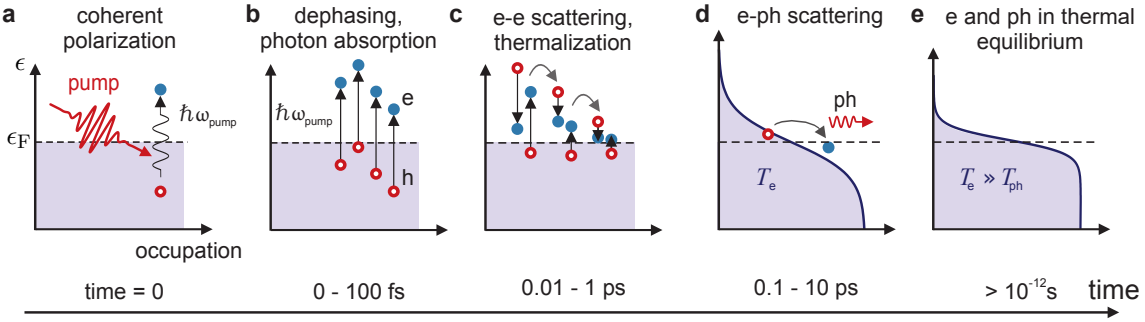

Figure 2.2. | Ultrafast excitation of metals. a) The femtosecond laser pulse creates a coherent polarization of states above and below the Fermi energy in the metal. (b) After a few femtoseconds, dephasing quenches this polarization and creates pairs of electrons and holes. (c) Electron-electron interaction thermalizes the electronic system, which can again be described with Fermi-Dirac statistics with a higher temperature. (d) Electrons interact with phonons (e-ph) and bring them out of equilibrium. (e) On much longer time scales, all subsystems reach an equilibrium with the same temperature. This figure is taken from [118] with the permission of T. Kampfrath.

2.1.2 Ultrafast optical excitation of electrons and subsequent dynamics

Femtosecond laser pulses are used throughout this thesis as a tool to drive ultrafast processes in metallic heterostructures. Once a laser pulse is partly absorbed in metallic layers, it brings all subsystems out of equilibrium [72]. Each subsystem eventually relaxes back to its equilibrium on different time scales, as shown Fig. 2.2.

First, the electric field of the ultrashort laser pulse with angular frequency ω induces a coherent superposition composed of pairs of states above and below the Fermi energy ϵ_F. After a few fs, this coherence has relaxed, and one can characterize the electronic system by occupation numbers [4]. The transition rate of this process is given by Fermi's golden rule

$$\Omega_{ij} = \frac{2\pi}{\hbar}|M_{ij}|^2\delta\left(\epsilon_i - \epsilon_j - \hbar\omega\right), \tag{2.8}$$

where M_{ij} is the matrix element of the electric dipole operator, and $\hbar\omega$ is the energy difference between initial and final states.

Now, the electronic system is in a non-equilibrium state that can be described by occupation numbers, which, in general, do not obey Fermi-Dirac statistics. Due to electron-electron (e-e) scattering, more electron-hole pairs are created, known as carrier multiplication. On a time scale of 10-100 fs, electrons thermalize, and the occupation number can be again approximated by a Fermi-Dirac distribution [72].

In parallel with e-e scattering, due to electron-phonon (e-p) scattering, energy is transferred from electrons to the ionic lattice. Therefore, the electron temperature decreases, while the phonon temperature increases. On the time scale of 100 fs - 1 ps, the electronic and

phononic subsystems equilibrate and reach the same temperature [72]. The energy transfer from electrons to phonons can be described by a two-temperature model (2TM), which is described in appendix A.2. Finally, heat will diffuse to the surroundings on a much longer time scale.

2.2 Electron transport

Electron and spin transport are the central phenomena of this thesis. Generally, they can be driven by spatial gradients of electronic occupation numbers like gradients of electrostatic potential, chemical potential (electron density) or temperature [7]. In this section, our primary focus will be on electron transport, while the description of spin transport is provided in section 2.4.

First, we present the classical Drude model as a simple toy model to find the response to an electric field, i.e., the gradient of an electrostatic potential. Subsequently, we will introduce semiclassical models to describe electron transport.

2.2.1 Classical transport due to electric fields: Drude Model

Originally, Paul Drude imagined a solid as an electron gas, where electrons scatter from ions with a frequency τ_{D}^{-1}. In the presence of an external force, electrons move along the direction of the applied force. When electrons scatter off, e.g., ions, they randomize their velocities, which acts like a friction force on average. One can write the classical equation of motion as [7]

$$\dot{\boldsymbol{p}} = -\frac{\boldsymbol{p}}{\tau_{\mathrm{D}}} + \boldsymbol{F}, \tag{2.9}$$

where the notation $\dot{\boldsymbol{p}} = \frac{\mathrm{d}}{\mathrm{d}t}\boldsymbol{p}(t)$ is used, $\boldsymbol{p} = m_{\mathrm{e}}\boldsymbol{v}$ is the momentum of electrons, and the force is $\boldsymbol{F} = -e(\boldsymbol{E} + \boldsymbol{v} \times \boldsymbol{B})$. And the related current density reads

$$\boldsymbol{j} = -\mathcal{N} e \boldsymbol{v}, \tag{2.10}$$

where $\mathcal{N} = N/V$ is the number of electrons per unit volume V. One can solve Eq. (2.9) for a DC electric field using a steady state approximation (i.e. $\dot{\boldsymbol{p}} = 0$). The resulting current density is then [7]

$$\boldsymbol{j} = \sigma_0 \boldsymbol{E} \qquad \text{with} \quad \sigma_0 = \frac{e^2 \mathcal{N} \tau_{\mathrm{D}}}{m_{\mathrm{e}}}. \tag{2.11}$$

2.2.2 Semiclassical equation of ballistic electron motion

In contrast to the classical particles of the Drude model, electrons are more appropriately described as quantum-mechanical wave packets that propagate in a crystalline lat-

tice according to the Schrödinger equation. A semiclassical model addresses how the *mean* position $\boldsymbol{r}$ and the *mean* wave vector $\boldsymbol{k}$ of each electron wave packet evolves when an external field is applied and when scattering can be neglected. The semiclassical equations of motion are [7]

$$\dot{\boldsymbol{r}} = \boldsymbol{v}_b(\boldsymbol{k}) = \frac{1}{\hbar}\partial_{\boldsymbol{k}}\epsilon_b(\boldsymbol{k}), \tag{2.12a}$$

$$\hbar\dot{\boldsymbol{k}} = \boldsymbol{F}, \tag{2.12b}$$

where $\epsilon_b(\boldsymbol{k})$ is the band structure, and $\boldsymbol{v}_b(\boldsymbol{k})$ is the group velocity of the packet. Thus, in the absence of collisions, the position $\boldsymbol{r}$ and wavevector $\boldsymbol{k}$ of an electron can be fully predicted from the knowledge of the band structure $\epsilon_b(\boldsymbol{k})$ and the form of the external force $\boldsymbol{F}$ [7].

2.2.3 Boltzmann transport equation

Importantly, Eqs. (2.12) do not include electron scattering off impurities and imperfections in the crystal lattice. Instead of tracking the scattering of each electron, the Boltzmann approach considers the dynamics of the occupation numbers $n(\boldsymbol{r},\boldsymbol{k},t)$ of the Bloch states [7]. In equilibrium, electrons follow the Fermi-Dirac distribution $n_0(\boldsymbol{r},\boldsymbol{k},t)$. By applying an external force, one generates a non-equilibrium statistical distribution $n = n_0 + \Delta n$. Its dynamics is described by the Boltzmann equation [7]

$$\frac{\mathrm{d}n}{\mathrm{d}t} = \frac{\partial n}{\partial t}\Big|_{\mathrm{coll}}. \tag{2.13}$$

In the absence of collisions, $\frac{\mathrm{d}n}{\mathrm{d}t} = 0$, implying the volume element $(\mathrm{d}^3\boldsymbol{k}\ \mathrm{d}^3\boldsymbol{r})$ moves ballistically through $(\boldsymbol{r},\boldsymbol{k})$ phase space. In the presence of the collisions, we use the so-called relaxation time approximation and rewrite the right-hand side of Eq. (2.13) as $\frac{\partial n}{\partial t}|_{\mathrm{coll}} = -(n-n_0)/\tau_{\mathrm{D}}$. Assuming the occupation of each Bloch state is given by its energy, i.e., $n(\boldsymbol{k}) = n(\epsilon(\boldsymbol{k}))$, and performing the total derivative on the left side of Eq. (2.13), it gives [39]

$$\partial_t n + (\boldsymbol{F}\cdot\boldsymbol{v})\,\partial_\epsilon n + (\boldsymbol{v}\cdot\partial_{\boldsymbol{r}})\,n = -\frac{n-n_0}{\tau_{\mathrm{D}}}. \tag{2.14}$$

Note that $\boldsymbol{F}$ is a true driving force (e.g. electromagnetic force), but the gradient term $(\boldsymbol{v}\cdot\partial_{\boldsymbol{r}})$ acts as an entropic (statistic) driving force. This version of the Boltzmann transport equation describes how the occupation of particles evolve under an applied force and in the presence of scatterings. Knowing the occupation of electrons, the associated charge current reads as [7, 39]

$$\boldsymbol{j} = -e\sum_b \int \frac{\mathrm{d}^3\boldsymbol{k}}{(2\pi)^3}\ \boldsymbol{v}(\boldsymbol{k})\ \ n. \tag{2.15}$$

Since all partially filled bands contribute to this current, the total current is summed over all partially filled bands [7].

DC electron transport in metals

In the DC regime, the first term in Eq. (2.14) is zero, $\partial_t n = 0$. In order to simplify the Boltzmann equation, we use a diffusion approximation that assumes the changes in the occupation to be small $\Delta n \ll n_0$ [7, 39]. Using partial derivatives for $\partial_{\boldsymbol{r}} n\big(T(\boldsymbol{r}), \mu(\boldsymbol{r})\big)$ with respect to temperature T and chemical potential μ, one can rewrite the Eq. (2.14) as [7]

$$n = n_0 + \tau_{\mathrm{D}} \ (-\partial_\epsilon n_0)\, \boldsymbol{v}(\boldsymbol{k}) \left(-e\ \boldsymbol{\nabla}\mu_{\mathrm{c}} + \frac{\epsilon(\boldsymbol{k}) - \mu}{T}\ \boldsymbol{\nabla} T \right), \tag{2.16}$$

where $\mu_{\mathrm{c}} = -\phi + \frac{\mu}{e}$ is the electrochemical potential, which includes the electrostatic potential ϕ with $\boldsymbol{E} = -\boldsymbol{\nabla}\phi$. Inserting Eq. (2.16) into Eq. (2.15) gives [7]

$$\boldsymbol{j} = \sigma\ \boldsymbol{\nabla}\mu_{\mathrm{c}} + L\ (-\boldsymbol{\nabla} T), \tag{2.17}$$

where σ and L are given by [7, 39]

$$\sigma = \frac{e^2}{3} \int \mathrm{d}\epsilon\ v^2(\epsilon)\, \tau_D D(\epsilon)\, (-\partial_\epsilon n_0)\ , \tag{2.18}$$

$$L = \frac{e^2}{3} \int \mathrm{d}\epsilon\ v^2(\epsilon)\, \tau_D D(\epsilon)\ \ (\epsilon - \mu)\, (-\partial_\epsilon n_0). \tag{2.19}$$

Equations (2.17-2.19) are the central equations in electron transport, and one can derive various effects. According to Eq. (2.17), the driving force for an electronic current can be considered as either a gradient in temperature $\boldsymbol{\nabla} T$ or the electrochemical potential $\boldsymbol{\nabla}\mu_{\mathrm{c}}$.

In metals, $\partial_\epsilon n_0$ has a negligible value except around the Fermi energy. Here, one can approximate $-\partial_\epsilon n_0 = \delta(\epsilon - \epsilon_{\mathrm{F}})$ and find

$$\sigma_0 = \frac{e^2 v_{\mathrm{F}}^2\ \tau_D\ D(\epsilon_{\mathrm{F}})}{3}, \tag{2.20}$$

$$L_0 = -\frac{\pi^2 k_{\mathrm{B}}^2 T}{3e}\ \sigma', \tag{2.21}$$

where $\sigma' = \partial_\epsilon \sigma(\epsilon)|\ \epsilon = \epsilon_{\mathrm{F}}$. By inserting the free-electron-gas density of states $D(\epsilon_{\mathrm{F}}) = \frac{3\mathcal{N}}{m v_{\mathrm{F}}^2}$ into Eq. (2.20), one gets the Drude conductivity that is given in Eq. (2.11).

2.2.4 AC conductivity of a metal

In contrast to the above described DC transport, in the AC regime ($\partial_t n \neq 0$), one can solve Eqs. (2.14) and (2.15) in Fourier domain. We use the following definition

$$\boldsymbol{E}(t) = \int \mathrm{d}\omega \; \boldsymbol{E}(\omega)\, \mathrm{e}^{-\mathrm{i}\omega t}, \tag{2.22}$$

where $\boldsymbol{E}(\omega)$ is the Fourier transform of the oscillating electric field $\boldsymbol{E}(t)$. The frequency-dependent current density reads as [7]

$$\boldsymbol{j}(\omega) = \sigma(\omega)\, \boldsymbol{E}(\omega); \qquad \sigma(\omega) = \frac{\sigma_0}{1 - \mathrm{i}\omega\tau_\mathrm{D}}. \tag{2.23}$$

When $\omega = 0$, Eq. (2.23) correctly reduces to the DC case. At higher frequencies $\omega \gg 1/\tau_\mathrm{D}$, the conductivity simplifies to

$$\sigma(\omega) = \frac{e^2 v_\mathrm{F}^2 \; D(\epsilon_\mathrm{F})}{-3\mathrm{i}\omega}, \tag{2.24}$$

which implies that at high frequencies, $\sigma(\omega)$ does not depend on the collision rate τ_D^{-1} since electrons can follow one field oscillation without any collision.

2.2.5 Fully ballistic vs fully diffusive electron transport

We solve the Boltzmann equation (Eq. 2.14) for two extreme cases: i) the *ballistic regime*, where a scattering-free transport is assumed and ii) the *diffusive regime*, where electrons undergo many collisions and is valid only for times $t \gg \tau_\mathrm{D}$. We will discuss each extreme regime below.

Ballistic electron transport refers to collision-free electronic transport. Solving the Boltzmann equation (Eq. (2.14)) with the initial density $n(z, t = 0) = \delta(z)$ as an impulsive excitation and without any scattering processes gives

$$n(z,t) = \delta(v_{\boldsymbol{k},z} t - |z|), \tag{2.25}$$

which is called ballistic transport. For a spherical Fermi surface and $v_{\boldsymbol{k},z} = v_\mathrm{F}\cos\theta$ with θ being the angle between the $\boldsymbol{k}$ and z axis, the current density reads [221]

$$j_k(z,t) = \frac{z}{2 v_\mathrm{F} t^2}\, \Theta(v_\mathrm{F} t - |z|). \tag{2.26}$$

The current-pulse dispersion in Eq. (2.26) originates from the velocity distribution of the electrons moving ballistically at angle θ relative to the z-axis.

Diffusive transport refers to the other extreme mode of transport, which assumes that electrons undergo many collisions with frequency τ_D^{-1}. Solving the Boltzmann equations

(2.14) and)2.15), to initial condition $n\left(z, t=0\right) = \delta\left(z\right)$ and using the diffusive approximation ($\Delta n \ll n_0$) and the steady state approximation ($\partial_t n \approx 0$) without any external force ($\boldsymbol{F}$=0) gives

$$j\left(z,t\right) = \; -\mathcal{D}\;\partial_z\;\mathcal{N}\left(z,t\right); \qquad\qquad \mathcal{D} = \frac{\tau_{\mathrm{D}} v_F^2}{3}, \tag{2.27}$$

which is also called Fick's first law. Note that this equation is only valid for $t \gg \tau_{\mathrm{D}}$ due to the stationary approximation. Charge continuity is satisfied through

$$\partial_t \mathcal{N} + \partial_z\; j = 0. \tag{2.28}$$

Note that the DC conductivity σ_0 and diffusion coefficient $\mathcal{D}$ are related through the Einstein relation

$$\sigma_0 = e^2 D\left(\epsilon_{\mathrm{F}}\right)\;\mathcal{D}. \tag{2.29}$$

One can find the electron density by solving Eqs. (2.27) and (2.28) and it reads

$$\mathcal{N}\left(z,t\right) = \frac{1}{\sqrt{4\pi\mathcal{D}t}} \exp\left(-\frac{z^2}{4\mathcal{D}t}\right). \tag{2.30}$$

And the diffusive current is obtained by inserting Eq. (2.30) into Eq. (2.27) and it reads

$$j\left(z,t\right) = \frac{z}{2t\sqrt{4\pi\mathcal{D}t}} \exp\left(-\frac{z^2}{4\mathcal{D}t}\right), \tag{2.31}$$

which describes how an electronic current propagates in the diffusive regime. The associated dispersion is due to the electron scatterings.

Fig. 2.3(a) shows the snapshots of the electron current $j(z,t)$ in response to an impulse $n\left(z, t=0\right) = \delta\left(z\right)$ source for fully ballistic (blue curves) and fully diffusive (red curves) transport at $t = 1, 3, 5$ fs, assuming $v_{\mathrm{F}} = 1$ nm/fs and $\tau_{\mathrm{D}} = 10$ fs. One can see that the diffusive transport leads to a larger dispersion compared to ballistic transport due to the scattering events. Fig. 2.3(b) shows the peak of the current at different times. The peak position increases linearly for ballistic transport, but for diffusive transport it is proportional to $\propto\sqrt{t}$, as expected. The slope of these curves corresponds to the speed of propagation and it is shown in Fig. 2.3(c). At early times ($t < 20$ fs), the peak of the diffusive current is faster than the ballistic transport. This result is unphysical since the propagation speed cannot be larger than the Fermi velocity $v_{\mathrm{F}} = 1$ nm/fs. This problem arises since the steady-state approximation used in the fully diffusive transport model is invalid at early times.

The cross-over from ballistic to diffusive transport is called super-diffusive transport. We will address this mode of transport in Chapter 5.

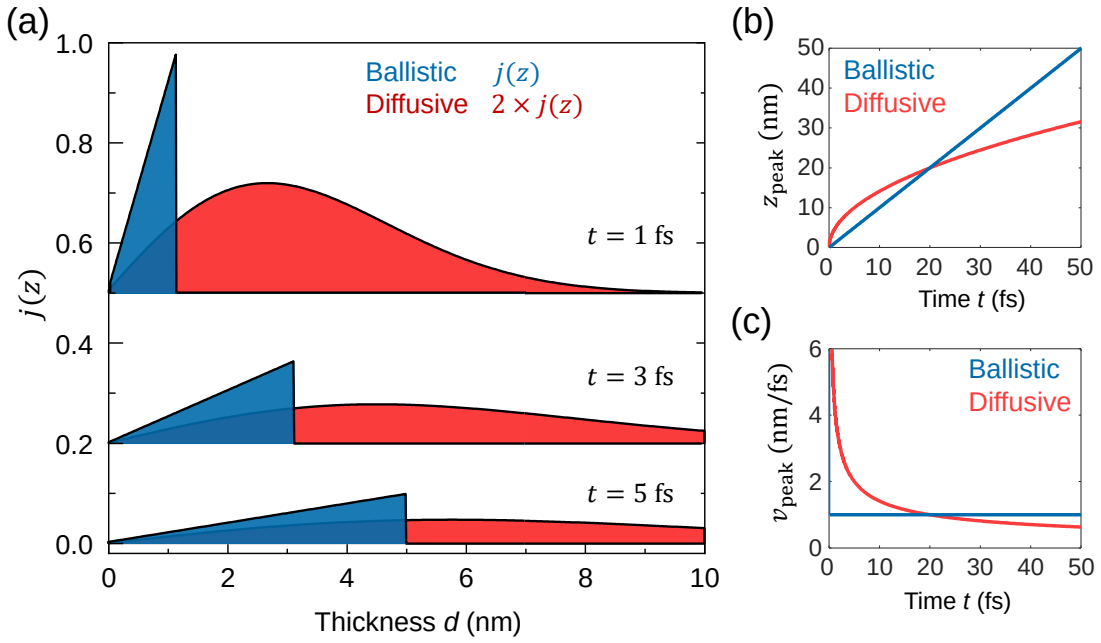

Figure 2.3. |Ballistic vs diffusive electron transport. (a) Snapshots of fully ballistic and fully diffusive transport current $j(z,t)$ at $t = \{1,3,5\}$ fs assuming $v_{\mathrm{F}} = 1$ nm/fs and $\tau_{\mathrm{D}} = 10$ fs. Curves are shifted laterally, and the diffusive current is multiplied by 2 for clarity. (b) Peak position evolution. (c) Peak velocities at different times. The diffusive model leads to an unphysical transport at early times that is faster than the Fermi velocity.

2.2.6 Interface conductance

In the previous section, we described electron transport in bulk metals. However, in the metallic heterostructures studied in this thesis, we encounter electron transport across interfaces. Electrons can transmit through or reflect from an interface, giving rise to an interface resistance. In a transmission channel shown in Fig. 2.4(a), assuming ballistic electron transport between the two leads, one can show the charge current due to the gradient of the electrochemical potential at the interface is [136]

$$J = G_{\mathrm{IF}} \left(\mu_{\mathrm{c}}^{\mathrm{L}} - \mu_{\mathrm{c}}^{\mathrm{R}} \right), \tag{2.32}$$

where $\mu_{\mathrm{c}}^{\mathrm{L}}$ and $\mu_{\mathrm{c}}^{\mathrm{R}}$ are the electrochemical potentials at the left and right sides of the interface, respectively, and G_{IF} is the interface conductance. The latter can be described by the Landauer-Büttiker formalism, and it is given by [136]

$$G_{\mathrm{IF}} = \frac{2e^2}{h} T_{\mathrm{LR}}, \tag{2.33}$$

where $T_{\mathrm{LR}} = \sum_{mn} |t_{mn}|^2$ and the sum is carried over all transverse modes indexed with mn, t_{mn} is the transmission probability calculated from the scattering matrix for mode mn,

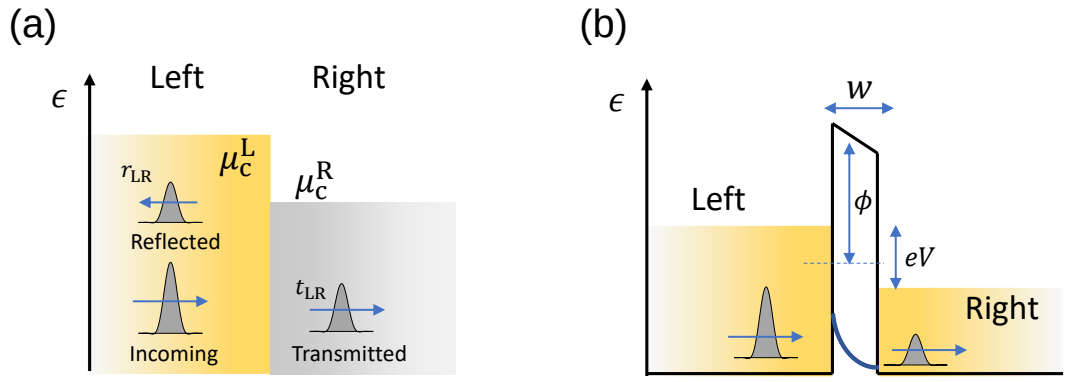

Figure 2.4. | Interface and tunneling conductance. (a) The interface conductance G_{IF} is given by considering the scattering matrix of the electronic wave function at an interface between two leads. (b) The tunneling conductance G_{Tu} for a tunnel barrier with height ϕ and width w.

$G_0 = \frac{e^2}{h}$ is the conductance quantum and the factor of 2 arises due to the spin degeneracy.

2.2.7 Tunneling conductance

Owing to the wave character of electrons, they can also be transported through a potential barrier by tunneling. For example, by applying a voltage over two conductors that are separated by a potential barrier [Fig. 2.4(b)], one can still measure a finite charge current through the barrier. Here, the electron's wavefunction decays exponentially in the barrier, and the transmission probability decreases as the thickness of the barrier increases. In the low-voltage regime, one can calculate the conductance of a tunnel barrier with a width w and a height ϕ [as shown in Fig. 2.4(b)] and it is given by [49, 161, 229]

$$G_{\mathrm{Tu}} = \frac{A}{w}\frac{G_0}{2\pi\lambda}\exp\left(-\frac{w}{\lambda}\right), \tag{2.34}$$

where A is the cross-section, $\lambda = \left(\sqrt{2m_e e\phi}/\hbar\right)^{-1}$ is the tunneling decay length through the insulators, which is typically in the order of a few angstroms [208]. Tunnel barriers have wide range of applications such as magnetic tunnel junctions [190, 274] and resonant tunneling diodes [6]. In Chapter 6, we will investigate spin transport through magnetic tunnel junctions.

2.3 Spin-related interactions

So far, we did not explicitly consider electron spin. Electrons possess an intrinsic angular momentum of $|\boldsymbol{S}| = \frac{1}{2}\hbar$, which is referred to as spin angular momentum. The total angular momentum of an electron can be represented as $\boldsymbol{J} = \boldsymbol{L} + \boldsymbol{S}$, with $\boldsymbol{L}$ denoting the orbital

angular momentum [181]. This angular momentum gives rise to magnetic moment within solids. Other particles such as protons and neutrons also have spin angular momentum of $|\boldsymbol{S}| = \frac{1}{2}\hbar$, but their contributions to the magnetic moment is negligible, specially on ultrafast time scales, due to their weak couplings to electrons.

2.3.1 Spin magnetic moment

The spin magnetic moment is given by [181]

$$\hat{\boldsymbol{\mu}}_{\mathrm{s}} = -\frac{g_{\mathrm{e}}\mu_{\mathrm{B}}}{\hbar}\,\hat{\boldsymbol{s}}, \tag{2.35}$$

where $\mu_{\mathrm{B}} = \frac{e\hbar}{2m_{\mathrm{e}}} = 5.8\ 10^{-5}$ eV/T is the Bohr magneton, $g_{\mathrm{e}} \approx 2$ is the g-factor, and $\hat{\boldsymbol{s}}$ is the spin angular momentum operator [18]. Conventionally, a set of eigenstates of commuting operators $\hat{\boldsymbol{s}}^2$ and $\hat{\boldsymbol{s}}_z$ are chosen as a basis for spin-subspace. One finds eigenvalues of these operators as $|\hat{\boldsymbol{s}}^2| = s\,(s+1)\,\hbar^2$ and $|\hat{\boldsymbol{s}}_z| = m_{\mathrm{s}}\hbar$, where $m_{\mathrm{s}} = \pm 1/2$ is a quantum number referring to "spin-up" and "spin-down" [18]. The minus sign in Eq. (2.35) means that the magnetic moment has an opposite sign compared to the associated angular momentum.

2.3.2 Single-electron relativistic Hamiltonian

Spin angular momentum is not covered in the standard Schrödinger wave equation. One can include spin by considering the Dirac equation instead. Expanding the Dirac Hamiltonian up to the first order in $1/c$, one obtains the following relativistic Hamiltonian [181]

$$\hat{H}_{\mathrm{SE}} = \hat{T} + \hat{T}_{\mathrm{rel}} + \hat{V}_{\mathrm{c}} + \hat{H}_{\mathrm{Darwin}} + \hat{H}_{\mathrm{Z}} + \hat{H}_{\mathrm{so}}, \tag{2.36}$$

where $\hat{T}$ is the kinetic energy operator, and $\hat{T}_{\mathrm{rel}}$ is its relativistic correction. The third term $\hat{V}_{\mathrm{c}}$ is the potential energy, and the term $\hat{H}_{\mathrm{Darwin}}$ is responsible for a relativistic correction known as Zitterbewegung [181]. The relativistic terms $\hat{T}_{\mathrm{rel}}$ and $\hat{H}_{\mathrm{Darwin}}$ are typically negligible compared to the other terms. For spintronics, Zeeman and spin-orbit interactions are the most relevant terms, as detailed in the following.

Zeeman interaction.

The fifth term in Eq. (2.36), $\hat{H}_{\mathrm{Z}}$ is called Zeeman interaction and describes the interaction of an electron magnetic moment $\hat{\boldsymbol{\mu}}_{\mathrm{e}}$ with a magnetic field $\boldsymbol{B}$ as [181]

$$\hat{H}_{\mathrm{Z}} = -\hat{\boldsymbol{\mu}}_{\mathrm{e}} \cdot \boldsymbol{B}. \tag{2.37}$$

It implies that electrons with a magnetic moment anti-parallel to the magnetic field have a lower energy. This effect was discovered by Pieter Zeeman, who reported splitting of the excitation spectrum of sodium under a constant magnetic field [238].

Spin-orbit interaction.

The last term $\hat{H}_{\mathrm{so}}$ can be understood as the interaction of spin and orbital motion. In the

rest frame of the moving electron, the total electric field $\boldsymbol{E}$ in the lab frame transforms into an effective magnetic field equal to $\boldsymbol{B}^{\text{eff}} = -\frac{\boldsymbol{v}\times\boldsymbol{E}}{c^2}$ where $\boldsymbol{v}$ is the speed of the electron. Typical values are $B^{\text{eff}} \approx 4Z$ Tesla, where Z is the proton number of the considered atom. Similar to the Zeeman interaction in Eq. (2.37), one can write [87, 181, 260]

$$\hat{H}_{\text{so}} = -\hat{\boldsymbol{\mu}}_{\text{s}} \cdot \boldsymbol{B}^{\text{eff}}. \tag{2.38}$$

One can estimate the order of magnitude of the spin-orbit energy for heavy metals by $H_{\text{so}} \approx 0.1\ Z^4$ meV which lies in the THz regime (1 THz $\cdot 2\pi\hbar = 4.1$ meV). The effective magnetic field is much larger than the normal available magnetic fields in the lab. Thus, at least for heavy metals, the spin-orbit interaction is stronger than the Zeeman interaction.

2.3.3 Many-electron Hamiltonian

In a system with many electrons and ions, one uses a similar approach as for the single electron relativistic Hamiltonian. Here, the electric and magnetic field experienced by an electron is modified due to the motion of other electrons. In other words, $\boldsymbol{E}_i^{\text{tot}}$ contains the electric field of other electrons, and $\boldsymbol{B}_i^{\text{tot}}$ contains the magnetic field due to the spins and orbital motions of other electrons [87].

The molecular electronic Hamiltonian can be described by the Breit-Pauli Hamiltonian, which is approximated as [87]

$$\hat{H}_{\text{BP}} = \hat{H}_{\text{kin}} + \hat{H}_{\text{cou}} + \hat{H}_{\text{Z}} + \hat{H}_{\text{so}} + \hat{H}_{\text{ss}} + \hat{H}_{\text{ee}}, \tag{2.39}$$

Here, $\hat{H}_{\text{kin}}$ is the kinetic energy operator summed over all electrons, $\hat{H}_{\text{cou}}$ contains electron-ion and ion-ion Coulomb interaction summed over all electrons and ions, $\hat{H}_{\text{Z}}$ is the Zeeman interaction summed over all electrons and ions, and $\hat{H}_{\text{so}}$ is the spin-orbit interaction containing spin-same-orbit and spin-other-orbit interactions. All these Hamiltonians are generalizations of the single-electron Hamiltonian explained in previous section. Finally, $\hat{H}_{\text{ss}}$ is the spin-spin magnetic dipole interaction, and $\hat{H}_{\text{ee}}$ is the electron-electron Coulomb interaction that is in particular responsible for the exchange interaction.

Origin of magnetic ordering: exchange interaction

The spin-spin magnetic-dipole interaction is too weak to induce long range magnetic order in typical magnetic materials. Instead, exchange interaction is responsible for magnetic order in solids. It originates from a combination of the Pauli exclusion principle and the electron-electron Coulomb interaction $\hat{H}_{\text{ee}}$. Wolfgang Pauli postulated that the states of two electrons should differ at least in one quantum number. More precisely, since electrons are fermions and not distinguishable, their wave function should be antisymmetric upon exchanging electrons, i.e., $\Psi(\boldsymbol{r}_1, \boldsymbol{s}_1; \boldsymbol{r}_2, \boldsymbol{s}_2) = -\Psi(\boldsymbol{r}_2, \boldsymbol{s}_2; \boldsymbol{r}_1, \boldsymbol{s}_1)$, where 1 and 2 denote the two electrons [49, 181]. This means that $\Psi = 0$ if $\boldsymbol{r}_1 = \boldsymbol{r}_2$ and $\boldsymbol{s}_1 = \boldsymbol{s}_2$, implying that electrons with parallel spins keep distance from each other and, therefore, reduce their Coulomb energy with the price of an increase in the kinetic energy because Ψ becomes more curved. In certain cases, the reduction in Coulomb energy is favorable, and spins

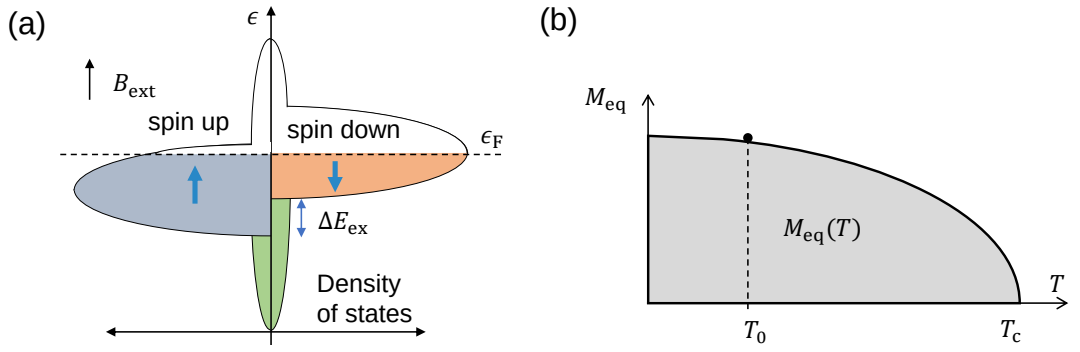

Figure 2.5. | Stoner model and equilibrium magnetization. (a) The density of states of a model band structure of a transition metal ferromagnet under an external magnetic field B_{ext} is shown. Electrons are populated up to the Fermi energy ϵ_{F}. Two spin channels (spin up/down) in the d-band is split by an exchange energy ΔE_{ex}, where spin-up is shown in blue and spin-down in red. The sp-band is shown in green with larger bandwidth compared to the d-band. A net magnetization is resulting due to the population asymmetry in the spin-up and spin-down channels. (b) Temperature-dependent magnetization of a typical ferromagnet, where magnetization vanishes above the Curie temperature.

align parallel with each other and, thus, magnetic order arises.

2.3.4 Itinerant ferromagnetism: Stoner model

In this thesis, we mainly focus on 3d transition metals like Fe, Co, Ni, and their alloys, which show itinerant ferromagnetism. These metals have more-than-half-filled 3d bands.

The Stoner model is presumably the simplest approach to describe itinerant magnetism in transition metals [Fig. 2.5(a)]. Here, it is assumed that the conduction electrons are also responsible for magnetism. In other words, the Stoner model uses Bloch's description of electrons where e-e interaction is accounted by a mean field proportional to the magnetization $\boldsymbol{M}$. Below, we will give a short overview of the Stoner model.

Stoner Model and equilibrium magnetization

Starting point is the Hubbard model [181], whose Hamiltonian reads as

$$\hat{H} = \sum_{\boldsymbol{k},\mathfrak{s}} \xi_k \widehat{\mathcal{N}}_{\boldsymbol{k},\mathfrak{s}} + \frac{I}{V^{\text{F}}} \sum_{\boldsymbol{k},\boldsymbol{k}'} \widehat{\mathcal{N}}_{\boldsymbol{k},\uparrow} \widehat{\mathcal{N}}_{\boldsymbol{k},\downarrow}, \tag{2.40}$$

where ξ_k is the kinetic energy of a Bloch electron with wavevector amplitude $k = |\boldsymbol{k}|$, I is the strength of the effective Coulomb coupling (Stoner parameter), $\widehat{\mathcal{N}}_{\boldsymbol{k},\mathfrak{s}}$ is the number operator for an electron with momentum $\hbar\boldsymbol{k}$, $\mathfrak{s} = \pm 1$ refers to electron spin, and V^{F} is the volume of the ferromagnet. The density of electrons with spin $\mathfrak{s}$ is

$$\mathcal{N}_{\mathfrak{s}} = \frac{1}{V^{\mathrm{F}}} \sum_{\boldsymbol{k}} \left\langle \widehat{\mathcal{N}}_{\boldsymbol{k},\mathfrak{s}} \right\rangle. \tag{2.41}$$

The Stoner model uses a mean-field approximation [181] for the second term in Eq. (2.40), so that the mean-field Hamiltonian reads as

$$\hat{H}^{(\mathrm{mf})} = \sum_{\boldsymbol{k},\mathfrak{s}} \epsilon_{k,\mathfrak{s}} \widehat{\mathcal{N}}_{\boldsymbol{k},\mathfrak{s}} - IV^{\mathrm{F}} \mathcal{N}_{\uparrow} \mathcal{N}_{\downarrow}, \tag{2.42}$$

with energy

$$\epsilon_{k,\mathfrak{s}} = \xi_k + I\mathcal{N}_{-\mathfrak{s}}. \tag{2.43}$$

In equilibrium, majority and minority electrons' expectation value $\left\langle \widehat{\mathcal{N}}_{\boldsymbol{k},\mathfrak{s}} \right\rangle$ are given by the Fermi-Dirac function $n^f_{\mu_{\mathfrak{s}},T}\left(\epsilon_{\boldsymbol{k},\mathfrak{s}}\right)$ with a spin-dependent chemical potential $\mu_{\mathfrak{s}}$ and a spin-independent temperature T

$$\left\langle \widehat{\mathcal{N}}_{\boldsymbol{k},\mathfrak{s}} \right\rangle = n^f_{\mu_{\mathfrak{s}},T}\left(\epsilon_{\boldsymbol{k},\mathfrak{s}}\right), \tag{2.44}$$

and the chemical potentials $\mu_{\mathfrak{s}}$ are defined by the condition that

$$\mathcal{N}_{\mathfrak{s}} = \frac{1}{V^{\mathrm{F}}} \sum_{\boldsymbol{k}} n^f_{\mu_{\mathfrak{s}},T}\left(\epsilon_{\boldsymbol{k},\mathfrak{s}}\right). \tag{2.45}$$

The total particle density is defined as

$$\mathcal{N} = \mathcal{N}_{\uparrow} + \mathcal{N}_{\downarrow}, \tag{2.46}$$

and the magnetization density is

$$m = \mathcal{N}_{\uparrow} - \mathcal{N}_{\downarrow}. \tag{2.47}$$

Combining Eqs. (2.42,2.43,2.46,2.47), one gets the spin-dependent Stoner energies [181]

$$\epsilon_{k,\mathfrak{s}} = \left(\xi_k + \frac{I\mathcal{N}}{2}\right) - \frac{I}{2}\mathfrak{s}m, \tag{2.48}$$

where energy bands are split by an amount $\Delta\epsilon_{\mathrm{ex}} = Im$. One can define the spin-independent chemical potential and the spin voltage/accumulation as [30, 181, 205]

$$\mu = \frac{1}{2}\left(\mu_{\uparrow} + \mu_{\downarrow}\right), \quad \mu_s = \left(\mu_{\uparrow} - \mu_{\downarrow}\right). \tag{2.49}$$

Using the spin-dependent density of states $D_{\mathfrak{s}} = \sum_{\boldsymbol{k}} \delta(\epsilon - \epsilon_{\boldsymbol{k},\mathfrak{s}})$, the magnetization density is found to be

$$m = \int \mathrm{d}\epsilon \, \Big[D_{\uparrow}(\epsilon) n^f_{\uparrow}(\epsilon) - D_{\downarrow}(\epsilon) \, n^f_{\downarrow}(\epsilon) \Big]. \tag{2.50}$$

Here, the density of states for majority and minority spins are related to the spin-independent density of state $D(\epsilon)$ at zero magnetization as [181]

$$D_{\mathfrak{s}} = D\left(\epsilon + \frac{I}{2}\mathfrak{s}m\right). \tag{2.51}$$

Equations (2.50) and (2.51) summarize the definition of itinerant magnetism in the Stoner model and it is shown in Fig. 2.5(a). The Pauli spin susceptibility $\chi_s = \frac{\partial m}{\partial \mu_s}$ is defined as [205]

$$\chi_s^{-1} = \frac{1}{2}\left(\frac{1}{D_{\uparrow}} + \frac{1}{D_{\downarrow}}\right) - I, \tag{2.52}$$

where a positive spin susceptibility $\chi_s > 0$ guarantees a stable ferromagnetic equilibrium.

Stoner Criterion

Stoner was able to explain when it is energetically favorable for a metal to split its density of states and, thus, become ferromagnetic. The energy cost to split the bands by an infinitesimal amount δ is equal to $\Delta E_K = D\left(\epsilon_F\right)\delta^2$. But the Coulomb interaction favors band splitting by an amount $\Delta E_{\mathrm{C}} = -I \, D^2\left(\epsilon_F\right)\delta^2$. Therefore, band splitting is favorable only when $|\Delta E_{\mathrm{C}}| > |\Delta E_K|$, and consequently, the Stoner criterion reads as

$$ID\left(\epsilon_F\right) > 1. \tag{2.53}$$

In 3d transition metals, only metals with more-than-half-filled shells, such as Fe, Co and Ni, show itinerant magnetism since they have many electrons (6-8 electrons) in the d-band, and therefore, the effective Coulomb interaction I is large.

Temperature dependence

At a critical temperature, called Curie temperature T_{c}, a phase transition appears, and the magnetic order vanishes [see Fig. 2.5(b)] [181]. Magnetization as a function of temperature $M(T)$ close to the T_{c} can be empirically described by $\sim (T_{\mathrm{c}} - T)^{\alpha}$ where α is the critical exponent [49].

The Stoner model neglects all transverse excitations and predicts Curie temperature 5-10 times larger compared to the measured experimental values, but surprisingly a correct exponent $\alpha = 1/2$ [181]. Therefore, one should treat the Stoner model as a phenomenological model and use the measured macroscopic parameters like spin-susceptibility and $M(T)$ curve to model experiments.

Spin waves (magnons) at non-zero temperatures can be included through Heisenberg model to predict Curie temperature closer to experimental values [181].

2.4 Spin transport

As discussed in the previous sections, electronic transport in metals depends on the density of states, especially in the vicinity of the Fermi energy. In the Stoner model of a ferromagnet like Fe, the band structure of spin-up and spin-down are shifted in energy [see Eq. (2.51) and Fig. 2.5(a)]. This means that electronic transport is spin-dependent in a ferromagnet, and therefore, a charge current is spin-polarized. One can introduce a simple model to describe the spin transport in a ferromagnet: the Mott's two-channel model.

2.4.1 Two-channel model of spin transport

The density of states in a ferromagnet fulfills $D^{\downarrow}(\epsilon_{\mathrm{F}}) > D^{\uparrow}(\epsilon_{\mathrm{F}})$. Because of the resulting larger phase for spin-conserving scattering, spin-down electrons experience higher scattering rate, $\tau_{\mathrm{D}}^{\downarrow} < \tau_{\mathrm{D}}^{\uparrow}$. Occasionally, electrons can flip their spin during some scattering events, which is characterized by the characteristic time τ_{sf}. Consequently, the two spin channels are coupled, and one needs to solve the spin-dependent coupled Boltzmann equations [249] to find spin-dependent conductivities $\sigma^{\uparrow}$and $\sigma^{\downarrow}$. In the limit of weak spin-flip scatterings, the total charge current in a ferromagnet reads

$$j_{\mathrm{c}} = j^{\uparrow} + j^{\downarrow} = \sigma_{\mathrm{F}} E, \tag{2.54}$$

and $\sigma_{\mathrm{F}} = \sigma^{\uparrow} + \sigma^{\downarrow}$. In the bulk ferromagnet, the majority spin channel, denoted as up spins, has higher conductivity $\sigma^{\uparrow} > \sigma^{\downarrow}$. Consequently, we define $\sigma^{\uparrow} = \alpha_{\mathrm{F}}\sigma_{\mathrm{F}}$ and $\sigma^{\downarrow} = (1-\alpha_{\mathrm{F}})\sigma_{\mathrm{F}}$ where $\alpha_{\mathrm{F}} > 0.5$ is a dimensionless factor that describes the asymmetry of conduction in a ferromagnetic metal. A current of spin angular momentum known as *spin current* is defined as

$$j_{\mathrm{s}} = j^{\uparrow} - j^{\downarrow} = P\sigma_{\mathrm{F}}\, E, \tag{2.55}$$

where $P = j_{\mathrm{s}}/j_{\mathrm{c}} = 2\alpha_{\mathrm{F}} - 1$ is the degree of spin polarization. A non-magnetic metal (N) like Pt and W does not have a spin-polarization ($P = 0$), while a ferromagnetic metal (F) like Fe and Co has a positive spin polarization ($P > 0$).

2.4.2 Ultrafast spin transport across an interface

In this thesis, we deal with ultrafast spin transport across a F|N interface [see Fig. 2.6]. Before the fs laser pulse arrives, the occupations $n^{X\mathfrak{s}}(\epsilon, t)$ are given by the Fermi-Dirac function $n_0(\epsilon)$ at temperature T_0 and chemical potential μ_0, where X=F or N refers to the layer and $\mathfrak{s} = \uparrow, \downarrow$ refers to the electron spin.

The pump pulse deposits energy in the F|N system and brings both layers out of equilibrium, resulting in electron occupations $n^{X\mathfrak{s}} = n_0 + \Delta n^{X\mathfrak{s}}$. In the framework of the Stoner model (Section 2.3), and using Boltzmann-type rate equations, the spin-resolved electron

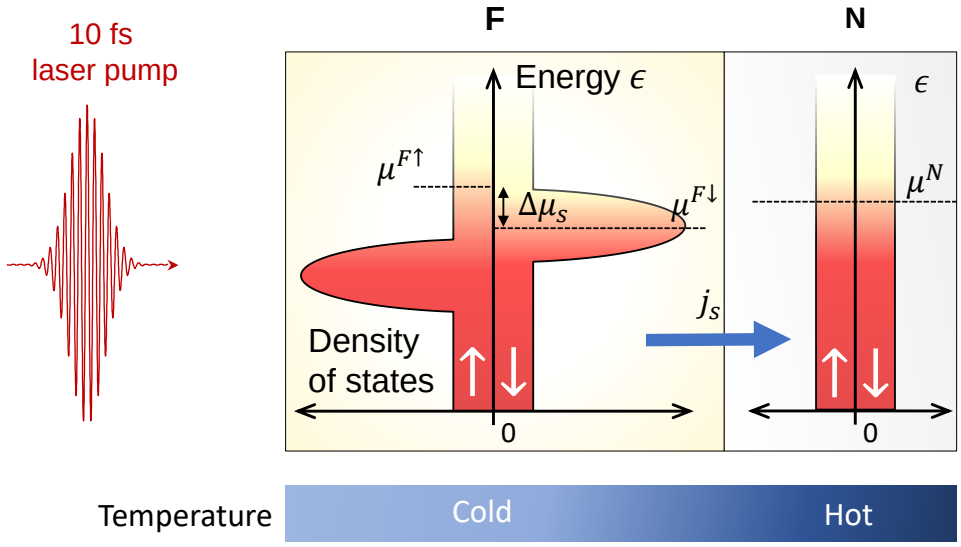

Figure 2.6. | Ultrafast spin current. A fs laser pulse deposits energy in a F|N heterostructure and brings both systems out of equilibrium. An ultrafast spin voltage, i.e., splitting of chemical potentials, builds up in the F layer, since spin-up and spin-down have different densities of states. Moreover, there is a finite temperature difference between F and N layers due to the different pump absorption and different electronic heat capacities. As a result, an ultrafast spin current is injected into the N layer due to the gradient of both spin voltage and temperature across the interface.

current through the F|N interface is given by [205]

$$J^{\mathfrak{s}} = \int \mathrm{d}\epsilon \left(n^{F\mathfrak{s}} - n^{N\mathfrak{s}}\right) g^{\mathfrak{s}}_{\mathrm{tr}}, \tag{2.56}$$

where $J^{\mathfrak{s}} = A^{\mathrm{F|N}} j^{\mathfrak{s}}$ is the spin current, $A^{\mathrm{F|N}}$ is the relevant area of the F|N stack, $g^{\mathfrak{s}}_{\mathrm{tr}}(\epsilon) = \left(T^{\mathfrak{s}}_{\mathrm{tr}} D^{F\mathfrak{s}} D^{N\mathfrak{s}}\right)(\epsilon)$ and $T^{\mathfrak{s}}_{\mathrm{tr}}(\epsilon)$ is a spin-dependent interface transmittance. Note that Eq. (2.56) yields zero spin transfer before the pump pulse arrives because in this case, all distribution functions $n^{F\mathfrak{s}}$ and $n^{N\mathfrak{s}}$ equal the same Fermi-Dirac distribution n_0.

Assuming $\Delta n^{X\mathfrak{s}}$ is non-zero only in a narrow energy window around the chemical potential μ_0 of the unperturbed system, one can use the Sommerfeld expansion and linearize $g^{\mathfrak{s}}_{\mathrm{tr}}(\epsilon)$ around the chemical potential. Further, assuming a vanishing out-of-plane charge current in F|N thin film due to the fast screening $J_c = J^{\uparrow} + J^{\downarrow} = 0$, and assuming chemical potentials for spin-up and spin-down electrons in the N layer are the same, the net spin current $J_s = J^{\uparrow} - J^{\downarrow}$ across the interface is

$$J_s = g_{\mathrm{tr}}(\mu_0)\,\Delta\mu_s + s^{\uparrow}_{\mathrm{tr}}(\mu_0)\left(\Delta T^{F\uparrow} - \Delta T^{N\uparrow}\right) - s^{\downarrow}_{\mathrm{tr}}(\mu_0)\left(\Delta T^{F\downarrow} - \Delta T^{N\downarrow}\right), \tag{2.57}$$

where $\Delta\mu_s = \mu^{F\uparrow} - \mu^{F\downarrow}$ is the spin voltage, $g^{-1}_{\mathrm{tr}} = \left[\left(g^{\uparrow}_{\mathrm{tr}}\right)^{-1} + \left(g^{\downarrow}_{\mathrm{tr}}\right)^{-1}\right]/2$ is the spin transport conductance, and $s^{\mathfrak{s}}_{\mathrm{tr}} = \frac{\pi^2 k_{\mathrm{B}}^2 T_0}{3} g_{\mathrm{tr}}\, g^{\mathfrak{s}\prime}_{\mathrm{tr}}/g^{\mathfrak{s}}_{\mathrm{tr}}$. The first term in Eq. (2.57) is due to the interfacial difference of the spin voltage, and the second and third term is due to

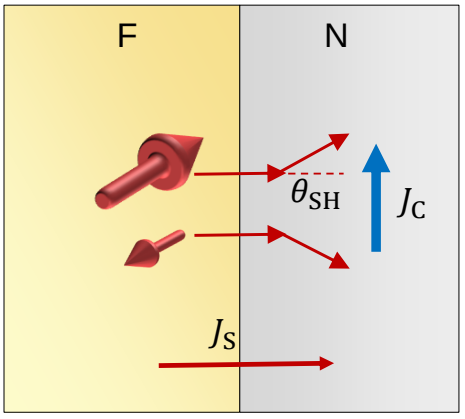

Figure 2.7. | Inverse spin Hall effect. The spin current $\boldsymbol{J}_S$ that is injected from F into the N layer, is transformed into a transverse charge current though inverse spin Hall effect (ISHE). The efficiency of the spin to charge conversion (SCC) is quantified with spin Hall angle θ_{SH}.

the difference of the temperature for electrons with spin up and down across the F and N interface. More details about the ultrafast spin transport in the F|N system is given in Chapter 4 and appendix A.1.

2.4.3 Inverse spin Hall effect

The spin current J_S that is injected into the N layer can be measured by using inverse spin-Hall effect (ISHE). In the non-magnetic layer N with spin-polarization $P = 0$, electrons with opposite spin are deflected by the spin-orbit interaction in opposite directions as shown in Fig. 2.7. Therefore, this out-of-plane spin current is transformed into a transverse charge current with efficiency $\theta_{SH} = J_C/J_S$, where θ_{SH} represents spin Hall angle [218].

Three primary microscopic mechanisms are responsible for deflecting spins in opposite directions in ISHE, and these mechanisms are elaborated upon below.

Intrinsic contribution. The intrinsic deflection mechanism does not require any scattering event. In principle, a Bloch electron moving in a perfect crystal is subject to an intrinsic spin-orbit force [Fig. 2.8(a)]. This force deflects electrons in opposite directions based on orientation of their spins. The induced anomalous velocity is proportional to the Berry curvature [173, 187], which acts like a magnetic field in momentum space.

Skew scattering. The skew-scattering mechanism involves spin-dependent electron scattering off an impurity where electrons change their direction depending on their spin [231] [see Fig. 2.8(b)]. In a simplified picture, skew scattering arises from the spin-orbit coupling in the disorder potential [231]. This contribution is proportional to the electron scattering time τ_D.

Side-jump scattering. This mechanism as shown in Fig. 2.8(c) is an elastic scattering

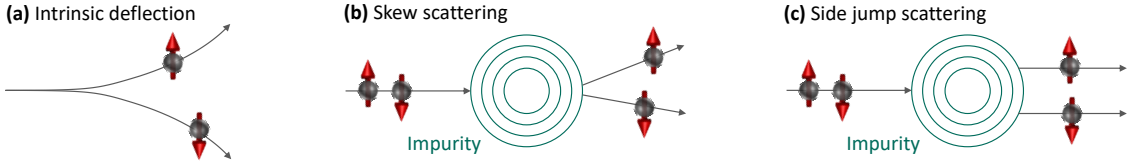

Figure 2.8. | Microscopic mechanisms of the inverse spin-Hall effect (ISHE). (a) The intrinsic mechanism which deflects spins to opposite directions and perpendicular to the driving electric field due to the spin-orbit coupling. (b) Skew scattering as an extrinsic mechanism which involves spin-dependent scattering off impurities. (c) side-jump scattering as an extrinsic mechanism, which involves deflection of spins in opposite direction while conserving its momentum. Figure is redrawn from [77] with permission of O. Gückstock and T. S. Seifert.

process where the electron momentum is conserved but is displaced depending on its spin [231]. The side-jump scattering arises due to the presence of impurities, but is independent of the electron scattering time τ_D [231, 259].

2.5 Electromagnetic wave propagation

The generation and propagation of THz electromagnetic (EM) waves in metallic heterostructures are central to this thesis. Upon excitation of an F|N heterostructure with a fs laser pulse, we have seen that an ultrafast spin current is injected into the N layer (Section 2.3) and transformed into a transverse charge current due to the ISHE (Section 2.4). This ultrafast transverse charge current acts as a Hertzian dipole and thus radiates an EM wave that lies in the THz frequency range. In this section, we will address the THz generation and propagation in these systems.

2.5.1 THz propagation

We consider EM waves propagating along the z direction for the experimental geometry shown in Fig. 2.9 with translational symmetry along x-y direction, and we assume the pump spot is much larger than the emitted THz wavelengths. Their equation of motion, the Helmholtz equation, reads [182]

$$\left(\partial_z^2 + \frac{\omega^2}{c^2}\right) E(z,\omega) = -\frac{\mathrm{i}\omega}{c} Z_0 \, j_{\mathrm{tot}}(z,\omega), \tag{2.58}$$

where $Z_0 = \sqrt{\mu_0/\varepsilon_0} = 376.73\ \Omega$ is the vacuum impedance. In general, $j_{\mathrm{tot}} = j_{\mathrm{c}} + j_{\mathrm{ind}}$, where j_{c} is the external or primary charge current (e.g., the optically induced charge current), and j_{ind} is the current that is induced by the emerging THz EM waves in the medium. To simplify this complicated feedback situation, we consider a homogenous and isotropic medium.

First, we consider a medium without an external source $j_{\mathrm{c}} = 0$. Ohm's law implies that $j_{\mathrm{ind}} = \sigma E$ and, consequently, Eq. (2.58) reads

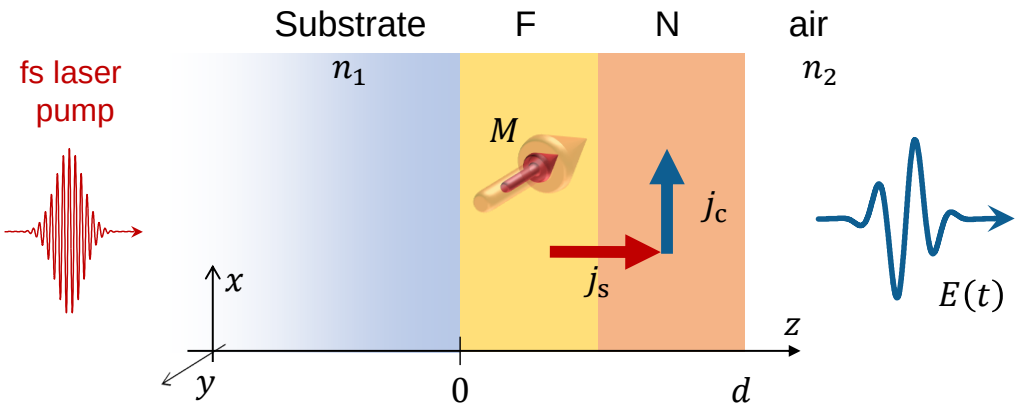

Figure 2.9. | Electric vs magnetic dipole radiation. A fs laser pulse excites an F|N heterostructure leads to (1) transverse charge current in the N layer and subsequent electric dipole radiation, and (2) ultrafast demagnetization of the F layer and subsequent magnetic dipole radiation.

$$\left(\partial_z^2 + k^2\right) E\left(z,\omega\right) = 0, \tag{2.59}$$

where $k^2 = \frac{\omega^2}{c^2} n^2 = \frac{\omega^2}{c^2}\left(1 + \frac{\mathrm{i}cZ_0}{\omega}\sigma\right)$, and n is the refractive index of the medium [182]. The solution of the above equation is a plane wave of the form

$$E\left(z,t\right) = E_0 \mathrm{e}^{\mathrm{i}\left(k_z z - \omega t\right)}, \tag{2.60}$$

where E_0 is the amplitude of the wave, k_z is the z-component of the spatial angular frequency.

2.5.2 THz emission

In this section, we focus on EM-wave emission by electric and magnetic dipoles. The F|N film with conductivity $\sigma(z,\omega)$ is between two half-spaces with refractive indices n_1 and $n_2 \approx 1$, as shown in Fig. 2.9. The laser pulse induces a combination of electric and magnetic dipole inside the film which radiates THz pulses as shown in Fig. 2.9. The electric field of the emitted electromagnetic wave is given by

$$E\left(z,\omega\right) = \int \mathrm{d}z' G\left(z,z',\omega\right) S\left(z',\omega\right), \tag{2.61}$$

where $S\left(z',\omega\right) = -\frac{\mathrm{i}\omega}{c} Z_0 \ \left(j_\mathrm{c}\left(z',\omega\right) + j_\mathrm{ind}\left(z',\omega\right)\right)$ is the source term. The induced current is $j_\mathrm{ind}\left(z',\omega\right) = \sigma(z',\omega) E\left(z',\omega\right)$ according to Ohm's law. The Green's function $G\left(z,z',\omega\right)$ describes the emission and propagation of an electric field from a δ-like source at position

z' in front of a half-space and it is given by [118, 224]

$$G\left(z,z',\omega\right) = \frac{\mathrm{e}^{\mathrm{i}k_2 z}}{2\mathrm{i}k_2}\left(\mathrm{e}^{-\mathrm{i}k_2 z'} + r_{21}\mathrm{e}^{\mathrm{i}k_2 z'}\right), \tag{2.62}$$

where the term $r_{21}\mathrm{e}^{\mathrm{i}k_2 z'}$ arises due to the reflection of the backward-propagating wave from left half-space and $r_{21} = (n_2 - n_1)/(n_2 + n_1)$ is the reflection coefficient. For thin films where $k_2 d \ll 1$, one can use Taylor expansion of the Green's function $G\left(z,z',\omega\right)$ with respect to z'. Further using thin film approximation, one finds the forward-propagating electric filed as

$$\begin{aligned} E\left(z,\omega\right) = -\frac{Z_0}{n_1(\omega) + n_2(\omega) + Z_0\int_0^d \mathrm{d}z'\ \sigma(z',\omega)} \\ \left[\int_0^d \mathrm{d}z' j_{\mathrm{c}}\left(z',\omega\right) - \frac{\mathrm{i}\omega n_1\left(\omega\right)}{c}\int_0^d \mathrm{d}z' z' j_{\mathrm{c}}\left(z',\omega\right)\right] \mathrm{e}^{\mathrm{i}k_2 z}. \end{aligned} \tag{2.63}$$

Here the first term is the zeroth order in z'^0 and is known as electric dipole (ED), and the second term is the first order in z'^1 and is known as electric quadrupole or magnetic dipole (MD). We will explain each term below in more details.

Electric-dipole radiation

The first term in Eq. (2.63) is of electronic dipole origin and usually dominates for a transverse charge current as shown in Fig. 9. In this case, the Eq. (2.63) can be further simplified and the electric field right behind the sample is given by

$$E_{\mathrm{ED}}\left(\omega\right) = -Z\left(\omega\right)\int_0^d \mathrm{d}z'\ j_c(z',\omega), \tag{2.64}$$

and the thin-film impedance is

$$Z\left(\omega\right) = \frac{Z_0}{n_1(\omega) + n_2(\omega) + Z_0\int_0^d \mathrm{d}z'\ \sigma(z',\omega)}. \tag{2.65}$$

Note that the thin-film impedance depends not only on the film conductivity, but also to the refractive index of the left and the right medium.

Magnetic-dipole radiation

Now we consider the magnetic dipole contribution in F|N structure shown in Fig. 2.9. We substitute the source term $j_c(z',\omega) = \partial_{z'} M_y(z',\omega)$ arising from ultrafast demagnetization in the F layer into the Eq.(2.63). This current distribution has a vanishing electric dipole moment, and the magnetic dipole contribution is

$$E_{\mathrm{MD}}\left(\omega\right) = -Z\left(\omega\right)\frac{\mathrm{i}\omega n_1\left(\omega\right)}{c}\int_0^d \mathrm{d}z'\ M_y\left(z',\omega\right), \tag{2.66}$$

where $Z\left(\omega\right)$ is the film impedance and it's given by Eq. (2.65). Note that the magnetic

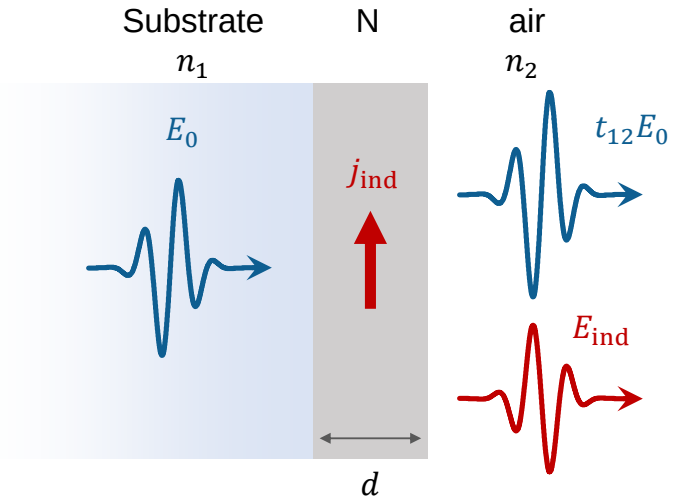

Figure 2.10. | THz transmission through a metallic thin film. The THz pulse E_0 is incident to a metallic thin-film. The THz pulse induces a charge current j_{ind} in the thin-film, which itself emits a THz pulse denoted as E_{ind}. The total transmitted THz pulse is $E_{\text{t}} = t_{12}E_0 + E_{\text{ind}}$ and $t_{12}E_0$ is the transmitted THz pulse from medium 1 to medium 2.

dipole contribution is usually much smaller than the electric dipole contribution.

2.5.3 THz transmission through metallic thin-films

In this section, we describe the basic principle of THz transmission through metallic thin-films. A THz pulse $E_0(z,\omega)$ inside the medium 1 [see Fig. 2.10] is incident on a thin-film with conductivity $\sigma(z',\omega)$. The THz electric field induces a charge current $j_{\text{ind}}(z',\omega)$ inside the thin-film which itself emits a THz pulse denoted as $E_{\text{ind}}(z,\omega)$. The transmitted electric field reads

$$E_{\text{t}}(z,\omega) = t_{12}E_0(z,\omega) + E_{\text{ind}}(z,\omega), \tag{2.67}$$

where $E_{\text{t}}(z,\omega)$ is the total THz transmitted field to the air, $t_{12} = 2n_1/(n_1+n_2)$ is the Fresnel transmission coefficient and $E_{\text{ind}}(z,\omega)$ is the THz pulse emitted due to the induced current. One can use a thin-film approximation where electric field is constant inside the thin film and find the ratio of the transmitted field over the incident field as [74, 224]

$$T(\omega) = \frac{E_{\text{t}}(\omega)}{E_0(\omega)} = \frac{2n_1}{n_1 + n_2 + Z_0\int_0^d \mathrm{d}z'\sigma(z',\omega)}. \tag{2.68}$$

The transmitted THz pulse depends on the the film conductivity and refractive indices of both media. Knowing the refractive indices, one can use THz transmission measurements to determine the conductivity of a thin metal film. We will discuss this in more details in Chapter 3.

3

Experimental methods

A linear time-invariant (LTI) system can be fully characterized by its impulse response. In a mathematical representation, an impulse is a Dirac delta function that describes an extremely short pulse with an extremely large amplitude. Here, we use ultrashort intense laser pulses as our impulse to drive spin-caloritronic effects in magnetic thin films. The ultrashort laser pulse heats the magnetic heterostructure and drives different magnetic phenomena. We use THz spectroscopy to measure the impulse response of the magnetic system reliably. In particular, THz emission and transmission spectroscopy are used in this thesis to measure spintronic effects with large bandwidth from 0.5-30 THz.

3.1 Laser systems

An ultrashort laser pulse is critical to study ultrafast phenomena. Laser systems can provide ultrashort pulses on the femtosecond (1 fs = 10^{-15} s) time scale. A typical laser system consists of a pump laser, an active medium, and an optical cavity. The pump laser creates a population inversion inside the active medium, allowing for the process of stimulated emission. Finally, a pulsed-operation mode is achieved through Kerr lensing inside the active medium with large gain bandwidth [65]. In this thesis, a titanium-doped sapphire (Ti:Sa) is used as the active medium with a gain range from 670 to 850 nm [65].

Two complementary laser systems are used in this thesis: a Megahertz laser oscillator with a high repetition rate (80 MHz) and low pulse energy ($\sim$ 11 nJ) [28], and an amplified laser system with a low repetition rate (1 kHz) and high pulse energy ($\sim$ 7 mJ) [150]. The latter is utilized to generate strong THz fields, which allows for probing and driving elementary excitations in solids such as phonons and magnons [53, 119]. In most of this thesis, the oscillator-based setup is used for THz spectroscopy. This laser system is substantially easier to operate while delivering a similar signal-to-noise ratio compared to the amplified laser system, and it provides short laser pulses with a time resolution of $\sim$10 fs. In Chapter 7, the amplified laser system is used to generate an intense THz electric field.

3.1.1 Megahertz laser oscillator

The megahertz laser oscillator used in this research (Figure 3.1) is the compact M1 from FEMTOLASERS. It is driven by a continuous-wave laser at a wavelength of 532 nm (Coherent Verdi G8). The laser system achieves mode locking by Kerr lensing inside the Ti:Sa active medium, thereby amplifying the most intense modes. The laser system generates ultrashort pulses with a central wavelength of 800 nm, a duration of 10 fs, a

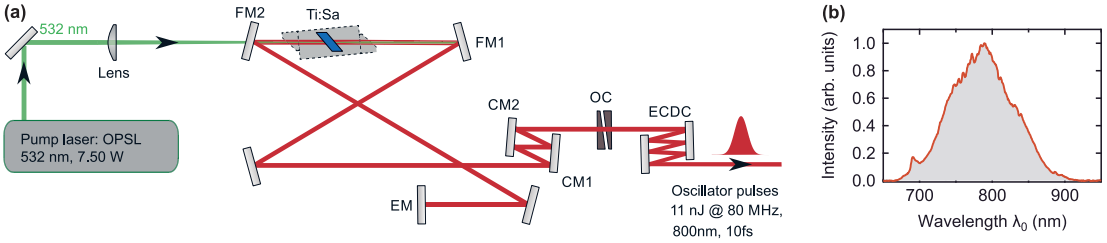

Figure 3.1. | MHz laser system. **(a)** A continuous wave laser at the center wavelength at 532 nm pumps the Ti:Sa crystal which serves as an active medium. The optical cavity consists of two focusing mirrors (FM) which provide high intensities inside the crystal for model locking through Kerr lensing, an end mirror (EM), a pair of chirped mirrors (CM1/2) to compensate the optical dispersion in the cavity, and a partially transmissive out-coupling mirror (OC). Finally, an external cavity dispersion control (ECDC) is used to fine-tune the pulse duration. **(b)** The spectrum of the output laser pulse shown in panel (a). The FWHM is larger than 100 nm, corresponding to pulses with a duration of approx. 10 fs. This figure is taken from Ref. [77] with permissions of O. Gückstock, S. F. Mährlein and L. Braun.

pulse energy of ∼11 nJ, and a repetition rate of ∼80 MHz. The dispersion introduced by the gain medium and other components is compensated with chirped mirrors (CM1/2). Finally, the output of the system is split into a ratio of 80:20 to serve as a pump for THz generation and a probe path for detection, respectively. More details on this laser system can be found in reference [28].

3.1.2 Kilohertz laser amplifier

The amplified laser system uses a femtosecond laser oscillator (COHERENT VITARA-T) that operates at a repetition rate of 80 MHz, a pulse duration of 25 fs and a central wavelength of 790 nm. The output from this oscillator is split, with 25% going towards the detection path and 75% towards the subsequent laser amplifier.

This system employs a combination of a regenerative amplifier (Coherent Legend Elite Duo) followed by a cryogenic amplifier (COHERENT Cryo-SPA) to achieve an amplification of about 10^6. In order to prevent damage to the optical components and avoid nonlinear effects, the pulse peak intensity is lowered by stretching the pulse duration to hundreds of picoseconds with a grating stretcher with high group velocity dispersion. Additionally, the average heat load on the optical components is minimized by reducing the repetition rate to 1 kHz using two Pockels cells. More details can be found in [150].

This laser system uses three stages of amplification which results in pulses with a repetition rate of 1 kHz, pulse energy of 21 mJ, and a central wavelength of 800nm. Then, the amplified pulse is divided into three output beams with an average pulse energy ∼ 7 mJ. Finally, using a grating compressor, the pulse duration is shortened to 35fs. For further information look at Ref. [86, 150].

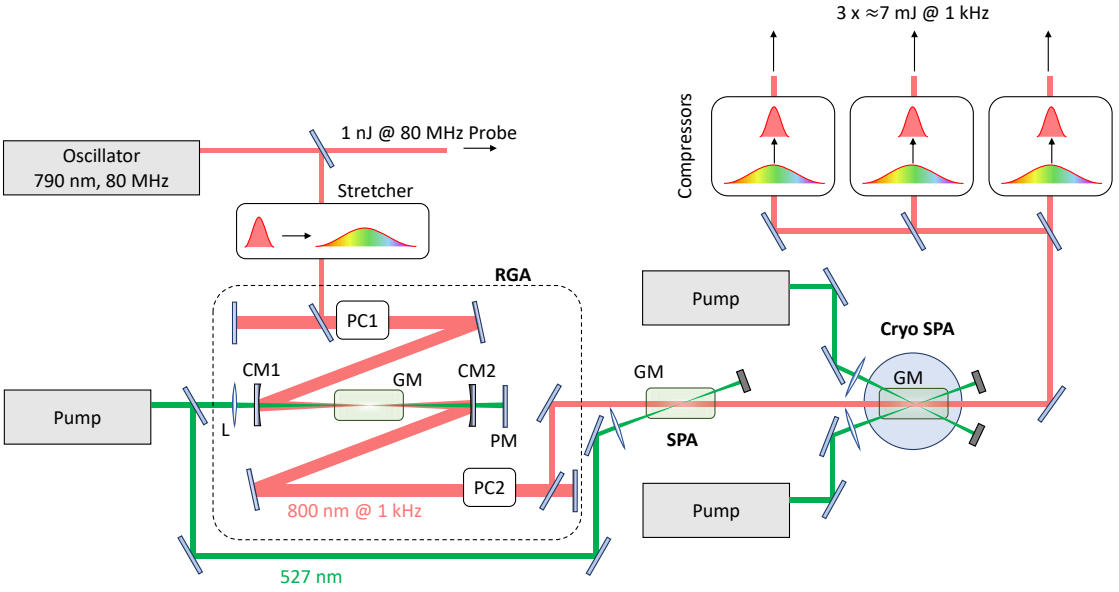

Figure 3.2. | Kilohertz laser system. The kHz laser system consists of an oscillator and three amplification stages with Ti:Sa as gain medium (GM), where they are pumped with an Nd:YLF laser at a center wavelength of 527 nm with a repetition rate of 1 KHz. The oscillator provides a train of short pulses at MHz frequencies at a center wavelength of 790 nm. The oscillator pulses are subsequently stretched by a grating stretcher to prevent damage to optical components and then sent to the optical cavity for the first amplification stage, known as the regenerative amplifier (RGA). One pulse from the MHz oscillator is picked by the first Pockels cell (PC1), enters the cavity, and undergoes as many as $\sim$ 13 round trips. During each round trip, the pulse is amplified inside the Ti:Sa gain medium until the second Pockels cell (PC2) outcouple the amplified pulse out of the cavity. This pulse is further amplified by a single-pass amplifier (SPA) and a cryogenic amplifier (Cryo SPA). Finally, the amplified pulse is separated into three output with an average pulse energy of $\sim$7 mJ and then compressed to a pulse duration of 35 fs using a grating compressor. This figure is taken from Ref. [86] with permissions of J. Heitz.

3.2 THz generation

THz-emission mechanisms can be categorized into i) resonantly induced photocurrents like in spintronic THz emitters (STEs) [119, 218], and ii) off-resonant charge motion, like optical rectification process in organic [281] and inorganic crystals [91, 92]. Below, we will explain each mechanism shortly.

3.2.1 Optical rectification

Optical rectification is a nonlinear optical process that converts broadband visible or near-infrared (NIR) laser light with frequencies ω_i into a THz wave with frequency $\omega_{\mathrm{THz}} = \omega_2 - \omega_1$. In an optical rectification process, the broadband laser pulse passes through a nonlinear crystal with a large nonlinear susceptibility $\chi^{(2)}$ where different frequencies of the pump mix and induce polarization at THz frequencies. The efficiency of the optical rectification process depends on several factors, including the strength of the nonlinearity,

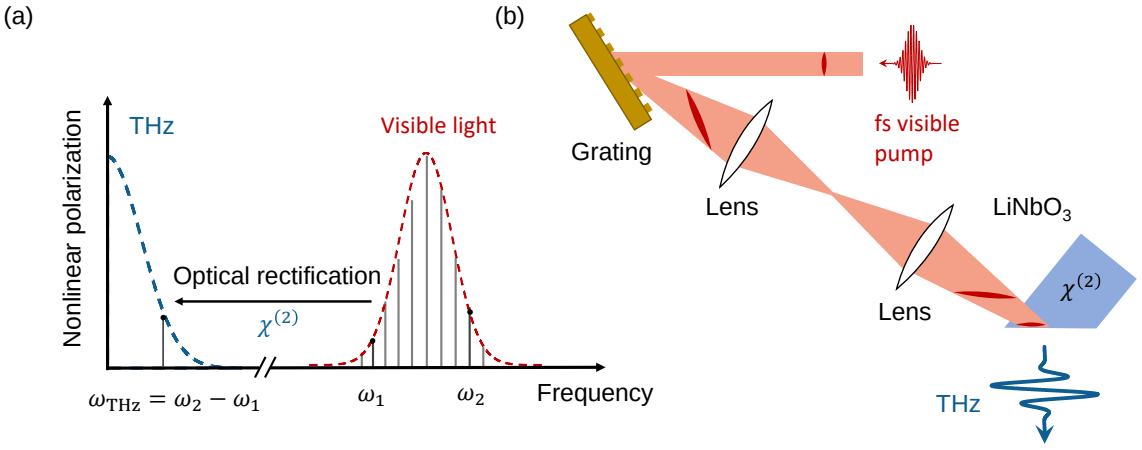

Figure 3.3. | THz generation by optical rectification. **(a)** Visible light passes through a medium with a large non-linear susceptibility $\chi^{(2)}$ wherein different frequencies ω_i mix and their difference $\omega_{\mathrm{THz}} = \omega_2 - \omega_1$ is generated. **(b)** Schematic of the THz generation set up with $LiNbO_3$ with tilted pump pulse wave-front. It consists of two cylindrical lenses, a grating and $LiNbO_3$ prism with specific cut. The orange color shows the pump path and the dark red is the pump wave front. The panel (a) of this figure is redrawn from Ref. [118] with permission of T. Kampfrath and panel (b) is inspired from Ref. [91].

the intensity of the light, and the phase matching conditions, i.e., the difference between the optical group velocity and the THz phase velocity. In materials such as ZnTe and GaP, collinear phase matching is achieved by appropriate pump wavelength and polarization [272], crystal orientation, and the choice of small crystal thicknesses [25]. Collinear phase matching cannot be achieved for materials with a large refractive index like lithium niobite ($LiNbO_3$). For these materials, phase matching is realized by tilting the pump pulse wave-front with a grating [91, 272], as shown in Figure 3.3(b). $LiNbO_3$ can generate THz pulses with a peak electric field beyond 1MV/cm with a spectrum covering the range between 0.1 and 3.5 THz [54, 272, 277].

3.2.2 Spintronic THz emitter

An STE consists of a ferromagnetic layer F, such as CoFeB or Fe, and a paramagnetic layer N with a large spin Hall angle like Pt and W [218]. Upon fs laser heating of the F|N heterostructure, the ferromagnet demagnetizes on a time scale of 100-300 fs [16, 276]. The pump also triggers a spin current $j_s(t)$ from F into the N layer [119, 218]. The spin current inside the non-magnetic layer N is then transformed into a transverse charge current $j_c(t)$ due to the ISHE $j_c(\omega) = e\ \theta_{SH}(\omega)\ j_s(\omega)$, where the spin Hall angle θ_{SH} measures the efficiency of spin-to-charge conversion. There are two contributions to the total THz electromagnetic (EM) radiation: i) magnetic dipole radiation E_M resulting from ultrafast demagnetization of the ferromagnet; and ii) electric dipole radiation due to the transverse charge current inside the Pt. The radiation from electric dipole is typically much larger than the magnetic dipole $E_{j_c} \gg E_M$ for typical spintronic materials [218]. Therefore, the

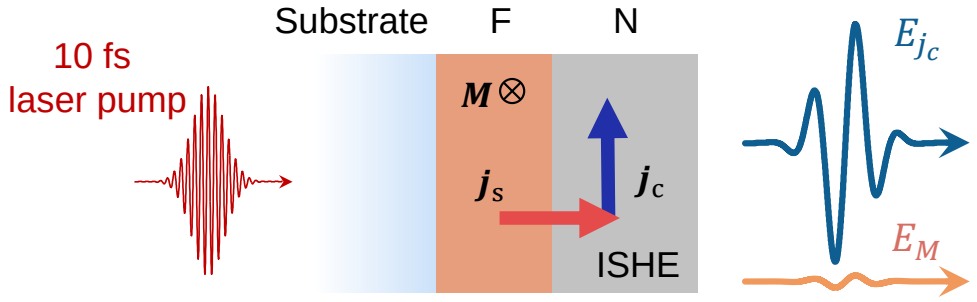

Figure 3.4. | Schematic of a spintronic THz emitter. A fs laser pump heats and demagnetizes the ferromagnet F in a time scale of 100-300 fs, which triggers a spin current j_s into then= Pt layer. This spin current is then transformed into a transverse charge current $j_c = \theta_{SH} j_s$ inside the N layer due to the ISHE. This transverse charge current acts as an electric dipole and readies THz pulse with electric field E_{j_c}. The demagnetization of the ferromagnet acts as a magnetic dipole and it also emit THz pulse with electric field E_M. Typically, the total emission is dominated by E_{j_c} because in most relevant cases $E_{j_s} \gg E_M$ [218].

emitted THz field is

$$E(\omega) = Z_{\mathrm{F|N}}(\omega) \int_0^{d_{\mathrm{Pt}}} dz'\, j_c(z', \omega), \tag{3.1}$$

where $Z_{\mathrm{F|N}}(\omega)$ is the STE conductivity and it is given by Eq. (2.65). Assuming the spin current decays exponentially inside the Pt layer, the electric field simplifies to

$$E(\omega) = e\, Z_{\mathrm{F|N}}\, j_s(\omega)\, \theta_{\mathrm{Pt}} \tanh\left(\frac{d_{\mathrm{Pt}}}{2\lambda_{\mathrm{Pt}}}\right), \tag{3.2}$$

where λ_{Pt} is the spin current relaxation length in Pt and the term $\tanh(\frac{d_{\mathrm{Pt}}}{2\lambda_{\mathrm{Pt}}})$ arises due to the Fabry-Perot behavior of the charge current inside the Pt [218]. When the thickness of the Pt layer is larger than the spin current relaxation length, one can approximate Eq. (3.2) to

$$E(\omega) = e\, Z_{\mathrm{FN}}\, j_s(\omega)\, \theta_{\mathrm{Pt}} \lambda_{\mathrm{Pt}}. \tag{3.3}$$

The spin current is proportional to the deposited energy density inside the ferromagnet $j_s(\omega) \propto A_F/d_F$ where A_F is the fraction of the pump pulse absorbed in the ferromagnet and d_F is the thickness of the ferromagnet. The dynamics and the amplitude of the $j_s(\omega)$ will be discussed in details in chapter 4.

The polarization of the emitted THz pulse is perpendicular to the magnetization $\boldsymbol{M}$, which can be fully controlled by an external magnetic field B_{ext}. This allows for easy polarization rotation without power-loss [79]. The STE offers more benefits such as large and gap-less spectral bandwidth and scalability [218], which will be discussed in Chapter 7.

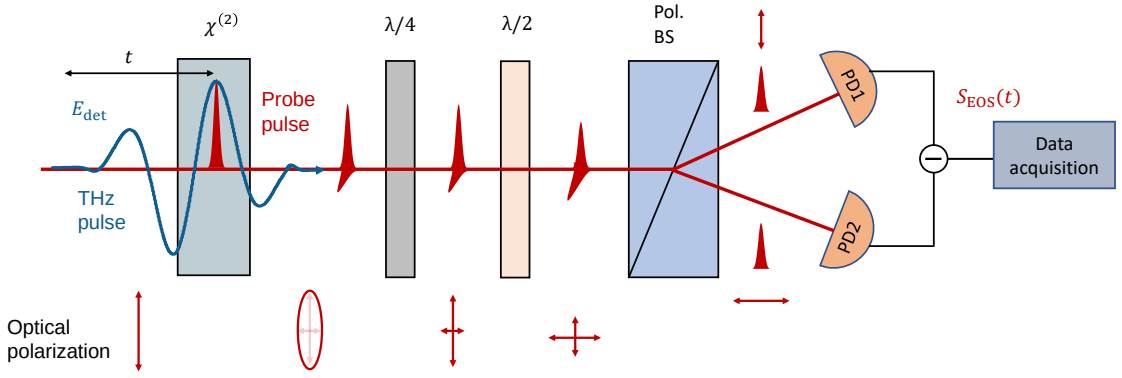

Figure 3.5. | Electro-optic sampling and balanced detection. A femtosecond linearly polarized probe pulse co-propagates with the THz pulse through an electro-optic crystal with a large nonlinear susceptibility $\chi^{(2)}$. The THz electric field transiently changes the refractive index of the nonlinear medium. The probe pulse polarization changes from linear to elliptical by passing through the detection crystal. The change in probe polarization is measured with a balanced detection setup consisting of a $\lambda/4$ waveplate, a $\lambda/2$ waveplate, a polarizing beam splitter (pol. BS), and two photodiodes (PD1/2). The $\lambda/4$ waveplate transforms the small ellipticity into a linearly polarized beam with small rotation. The subsequent $\lambda/2$ waveplate rotates the polarization by 45° with a slight imbalance. Subsequently, the polarizing beam splitter separate the s and p polarization, which is then measured with two photodiodes. The difference in the signals measured with photodiodes is proportional to the amplitude of the THz electric field at a given THz-probe pulse delay t. The THz waveform can be fully retrieved by varying the delay t. This figure is adapted and redrawn from [284].

3.3 THz electric field detection

THz electric field is measured by electro-optic sampling (EOS) within this thesis. EOS allows one to measure both the amplitude and phase of the THz pulse simultaneously [121, 141]. This is a significant advantage of the THz time-domain spectroscopy compared to other methods, which rely on Kramers-Kroning relations to retrieve the phase of the signal [25]. We use Pockels effect for EOS, which will be explained in the next section.

3.3.1 Electro-optic effect

The linear electro-optic effect, also known as the Pockels effect, describes a change in the refractive index of a medium caused by an applied electric field. This is a $\chi^{(2)}$-effect and, therefore, only occurs in a medium with broken inversion symmetry. The THz pulse induces a transient birefringence in the detection crystal proportional to the THz electric field $\Delta n(t) \propto E_{\mathrm{THz}}(t)$ which can be measured by a co-propagating short probe pulse [279]. Typical materials used as detection crystals in this thesis are ZnTe and GaP [121, 141].

To detect a THz pulse, a linearly polarized probe pulse co-propagates with the THz pulse through a detection crystal. The probe pulse polarization changes from linear to elliptical due to the induced birefringence in the detection crystal. This induced probe ellipticity is measured with a balanced-detection setup, which is explained in the next section.

3.3.2 Balanced detection

The induced probe ellipticity after the detection crystal is measured with a balanced-detection setup consisting of a $\lambda/4$ and a $\lambda/2$ waveplate, a polarizing beam splitter, and two photodiodes. The $\lambda/4$ waveplate transform the induced ellipticity into a linear polarization, which is now rotated slightly compared to the original polarization. The $\lambda/2$ waveplate is aligned to rotate the probe polarization by 45° such that the polarizing beam splitter separates it into two orthogonal linearly-polarized beams with slight imbalance due to the THz pulse. This slight imbalance is measured by subtracting the signals from the two photodiodes. In the absence of a THz pulse, the intensity of light at the two photo diodes are equal which implies a zero signal.

In a linear regime, i.e., for small probe ellipticities, under perfect phase matching conditions and assuming a δ-like probe pulse, one can relate the measured photodiode intensities I_1 and I_2 to the transient THz electric field E_{det} at the detector position by [107]

$$S_{\mathrm{EOS}}(\tau) = \frac{I_2 - I_1}{I_2 + I_1} = \frac{2\pi d_{\mathrm{det}} n_0^3 r_{41}}{\lambda_{\mathrm{pr}}} E_{\mathrm{det}}(\tau), \tag{3.4}$$

where $S_{\mathrm{EOS}}(\tau)$ is the EOS signal, d_{det} is the detection crystal thickness, n_0 is the crystal refractive index, λ_{pr} is the probe central wavelength, and r_{41} is the effective electro-optic coefficient capturing the efficiency of the electro-optic effect. However, this is not accurate for broadband THz spectroscopy.

3.3.3 From EOS signal to electric field

Typically, phase matching condition is not fulfilled for a broadband THz electric field at the detector position. To detect a broadband THz electric field E_{det} from the EOS signal S_{EOS}, one needs to carefully model the detection response function H_{EOS}, considering phase matching conditions and dispersions of both refractive index and the second order susceptibility $\chi^{(2)}$ in the THz range [121, 141]. In the linear regime, Eq. (3.4) becomes a convolution of the form

$$S_{\mathrm{EOS}}(t) = \left(H_{\mathrm{EOS}} * E_{\mathrm{det}}\right)(t), \tag{3.5}$$

where H_{EOS} captures the EOS in the detection crystal. THz electric field can be simply calculated in the frequency domain by $E_{\mathrm{EOS}}(\omega) = S_{\mathrm{EOS}}(\omega) / H_{\mathrm{EOS}}(\omega)$ where a Fourier transformation with respect to t is used.

3.4 THz spectroscopy

THz spectroscopy is used here to monitor the spin dynamics. Two main techniques are used: i) THz-emission spectroscopy (TES) and ii) THz-transmission spectroscopy (TTS). In both techniques, we use a double-modulated pump pulse. First, a mechanical chopper

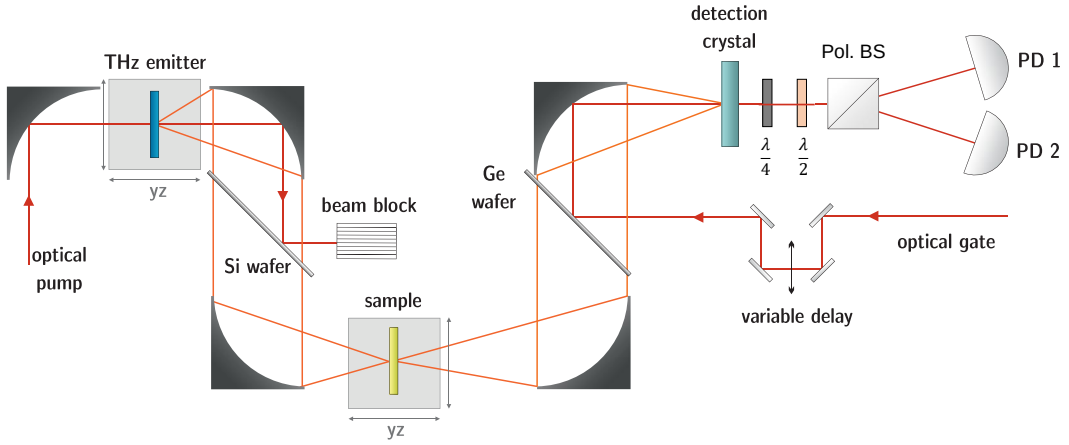

Figure 3.6. | THz emission and THz transmission spectroscopy. In THz emission mode, a magnetic heterostructure sample (THz emitter) is placed in the first focus and there is no sample in the second focus. The optical pump is focused into the sample by the first parabolic mirror and generates a THz electromagnetic field. The emitted THz electric field is divergent and it is collimated by the subsequent parabolic mirror. Si and Ge wafers are transparent for THz frequencies, while they reflect the transmitted optical pump. The THz field is then refocused into the detection crystal. The optical probe (gate) is also focused into the detection crystal and co-propagates with THz pulse. The THz signal is subsequently measured via EOS. In THz transmission mode, a THz emitter is placed in the first focus and the sample is placed in the second focus. The generated THz pulse now is focused into the sample and interacts with it. The transmitted THz pulse is then measured similarly via EOS. The figure is taken from Ref. [77] with permission of Oliver Gückstock.

modulates the pump pulse intensity at frequency $f_{\text{Chopper}} = 30$ KHz to mitigate the $1/f$ noise. Second, the delay between the pump and the probe pulse t is modulated with a shaking reflectometer at frequency $f_{\text{shaker}} = 25$ Hz for fast scanning of the THz waveform. Combining both modulations, the setup can achieve a shot-noise-limited detection of the THz signal.

3.4.1 THz emission spectroscopy

THz emission spectroscopy (TES) is the primary method used in this thesis. The general layout of TES is shown in Fig. 3.6. Here, for instance, an F|N sample is placed in the first focus without any sample at the second focus. The pump pulse heats the F|N sample and triggers a spin current $j_s(t)$ from F into the N layer. As detailed in section 3.2, the spin current leads to the emission of a THz EM wave with electric field proportional to the spin current $E_{\text{sam}}(t) \propto j_s(t)$. The electric field of the THz pulse $E_{\text{sam}}(t)$ is detected via EOS sampling and balanced detection as shown in the Fig. 3.6. The objective here is to extract the spin current $j_s(t)$ in magnetic heterostructures from the measured EOS signal $S_{\text{EOS}}(t)$. Below, we will explain this procedure step by step.

THz pulse propagation

The THz EM wave emitted from the sample propagates to the detection crystal. The electric field of the THz wave directly behind the sample $E_{\text{sam}}(t)$, and at the detector position $E_{\text{det}}(t)$ are related through the convolution of the form

$$E_{\text{det}}(t) = (H_{\text{prop}} * E_{\text{sam}})(t), \tag{3.6}$$

where $H_{\text{prop}}(t)$ captures the THz pulse propagation from the sample to the detector. The THz-pulse-propagation transfer function $H_{\text{prop}}(t)$ can be determined by using a reference emitter based on optical rectification. Here, we use a well-known reference emitter, such as 50-µm-thick GaP(110) crystal, in the first focus close to the sample of interest. The GaP crystal emits a THz wave $E_{\text{sam}}^{\text{GaP}}(t)$ which propagates to the detector crystal $E_{\text{det}}^{\text{GaP}}(t)$. In the frequency domain, the propagation transfer function is given by $H_{\text{prop}}(\omega) = E_{\text{sam}}^{\text{GaP}}(\omega)/E_{\text{det}}^{\text{GaP}}(\omega)$. Note that $E_{\text{sam}}^{\text{GaP}}(\omega)$ is calculated and $E_{\text{det}}^{\text{GaP}}(\omega)$ is measured with EOS.

Spin current extraction

Once measuring the THz-pulse-propagation H_{prop} and EOS transfer functionsH_{EOS}, we can extract the spin current from EOS signal. In frequency domain, the EOS signal $S_{\text{EOS}}(\omega)$ is related to the $E_{\text{sam}}(\omega)$ by

$$E_{\text{sam}}(\omega) = \frac{S_{\text{EOS}}(\omega)}{H_{\text{EOS}}(\omega) H_{\text{prop}}(\omega)}. \tag{3.7}$$

Finally, the spin current is found through the relation

$$j_{\text{s}}(\omega) = \frac{E_{\text{sam}}(\omega)}{eZ(\omega)\theta_{\text{SH}}\lambda_{\text{N}}}. \tag{3.8}$$

The film impedance $Z(\omega)$ can be measure by TTS that is described in the next section.

3.4.2 THz transmission spectroscopy

THz-transmission spectroscopy aims at measuring the frequency-dependent impedance $Z(\omega)$ of a sample. In metallic samples, one can extract the electrical conductivity $\sigma(\omega)$ from the frequency-dependent impedance $Z(\omega)$ as detailed in Chapter 2. One can use the Drude model (described in section 2.2) for the measured film conductivity $\sigma(\omega)$ to find the electron scattering time τ_{D}.

In TTS, the THz emitter is placed in the first focus and the sample of interest is placed in the second focus as shown in Figure 3.6. The transmitted THz signal through the sample $S_{\text{sample}}(\omega)$ and the bare substrate $S_{\text{substrate}}(\omega)$ is measured via EOS. The complex-valued sample THz transmission $T(\omega)$ is then found from the ratio between the two signals

$$T(\omega) = \frac{S_{\text{sample}}(\omega)}{S_{\text{substrate}}(\omega)} = \frac{2n_1(\omega)}{Z_0} Z_{\text{sam}}(\omega) = \frac{2n_1(\omega)}{n_1(\omega) + n_2(\omega) + Z_0 \int_0^d dz' \sigma(z', \omega)} \tag{3.9}$$

where n_1 and n_2 are the refractive indices of the substrate and air, respectively. More details about the derivation of the formula above is given in section 2.5.

4

Laser-induced terahertz spin transport in magnetic nanostructures arises from the same force as ultrafast demagnetization

Laser-induced terahertz spin transport (TST) and ultrafast demagnetization (UDM) are central but so far disconnected phenomena in femtomagnetism and terahertz spintronics. Here, we use broadband terahertz emission spectroscopy to reliably measure both processes in one setup. We find that the rate of the UDM in a single simple ferromagnetic metal film F such as $Co_{70}Fe_{30}$ or $Ni_{80}Fe_{20}$ has the same time evolution as the TST from F into an adjacent normal-metal layer N such as Pt or W. As this remarkable agreement refers to two very different samples, an F layer vs an F/N stack, it does not result from the trivial fact that TST out of F reduces the F magnetization at the same rate. Instead, our observation strongly suggests that UDM in F and TST in F/N are driven by the same force, which is fully determined by the state of the ferromagnet. An analytical model quantitatively explains our measurements and reveals that both UDM in the F sample and TST in the associated F/N stack arise from a generalized spin voltage, i.e., an excess of magnetization, which is defined for arbitrary, nonthermal electron distributions. We also conclude that contributions due to a possible temperature difference between F and N, i.e., the spin-dependent Seebeck effect, and optical intersite spin transfer are minor in our experiment. Based on these findings, one can apply the vast knowledge of UDM to TST to significantly increase spin-current amplitudes and, thus, open up new pathways toward energy-efficient ultrafast spintronic devices.

Publication information

This chapter was published as **Laser-induced terahertz spin transport in magnetic nanostructures arises from the same force as ultrafast demagnetization** by Reza Rouzegar, Liane Brandt, Lukáš Nádvorník, David A. Reiss, Alexander L. Chekhov, Oliver Gueckstock, Chihun In, Martin Wolf , Tom S. Seifert, Piet W. Brouwer, Georg Woltersdorf, Tobias Kampfrath in Physical Review B **106**, 144427 (2022) [205]. DOI: https://doi.org/10.1103/PhysRevB.106.144427.

Author contributions

RR and TK conceived the experiments. RR performed the experiment and analyzed the data. The samples were fabricated by LB and GW. The theory was done by PB, TK and DR. The manuscript was written by RR and TK with help and discussion contributions of all authors.

4.1 Motivation

Fundamental operations in future spin-based electronics are the manipulation of magnetic order, the transport of spin angular momentum and the detection of spin dynamics [251]. The research fields of femtomagnetism and terahertz spintronics aim to push the three operations to femtosecond time scales and, thus, terahertz bandwidth [57, 60, 126, 127, 153, 251, 257]. Figure 4.1 shows the model systems in which two key phenomena of ultrafast spin dynamics are studied extensively: a single ferromagnetic metal layer F [Fig. 4.1(a)] and a F|N stack, where N is a normal-metal layer [Fig. 4.1(b)].

4.1.1 Ultrafast demagnetization (UDM)

In F samples, uniform excitation by a femtosecond laser pulse induces ultrafast demagnetization [UDM; Fig. 4.1(a) [16, 94, 126, 132, 204, 262]. This effect reveals the time scales of elementary spin interactions with electron orbital and lattice degrees of freedom and is a central ingredient for ultrafast magnetization switching [57, 127]. Recent experiments on ferromagnetic Fe indicate that, on a time scale of 100 fs and above, the UDM dynamics are independent of the pump photon energy and only determined by the energy the laser pulse deposits in the electronic system [38, 236]. UDM is accompanied by transfer of spin angular momentum to the crystal lattice, as observed directly by ultrafast X-ray and electron diffraction probes [55, 239]. Rate-equation-type theories can successfully explain UDM and involve spin flips [35, 169], or magnon emission [18, 19, 132, 155, 247] due to electron scattering together with spin-orbit coupling. Alternatively, exact time propagation of small clusters [244] and time-dependent density-functional theory [133] were shown to be powerful approaches to modeling UDM.

4.1.2 Terahertz spin transport (TST)

In F|N stacks, uniform laser excitation not only triggers UDM, but also terahertz spin transport (TST) between F and N [Fig. 4.1(b)] [40, 57, 61, 119, 153, 154, 209, 246]. Such spin currents can be used to exert spin torque at ultrashort time and length scales. They may, thus, excite terahertz magnons [3, 137, 200] and, ultimately, switch magnetic order [127]. TST also serves to efficiently generate broadband terahertz electromagnetic pulses for photonic and spectroscopic applications [31, 63, 113, 163, 189, 217, 218, 224, 243, 255, 266, 268, 270].

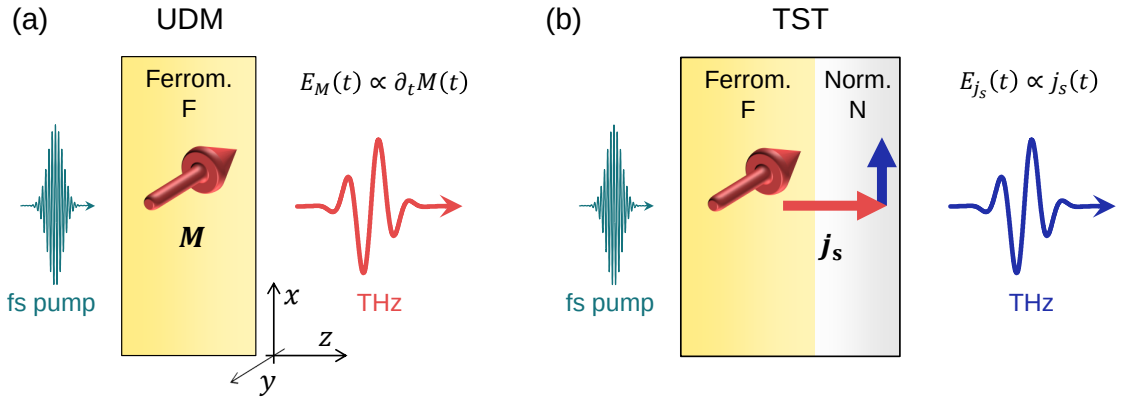

Figure 4.1. | Ultrafast demagnetization (UDM) vs terahertz spin transport (TST). (a) Side view of a single ferromagnetic metal layer (F) with magnetization $\boldsymbol{M} = M\boldsymbol{u}_y$ parallel to the y axis with unit vector $\boldsymbol{u}_y$. Excitation by a femtosecond (fs) laser pulse triggers UDM. The transient magnetic dipole gives rise to the emission of a terahertz (THz) pulse with field $E_M(t) \propto \partial_t M(t)$. **(b)** F|N stack consisting of F and an adjacent normal paramagnetic metal layer (N). Femtosecond laser excitation drives a spin current with density $\boldsymbol{j}_s(t) = j_s(t)\boldsymbol{u}_z$ from F to N. In N, $\boldsymbol{j}_s$ is converted into a charge current with density $\boldsymbol{j}_c(t) = j_c(t)\boldsymbol{u}_x$, leading to the emission of a terahertz electromagnetic pulse with electric field $E_{j_s}(t) \propto j_s(t)$ directly behind the sample. Both $E_M(t)$ and $E_{j_s}(t)$ are linearly polarized perpendicular to $\boldsymbol{M}$ and measured by electro-optic sampling.

To understand TST, it is important to note that the optical pump promotes electrons from initial states (such as $|i\rangle$) to excited states (such as $|e\rangle$). Two different mechanisms of spin transfer from F to N can occur: shift-type and band-type transport.

The shift-type mechanism is operative when states $|i\rangle$ and $|e\rangle$ are concentrated at the F|N interface and the spin polarization of $|e\rangle$ is more localized in N than that of $|i\rangle$. Optical excitation, thus, shifts spin polarization across the F|N interface, similar to shift photocurrents of electron charge (rather than spin) in the bulk [138, 175, 176] and at the surface [27, 34] of semiconductors. In magnetic heterostructures and alloys, this effect was predicted using time-dependent density-functional-theory calculations [52], termed optical intersite spin transfer (OISTR) and experimentally confirmed subsequently [93, 228, 234, 261].

In contrast, band-type transport occurs if $|i\rangle$ and $|e\rangle$ are Bloch-type electron states in F that have different band velocity, lifetime or energy. Consequently, pump excitation can lead to an imbalance in terms of electron transport across the F|N interface, resulting in a flow of spin-polarized electrons from F to N. This effect is reminiscent of injection charge photocurrents in semiconductors [27, 138, 176]. In metallic F|N structures, it was modeled using semiclassical Boltzmann-type transport equations, termed superdiffusive spin transport [14, 101, 177] and experimentally observed by optical pump-probe techniques [30, 61, 153, 209, 246], or terahertz emission spectroscopy [78, 119, 218, 224, 243, 268, 270].

An additional spin-current component can be triggered by excitation with circularly polarized light [98]. Its amplitude is proportional to the chirality of the pump polarization (positive, zero or negative) and typically two orders of magnitude smaller than the band-like component. Microscopically, this coherent effect was ascribed to an inverse spin-orbit

torque [98].

4.1.3 Spin voltage

From a more macroscopic viewpoint, spin transport can, in general, be driven by spatial gradients of the parameters that determine the local electron distribution in metals, that is, electrostatic potential, temperature and spin voltage [15, 67]. While the generation of out-of-plane electrostatic-potential gradients in metallic thin films is difficult due to strong instantaneous screening [14], temperature gradients can be generated by ultrafast optical excitation straightforwardly. They are expected to result in TST through the spin-dependent Seebeck effect, which was sometimes used to rationalize the spin currents observed in previous works [3, 44, 163, 224].

Interestingly, optical excitation of a ferromagnetic metal induces a transient excess of local spin density [30], too, which is also known as spin voltage or spin accumulation. On one hand, optically induced spin-voltage gradients were suggested to make a dominant contribution to TST [67]. On the other hand, theoretical arguments [18, 170, 171] indicate that the spin voltage, plus temperature differences between spin-up and spin-down electrons, could drive demagnetization. It follows that the seemingly disconnected phenomena of TST and UDM may share a common driving force: the spin voltage [30, 43, 143].

Direct experimental evidence for this exciting conjecture is, however, missing, and the relative strength of the competing Seebeck-type transport along temperature gradients and the interfacial OISTR remains unclear. Likewise, it is far from obvious whether concepts like spin voltage and temperature can be applied to nonthermal electron states that prevail in the first 100 fs after optical excitation and ultimately determine the bandwidth of terahertz spintronic devices.

4.1.4 This work

Here, we use terahertz emission spectroscopy to reliably measure UDM and TST in one setup. Our data reveal that the rate of UDM in F samples [Fig. 4.1(a)] and the rate of TST in F|N stacks [Fig. 4.1(b)] have identical time evolution. The measurements along with an analytical model based on Boltzmann-type rate equations and the Stoner approach to ferromagnetism show that UDM and TST are driven by a common dominant force: a generalized spin voltage of the electrons in F, which scales with the instantaneous excess spin density. In contrast, Seebeck-type contributions due to optically induced temperature gradients and interfacial OISTR are found to make a minor contribution to the terahertz signal.

Importantly, both spin voltage and electron temperature can be defined for arbitrary, nonthermal electron distributions, which often prevail in experiments with femtosecond laser pulses.

These insights open up entirely new perspectives and synergies because they allow us to better understand and ultimately optimize TST by exploiting the extensive knowledge

about UDM. For example, our results indicate that the temporal onset of TST is only determined by the duration of the femtosecond pump pulse. They suggest that the amplitude of TST can, in principle, be increased by one order of magnitude.

4.2 Experimental setup

Samples and excitation

As F materials, we choose the metallic ferromagnets $Co_{70}Fe_{30}$ (CoFe), $Co_{40}Fe_{40}B_{20}$ (CoFeB) and $Ni_{80}Fe_{20}$ (NiFe), whose metallic components are predominantly ferromagnetic transition metals. We choose NiFe since it has a significantly larger electron-spin relaxation time than CoFeB and CoFe [158].

For N, we choose the spin-to-charge-current conversion materials Pt and W because they exhibit large yet opposite spin Hall conductivities [218]. Two thin films of F and F|N are grown by magnetron sputtering on the same diamond substrate, which is transparent at all relevant terahertz and optical frequencies. The deposition is performed at an Ar pressure of 4×10^{-3} mbar at growth rates between 0.2 Å/s and 1 Å/s, depending on the material. Half of the substrate is covered by a metallic mask during deposition of the N material, thereby resulting in an F sample and an F|N stack on the same substrate and in the same run. All samples are protected by a 10 nm thick Al_2O_3 layer grown by atomic layer deposition.

The direction of the sample magnetization $\boldsymbol{M}$ is set by an external magnetic field of about 10 mT either parallel or antiparallel to the y-axis unit vector $\boldsymbol{u}_y$ [Fig. 4.1(a)]. The sample under investigation is excited with linearly polarized laser pulses (wavelength of 800 nm, duration of about 10 fs and pulse energy of 2 nJ) from a Ti:sapphire laser oscillator (repetition rate of 80 MHz) under normal incidence. The pump beam diameter at the sample position is approximately 25 µm full width at half maximum of the intensity.

The total thickness of the metal stack is significantly smaller than the penetration depth of the pump field (30 nm). As a consequence, and as confirmed by calculations, the pump field is constant throughout the thickness of the metal film to very good approximation.

Measurement of UDM and TST

Terahertz field emission— To measure the dynamics of the magnetization $\boldsymbol{M}(t) = M(t)\boldsymbol{u}_y$ of an F sample [Fig. 4.1(a)] and of the spin current flowing from F into an adjacent N [Fig. 4.1(b)] vs time t, the concomitantly emitted terahertz electromagnetic pulse is used as a probe. UDM [Fig. 4.1(a)] implies a dynamic magnetic dipole that generates an electromagnetic pulse [17, 100, 215, 276] with an electric field

$$E_M(t) \propto d_\mathrm{F}\ \partial_t M(t) \tag{4.1}$$

directly behind the sample (see Appendix A.1). Here, $\partial_t = \partial/\partial t$ denotes the time derivative, and d_F is the thickness of F.

In TST [Fig. 4.1(b)], the spin-current density $\boldsymbol{j}_s(t) = j_\mathrm{s}(t)\boldsymbol{u}_y$ across the F|N interface is instantaneously converted [223] into a transverse charge-current density proportional to $j_\mathrm{s}(t)$ by the inverse spin Hall effect in N. It results in a time-dependent electric dipole and, thus, emission of an electromagnetic pulse with transient electric field [218, 243, 268, 270]

$$E_{j_\mathrm{s}}(t) \propto j_\mathrm{s}(t) \tag{4.2}$$

behind the sample (see Appendix A.1). As the dynamics are driven by a femtosecond laser pulse, the bandwidth of E_M and E_{j_s} is expected to extend to frequencies well above 10 THz.

In our setup, we detect any transient electric field $E(t)$ such as $E_{j_\mathrm{s}}(t)$ and $E_M(t)$ by electro-optic sampling [121, 141, 193, 264] where a probe pulse (0.6 nJ, 10 fs) co-propagates with the terahertz pulse through an electro-optic crystal. The ellipticity $S(t)$ accumulated by the sampling pulse is measured as a function of the delay t between terahertz and sampling pulse by means of a polarization-sensitive optical bridge, which consists of a quarter-wave plate, a polarizing beam splitter and two balanced photodiodes. As electro-optic crystal, we use GaP(110) (thickness of 250 µm) or ZnTe(110) (1 mm or 10 µm). All experiments are performed at room temperature in a dry N_2 atmosphere.

From signals to fields

To focus on magnetic effects, we only consider the signal component odd in the sample magnetization,

$$S(t) = \frac{S(t, +\boldsymbol{M}) - S(t, -\boldsymbol{M})}{2}, \tag{4.3}$$

The waveform $S(t)$ is related to the terahertz electric field $E(t)$ directly behind the sample by the convolution [222]

$$S(t) = (H_{SE} * E)(t) = \int d\tau\, H_\mathrm{SE}(t-\tau)E(\tau). \tag{4.4}$$

The transfer function $H_\mathrm{SE}(t)$ connects S and E and accounts for the terahertz pulse propagation to the detection and the electro-optic-sampling process [27, 222, 276]. We determine H_SE by using a well-understood reference emitter, GaP(110), with a thickness of 50 µm [222]. To numerically solve Eq. (4.4) for $E(t)$, the convolution is time-discretized and recast in the form of a matrix equation [222]. From $E(t)$, we obtain $\partial_t M(t)$ [Eq. (4.1)] and $j_\mathrm{s}(t)$ [Eq. (4.2)] straightforwardly with an estimated time resolution of 40 fs.

Expected signal contributions

In general, the incident pump pulse generates a photocurrent inside the sample whose local amplitude is proportional to the local pump intensity. The time-dependent photocurrent gives rise to the emission of an electromagnetic pulse with an electric field E that has contributions proportional to the electric-dipole (ED) and the magnetic-dipole (MD) moment of the photocurrent distribution,

$$E = E_\mathrm{ED} + E_\mathrm{MD}. \tag{4.5}$$

ED fields are proportional to the spatially integrated photocurrent density. Therefore, to obtain ED radiation from a photocurrent, spatial inversion symmetry must be broken, either by the sample structure (structural inversion asymmetry, SIA) or by the perturbing light field (light-induced inversion asymmetry, LIA). We can, thus, write

$$E_{\mathrm{ED}} = E_{\mathrm{SIA}} + E_{\mathrm{LIA}} \tag{4.6}$$

The F|N sample obviously possesses SIA. The THz emission due to the TST in an F|N sample E_{j_s} is of SIA orgion. Photocurrents due to LIA can arise from gradients of the pump field along the sample normal. When the sample is turned by 180° around an axis parallel to its magnetization, E_{SIA} changes sign, whereas E_{LIA} does not,

$$E_{\mathrm{SIA}}^{180^\circ} = -E_{\mathrm{SIA}}^{0^\circ} \quad \text{and} \quad E_{\mathrm{LIA}}^{180^\circ} = E_{\mathrm{LIA}}^{0^\circ} \tag{4.7}$$

An example of MD-type radiation E_{MD} is the the emitted THz field E_M from the F sample due to the UDM. The field E_{MD} is invariant when the sample is turned by 180°,

$$E_{\mathrm{MD}}^{0^\circ} = E_{\mathrm{MD}}^{180^\circ}. \tag{4.8}$$

Note that the photocurrent generates a forward (fw)- and a backward (bw)-propagating wave. The forward-propagating field E^{fw} and the backward-propagating field E^{bw} right in front of the thin film are related to each other by

$$E_{\mathrm{ED}}^{\mathrm{bw}} = E_{\mathrm{ED}}^{\mathrm{fw}} \quad \text{and} \quad E_{\mathrm{MD}}^{\mathrm{bw}} = -E_{\mathrm{MD}}^{\mathrm{fw}} \tag{4.9}$$

In our terahertz emission experiments, it is crucial to accurately separate signals that have electric-dipole (ED) and magnetic-dipole (MD) character. For this purpose, we developed three different methods the results of which are finally compared to each other.

Magneto-optic probing

For comparison to UDM probed by terahertz spectroscopy [Eq. (4.1)], we also conduct a pump-probe experiment, in which the pump-induced change $\Delta M(t)$ in the F-sample magnetization is interrogated by an optical probe pulse through the transient magneto-optic Kerr effect (MOKE) [38]. We measure both the MOKE-induced rotation and ellipticity of the probe-pulse polarization behind the sample [205, 206].

Note that the pump-induced MOKE signal contains contributions from $\Delta M(t)$ and changes in the magneto-optic coefficients. A separation and deconvolution procedure [38] allow us to extract $\Delta M(t)$ from the MOKE trace with a time resolution of 130 fs, provided the pump-pulse energy has not yet been transferred from the electrons into the phonons of F. At later pump-probe delays of typically $t > 0.3$ ps , the increased phonon temperature leads to additional signal contributions unrelated to $\Delta M(t)$ [38].

4.3 Results

4.3.1 Terahertz emission signals

Figures 4.2-4.5 display typical terahertz electro-optic signals $S_{\mathrm{F|N}}(t)$ and $S_{\mathrm{F}}(t)$ from, respectively, F|N and F samples with F=CoFe(3 nm) and N=Pt(3 nm). According to Eq. (4.3), all waveforms are odd with respect to the magnetization $\boldsymbol{M}$. The signal components even in $\boldsymbol{M}$ are more than 40 times smaller [205]. The polarization of the terahertz pulses associated with $S_{\mathrm{F|N}}(t)$ and $S_{\mathrm{F}}(t)$ is linear with the electric field perpendicular to $\boldsymbol{M}$ [205], consistent with the emission scenarios of Figure 4.1.

Note that the total film thickness is chosen sufficiently small to prevent any pump gradients in the film and consequently a LIA-type contribution.

We propose three separation procedures to separate different contributions in THz emission signals. Note that all three separation procedures rely on the assumption that the terahertz emission signal from a sufficiently thin F|N stack with N=Pt arises from TST and the ISHE and is, thus, of ED/SIA-type. According to Eq. (4.7), the terahertz electric field directly behind the metal stack fulfills

$$E_{\mathrm{F|N}}^{180^\circ}(t) = -E_{\mathrm{F|N}}^{0^\circ}(t)\,, \tag{4.10}$$

provided the excitation conditions for the two configurations are identical.

A. Symmetrized sample-turning technique

Experiment design. The optical properties of the sample structure were symmetrized by using a cap window (cap) that is identical to the substrate (sub) window [Fig. 4.2 (a,b)]. We first measured the terahertz signal in the configuration of Fig. 4.2 (a). Each sample contained regions with the structures sub||F||cap and sub||F|N||cap, which were addressed by translating the sample perpendicular to the incident pump beam. In this way, we obtained signals $S_{\mathrm{F}}^{0^\circ}(t)$ and $S_{\mathrm{F|N}}^{0^\circ}(t)$.

By rotating the sample by 180° around the magnetization direction, we obtained the configuration of Fig. 4.2 (b) and, thus, signals $S_{\mathrm{F}}^{180^\circ}(t)$ and $\mathrm{S}_{\mathrm{F|N}}^{180^\circ}(t)$. From Eq. 4.7, we expect that the terahertz signals fulfill $S_{\mathrm{F|N}}^{180^\circ}(t) = -S_{\mathrm{F|N}}^{0^\circ}(t)$. Any deviations from this relationship are indicative of altered sample position, altered absorptance of the pump beam and altered outcoupling of the terahertz beam between the two configurations.

F|N sample. Figure 4.2 (c) shows typical terahertz signals $S_{\mathrm{F|N}}^{0^\circ}(t)$ and $S_{\mathrm{F|N}}^{180^\circ}(t)$ taken in the configurations of Figs. Fig. 4.2 (a) and Fig. 4.2 (b). We observe that $S_{\mathrm{F|N}}^{180^\circ}(t)$ differs from $-S_{\mathrm{F|N}}^{0^\circ}(t)$ by a scaling factor of $a = 2$. We attribute the scaling factor $a \neq 1$ to the air gap between the F|N stack and the attached cap window. This air gap acts like an optical cavity and breaks the macroscopic symmetry of the sample, thereby resulting in different pump absorptance in the 0° and 180° configuration.

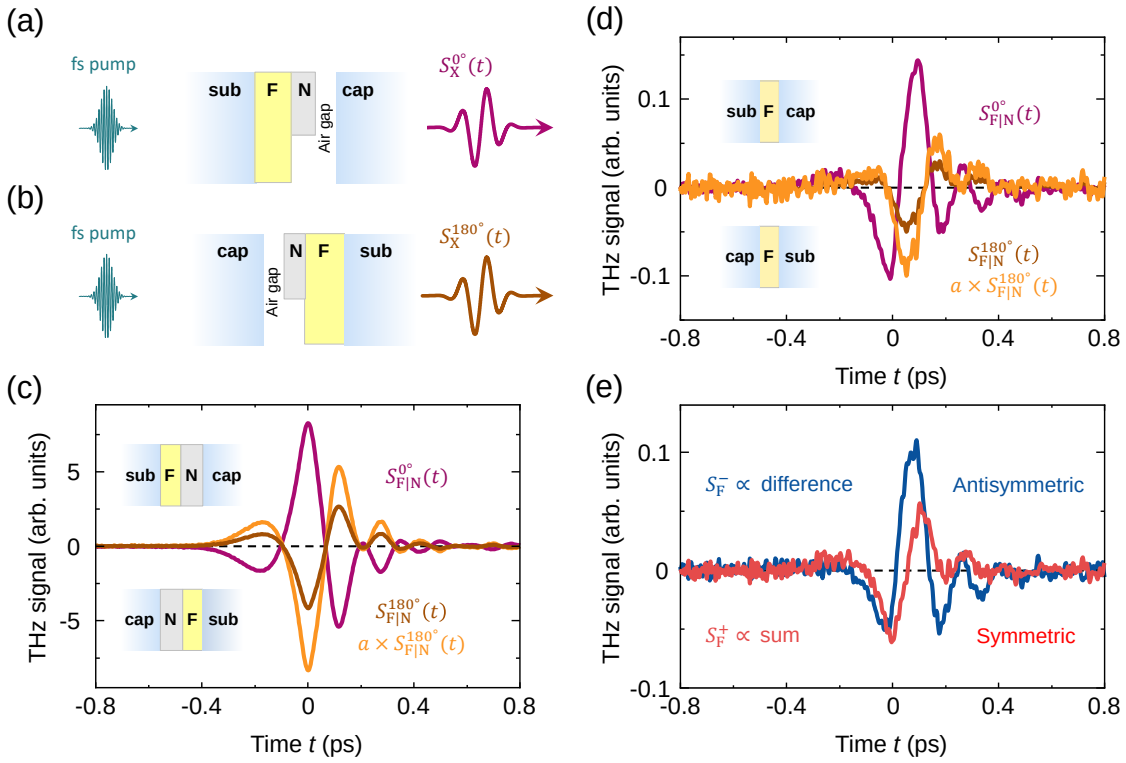

Figure 4.2. | Symmetrized sample-turning technique. **(a)** 0°-configuration of the combined F|N and F samples with F= CoFe(3 nm), N= Pt(3 nm) and diamond as substrate and cap material. The N layer covers half of the F film, thereby enabling measurements on both F and F|N by lateral translation of the sample. The sample is symmetrized by a cap window that is identical to the substrate. An unwanted air gap (estimated thickness of 1 µm) forms when the cap window is attached to the sample. **(b)** The 180°-configuration is achieved by rotating the 0° configuration by 180° around an axis parallel to the external magnetic field. **(c)** Terahertz emission signals $S_{F|N}^{0^\circ}(t)$ and $S_{F|N}^{180^\circ}(t)$ from the F|N stack. Note that $S_{F|N}^{0^\circ}(t)$ and $S_{F|N}^{180^\circ}(t)$ differ by a scaling factor of $a = 2$ because of different pump absorptance. **(d)** Same as panel (c), but for a single F layer. **(e)** Resulting symmetric signal $S_F^+(t)$ and antisymmetric signal $S_F^-(t)$ with respect to sample turning.

We confirmed this notion theoretically by calculations of the sample absorptance. It was found that an air gap of the order of 1 µm can easily lead to a variation of the pump absorptance by a factor of 2 when the sample is turned by 180°.

To test the air-gap conjecture experimentally, we used an F|N sample with fused-silica substrate. The formation of the air gap was prevented by using glycerin as liquid between the F|N film and the cap window. The refractive index of glycerin (1.473 at 800 nm) equals that of fused silica (1.455), resulting in a more symmetric sample. The terahertz emission signals of Fig. 4.3 confirm that Eq. 4.10 was fulfilled to very good approximation for the sample without air gap.

F sample. Figure 4.2 (d) shows the terahertz signals $S_F^{0^\circ}(t)$ and $S_F^{180^\circ}(t)$. In general, the terahertz radiation emitted from the F sample has both antisymmetric and symmetric contributions. We can use the factor $a = 2$ as obtained from the F|N sample on the same substrate and accordingly correct for the different pump absorptance by replacing $S_F^{180^\circ}(t)$

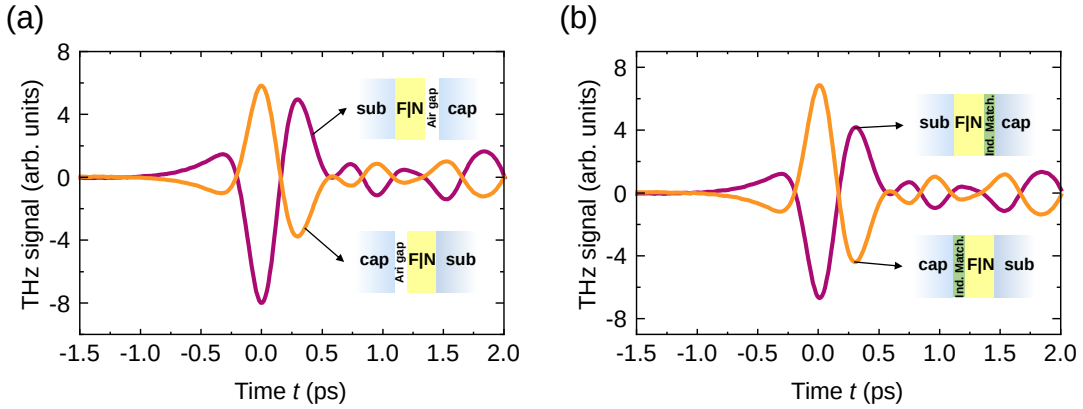

Figure 4.3. | Impact of air gap. (a) The sample is an F|N stack with F= CoFeB(3 nm), N= W(3 nm) and a fused silica window (500 µm) as substrate and cap. (a) The cap window is pressed against the sample, and signals $S^{0^\circ}_{\mathrm{F|N}}(t)$ and $S^{180^\circ}_{\mathrm{F|N}}(t)$ of significantly different amplitude are observed. **(b)** The formation of an air gap between F|N stack and cap window is prevented by filling with refractive-index-matching glycerin. The resulting signals fulfill $S^{0^\circ}_{\mathrm{F|N}}(t) \propto S^{180^\circ}_{\mathrm{F|N}}(t)$.

by $aS^{180^\circ}_{\mathrm{F}}(t)$.

The assumptions of this procedure are that (i) the pump absorption is homogenous over the sample area and that (ii) the air gap is the same in both configurations.

The symmetric and asymmetric signal contribution of S_{F} is extracted by calculating the sum and difference according to

$$S^{\pm}_{\mathrm{F}}(t) = \frac{S^{0^\circ}_{\mathrm{F}}(t) \pm aS^{180^\circ}_{\mathrm{F}}(t)}{2}. \tag{4.11}$$

As seen in Fig. 4.2 (e), symmetric and antisymmetric signals have comparable magnitude.

B. Generalized sample-turning technique

This method is similar to the symmetrized-sample technique but without cap window. The asymmetric sample geometry is captured by a linear transfer function.

Experiment design. We first measured signals in the $\theta = 0^\circ$ configuration [FFig. 4.4 (a)] in sub||F|N and sub||F regions, yielding signals $S^{0^\circ}_{\mathrm{F}}(t)$ and $S^{0^\circ}_{\mathrm{F|N}}(t)$. By rotating the sample by 180° around the magnetization direction, we obtained the $\theta = 180^\circ$ configuration of Fig. 4.4 (b) and, thus, signals $S^{180^\circ}_{\mathrm{F}}(t)$ and $S^{180^\circ}_{\mathrm{F|N}}(t)$.

Note that turning of the F|N sample does in general not yield $S^{180^\circ}_{\mathrm{F|N}}(t) = -S^{0^\circ}_{\mathrm{F|N}}(t)$ [see Eq. 4.10] because excitation and emission conditions are altered upon sample turning. The two signals are, however, connected by a linear relationship (convolution) through

$$S^{0^\circ}_{\mathrm{F|N}}(t) = -(H_{\mathrm{st}} * S^{180^\circ}_{\mathrm{F|N}})(t)\,. \tag{4.12}$$

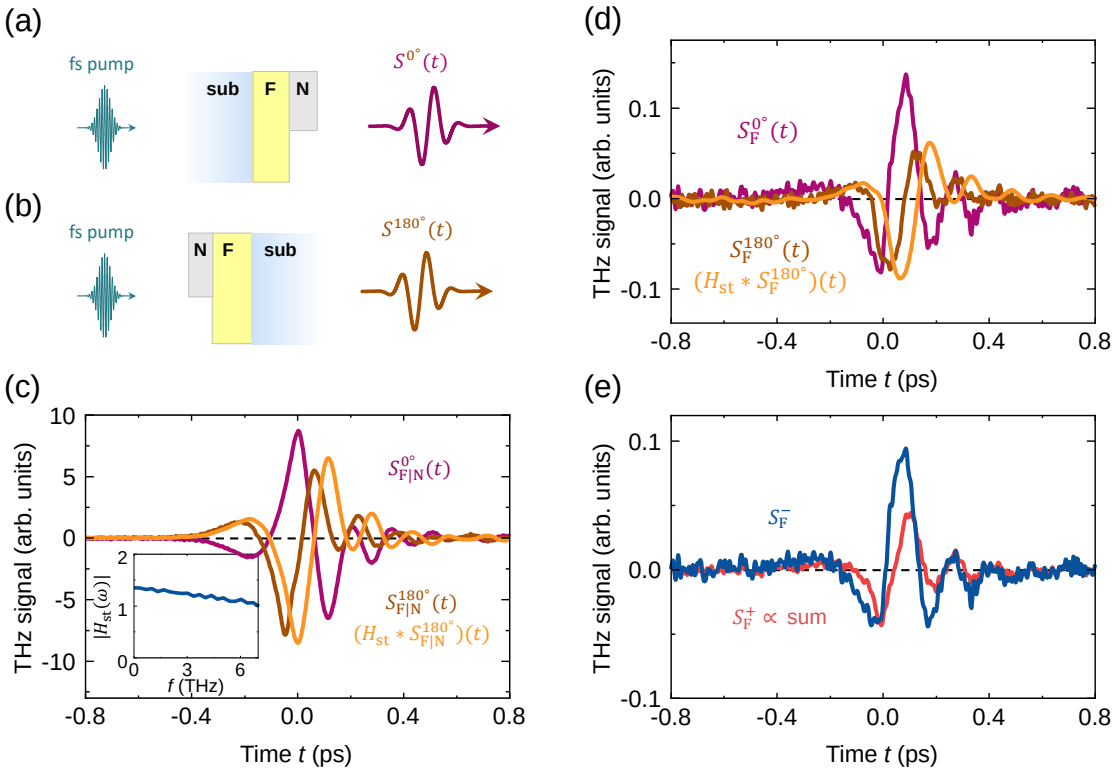

Figure 4.4. | Generalized sample-turning technique. (a) 0°-configuration of the combined F|N and F samples with F= CoFe(3 nm), N= Pt(3 nm) and diamond as substrate. The N layer covers half of the F film, thereby enabling measurements on both F and F|N by lateral translation of the sample. **(b)** The 180°-configuration is achieved by rotating the0°-configuration by 180° around an axis parallel to the external magnetic field. **(c)** Terahertz emission signals $S^{0^\circ}_{\mathrm{F|N}}(t)$ and $S^{180^\circ}_{\mathrm{F|N}}(t)$ from the F|N stack. The two signals allow us to infer the transfer function H_{st} whose amplitude spectrum $|H_{\mathrm{st}}(\omega)|$ is shown in the inset. For comparison, $(H_{\mathrm{st}} * S^{180^\circ}_{\mathrm{F|N}})(t)$ (orange solid line) is also displayed. **(d)** Same as panel (c), but for a single F layer. **(e)** Resulting symmetric signal $S^{+}_{\mathrm{F|N}}(t)$ and antisymmetric signal $S^{-}_{\mathrm{F|N}}(t)$ with respect to sample turning.

The sample turning transfer function H_{st} captures the effect of the different excitation conditions (such as the different temporal and spatial pump-pulse profile arriving at the metal layer) and altered emission conditions (such as the propagation through the substrate).

Because $S_{\mathrm{F|N}}$ is dominated by ED radiation, we expect that the ED component of the signal from the F sample is subject to the same relationship, that is, $S^{0^\circ}_{\mathrm{F}}(t) = -(H_{\mathrm{st}} * S^{180^\circ}_{\mathrm{F}})(t)$. Consequently, we can use the terahertz emission signals from the F|N sample to determine H_{st} and to, thus, eliminate the ED contribution to the terahertz signal from the F sample. In other words, H_{st} corrects for the different photonic environment due to the sample turning.

F|N sample. Figure 4.4(c) shows the terahertz signals $S^{0^\circ}_{\mathrm{F|N}}$ and $S^{180^\circ}_{\mathrm{F|N}}$. As expected, the two signals are not merely reversed versions of each other. They are delayed with respect to each other and have slightly different shape. We numerically solve Eq. (4.12) for H_{st} in the frequency domain. The modulus $|H_{\mathrm{st}}(\omega)|$ is plotted as a function of frequency $\omega/2\pi$

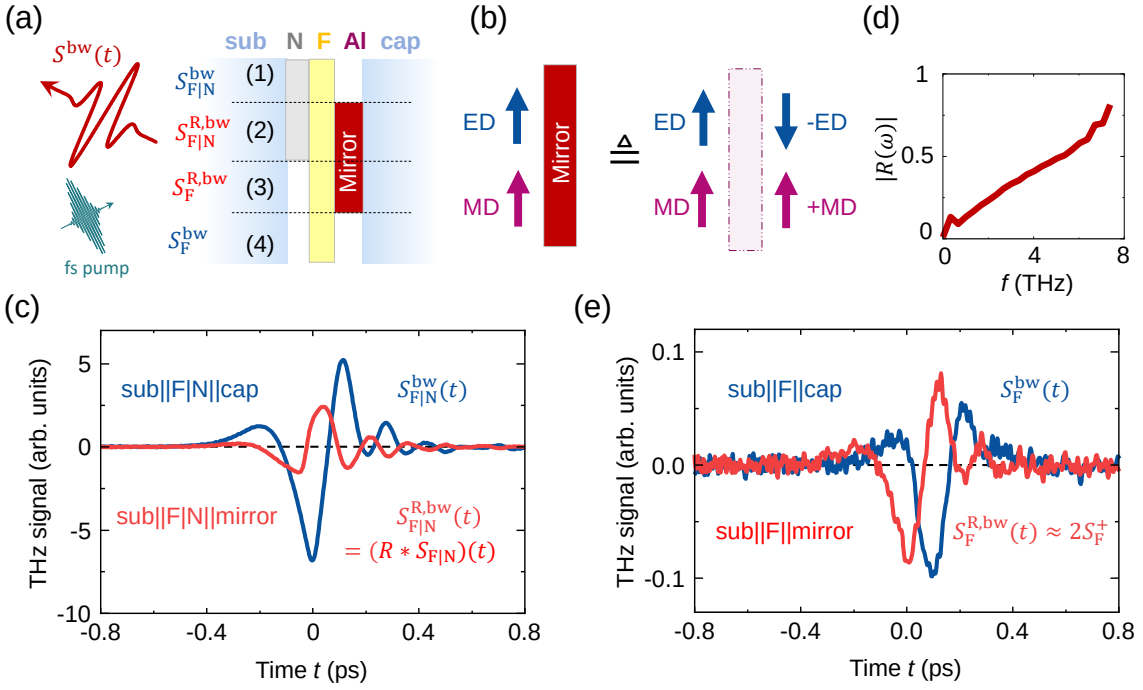

Figure 4.5. | Mirror technique. **(a)** Terahertz emission setup in reflection mode with a mirror attached to the F|N film. The mirror is made of Al that is pressed to the sample, F= CoFe(3 nm) and N= Pt(3 nm). The sample consists of four regions (1)-(4), which are accessible by the pump beam by lateral shifting of the sample. **(b)** Superposition of primary ED and MD with their image dipoles induced by the Al mirror. Note that the mirror ED has opposite sign. **(c)** Terahertz emission signals from the F|N sample combined with Al mirror and cap window. **(d)** The modulus of the $|R(\omega)|$ where $R(\omega) = S^{\mathrm{R,bw}}_{\mathrm{F|N}}(\omega)/S^{\mathrm{bw}}_{\mathrm{F|N}}(\omega)$ in the frequency domain. **(e)** Terahertz emission signals from the F sample with Al mirror and cap window.

in the inset of Fig. 4.4(c) and shows that $H_{\mathrm{st}}\ (\omega)$ has a nontrivial frequency dependence. As a check, Fig. 4.4(c) also shows $(H_{\mathrm{st}} * S^{180^\circ}_{\mathrm{FN}})\,(t)$, which agrees well with $-S^{0^\circ}_{\mathrm{FN}}$.

F sample. Figure 4.4(d) shows the terahertz emission signals $S^{0^\circ}_{\mathrm{F}}$ and $S^{180^\circ}_{\mathrm{F}}$. The orange solid line shows the calculated signal $(H_{\mathrm{st}} * S^{180^\circ}_{\mathrm{F}})\,(t)$, which is different from $-S^{0^\circ}_{\mathrm{F}}\,(t)$, thereby indicating a sizeable MD contribution to the signal.

The symmetric signal, which is proportional to the MD is

$$S^{+}_{\mathrm{F}} = \frac{S^{0^\circ}_{\mathrm{F}}\,(t) + (H_{\mathrm{st}} * S^{180^\circ}_{\mathrm{F}})\,(t)}{n_1 + n_2}, \tag{4.13}$$

where n_1 and $n_2 \approx 1$ are the refractive index of the substrate and air, respectively. The antisymmetric signal thus is given as

$$S^{-}_{\mathrm{F}} = S^{0^\circ}_{\mathrm{F}}\,(t) - n_1 S^{+}_{\mathrm{F}}. \tag{4.14}$$

Symmetric and antisymmetric signals are shown in Fig. 4.4(e).

C. Mirror technique

This separation method is quite complementary to the sample-turning techniques. It relies on Eqs. (4.5) and (4.9).

Experiment design. We measured the terahertz radiation emitted into the backward (reflection) direction. Importantly, an Aluminum mirror was pressed against the thin film to superimpose the forward-emitted terahertz radiation onto the backward-emitted terahertz field [see Fig.4.5(a)]. We obtained terahertz signals that arose from the total backward-propagating fields

$$E^{\mathrm{R,bw}} = r_{\mathrm{m}} E^{\mathrm{fw}} + E^{\mathrm{bw}}, \tag{4.15}$$

where r_{M} is the Fresnel reflection coefficient of the mirror. Owing to Eqs. (4.5), (4.9) and (4.15), we have

$$E^{\mathrm{R,bw}} = (1 + r_{\mathrm{m}})\, E^{\mathrm{fw}}_{\mathrm{ED}} + (1 - r_{\mathrm{m}})\, E^{\mathrm{fw}}_{\mathrm{MD}}. \tag{4.16}$$

Therefore, measurement of $E^{\mathrm{R,bw}}$ from a good mirror allows one to extract $E^{\mathrm{fw}}_{\mathrm{ED}}$ and $E^{\mathrm{fw}}_{\mathrm{MD}}$. For a perfect metal mirror and neglecting reflection echoes, we have $r_{\mathrm{m}} = -1$ and, thus, $E^{\mathrm{R,bw}} = 2E^{\mathrm{MD}}_{\mathrm{fw}}$ because the image ED cancels the primary ED [Fig. 4.5(b)]. In contrast, the image MD is equal to the primary MD and, thus, doubles the amplitude of the emitted field.

In reality, departures from $r_{\mathrm{m}} = -1$ are expected, for instance due to an air gap between mirror and the sample thin film. To model the impact of the attached Al mirror, we neglect reflection echoes and obtain $r_{\mathrm{m}} = r_{\mathrm{m0}} \exp(2\mathrm{i}\omega d_{\mathrm{gap}}/c)$, where $r_{\mathrm{m0}} = -1$, d_{gap} is the air gap between the mirror and the film, ω is the angular frequency of the terahertz wave, and c is the vacuum speed of light.

Our sample structure [Fig. 4.5(a)] has four different regions: (1) sub||F|N||sub, (2) sub||F|N||Al, (3) sub||F||Al and (4) sub||F||sub. The four regions can be accessed by moving the sample structure laterally. The four regions can be accessed by moving the sample structure laterally.

F|N sample. Figure 4.5(c) shows terahertz emission signals from the F|N sample where F= CoFe(3 nm) and N= Pt(3 nm). The blue solid line is the signal $S^{\mathrm{bw}}_{\mathrm{F|N}}$ from the sub||F|N||sub region. It is dominated by ED radiation [see Eq. (4.10)]. The red solid line in Fig. 4.5(c) displays the terahertz signal from the sub||F|N||Al region denoted as $S^{\mathrm{R,bw}}_{\mathrm{F|N}}$. We still observe a sizable signal, which indicates that $r_{\mathrm{m}} \neq -1$.

Fig. 4.5(d) shows the modulus of the ratio R of the two signals $S^{\mathrm{R,bw}}_{\mathrm{F|N}}$ and $S^{\mathrm{bw}}_{\mathrm{F|N}}$ in the frequency domain. We observe that $|R(\omega)|$ grows linearly with frequency $\omega/2\pi$. The linear frequency dependence agrees with our model [Eq. (4.16)], which predicts $R \sim 1 + r_{\mathrm{m}} = 1 + r_{\mathrm{m0}} \exp(2\mathrm{i}\omega d_{\mathrm{gap}}/c) \approx 2\mathrm{i}\omega d_{\mathrm{gap}}/c$ and, thus, $|R| \sim 2\omega d_{\mathrm{gap}}/c$. By comparing this expression to the slope of the curve in the inset of Fig. 4.5(d), we find that the effective thickness d_{gap} of the air gap is of the order of 2 µm. From the root mean square of the two signal curves in Fig. 4.5(c), we estimate that the Al mirror quenches 65% of the ED signal on average.

F sample. The blue solid line in Fig. 4.5(e) is the terahertz signal $S^{\mathrm{bw}}_{\mathrm{F}} = S^{+}_{\mathrm{F}} + S^{-}_{\mathrm{F}}$ from the sub||F||sub region where S^{-}_{F} is due to the ED contribution (mainly due to SIA) in which

the mirror image-dipole is negative, and S_F^+ is the MD contribution due to UDM in which the mirror image-dipole is positive as shown in Fig. X4.5(b).

From our considerations above, we estimate that 65% of the ED signal S_F^- of the F sample is quenched by the Al mirror. On the other hand, the Al mirror is expected to approximately increase the MD contribution S_F^+ by a factor of about 2. Assuming that the ED radiation from the F sample is of comparable or smaller magnitude than the MD signal, the signal from the sub||F||Al region is dominated by MD radiation. This signal is shown in Fig. 4.5(e).

Comparison of the three different techniques

Figure 4.6(a) shows the three signals from the F sample that symmetric either with respect to sample turning by 180° (sample turning techniques) or with respect to the forward- and backward-emitted waves (mirror technique). The signals are normalized to their respective maximum.

We find that all three signals agree with each other, even in details. This agreement of the three techniques, suggests that the symmetric component $S_F^+(t)$ contains the contribution E_M due to UDM [Fig. 4.1(a)]. Assuming that S_F^+ solely arises from E_M, we retrieve $E_M(t)$ and, thus, the evolution of the magnetization change $\Delta M(t)$. To compare $\Delta M(t)$ to the transient MOKE signals (Section 4.2), we match the lower time resolution of the MOKE waveform by convoluting $\Delta M(t)$ with a Gaussian of 123 fs full width at half maximum. The accordingly filtered $\Delta M(t)$ from the terahertz measurements is shown in Fig. 4.6(b) (red curve) along with the magnetization dynamics measured by the transient MOKE (black curve).

The initial quenching dynamics of the two signals agree fully. However, for times $t > 0.3$ ps, $\Delta M(t)$ evolves somewhat more slowly for the MOKE-based signal than for the terahertz-derived dynamics. We ascribe this moderate discrepancy to MOKE-signal contributions that are unrelated to magnetization dynamics and instead arise from pump-induced heating of the crystal lattice [38]. We conclude that the sign, magnitude and shape of the terahertz-emission-derived $\Delta M(t)$ is fully consistent with the notion that the signal $S_F^+(t)$ arises from UDM of the F sample as given by Eq.(4.1).

4.3.2 UDM vs TST

We can now directly compare the terahertz signal waveforms $S_F^+(t)$ due to UDM of a single layer of F=CoFe [Fig. 4.1(a)] with waveforms $S_{F|N}^-(t)$due to TST from F into N=Pt [Fig. 4.1(b)]. The result is shown in Fig. 4.7(a) and reveals a remarkable correlation: The terahertz signals $S_F^+(t)$ and $S_{F|N}^-(t)$ exhibit completely identical dynamics: $S_{F|N}^-(t) \propto S_F^+(t)$.

We emphasize that we make analogous observations for two other ferromagnets, F=CoFeB and NiFe [Fig. 4.7(a)], as well as for W as N material [Fig. 4.7(c)]. Interestingly, as seen in Fig. 4.7(e), the terahertz emission signals $S_F^+(t)$ for F=CoFeB (dashed black line) and NiFe (blue solid line) have a significantly different shape: While the global minimum and

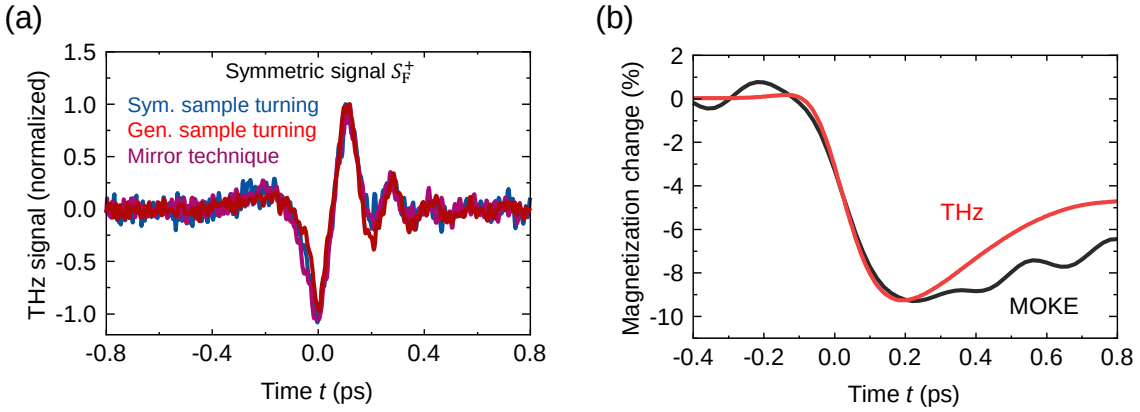

Figure 4.6. | THz symmetric signal vs MOKE. (a) Comparison of symmetric signals from techniques A-C. The three curves are signals from CoFe(3 nm) films, symmetric either with respect to sample turning by 180° (sample turning techniques) or with respect to the forward- and backward-emitted waves (mirror technique). **(b)** Extracted magnetization dynamics from $S_F^+(t)$ of panel (a) (red curve), along with magnetization dynamics as measured by the magneto-optic Kerr effect (MOKE, black curve). The magnetization evolution derived from the terahertz (THz) signal was convoluted with a Gaussian (123 fs full width at half maximum) to match the time resolution of the MOKE measurement.

maximum of the signals for F=CoFeB have approximately the same magnitude, the magnitude of the minimum signal for F=NiFe is a factor of about 2 larger than the magnitude of the maximum. These drastic differences are also observed in the spectra of the signals [205] and the resulting magnetization evolution $M(t)$ [see Fig. S9 in [205]]. They indicate significantly different dynamics for the two ferromagnets CoFeB and NiFe.

Strikingly, however, the agreement of the dynamics of $S_F^+(t)$ and $S_{F|N}^-(t)$ for each of the F materials remains [Fig. 3(a)]. These observations are confirmed for different thicknesses of F=CoFeB and NiFe [205] and for an electro-optic terahertz detector with enhanced sensitivity at frequencies above 20 THz [205].

Our observation $S_{F|N}^-(t) \propto S_F^+(t)$ and the origins of $S_F^+(t)$ [Eq. (4.1)] and $S_{F|N}^-(t)$ [Eq. (4.2)] imply that

$$j_s(t) \propto \partial_t M(t). \tag{4.17}$$

In other words, our terahertz emission signals show directly that, on ultrafast time scales, the photoinduced spin current in an F|N stack has a temporal evolution that is identical to that of the rate of photoinduced magnetization quenching of an F sample.

The most explicit manifestation of Eq. (4.17) is Fig. 4.7(b), which shows the actual dynamics of j_s and $\partial_t M$ as retrieved from the signals $S_{F|N}^-(t)$ and $S_F^+(t)$(see Section 4.2). As expected from the terahertz signals $S_F^+(t)$ and $S_{F|N}^-(t)$, both $j_s(t)$ and $\partial_t M(t)$ evolve quite differently for the samples with F=CoFeB and NiFe. They decay markedly slower for NiFe than for CoFeB.

Equation (4.17) summarizes our central experimental result. We stress that $j_s(t)$ and $\partial_t M(t)$ refer to very different samples F|N vs F. Consequently, Eq. (4.17) does not arise from the trivial fact that transport from F to N reduces the F magnetization at the same

rate. In our experiment, the rate $\partial_t M(t)$ is measured for a simple F sample, in which spin transport out of F is disabled. Therefore, the identical dynamics of $\partial_t M(t)$ and $j_s(t)$ reveals a profound relationship between UDM of an F sample [Fig. 4.1(a)] and TST in an F|N stack [Fig. 4.1(b)].

4.3.3 Driving force

Relevant mechanisms.—As summarized in Section 4.1, TST as observed here can arise from band-like transport, shift-like transport (OISTR) and inverse spin-orbit torque. The latter is typically two orders of magnitude smaller than the remaining contributions [98]. In addition, in our experiment, the pump pulses are linearly (not circularly) polarized, and we do not find a THz field component parallel to the sample magnetization [205]. Therefore, inverse spin-orbit torque is negligible here.

Likewise, we can safely exclude that OISTR makes a significant contribution to the terahertz emission signal from the F|N stacks studied here. First, OISTR should have a relaxation length of less than a unit cell width in N (0.4 nm in Pt), which is significantly smaller than measured spin-current relaxation lengths [224, 270] (1.2 nm in [224]). Second, while OISTR should not be effective through intermediate layers, experiments report a sizeable spin-current decay length of several nanometers [224] in a Cu intermediate layer [224, 268]. Third, for OISTR, the spin-current density $j_s(t)$ should rise and fall like the intensity envelope of the pump pulse. In contrast, the initial peak of the measured $j_s(t)$ is much wider [100-130 fs full width at half maximum, Fig. 4.7(b)] than our time resolution (about 40 fs).

We, thus, conclude that the TST observed here is dominated by band-like transport.

Model.—To better understand the connections between UDM and TST, we develop a simple microscopic model of these processes. To this end, we follow Ref. [169] and treat the electronic structure and the ferromagnetism of F in the framework of the Stoner model [181, 238] and describe the dynamics with Boltzmann-type rate equations [4]. Accordingly, the schematic of Fig. 4.8(a) displays the density of states of spin-up ($\uparrow$) and spin-down ($\downarrow$) electrons vs single-electron energy ϵ.

We assume that UDM primarily arises from quasi-elastic spin flips [132] [white arrow in Fig. 4.8(a)] and that the pump pulse can be considered a small perturbation of the system. At a given ϵ, the probability of a spin-flip event is proportional to the difference $n^{F\uparrow}(\epsilon,t) - n^{F\downarrow}(\epsilon,t)$, where $n^{F\sigma}(\epsilon,t) = n_0(\epsilon) + \Delta n^{F\sigma}(\epsilon,t)$ denotes the occupation number of a Bloch state with spin σ ($\uparrow$ or $\downarrow$) and energy ϵ in F. It is a sum of the distribution n_0 of the unexcited sample and the pump-induced changes $\Delta n^{F\sigma}$. The rate $\partial_t M(t)$ of magnetization change is obtained by integrating over all energies ϵ.

Similarly, the spin current $j_s(t)$ from F to N in the F|N stack is inferred by counting all spin transmission events across the F|N interface [Fig. 4.8(b)]. As detailed in the Appendix A.1, we find that

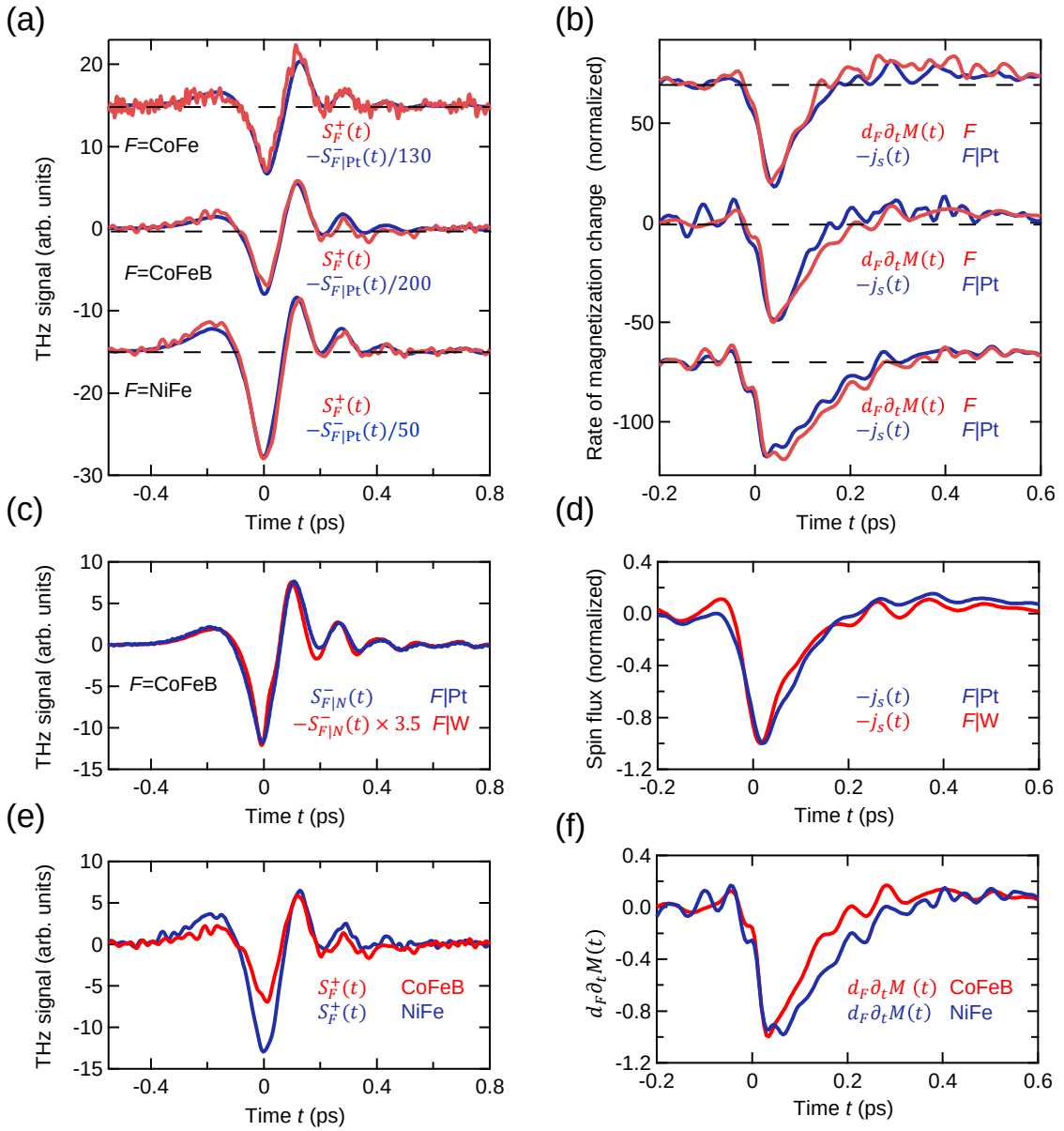

Figure 4.7. | Terahertz emission due to TST in F|N stacks vs UDM in F samples. **(a)** Terahertz signal $S^{-}_{\mathrm{F|N}}(t)$ from an F|N stack with F=CoFe(3 nm) and N=Pt(3 nm), antisymmetric with respect to sample turning about $\boldsymbol{M}$ (blue solid line), vs terahertz signal $S^{+}_{\mathrm{F}}(t)$ from a single F layer, symmetric with respect to sample turning (red solid line). The curves below show analogous signals for F and F|N samples with F=CoFeB(5 nm) and F=NiFe(9 nm). Curves are scaled by the indicated factors and offset vertically for clarity. **(b)** Temporal evolution of the spin current $j_s(t)$ flowing in the F|N sample and of the rate of change $\partial_t M(t)$ of the F sample's magnetization times the F thickness d_{F}, as extracted from the data of panel (a). Curves are vertically offset and normalized to their minima to allow for a better comparison of the relaxation dynamics. **(c)** Direct comparison of the signals $S^{-}_{\mathrm{F|N}}(t)$ from the stacks F|Pt(3 nm) and F|W(3 nm) with F= CoFeB(3 nm) and **(d)** the resulting spin current dynamics. **(e)** Direct comparison of the signals $S^{+}_{\mathrm{F}}(t)$ from single F=CoFeB(3 nm) (red) and NiFe(3 nm) (blue) films and **(f)** the resulting rate of magnetization change.

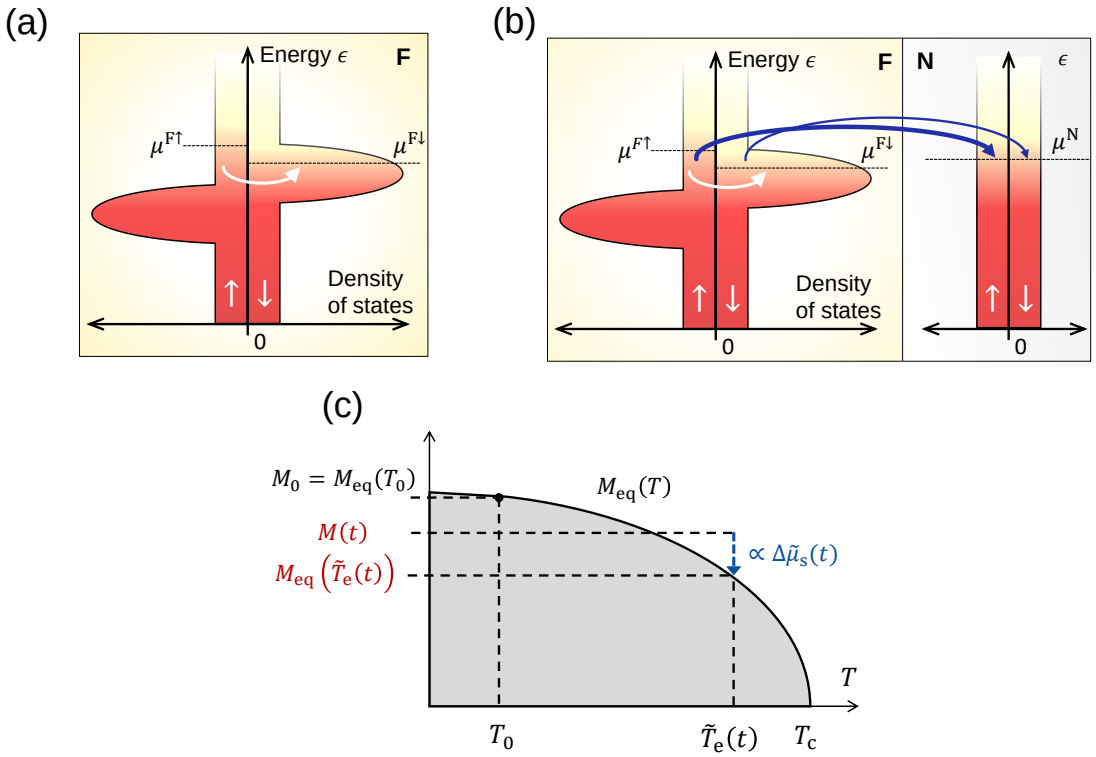

Figure 4.8. | Simple model of UDM and TST. (a) UDM. Schematic of the density of states of spin-up (↑) and spin-down (↓) Bloch electrons of a metallic ferromagnet such as Fe in the framework of the Stoner model. Quasi-elastic spin-flip scattering events (white curved arrow) lead to transfer of spin angular momentum to the crystal lattice. **(a)** TST. N acts as an additional sink of spin angular momentum through spin-conserving electron transfer across the F|N interface (blue curved arrows). In (a) and (b), the spin transfer rate scales with the generalized spin voltage $\Delta\tilde{\mu}_s$ [Eq. (4.18)], which equals $\mu^{F\uparrow} - \mu^{F\downarrow}$ in the case of Fermi-Dirac electron distributions. **(c)** Illustration of the interplay of spin voltage, electron temperature and magnetization according to Eq. (4.20). At time $t = 0$, the pump pulse excites the sample with temperature T_0, causing a time-dependent uniform increase of the generalized electronic temperature to $\tilde{T}_e(t) = T_0 + \Delta\tilde{T}_e$ (dashed line). At any subsequent time $t > 0$, the system aims to change its magnetization from the instantaneous value $M(t)$ to $M_{eq}(\tilde{T}_e(t))$, where M_{eq} is the equilibrium magnetization versus temperature T (black solid line). The spin voltage $\Delta\tilde{\mu}_s(t)$ is proportional to the excess magnetization $M(t) - M_{eq}(\tilde{T}_e(t))$ [blue dashed arrow, see Eq. (4.20)]. Note that this consideration is strictly valid only in the small-perturbation regime where $M(t) \approx M_0$ (see Appendix A.1).

$$\left.\begin{matrix}\partial_t M\,(t)\\ j_s\,(t)\end{matrix}\right\} \propto \Delta\tilde{\mu}_s\,(t) + (\text{Seebeck contribution})\,, \tag{4.18}$$

where the quantity

$$\Delta\tilde{\mu}_s\,(t) = \int \mathrm{d}\epsilon\ \left(n^{F\uparrow} - n^{F\downarrow}\right)(\epsilon, t) \tag{4.19}$$

has the same form for $\partial_t M\,(t)$ and $j_s\,(t)$, whereas the Seebeck contribution differs. Remarkably, Eq. (4.18) is fully consistent with our central experimental finding [Eq. (4.17)] if $\Delta\tilde{\mu}_s$ dominates. Consequently, we consider $\Delta\tilde{\mu}_s$ and the Seebeck terms in more detail.

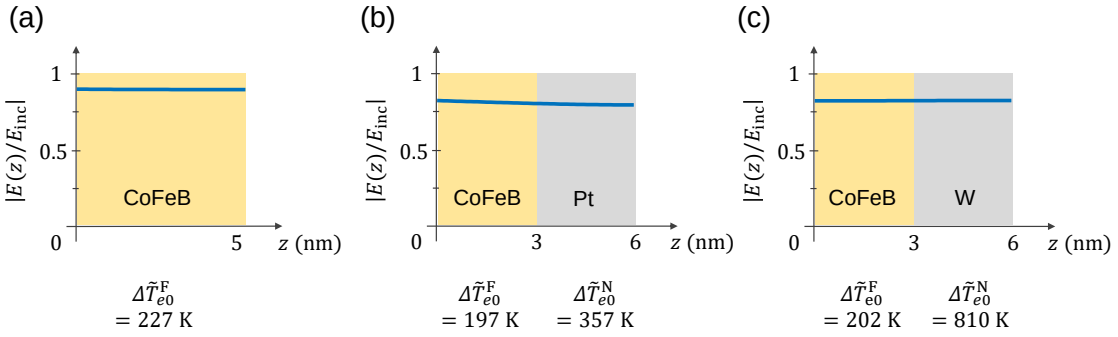

Figure 4.9. | Initial electronic temperature increase in F vs F|N. Amplitude of the pump field along the sample normal for **(a)** a single CoFeB(6 nm) film and stacks of **(b)** CoFeB(3 nm)|Pt(3 nm) and **(c)** CoFeB(3 nm)|W(3 nm), normalized to the amplitude of the incident field. At the bottom, the calculated values of the peak change in the electronic temperature right after excitation with an incident fluence of 0.1mJ/cm^2 are shown.

Spin voltage.—If the occupation numbers $n^{\mathrm{F}\sigma}$ in Eq. (4.19) are Fermi-Dirac functions with chemical potentials $\mu^{\mathrm{F}\sigma}$, $\Delta\tilde{\mu}_{\mathrm{s}}$ equals the spin voltage [67, 78] $\mu^{\mathrm{F}\uparrow} - \mu^{\mathrm{F}\downarrow}$ indicated in Fig. 4.8(a) and (b). Therefore, $\Delta\tilde{\mu}_{\mathrm{s}}$ can be considered a generalized spin voltage that is caused by an electron distribution with an arbitrary, possibly nonthermal imbalance $\Delta n^{\mathrm{F}\uparrow} - \Delta n^{\mathrm{F}\downarrow}$. Upon absorption of the pump pulse, $\Delta\tilde{\mu}_{\mathrm{s}}$ rises immediately because spin-up and spin-down electrons in a Stoner-type ferromagnet possess a very different electronic density of states around the Fermi level [see Fig. 4.8(a)].

Impact of temperature gradients.—The Seebeck-type term [15] in Eq. (4.18) is proportional to the difference $\Delta\tilde{T}^{\mathrm{F}\uparrow} - \Delta\tilde{T}^{\mathrm{F}\downarrow}$ in the case of $\partial_t M\,(t)$ [Eq. (A.17)], whereas it equals a linear combination of $\Delta\tilde{T}^{\mathrm{F}\uparrow} - \Delta\tilde{T}^{\mathrm{N}\uparrow}$ and $\Delta\tilde{T}^{\mathrm{F}\downarrow} - \Delta\tilde{T}^{\mathrm{N}\downarrow}$ for $j_{\mathrm{s}}\,(t)$ [Eq. (A.18)]. Here, $\Delta\tilde{T}^{\mathrm{X}\sigma}$ is the pump-induced change in the generalized temperature of electrons with spin σ in X=F or N. It scales with the electronic excess energy [Eqs. (A.35) and (**??**)] and equals the conventional temperature change once the electron distribution is thermal.

To estimate the F|N peak temperature differences $\Delta\tilde{T}^{\mathrm{F}\sigma}_0 - \Delta\tilde{T}^{\mathrm{N}\sigma}_0$ directly after excitation by the pump pulse, we assume the same temperature for spin-up and spin-down electrons and an incident fluence of 0.1 mJ/cm^2. For CoFeB(3 nm)|Pt(3 nm), we obtain $\Delta\tilde{T}^{\mathrm{F}\sigma}_0 - \Delta\tilde{T}^{\mathrm{N}\sigma}_0 = 160$ K. This value is sizeable because it is comparable to the temperature increase $\Delta\tilde{T}^{\mathrm{F}\sigma}_0 = 200$ K of F.

To evaluate the impact of the initial F|N temperature difference on spin transport, we note that the Seebeck contribution to $\partial_t M\,(t)$ and $j_{\mathrm{s}}\,(t)$ in Eq. (4.18) is a linear combination of very different terms: $\Delta\tilde{T}^{\mathrm{F}\uparrow} - \Delta\tilde{T}^{\mathrm{F}\downarrow}$ vs $\Delta\tilde{T}^{\mathrm{F}\sigma} - \Delta\tilde{T}^{\mathrm{N}\sigma}$. Therefore, the Seebeck component would result in different dynamics of $\partial_t M\,(t)$ and $j_{\mathrm{s}}\,(t)$ if it was significant. However, as we observe identical dynamics [Fig. 4.7(a) and (b)], the Seebeck terms very likely play a minor role in our photoexcited F and F|N samples.

To check this conclusion further, we compare the spin-current dynamics in CoFeB(3 nm)|Pt(3 nm) to that in CoFeB(3 nm)|W(3 nm), the latter of which exhibits an about 4 times larger electronic temperature difference $\Delta\tilde{T}^{\mathrm{F}\sigma}_0 - \Delta\tilde{T}^{\mathrm{N}\sigma}_0 = 608$ K directly after pump excitation. If a Seebeck contribution was relevant, one should observe different spin-current

dynamics in the two samples. Again, however, we observe almost identical dynamics [Fig. 4.7(c) and (d)]. Therefore, TST and UDM in our samples are predominantly driven by a transient spin voltage rather than temperature gradients.

According to Eqs. (A.17) and (A.18), two reasons can explain the negligible Seebeck contribution in our data. (i) The Seebeck coefficients are small, and/or (ii) the electronic temperature differences $\Delta\tilde{T}^{\mathrm{F}\uparrow} - \Delta\tilde{T}^{\mathrm{F}\downarrow}$ and $\Delta\tilde{T}^{\mathrm{F}\sigma} - \Delta\tilde{T}^{\mathrm{N}\sigma}$ relax faster than our time resolution of 40 fs. We consider it unlikely that reason (i) applies universally to the manifold of samples studied here. In contrast, scenario (ii) is very plausible because energy transport can be very efficient directly after optical excitation. During this early stage, a large fraction of the excited electrons is found at energies of up to $\hbar\omega_{\mathrm{p}} = 1.6$ eV above the Fermi level, where $\hbar\omega_{\mathrm{p}}$ is the pump photon energy. Each of these electrons carries up to 2 orders of magnitude more energy than a thermal electron relative to the Fermi level [222]. Consequently, energy equilibration between F and N is expected to be much faster than spin equilibration by spin transport, where constantly $\hbar/2$ of spin angular momentum is transferred per electron, independent of the electron energy.

To summarize, our experiments strongly indicate that temperature differences between spin-up and spin-down electrons and electrons in F and N make a minor contribution to UDM and TST. This behavior likely arises because all electronic subsystems Xσ attain approximately equal generalized temperatures faster than our time resolution of 40 fs. Consequently, we consider only one common generalized electron temperature $\Delta\tilde{T}^{\mathrm{X}\sigma} = \Delta\tilde{T}_{\mathrm{e}}$ in the following.

Dominant driving force.—Our observations [summarized by Eq. (4.17)] and modeling [leading to Eq. (4.18)] directly imply that the generalized spin voltage $\Delta\tilde{\mu}_{\mathrm{s}}$ of F is the dominant driving force of both UDM [Fig. 4.1(a)] and TST [Fig. 4.1(b)]. Therefore, the traces of $\partial_t M(t)$ and $j_{\mathrm{s}}(t)$ in Fig. 4.7(b) directly monitor the evolution $\Delta\tilde{\mu}_{\mathrm{s}}(t)$ of the spin voltage. Notably, the dynamics for CoFeB and CoFeB|Pt agree well with a spin-voltage transient of Fe on W that was measured by time-resolved photoelectron emission spectroscopy recently [30].

We expect the spin voltage to be larger when the magnetization of F is further away from its instantaneous equilibrium value. Indeed, our modeling in Appendix A.1 shows that, in the limit of uniform electron temperature and small transient magnetization changes [$M(t) \approx M_0$], the generalized spin voltage scales according to

$$\Delta\tilde{\mu}_{\mathrm{s}}(t) \propto M(t) - M_{\mathrm{eq}}\left(\tilde{T}_{\mathrm{e}}(t)\right). \tag{4.20}$$

In other words, $\Delta\tilde{\mu}_{\mathrm{s}}(t)$ is proportional to the transient excess spin density, that is, the difference between the instantaneous magnetization $M(t)$ and the equilibrium magnetization $M_{\mathrm{eq}}\left(\tilde{T}_{\mathrm{e}}(t)\right)$ that would be attained at the instantaneous generalized electron temperature $\tilde{T}_{\mathrm{e}}(t) = T_0 + \Delta\tilde{T}_{\mathrm{e}}(t)$. This remarkable and highly intuitive theoretical result is illustrated by Fig. 4.8(c).

D. Modeling the spin dynamics

To understand the shape of the temporal evolution of $\Delta\tilde{\mu}_{\mathrm{s}}$ and, thus, $\partial_t M(t)$ in the

F sample and j_s in the F|N stack, we remark that $\Delta\tilde{\mu}_s$ and the uniform generalized electron excess temperature $\Delta\tilde{T}_e$ are connected by Eqs. (4.18) and (4.20). As shown in Appendix A.1, one obtains

$$\Delta\tilde{\mu}_s(t) \propto \Delta\tilde{T}_e(t) - \Gamma_{es}\int_0^\infty d\tau\ e^{-\Gamma_{es}\tau}\ \Delta\tilde{T}_e(t-\tau), \tag{4.21}$$

where Γ_{es}^{-1} is the time constant of electron-spin equilibration. To illustrate Eq. (4.21), we consider a step-like increase of the generalized uniform electron temperature. Once $\Delta\tilde{T}_e$ jumps to a nonzero value, $\Delta\tilde{\mu}_s(t)$ follows without delay according to the first term on the right-hand side of Eq. (4.21). It triggers transfer of spin angular momentum from the F electrons into the F lattice (UDM) and, possibly, into N (TST). The loss of excess magnetization, however, decreases $\Delta\tilde{\mu}_s$ through Eq. (4.20). Consequently, $\Delta\tilde{\mu}_s$ decays on the time scale Γ_{es}^{-1}, as dictated by the second term of Eq. (4.21).

In our experiment, the excess energy of the F electrons and, thus, $\Delta\tilde{T}_e$ rise instantaneously upon pump-pulse excitation, and they subsequently decay due to energy transfer to the crystal lattice [4, 95]. As shown in Appendix A.1, we can accordingly model the evolution of $\Delta\tilde{T}_e$ by

$$\Delta\tilde{T}_e(t) \propto \Theta(t)\left[(1-R)\,e^{-\Gamma_{ep}t} + R\right], \tag{4.22}$$

where $\Theta(t)$ is the Heaviside step function, Γ_{ep}^{-1} is the time constant of electron-phonon equilibration, and R is the ratio of electronic and total heat capacity of the sample. With these assumptions, Eqs. (4.18) and (4.21) yield the simple result

$$\left.\begin{matrix}\partial_t M(t)\\ j_s(t)\end{matrix}\right\} \propto \Theta(t)\left[A_{es}e^{-\Gamma_{es}t} - A_{ep}e^{-\Gamma_{ep}t}\right], \tag{4.23}$$

where $A_{es} = (\Gamma_{es} - R\Gamma_{ep})/(\Gamma_{es}-\Gamma_{ep})$ and $A_{ep} = (1-R)\Gamma_{ep}/(\Gamma_{es}-\Gamma_{ep})$. We apply Eq. (4.23) to our measured data in Fig. 4.10 in two steps. First, to account for the experimental time resolution, Eq. (4.23) is convoluted with a Gaussian of 40 fs full width at half maximum, which matches the initial rise time of the calculated and all measured $\partial_t M(t)$ and $j_s(t)$. Second, we take only Γ_{es} and the rather trivial overall amplitude as free sample-dependent fit parameters. For Γ_{ep} and R, literature values are assumed (see [205]). Figure 4.10 demonstrates that Eq. (4.23) excellently describes the experimentally determined $\partial_t M(t)$ and $j_s(t)$.

4.4 Discussion

Our experiments show that UDM of an F sample and TST in a F|N stack exhibit identical temporal dynamics [Fig. (4.7) and Eq. (4.17)]. Combination of this observation with our model [Eq. (4.18)] implies that UDM and TST are predominantly driven by the spin voltage $\Delta\tilde{\mu}_s(t)$ rather than temperature gradients. The modeling also very well captures the temporal dynamics of $\partial_t M(t)$ and $j_s(t)$ by only three parameters: Γ_{es}, Γ_{ep} and R [Fig. (4.10) and Eq. (4.23)]. In the following, we discuss the impact of N and F materials on the dynamics of $\Delta\tilde{\mu}_s(t)$ and potential extensions of our model.

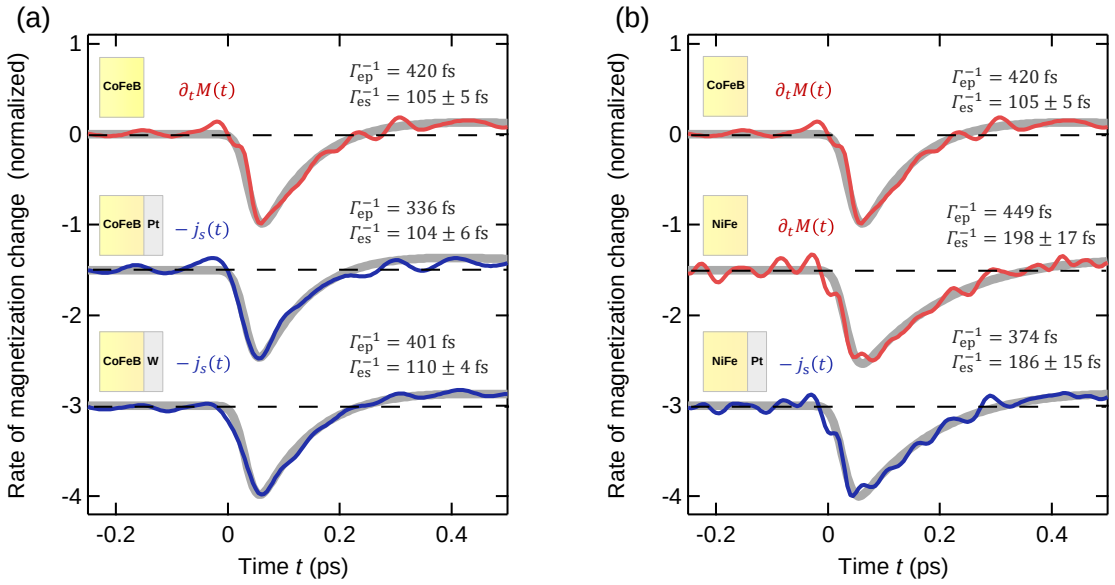

Figure 4.10. | Measured and modeled dynamics of the rate of magnetization change $\partial_t M(t)$ in F samples and the spin-current density $j_s(t)$ from F to N in F|N stacks. (a) Evolution of $\partial_t M(t)$ of an F=CoFeB sample (red solid line) and $j_s(t)$ in F|Pt and F|W stacks (blue solid lines). Grey solid lines are fits based on Eq. (4.23) with Γ_{es} and the overall amplitude scaling as the only fit parameters. (b) Analogous to (a), but for $\partial_t M(t)$ in CoFeB and $j_s(t)$ in NiFe and NiFe|Pt.

4.4.1 Impact of N and F on dynamics

Impact of N— At first glance, Fig. 4.1 suggests that the presence of N modifies the dynamics of the spin voltage in F due to (i) additional spin relaxation, which increases Γ_{es}, and (ii) different overall cooling dynamics of the electrons, which alters Γ_{ep}. However, the identical temporal evolution of $\Delta\tilde{\mu}_s$ in the F and F|N samples [Fig. 4.7(b), (d)] shows that the coupling to N does not significantly perturb the dynamics of (i) spins and (ii) electrons in F.

To discuss this behavior quantitatively, we consider Eq. (4.23) and note that the slope of the curves $\partial_t M(t)$ and $-j_s(t)$, normalized to the respective minimum, approximately equals $-(\Gamma_{es} + \Gamma_{ep})$ right after excitation (Fig. 4.10). The reason is that both electron-spin (Γ_{es}) and electron-phonon (Γ_{ep}) equilibration contribute to the decay dynamics of $\Delta\tilde{\mu}_s$. For an F sample with F=CoFeB, we find $\Gamma_{es}^{-1} = 104$ fs [Fig. 4.105(a)], which agrees with previous reports [83] and is four times smaller than $\Gamma_{ep}^{-1} = 420$ fs. Therefore, we have $\Gamma_{es} \gg \Gamma_{ep}$, and the slope of the initial decay of $\partial_t M(t)$ is dominated by Γ_{es}.

When N=Pt is attached to CoFeB, we expect a larger Γ_{es} (due to the new spin dissipation channel of TST) and an increase of Γ_{ep} by 20% (see Table S2 in [205]). In contrast, we experimentally observe an equally fast decay of $\partial_t M(t)$ and $j_s(t)$ [Fig. 4.10(a)], as confirmed by our fits, which yield a very similar Γ_{es}^{-1} for CoFeB and CoFeB|Pt. Therefore, the time constant Γ_{es}^{-1} of F and F|N samples is almost the same. In other words, TST into the Pt layer does surprisingly not accelerate spin-electron equilibration (Γ_{es}) in CoFeB, and the slightly faster electron cooling (Γ_{ep}) is negligible because $\Gamma_{ep} \ll \Gamma_{es}$. This finding

is further supported by the nearly identical spin-current dynamics $j_s(t)$ in CoFeB|W and CoFeB|Pt [Figs. 4.7(d) and 4.10(a)]. We, thus, reveal a large potential for increasing the amplitude of TST, which in our samples has only a minor impact on electron-spin equilibration.

Impact of F material— We finally test NiFe as F material because its Γ_{es} is known to be substantially smaller than for CoFeB [158]. Indeed, both $\partial_t M(t)$ and $j_s(t)$ decay 50% more slowly for NiFe ($\Gamma_{es}^{-1} \approx 200$ fs) than for CoFeB ($\Gamma_{es}^{-1} \approx 100$ fs) [Figs. 4.7(f) and 4.10(b)]. This observation is consistent with previous work [158] in which a slower electron-spin relaxation for NiFe (demagnetization time of 190 fs) than for Fe (demagnetization time of 100 fs) was reported. In contrast, Γ_{es} remains the same for the NiFe|Pt and NiFe samples within our experimental uncertainty.

4.4.2 Model implications

Our experimental results and the model developed here have important implications regarding the magnitude of the spin current and its relaxation time.

Fluence dependence.— First, we emphasize that Eq. (4.20) and, thus, Fig. 4.8(c) are even valid for large excitation fluences, provided one considers small times $t_0 \ll 1/\Gamma_{es}$ directly after optical sample excitation, that is, when the magnetization is still unchanged ($M(t_0) \approx M_0$, see Appendix A.1). According to Eq. (4.20) and Fig. 4.8(c), an increase of the pump fluence and, thus, the peak electron temperature $\tilde{T}_e(t_0)$ should result in a monotonically increasing spin-current amplitude $j_s(t_0)$. However, once $\tilde{T}_e(t_0)$ exceeds the Curie temperature T_C, an abrupt saturation of $j_s(t_0)$ and, thus, the emitted terahertz peak field should occur. These expectations were recently confirmed in a terahertz emission study, in which the pump fluence was varied over a large range [255].

Temperature dependence.— According to our model, the time constant Γ_{es}^{-1} is proportional to the magnetic spin susceptibility χ^F of the F material [Eq. (A.33)]. Because χ^F increases with the equilibrium temperature T_0 up to the Curie temperature T_C [Eq.(A.23)], our model implies a slowing down of UDM and TST as T_0 increases. For UDM, this notion is consistent with previous experiments [204] and simulations [169]. For TST, it is subject of ongoing experiments.

The preceding considerations are certainly qualitative, but nevertheless demonstrate the predictive power of our model.

4.4.3 Possible model extensions

Our analytical model of UDM and TST successfully describes all experimental observations of this work and makes predictions about the fluence and temperature dependence of UDM and TST, which are consistent with previous studies. It even applies to nonthermal electron distributions, which are ubiquitous in the first 100 fs following optical excitation of metals [222].

The central ingredients of our model are the Stoner approach to the electronic structure,

rate equations and quasi-elastic electron scattering to describe the dynamics of the Bloch states and the linearization of energy-dependent coefficients around the Fermi energy. A uniform electronic temperature in the vicinity of the F|N interface followed from a comparison of experiment and theory, as addressed in section 4.3. In the following, we discuss the soundness of other relevant model assumptions and possible extensions if other material systems or observables are of interest.

The Stoner model as phenomenological model.— The Stoner model is presumably the simplest approach to ferromagnetism in a single-electron framework [181]. It includes the exchange interaction between electrons through an effective magnetic field that is proportional to the mean local spin polarization. Therefore, the Stoner model captures magnons only through their mean impact on the spin polarization but neglects the transverse spin fluctuations they induce.

Despite these restrictions, the Stoner model is routinely used to successfully explain magnetoresistive phenomena such as tunneling and giant magnetoresistance [238] and spin-caloritronic effects such as the spin-dependent Seebeck and the anomalous Nernst effect [15, 24]. The Stoner model was also successfully used for numerical simulations of UDM of 3d-type metallic ferromagnets [169] and to fit instantaneous photoelectron emission spectra of optically excited Co [56]. In the latter case, however, partially unrealistic values of the Stoner-model fit parameters emerged. We conclude that the Stoner model provides a good phenomenological description of various magnetism phenomena, but the values of the microscopic parameters should not be overinterpreted.

Consequently, in our treatment (Appendix B A.1), all microscopic Stoner-model parameters are eventually replaced by macroscopic observables such as the temperature-dependent equilibrium magnetization M_{eq} and the magnetic spin susceptibility χ^{F}.

Beyond the Stoner model.— An extended description of our experiment could make use of an sd-type model, in which localized magnetic moments and their transverse fluctuations are described by a Heisenberg Hamiltonian for d-type electrons, whereas band-like spin transport arises from s-like electrons [18, 155, 247].

Recently, sd-type descriptions of UDM [18, 155, 247] and TST [18, 247] were established. They should enable a better understanding of the role of magnons and possibly allow one to calculate more complex observables such as photoelectron emission spectra [40, 93]. A future task is to extend the sd-type approach to more complex magnets such as ferrimagnets [99] and to nonthermal electron [38] and magnon [151] distributions.

Electron scattering and moment expansion.— So far, we model electron scattering without spin conservation as quasi-elastic single-electron processes. Therefore, electron-electron collisions that do not conserve the total electron spin are neglected. They could be accounted for with a more elaborate treatment [169], which is not implemented here for the sake of simplicity. Spin-conserving electron-electron scattering is, however, fully accounted for.

Our model assumes that microscopic quantities such as the electronic density of states [Fig. 4.8(c)] can be linearized around the Fermi energy. As detailed in Ref. [38], this assumption is justified because, only 30 fs after optical excitation, the transient electron

distribution is most likely significantly less than 1 eV wide. On this energy scale, the calculated density of states of Fe, Co and Ni varies roughly linearly [76]. Note that a possible Stoner gap in the single-electron excitation spectrum is not relevant in our model. The considered spin-flip processes arise from electron-impurity and electron-phonon scattering and, thus, do not constrain the scattering phase space due to conservation of the electron wavevector.

Crystal lattice dynamics.— Each electronic spin-flip event in our model implies transfer of angular momentum to the crystal lattice. One could further resolve this transfer with respect to phonon wavevector and frequency by suitable rate equations for the crystal-lattice degrees of freedom. Such an extension could be interesting for the description of diffraction experiments resolving ultrafast motion of the crystal lattice [55, 239]

Spin voltage in N.— Our model neglects a possible spin voltage in N throughout the considered time interval. This assumption is justified for Pt because its spin relaxation time of 15 fs [68] is shorter than all other time scales in our experiment. However, for N materials with longer spin relaxation time, a sizeable spin accumulation can be expected that hampers and possibly slows down the spin transfer from F to N. This expectation is consistent with numerical simulations of spin transport in Fe|Ru stacks, which indicated a significant spin accumulation in the Ru regions close to the Fe|Ru interface along with slower spin-transport dynamics [119]. This feedback effect could be straightforwardly included in our model by allowing for a nonvanishing spin voltage in the N layer.

To summarize, the preceding discussion shows that the assumptions of our modeling are justified and that its scope in terms of materials and observables can be extended even further by moderate extensions.

4.5 Conclusions

Our experiments and analysis based on a simple model of UDM and TST allow us to draw significant conclusions from both a fundamental and applied viewpoint.

Spin voltage vs temperature gradient.— UDM and TST are driven by the same force: a generalized spin voltage [Eq. (4.19)], which quantifies the excess of spin polarization relative to the current equilibrium value [see Fig. 4.8(c) and Eq. (4.20)]. We suggest to term the heat-induced spin voltage the pyrospintronic effect because it is analogous to the pyroelectric effect of a pyroelectric material, in which the spontaneous electric polarization is forced to follow the instantaneous temperature. The pyrospintronic effect is a predominantly ultrafast effect because the relaxation time of the spin voltage is limited by the electron-spin relaxation time, which typically amounts to 100 fs and less in typical metallic ferromagnets.

We emphasize that our measured spin current is not the result of a spin-dependent Seebeck effect: [15] To quantitatively explain our data, we neither have to assume a temperature difference between F and N nor between majority and minority electrons in F. It appears that temperature gradients become relevant (i) on longer time scales, when the spin voltage has decayed, or (ii) in structures where F is not excited, implying no change in spin

voltage. An example of (i) is the spin-dependent Seebeck effect under stationary conditions [96, 166, 256]. An example of (ii) is an F|Pt stack with an insulating F material such as yttrium iron garnet [124, 222], which is not excited when the photon energy of the pump pulse is smaller than the electronic bandgap.

Spin-voltage decay.— After the pump pulse has excited the electronic system of F, the generalized spin voltage and, thus, $\partial_t M\,(t)$and $j_\mathrm{s}\,(t)$ jump to a nonzero value and subsequently relax by electron-spin equilibration, while the significantly slower electron-phonon equilibration has a minor influence. Our results also strongly suggest that the impact of TST on Γ_es is negligible in our experiments.

The previous conclusion implies that the photoinduced spin voltage primarily decays due to spin-flip processes in F also in the F|N stack. In other words, only a small fraction of the available excess spin angular momentum is transferred to N. We, thus, anticipate that the spin-current amplitude can, in principle, be increased significantly by using more transparent F|N interfaces [147] and F materials with larger electron-spin relaxation time Γ_es^{-1}.

Peak current and bandwidth.— Regarding speed and bandwidth, we note that the temporal onset of TST is truly ultrafast and predominantly only limited by the duration of the pump pulse depositing energy in the electrons of F [see Eq. (4.21) and Fig. 4.10. This feature is in remarkable contrast to the interfacial spin Seebeck effect [222], where carrier multiplication is required to reach maximum spin current.

To optimize the peak amplitude and relaxation time of the spin current in metallic F|N stacks, Appendix A.1 provides relationships of these characteristics to microscopic and macroscopic material quantities.

Impact on other research fields.—Importantly, our study allows us to apply the extensive knowledge about UDM of F samples to TST from F to an adjacent layer N. This insight is expected to be very helpful to boost spin-current amplitudes in numerous applications such as spin torque, [3, 137] spintronic terahertz emitters [218, 243, 268, 270] and, potentially, energy harvesting [125]. Our findings also provide a new straightforward link between concepts of femtomagnetism and spintronics. In particular, terahertz emission spectroscopy holds great promise to be an excellent ultrafast monitor of the evolution of the generalized spin voltage.

5

Accessing ultrafast spin-transport dynamics in copper using broadband terahertz spectroscopy

We study the spatiotemporal dynamics of ultrafast electron spin transport across nanometer-thick copper layers using broadband terahertz spectroscopy. Our analysis of temporal delays, broadening and attenuation of the spin-current pulse revealed ballistic-like propagation of the pulse peak, approaching the Fermi velocity, and diffusive features including a significant velocity dispersion. A comparison to the frequency-dependent Fick's law identified the diffusion-dominated transport regime for distances >2 nm. The findings lie the groundwork for designing future broadband spintronic devices.

Publication information

This chapter is accepted in Physical Review Letter as **Accessing ultrafast spin-transport dynamics in copper using broadband terahertz spectroscopy** by Jiří Jechumtál, Reza Rouzegar, Oliver Gueckstock, Christian Denker, Wolfgang Hoppe, Quentin Remy, Tom S. Seifert, Peter Kubaščík, Georg Woltersdorf, Piet W. Brouwer, Markus Münzenberg, Tobias Kampfrath, and Lukáš Nádvorník [106]. DOI: https://doi.org/10.48550/arXiv.2310.12082

Author contributions

LN, RR and JJ conceived the experiments. RR, JJ and LN performed the experiment and analyzed the data. The samples were fabricated by CD, MM, WH and GW. The theory was done by TK, PB, RR and LN. The manuscript was written by RR, JJ, TK and LN with help and discussion contributions of all authors.

5.1 Motivation

Following the rapid development of terahertz (THz) and antiferromagnetic spintronics [115, 185], THz spin currents (TSCs) are expected to play an essential role in concepts of future large-bandwidth spintronic devices [114]. For example, very recently, THz-pulse-driven TSCs were used to manipulate an antiferromagnetic memory bit on sub-picosecond time scales [20]. Another and complementary trigger of TSCs is optical excitation of

thin-film multilayers by femtosecond laser pulses. This approach was successfully used for ultrafast spin-torque generation [26, 43, 154, 164, 200, 209, 214] or spintronic THz emission [31, 79, 99, 119, 189, 207, 218, 220, 282]. The latter concept has also found utility in THz investigation of formation [196, 203, 205] and dynamics [75, 80, 109, 163, 184] of ultrafast spin transport itself.

Following the theory works on TSCs [14, 116, 209, 283], there is a rising number of experimental studies in the last years. For example, previous experiments inferred the temporal dynamics of a TSC after traversing distance d from its impact on the magnetization of an adjacent layer [43, 164, 214] or by optical second-harmonic generation [164, 165]. Other works also addressed the spatial evolution of TSCs, i.e, the amplitude reduction of emitted THz pulses with increasing d, and deduced the relaxation length of the underlying TSCs [75, 224]. However, to reveal the complex propagation character of the ultrafast spin transport, direct experimental detection of the entire spatiotemporal evolution of the TSC dynamics, including its absolute temporal delay is required.

5.2 Spatiotemporal evolution of THz spin currents

In this Letter, we investigate such spatiotemporal evolution of sub-picosecond spin-current pulses through a thin copper layer of thickness d using time-domain THz emission spectroscopy with a high temporal resolution of 40 fs. By analyzing the THz signals, we directly infer the propagation speed of TSC pulses, their broadening and attenuation with d. We observe a ballistic-like propagation of the leading edge and peak of the TSC pulse with a speed approaching the Fermi velocity of Cu. The TSC pulse duration is found to increase by a factor >1.5 over a distance of $d = 8$ nm. Using a simple model based on a frequency-dependent Fick's law, we extract intrinsic spin-transport parameters, identify the dispersion of propagation velocities due to electron scattering as the source of the TSC pulse broadening and reveal diffusion as dominant spin-transport regime for $d > 2$ nm.

Our general approach to the generation, propagation and detection of a TSC is shown in Fig. 5.1. The sample is a $F\,|X|\,N$ trilayer [220] where F = CoFeB is a ferromagnetic thin film, N = Pt is a heavy metal with a large spin-Hall angle θ_{SH}, and X = Cu(d) is the interlayer with thickness d. First, a femtosecond laser pulse excites the $F|\mathrm{Cu}(d)|N$ sample and deposits the fraction A_{F}^{d} of the incident pump-pulse energy in F. It generates an ultrafast spin voltage $\mu_{\mathrm{s}}^{d}(t)$ in F [205] and, as a consequence, a sub-picosecond spin-current pulse $j_s(z=0,t)$ is launched from F into the intermediate Cu layer [205], where z is the out-of-plane coordinate (Fig. 5.1) and t is time. The amplitude of $\mu_{\mathrm{s}}^{d}(t)$ is assumed to scale with A_{F}^{d} and the corresponding normalized dynamics $\mu_{\mathrm{s}}(t) = \mu_{\mathrm{s}}^{d}(t)/A_{\mathrm{F}}^{d}$ to be d-independent. Second, the spin current propagates inside the X layer and undergoes attenuation and dispersion. We assume the propagation of the TSC proceeds in the linear-response regime and, thus, can be described inside X by the convolution relation [208]

$$j_{\mathrm{s}}(z,t) = \int \mathrm{d}t' \mu_{\mathrm{s}}(t')\, P(z, t-t')\,. \tag{5.1}$$

Here, the response function $P(z,t)$ is the spin-current density that would be obtained for

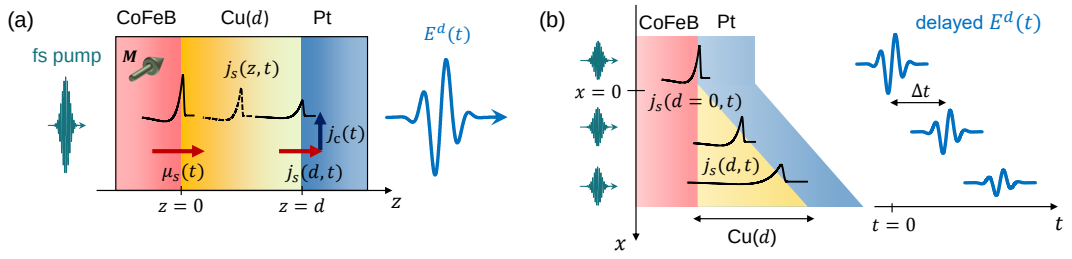

Figure 5.1. | THz spin current generation, propagation, and detection in a trilayer F|Cu(d)|Pt. (a) A fs laser pulse excites a ferromagnetic layer (F = CoFeB, in-plane magnetization $\boldsymbol{M}$, green arrow) and injects a spin current pulse $j_s(z=0,t)$ (red arrow) into an intermediate layer Cu with thickness d where it undergoes attenuation and dispersion. Finally, j_s is converted into a transverse charge current $j_c(t)$ in the Pt detection layer by the inverse spin Hall effect and radiates a THz pulse $E^d(t)$. (b) A sketch of the wedge design of the sample, showing the delayed, attenuated and broadened signals $j_s(d,t)$ and $E^d(t)$ for different d, selected by the corresponding pump-laser spot position x.

a $\delta(t)$-like spin voltage. Third, the current $j_s(z=d,t)$ arriving at the Pt detection layer is converted into a total transverse charge current $j_c(t) \propto \theta_{\mathrm{SH}} j_s(d,t)$ via the inverse spin Hall effect. We choose N = Pt because its large inverse spin Hall effect dominates all other spin-to-charge-current conversion processes in the system [78, 113, 282]. Finally, the $j_c(t)$ emits a THz pulse with the electric field

$$E^d(t) = eZ^d A_{\mathrm{F}}^d j_c(t) \propto Z^d A_{\mathrm{F}}^d j_s(z=d,t), \tag{5.2}$$

which is detected. Here, Z^d is the frequency-independent impedance of the sample. By measuring $E^d(t)$ for $d=0$, we obtain $\mu_s(t)$ from Eqs. (5.2) and (5.1). By increasing d, one can approximately reconstruct $j_s(z=d,t)$ in the Cu spacer.

We summarize that our interpretation of the evolution of j_s using Eq. (5.1) and (5.2) relies on the following assumptions: (i) $j_s(z=0,t)$ originates solely from $\mu_{\mathrm{s}}^d(t)$ in F [208]. (ii) Its amplitude scales with A_{F}^d [78, 205, 224]. (iii) The presence of the Cu layer does not change the dynamics of $\mu_s(t)$ in F [see Supplementary Fig. S2 in [106]]. (iv) $j_s(d,t)$ is fully absorbed and converted inside N [224]. (v) The measured $j_c(t)$ is exclusively due to spin-charge conversion in N = Pt, i. e., $\theta_{\mathrm{SH}} \neq 0$ only inside N [78, 80]. It follows that the values of Z^d and A_{F}^d impact only the amplitude of $j_s(d,t)$, not its dynamics.

In the experiment, we measure an electro-optical THz signal that is related to $E^d(t)$ by the convolution relation

$$S^d(t) = \left(H * E^d\right)(t). \tag{5.3}$$

Here, $H(t)$ is the setup transfer function that can be determined experimentally [134,

183]. Using Eq. (5.3), $E^d(t)$ is retrieved by the deconvolution procedure detailed in 3.4 [80, 109].

5.3 Samples and experiment

Our $F|\mathrm{Cu}|N$ stack has the layer structure $\mathrm{Co_{40}Fe_{40}B_{20}}(2\,\mathrm{nm})|\mathrm{Cu}(d)|\mathrm{Pt}(2\,\mathrm{nm})$ and is grown by electron-beam evaporation on a double-side polished $\mathrm{Al_2O_3}$ substrate [Fig. 5.1(a)]. On half the sample area, the Cu layer forms a wedge with a gradient of $\partial d/\partial x = 3.1$ nm/mm along the x direction [Fig. 5.1(b)]. This configuration allows us to conveniently select $d(x)$ in the range between 0 and 7.5 nm by positioning the pump laser beam at the appropriate position x. The other part of the sample lacks the wedge ($d = 0$) and forms a stripe of $F|N$ used for referencing.

To access relative amplitudes of $j_s(z,t)$ in Eq. (5.2), the sample is characterized for all d in terms of the absorbed pump-pulse energy fraction A_F^d in F and the total impedance Z^d using the THz transmission spectroscopy [see Fig. 5.2]. The measured Z^d are found to be almost frequency-independent up to 7 THz for all d [Fig. 5.2(b) and (c)]. For $d = 11$ nm, the stack conductance G is dominated by the Cu layer (Fig. 5.2) and, thus, the Drude model [183, 223] $G(\omega) \propto 1/(1 - \mathrm{i}\omega\tau)$ can be used to estimate the electron scattering time τ in Cu. Indeed, it provides a good fit to the data for $1 < \tau < 10$ fs [Fig. 5.2 (f)]. This τ is much smaller than the several tens of fs typical for epitaxial Cu layers [7, 71] and assigned to the polycrystalline nature of our evaporation-deposited wedge.

In the THz emission experiments, the sample is excited by a train of ultrashort laser pulses (wavelength 790 nm, duration 10 fs, repetition rate 80 MHz, energy per pulse 2 nJ) from a Ti:Sapphire laser oscillator. The pump beam is focused to a spot with a full width at half maximum (FWHM) of the intensity of ∼30 µm on the sample. Its lateral position x sets d with a precision of ∼0.1 nm [Fig. 5.1(b)]. The magnetization $\boldsymbol{M}$ of the F layer is controlled by an external magnetic field of ∼10 mT. The emitted THz electric field $E(t)$ is detected as an electrooptical (EO) signal $S(t)$ via EO sampling [121, 141] in a 250 µm thick GaP(110) crystal by using linearly polarized probe pulses (0.6 nJ) split from the pump beam. Even though the temporal resolution of the subsequent analysis is ∼40 fs, a continuously scanning delay line together with a high signal-to-noise ratio of our setup allows us to resolve the minimal increment of time t and, thus, also the temporal delays Δt of $S(t)$, as fine as 1.6 fs.

5.4 THz signals and spin currents

Typical THz-emission waveforms $S^d(t)$ from the CoFeB|Cu(d)|Pt samples are shown in Fig. 5.3(a). As d increases from 0 to 7.5 nm, the overall signal amplitude decreases by roughly a factor of 20. Interestingly, the absolute maximum and minimum of $S^d(t)$ undergo a gradual temporal shift Δt (dashed arrows), where Δt appears to be larger for the minimum.

To extract the TSC density $j_s(z = d, t)$ directly behind the Cu layer, we apply Eqs. (5.2)

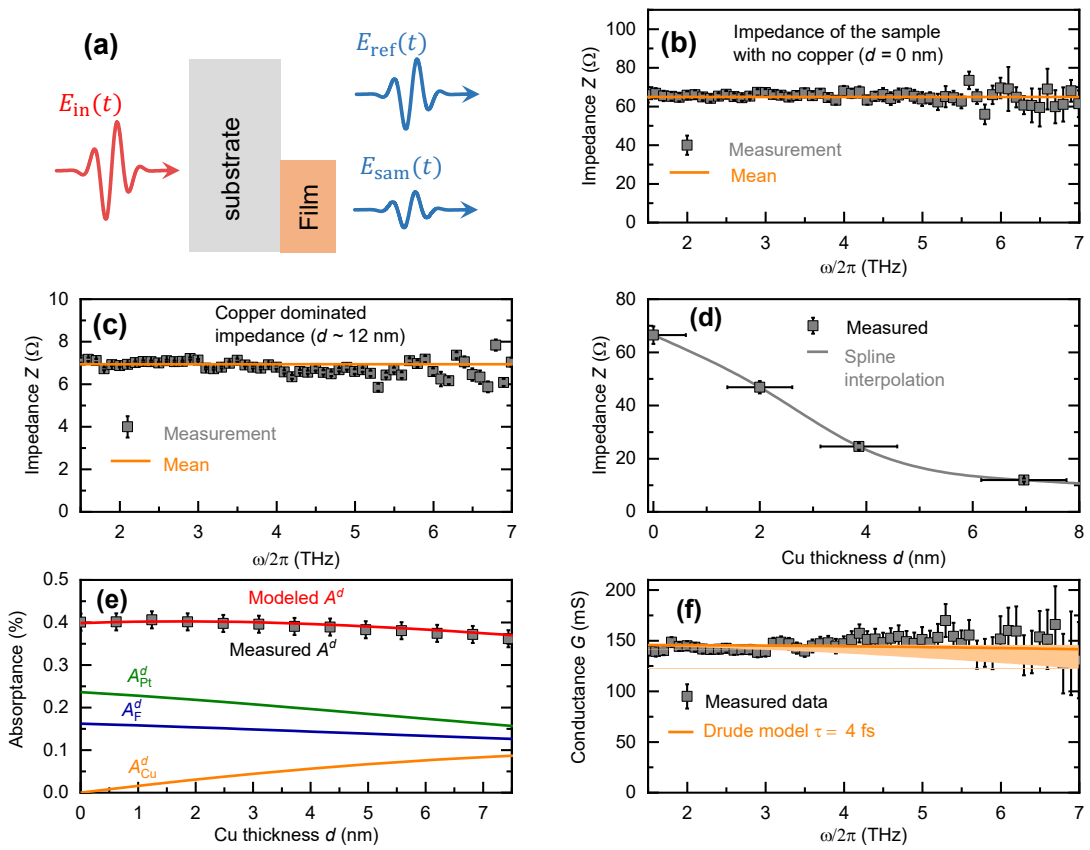

Figure 5.2. | Optical and THz properties of the trilayer. (a) Schematic of THz transmission spectroscopy as described in 3.4. (b) Measured frequency dependent THz impedance $Z(\omega)$ for the $F|\mathrm{Cu}(d=0)|N$ and (c) $F|\mathrm{Cu}(d=12\ \mathrm{nm})|N$ stacks with F = CoFeB(2nm) and N = Pt(2nm). $Z(\omega)$ is approximately constant in ω as shown by fits by a constant (orange horizontal lines), giving a mean Z for each Cu thickness d. (d) The extracted mean $Z(d)$ dependence for our full set of samples $F|\mathrm{Cu}(d)|N$. The grey curve is a spline-type interpolation used in the analysis. (e) Measured (grey points) and calculated (red curve) optical absorptance A^d of the whole $F|\mathrm{Cu}(d)|N$ stack series. The calculated A^d is the sum of the absorptance of Pt (A^d_{Pt}, green curve), CoFeB (A^d_{F}, blue curve) and Cu (A^d_{Cu}, orange curve). (f) Real part of the THz conductance $G(\omega)$ for $d = 11$ nm, obtained by the procedure described in 3.4. It is compared to the fit by a Drude model for $\tau = 4$ fs (orange curve) and 1 fs $< \tau <$ 10 fs (orange shaded area).

and (5.3) to $S^d(t)$ normalized by $Z^d A^d_{\mathrm{F}}$ and use assumptions (i-v) (See 3.4). Figure 5.3(b) shows the resulting $j_s(z=d,t)$ for various values of $z=d$ and, thus, provides the approximate spatial evolution of the ultrafast dynamics of the TSCs. The rise time of $j_{\mathrm{s}}(d=0,t)$ indicates that the time resolution of the extracted TSCs is 40 fs. Both the gradual attenuation and the rising temporal shift Δt of the THz signals $S^d(t)$ vs d are preserved in the TSCs [arrow in Fig. 5.3(b)]. Importantly, $j_{\mathrm{s}}(d,t)$ undergoes a notable broadening that is clearly visible for $j_{\mathrm{s}}(d=0,t)$ vs the normalized $j_{\mathrm{s}}(d=7.5\ \mathrm{nm},t)$ (red dashed line) without any further analysis. This behavior indicates that the TSC undergoes a significant dispersion.

To quantify these qualitative observations, we look at the details of the measured spin current by extracting temporal delay Δt, the full width at half maximum (FWHM), and

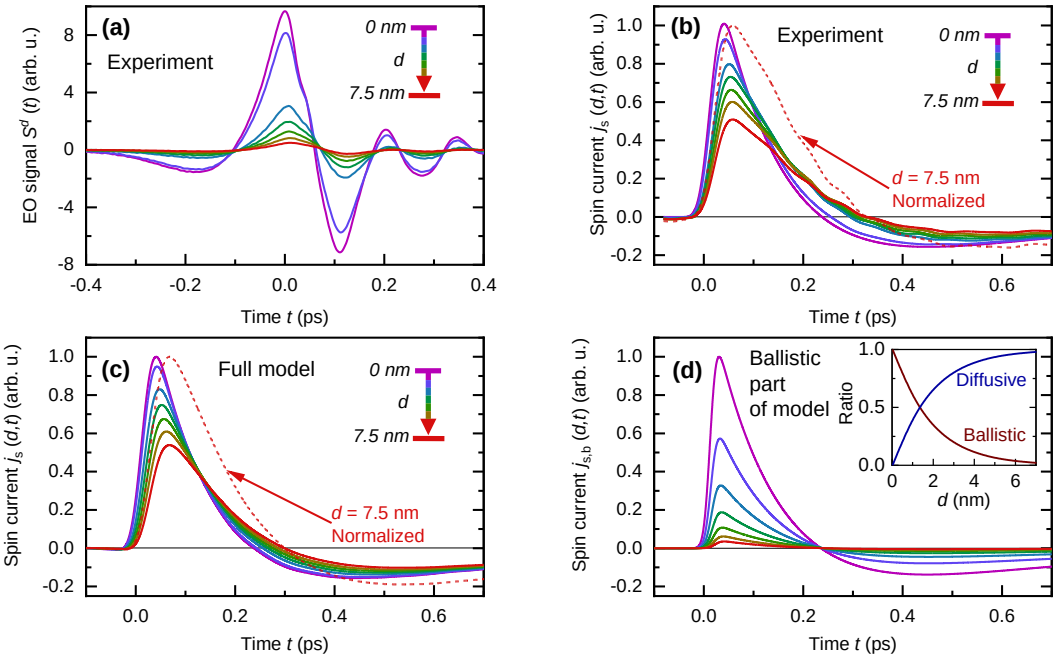

Figure 5.3. | THz spin currents $j_s(z,t)$ after traversing the Cu interlayer. (a) Measured THz emission signals $S^d(t)$ from $F|\mathrm{Cu}(d)|N$ stacks for d = 0, 0.6, 2.2, 3.4, 4.7, 5.9, 7.5 nm (color-coded). (b) Extracted spin-current dynamics $j_s(z = d, t)$ according to Eqs. (5.1) and (5.2). The dashed black arrow indicates the delay Δt of the current peak. (c) Spin currents $j_s(z = d, t)$ calculated using the spin-propagation model of Eqs. (5.1), (5.4), (5.5) with v_F = 1.1 nm/fs and τ = 4 fs. (d) The ballistic contribution to $j_s(z,t)$ by taking $\tau_{\mathrm{sf}} = \tau$ in Eq. (5.2). Red dashed curves are $j_s(z = d, t)$ for d = 7.5 nm with maximum normalized to unity. Inset: the ratio of ballistic and diffusive components in $j_s(z,t)$ as a function of d.

amplitude of the spin current pulses. First, we extract Δt relative to $j_s\,(d = 0, t)$ for the leading edge (at half maximum) and peak of the spin current for all measured d. The resulting Δt vs d [Fig. 5.4(a)] shows a monotonic nonlinear increase. The propagation velocity of the leading edge and peak of $j_s\,(d, t)$ can be obtained from fitting the mean slope of $\Delta t\,(d)$ (not shown), yielding a large propagation speeds of (0.6 ± 0.1) nm/fs and ≈ 0.4 nm/fs, respectively, almost reaching the Fermi velocity of electrons in Cu. Moreover, the pulse leading edge seems to propagate faster than the subsequent pulse peak. This behavior implies a broadening of the leading edge and, possibly, the whole TSC pulse $j_{\mathrm{s}}\,(d, t)$ as d increases. Second, the FWHM of $j_{\mathrm{s}}\,(d, t)$ vs d is shown in Fig. 5.4(b). Indeed, we find a significant pulse broadening from 100 fs at $d = 0$ by a factor of 1.5 at d = 7.5 nm of Cu. Third, the amplitude of the peak TSC decreases exponentially with d with a relaxation length of $\lambda_{\mathrm{rel}} = (11.1 \pm 0.3)$ nm [Fig. 5.4(c)].

Error analysis

The aim of the experiment is to resolve relatively small temporal shifts of emitted waveforms. Since the wedge design requires changing the position of the sample in order to

vary d, it is crucial to analyze potential associated sources of experimental uncertainties. These are (i) the Gouy phase shift [128, 144] of the emitted THz pulse, (ii) variations of the substrate thickness due to its lateral inhomogeneity, and (iii) long-term temporal drifts of the laser pulse train.

Mitigation of uncertainties. (i) We mitigate the potential Gouy phase shift, caused by a variation of z position of the sample due to lateral scanning over the wedge, by setting the sample plane normal to the z-axis and the propagation direction of the excitation laser beam with an accuracy of $< 0.1°$. A lateral displacement of the sample over 3 mm results in an apparent temporal shift of $S(t)$ of less than 0.1 fs. (ii) The impact of a thickness variation of the substrate (ii) is ruled out by repeating same lateral scanning by 3 mm over the reference part of the sample where the Cu interlayer thickness $d = 0$, resulting in negligibly small apparent temporal shifts of <1 fs [see Fig. 5.4(a)]. This test also confirms no impact of Gouy phase shifts. Finally, (iii) the long-term stability of the laser pulse train was addressed by the measurement protocol: each waveform recorded from the wedge part of the sample ($d > 0$) was complemented by a subsequent measurement of a waveform emitted from the reference part of the sample ($d = 0$), serving as a temporal referencing. The stability of these reference waveforms was, however, excellent and of the order of 1 fs.

5.5 Model

To better understand the observed TSC-pulse dynamics [Figs. 5.3(b) and 5.4(a-c)], in particular its edge and peak delay and temporal broadening, we make use of an analytical model of ultrafast spin transport in Cu [116, 283]. It relies on two macroscopic relationships that can be derived from the Boltzmann transport equation. (i) In a generalized version of Fick's law, $j_s(z,\omega) = -D_s(\omega)\,\partial_z \mu_s$, the diffusion coefficient is proportional to the Cu conductance. Thus, it has the same Drude-type frequency dependence, $D_s(\omega) \propto G(\omega) \propto 1/(1 - \mathrm{i}\omega\tau)$, with τ estimated in Fig. 5.2(f). And (ii) the time-domain continuity equation, $\partial_z j_s \propto -\partial_t \mu_s - 2\mu_s/\tau_{\mathrm{sf}}$, where the second term is due to the spin relaxation in Cu [13, 227, 231, 254].

By combining (i) and (ii) (see Appendix A.3), we find that the response function P [see Eq. (5.1)] can be written as the Fourier integral

$$P(z,t) = \int \mathrm{d}\omega \mathrm{e}^{\mathrm{i}k(\omega)z - \mathrm{i}\omega t}. \tag{5.4}$$

Here, for each frequency $\omega/2\pi$, the associated complex-valued wavevector k is given by the dispersion relation $\bar{c}^2 k^2 = \omega^2 + \mathrm{i}\omega\left(\tau^{-1} + 2\tau_{sf}^{-1}\right) - 2(\tau\tau_{\mathrm{sf}})^{-1}$ where $\bar{c} = v_{\mathrm{F}}/\sqrt{3}$ is the mean electron band velocity projected on the z direction. By considering that $\tau_{\mathrm{sf}} \gg \tau$ [13, 227, 231, 254], this relation simplifies to

$$\frac{\bar{c}^2 k^2}{\omega^2} = 1 - \frac{1}{\mathrm{i}\omega\tau}. \tag{5.5}$$

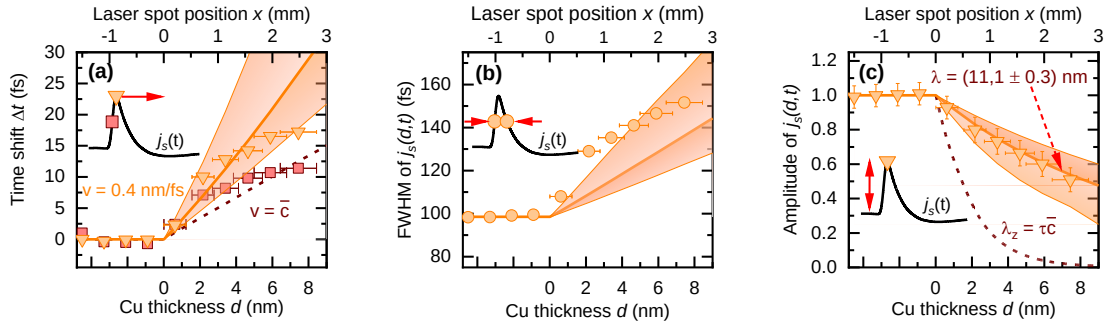

Figure 5.4. | Analysis of $j_s(d,t)$ from Fig. 2(b). (a) Delay Δt of the peak (orange triangles) and leading edge (red squares) of the spin current $j_s(z=d,t)$ as a function of Cu thickness d. (b) Full width at half maximum (FWHM) (circles) and (c) peak amplitude of $j_s(z=d,t)$ vs d. In all panels, results of the model with $v_F = 1.1 \pm 0.2$ nm/fs and $\tau = 4 \pm 2$ fs are shown by orange solid curves (central values) and orange shades (uncertainties). The results of the ballistic contribution are shown by dark-red dashed curves.

Eqs. (5.4) and (5.5) allow us to interpret TSC-pulse propagation through Cu as signal transmission. The frequency-dependent pulse group velocity $\partial_k \omega$ and attenuation Im $k\,(\omega)$ follow from the dispersion relation [Eq. (5.5)]. Note that the model captures both ballistic and diffusive transport, which prevail, respectively, for angular frequencies ω much larger and smaller than the rate τ^{-1} of electron scattering. For example, for $\omega \gg \tau^{-1}$, we can neglect the second term on the right-hand side of Eq. (5.5), and the TSC-pulse group velocity approaches the mean electron band velocity $\bar{c}$.

We use Eqs. (5.1), (5.4) and (5.5), the experimentally given $\mu_s\,(t)$, and the known $v_\mathrm{F} = 1.1$ nm/fs [71] and $\tau = 4$ fs [Fig. 5.2(f)] to calculate the resulting TSC dynamics. The calculated $j_\mathrm{s}\,(z=d,t)$ [Fig. 5.3(c)] agree well with the measured $j_\mathrm{s}\,(d,t)$ [Fig. 5.3(b)]. From the modeled dynamics, we extract the peak delay Δt, the pulse FWHM and peak amplitude of $j_\mathrm{s}\,(z=d,t)$ as a function of d and plot them as orange lines in Fig. 5.4(a)-(c). The orange shaded areas correspond to a small variation of v_F by ± 0.2 nm/fs and τ by ± 2 fs. We find reasonably good agreement of model and experiment, showing that the transport features can be explained by a combination of ballistic and diffusive components. However, we find that the model underestimates the TSC pulse broadening and has a slight mismatch with Δt.

5.6 Discussions

To get more insight into the role of electron scattering, we extract the ballistic component $j_\mathrm{s,b}\,(z,t)$ of the calculated $j_\mathrm{s}\,(z,t)$ by considering $\tau_\mathrm{sf} = \tau = 4$ fs in the full dispersion relation. This choice depolarizes all electrons that have experienced a scattering event and, thus, does not make them available for diffusive spin transport. The resulting ballistic component $j_\mathrm{s,b}\,(d,t)$ [Fig. 5.3(d)] decays considerably faster with increasing d than the diffusive component $j_\mathrm{s}\,(z,t) - j_\mathrm{s,b}\,(z,t)$, as also documented by the ratio of the 2 contri-

butions [inset in Fig. 5.3(d)]. For comparison, the parameters Δt and attenuation of the maximum of the ballistic component are shown in Fig. 5.4(a) and (c) as dark-red dashed curves. We see that the attenuation and broadening of the measured TSC pulses cannot be explained by scattering-free spin transport and requires a non-ballistic component. Indeed, the observed amplitude relaxation length of $\lambda_{\mathrm{rel}} \sim 11$ nm is about 5 times larger than the mean free-path of $\lambda_z = \bar{c}\tau \approx 2$ nm along z. Fig. 5.3(d) and 3(c) also highlight that the diffusion (scattering-based) transport modes are dominating the propagation for $d > 2$ nm.

Interestingly, the propagation speed of the TSC pulse front or its peak still reaches values close to v_{F} and almost matches wave-front velocity $\bar{c}$ expected by the model. This observation indicates that the leading parts of the TSC pulse are formed by electrons that experience only a few collisions, allowing the ultrafast (ballistic-like) spin signal propagation over length scales of more than 10 nm, not strictly limited by λ_z. To directly observe modes propagating at the speed v_F, it would be necessary to fulfill $\omega > 1/\tau$ by using materials with significantly larger τ by increasing the bandwidth of our experiment and analysis.

The source of the visible underestimate of the TSC pulse broadening by the used model [Fig. 5.4(b)] could lie in disregarding a possible initial velocity distribution at $t = 0$. Indeed, the varying z-component of the initial velocity $v_z = v_{\mathrm{F}} \cos(\theta)$ of electrons moving at angle θ from the out-of-plane z-axis might also induce an effective velocity distribution, not included in the model, and it can lead to an additional broadening of $j_{\mathrm{s}}(z = d, t)$ [164, 221]. However, if we apply the ballistic-only model with a homogeneous initial distribution of θ described in Methods in Ref. [221], it would induce a broadening by only a factor of ∼1.2 over 8 nm of Cu, i.e., a significantly smaller value than what was observed in the measured dynamics. In order to include a more realistic initial v_z-distribution in the model, one would need to analyze the orbital symmetry matching between CoFeB and Cu.

5.7 Summary

In summary, we employed time-domain THz emission spectroscopy to directly measure the spatial and temporal evolution of ultrafast spin currents triggered by optical excitation of metallic thin films. The observed temporal delays, significant broadening and attenuation of TSCs for varying Cu spacer thickness indicate diffusion-dominated spin transport and related dispersion of TSCs. A simple model based on the dynamic diffusion equation explains very well our data by assuming realistic values $v_{\mathrm{F}} = 1.1$ nm/fs and $\tau = 4$ fs. If confirms the dominant role of electron-scattering in TSCs for thicknesses $d > 2$ nm. Notably, the analysis of the TSC pulse font revealed that the spin current speeds approaching the Fermi velocity. This methodology facilitates practical implementation of spin currents in ultrafast spintronic devices. For spintronic emitters, we anticipate that Cu intermediate layer can be used to tune the spin current profile and consequently the performance of the spintronic THz emission.

6

Terahertz spin conductance probes of coherent and incoherent spin tunneling through MgO tunnel junctions

We study femtosecond spin currents through MgO tunneling barriers in CoFeB(2 nm)/ MgO(d)/Pt(2 nm) stacks by terahertz emission spectroscopy. To obtain transport information independent of extrinsic experimental factors, we determine the complex-valued spin conductance $\tilde{G}_d(\omega)$ of the MgO layer (thickness d = 0-6 Å) over a wide frequency range ($\omega/2\pi$ = 0.5-8 THz). In the time (t) domain, $G_d(t)$ has an instantaneous and delayed component that point to (i) spin transport through Pt pinholes in MgO, (ii) coherent spin tunneling and (iii) incoherent resonant spin tunneling mediated by defect states in MgO. A remarkable signature of (iii) is its relaxation time that grows monotonically with d to as much as 270 fs at d = 6 Å, in full agreement with an analytical model. Our results indicate that terahertz spin conductance spectroscopy will yield new and relevant insights into ultrafast spin transport for a wide range of materials.

Publication information

This chapter has been published on arXiv as **Terahertz spin conductance probes of coherent and incoherent spin tunneling through MgO tunnel junctions** by R. Rouzegar, M.A. Wahada, A.L. Chekhov, W. Hoppe, J. Jechumtál, L. Nádvorník, M. Wolf, T.S. Seifert, S.S.P. Parkin, G. Woltersdorf, P.W. Brouwer, T. Kampfrath, arXiv preprint arXiv:2305.09074, (under submission) [208]. DOI: https://doi.org/10.48550/arXiv.2305.09074

Author contributions

RR and TK conceived the experiments. RR performed the experiment and analyzed the data. The samples were fabricated by AW, WH and GW. The theory was done by TK, PB and RR. The manuscript was written by RR, TK and with help and discussion contributions of all authors.

6.1 Motivation

Transport of electron spin angular momentum is of central importance for future spintronic devices. To keep pace with other information carriers such as electrons in field-effect transistors [51] and photons in optical fibers [90], spintronic transport needs to be pushed to terahertz (THz) bandwidth and, thus, femtosecond time scales. Interesting applications of ultrafast spin transport include emission of broadband THz pulses [119] and generation of spin torque [126] for ultrafast magnetization switching.

To better understand and optimize THz spin transport, we need tools to adequately characterize it. An important quantity is the spin conductance $G = I_S/\Delta\mu_S$, which quantifies how much spin current I_S is obtained when a spin-voltage drop $\Delta\mu_S$ is applied across a conductor [Fig. 6.1(a)]. We focus on longitudinal spin transport, which can be described by populations of spin-up and spin-down electron states. At frequencies $\ll$1 THz, spin transport measurements typically rely on contacts [15, 156, 231]. At THz frequencies, however, measurement procedures of G still need to be developed.

In this work, we introduce an approach to measure the spin conductance of a thin film X between a ferromagnetic metal layer F and a heavy-metal layer H [Fig. 6.1(a)]. Using THz emission spectroscopy [220], we obtain the complex-valued spin conductance $\tilde{G}(\omega)$ at frequencies $\omega/2\pi$ = 0.5-8 THz. In the time domain, $G(t)$ vs time t can simply be understood as the spin current that would be obtained for a $\delta(t)$-like spin-voltage pulse. Our procedure is demonstrated for the ubiquitous tunnel-barrier material X = MgO and reveals dynamic signatures of coherent and incoherent spin tunneling. We expect that THz spin conductance spectroscopy will provide important insights into ultrafast spin transport in a wide range of materials.

6.2 THz spin-conductance spectroscopy

The general idea of THz spin-conductance spectroscopy is shown in Fig.6.1. It relies on a $F|X|H$ stack, where the ferromagnetic layer F (here CoFeB) serves as spin-current source, X is the layer under investigation, and the heavy-metal layer H (here Pt) acts as detector. First, a femtosecond laser pulse induces an ultrafast generalized spin voltage $\mu_S(t)$ in F = CoFeB [23, 205] that drives a spin current through X = MgO. Second, the spin current $j_S(t)$ arriving in the F = Pt detection layer is converted into an in-plane charge current $j_C(t) \propto j_S(t)$ by the inverse spin Hall effect (ISHE). Third, $j_C(t)$ gives rise to the emission of a measurable ultrashort THz electromagnetic pulse with electric field $E(t)$ [119, 218].

In the frequency domain, the spin conductance of MgO is given by an Ohm-type law, $\tilde{j}_S(\omega) = \tilde{G}_d(\omega)\,\tilde{\mu}_S(\omega)$, where d is the thickness of X. The spin voltage in Pt is neglected owing to the short spin lifetime in Pt [68]. To determine $\tilde{\mu}_S(\omega)$, we conduct a reference measurement on a sample without interlayer (i.e., $d = 0$), where $\tilde{j}_S^{\mathrm{ref}}(\omega) = \tilde{G}^{\mathrm{ref}}(\omega)\,\mu_S(\omega)$ with known $\tilde{G}^{\mathrm{ref}}$.

In our experiment, we measure electrooptic signals $S(t)$ and $S^{\mathrm{ref}}(t)$ rather than the emitted

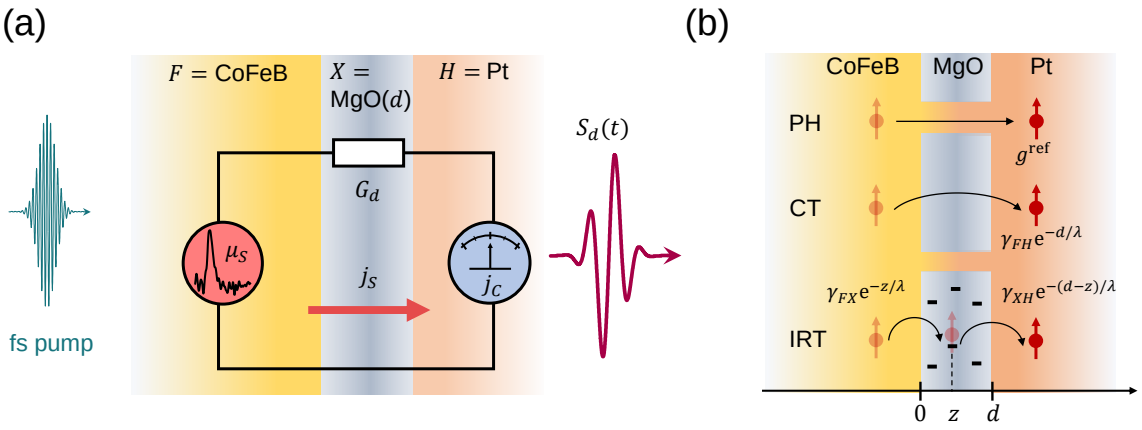

Figure 6.1. | Spin conductance spectroscopy of a layer X. (**a**) A $F|X|H$ stack is excited by a femtosecond laser pulse. The resulting transient spin voltage $\mu_\mathrm{s}(t)$ in the ferromagnetic layer F (here CoFeB) drives a spin current j_S through X (here MgO). The spin current arriving in the heavy metal layer H (here Pt) is converted into an in-plane charge current j_C that is measured by detecting the THz pulse it emits. The dynamics of $\mu_S(t)$ is determined using a sample with $d = 0$, which exhibits a spectrally flat interface spin conductance g^{ref}. **(b)** Considered spin-transport channels through MgO: flow through conducting pinholes (PH), coherent tunneling (CT) and incoherent resonant tunneling (IRT). For IRT, $\gamma_{FX}\,\mathrm{e}^{-z/\lambda}$ is the probability of an electron to tunnel from F = CoFeB to a defect at position z in X = MgO, whereas $\gamma_{XH}\,\mathrm{e}^{-(d-z)/\lambda}$ refers to the tunneling probability from z to H = Pt.

THz electric field $E(t)$. However, S and E are related by an instrument response function that cancels in the frequency domain when the reference measurement is considered [222]. As derived in Appendix A.4, the X spin conductance $\tilde{G}_d$ normalized to the frequency-independent reference conductance $\tilde{G}^{\mathrm{ref}}$ is fully determined by the observables $\tilde{S}$ and $\tilde{S}^{\mathrm{ref}}$ through

$$\frac{\tilde{G}_d(\omega)}{g^{\mathrm{ref}}} = \frac{\tilde{j}_S(\omega)}{\tilde{j}_S^{\mathrm{ref}}(\omega)} = \frac{\tilde{S}(\omega)}{\tilde{S}^{\mathrm{ref}}(\omega)}. \tag{6.1}$$

In the last step of Eq. (6.1), we took advantage of the facts that (i) the measured optical absorptance and THz impedance of all the samples of our experiment are the same and, thus, cancel, and that (ii) the spin conductance $\tilde{G}^{\mathrm{ref}}(\omega) = g^{\mathrm{ref}}$ of the $F|$Pt interface is constant over the frequency interval considered here (see Appendix A.4).

6.3 Experimental details

As spin conductor X, the nonmagnetic insulator MgO is chosen. It is extensively used as a tunnel barrier in magnetic tunnel junctions, which provide large tunneling magnetoresistance for applications in nonvolatile memory devices [5, 110, 258, 274].

The samples are sub||TaN(1.5 nm)|CoFeB(2 nm)|MgO(d)|Pt(2 nm)|TaN(1.5 nm) stacks with various MgO thicknesses of $0 \leqslant d \leqslant 15$ Å. The sample with $d = 0$ is the reference

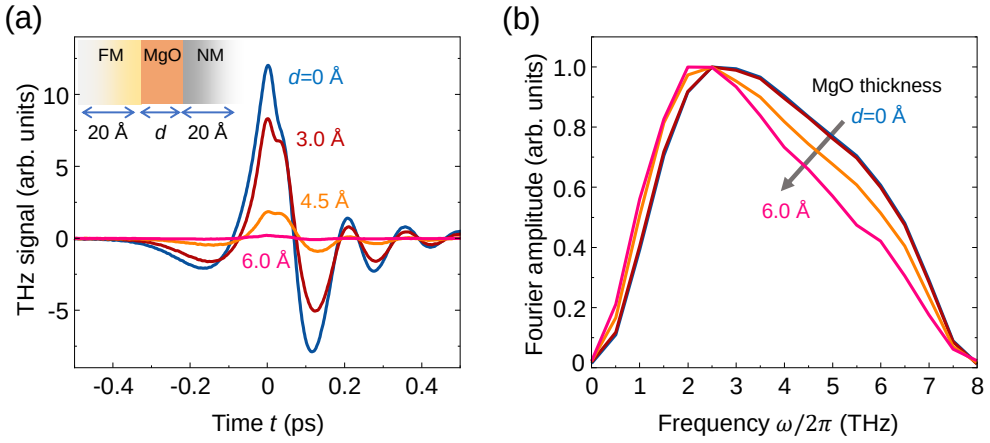

Figure 6.2. | THz-emission raw data from CoFeB(2 nm)|MgO(d)|Pt(2 nm). **(a)** Time-domain electro-optic THz signals $S_d(t)$ odd in the CoFeB magnetization $\boldsymbol{M}$ for various MgO thicknesses of d = 0, 3.0, 4.5 and 6.0 Å. The signal for $d = 0$ is the reference signal $S^{\text{ref}} = S|_{d=0}$. **(b)** Fourier amplitude spectra normalized to their maximum of the signals shown in panel (a).

sample. All layers are grown on an MgO substrate (sub) by DC magnetron sputtering in ultrahigh vacuum at a base pressure of 4×10^{-3} mbar, except the MgO layer, which is grown in the same vacuum chamber by radio-frequency sputtering using an off-axis gun tilted 90° from the substrate plane [256]. Atomic force microscopy shows a roughness <2 Å of all layers [256].

In the THz emission experiments [Fig. 6.1(a)], the F magnetization $\boldsymbol{M}$ of F = CoFeB is saturated by an external magnetic field of about 10 mT. The sample is excited by a train of linearly polarized ultrashort laser pulses (central wavelength 790 nm, nominal pulse duration 10 fs, pulse energy 2 nJ, repetition rate 80 MHz) from a Ti:Sapphire laser oscillator, focused to a spot of 30 µm full width of half maximum (FWHM) of intensity. The emitted THz pulse is detected by electro-optic sampling in a GaP(110) crystal (thickness 250 µm) using linearly polarized probe pulses (0.6 nJ) from the same laser. This procedure yields the THz signal $S(t)$ as a function of delay t between probe and THz pulse [205].

6.4 THz signals

Figure 6.2(a) and Fig. S1 in Ref. [207] show THz emission signals $S(t)$ odd in $\boldsymbol{M}$ from CoFeB|MgO|Pt stacks for various MgO thicknesses d. Signal components even in $\boldsymbol{M}$ are minor.

The signal for $d = 0$ is known to be dominated by ultrafast spin transport from CoFeB into Pt with $\tilde{G}_{d=0}(\omega) = g^{\text{ref}} = \text{const}_\omega$ [23, 78, 205, 218]. When d is increased from 0 Å to 6.0 Å, the signal amplitude decreases by a factor of 60 [Fig. 6.2(a)]. One can show that, in this range, the THz signal is dominated by spin transport from F through MgO into H and the ISHE in H, consistent with the signal origin for $d = 0$ (see S1 in [208]).

Interestingly, with increasing d, the signal amplitude not only drops, but the initially sharp temporal features become smoother [Fig. 6.2(a)]. This trend suggests the emergence of slower components in the spin-current dynamics $j_S(t)$. It is confirmed by the normalized Fourier spectra [Fig. 6.2(b)], whose width decreases with increasing d and whose maximum shifts to lower frequencies.

6.5 Frequency-domain spin conductance

To gain more intrinsic insight into the spin transport through MgO from the signals of Fig. 6.2, we make use of Eq. (6.1) to determine the normalized spin conductance $\tilde{G}_d(\omega)/g^{\mathrm{ref}}$ as a function of frequency $\omega/2\pi$ = 0.5-8 THz. The modulus $|\tilde{G}_d(\omega)/g^{\mathrm{ref}}|$ is displayed in Fig. 6.3(a). It consists of a frequency-independent component and an additional contribution below 3 THz. As expected from Fig. 6.2(a), we observe a drastic overall amplitude reduction with increasing d. At the same time, spectral weight is shifted to frequencies below 3 THz. The spectral phase $\arg \tilde{G}_d(\omega)$ [Fig. 6.3(b)] of the spin conductance and its slope vs ω increase with d, indicating an increasingly non-instantaneous response.

6.6 Time-domain spin conductance

To obtain the time-domain spin conductance $G_d(t)$, we inversely Fourier-transform $\tilde{G}_d(\omega)$. The resulting normalized $G_d(t)/g^{\mathrm{ref}}$ is shown in Fig. 6.4(a) for all MgO thicknesses.

Note that $G_d(t)$ can be considered as the spin current through MgO that is induced by an impulsive spin voltage. Therefore, $G_d(t)$ for $d = 0$ would ideally equal a $\delta(t)$-type signal. However, as the bandwidth of our setup is finite, the extracted $G_d(t)$ is the response to a broadened δ-like pulse $\delta_{\mathrm{exp}}(t)$. To achieve a unipolar $\delta_{\mathrm{exp}}(t)$, which is as short as possible and free of oscillations, we apply a suitable window function $\tilde{\delta}_{\mathrm{exp}}(\omega)$ to $\tilde{G}_d(\omega)/g^{\mathrm{ref}}$ prior to Fourier transformation [38]. Our $\tilde{\delta}_{\mathrm{exp}}(\omega)$ [dashed line in Fig. 6.3(a)] approaches zero at 12 THz. The resulting $\delta(t)$-type spin-voltage pulse $\delta_{\mathrm{exp}}(t)$ has a FWHM of 90 fs [dashed line in Fig. 6.4(a)] and defines the time resolution of $G_d(t)$.

For $d > 0$, the extracted $G_d(t)$ traces [Fig. 6.4(a)] consist of an initial instantaneous response with a shape similar to $\delta_{\mathrm{exp}}(t)$ plus a subsequently decaying component, whose relative weight increases with d. This result is fully consistent with the spectra of Fig. 6.3(a), where the broad background and feature below 3 THz correspond to the instantaneous and slower time-domain response [Fig. 6.4(a)].

6.7 Interpretation

Thin MgO films have been studied extensively in the past. For $d < 10$ Å, structural imperfections are reported, in particular oxygen vacancies [36, 123, 157, 167, 245, 252] and pinholes connecting F and H [130, 241]. Accordingly, we consider 3 possible contributions to the total spin current through MgO in CoFeB|MgO|Pt stacks [Fig. 6.1(b)]: (i) spin

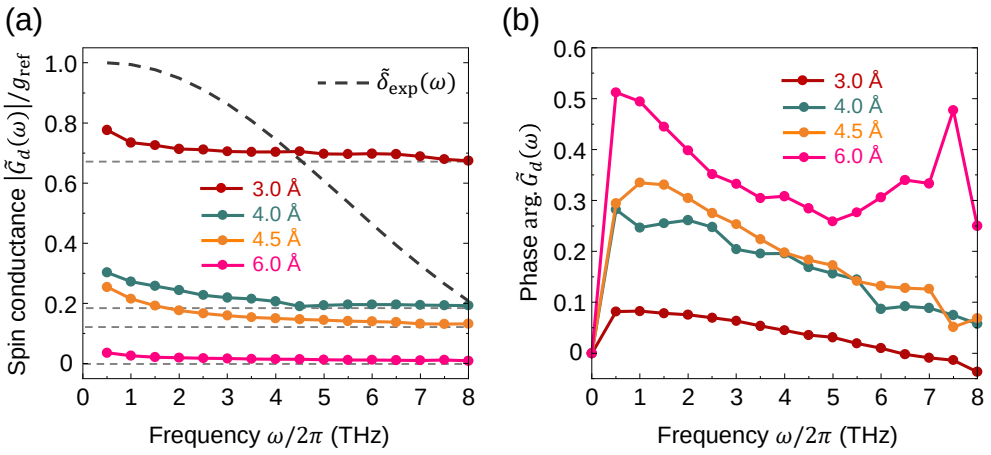

Figure 6.3. | Frequency-domain THz spin conductance $\tilde{G}_d(\omega)$ of MgO layers with various thicknesses d. **(a)** Fourier amplitude $\left|\tilde{G}_d(\omega)/g^{\rm ref}\right|$ vs frequency $\omega/2\pi$, where $g^{\rm ref} = \tilde{G}_{d=0}(\omega)$ is spectrally flat. The dashed line shows the Fourier transformation $\tilde{\delta}_{\rm exp}(\omega)$ of the experimental δ-function. **(b)** Spectral phase arg $\tilde{G}_d(\omega)$.

transport through Pt- or CoFeB-filled pinholes (PH) in the MgO film [131, 241], (ii) coherent off-resonant electron tunneling (CT) through the MgO tunnel barrier [32, 33, 159] and (iii) incoherent resonant tunneling (IRT) through intermediate defect states in the vicinity of the Fermi energy of the CoFeB and Pt layer[70, 240, 245, 252, 253]. As the currents (i)-(iii) add up independently [Fig. 6.1(b)], the spin conductance is the sum

$$G_d = G_d^{\rm PH} + G_d^{\rm CT} + G_d^{\rm IRT}. \tag{6.2}$$

While the PH and CT processes are instantaneous [139, 205] on the time scale of our experimental resolution of 90 fs [dashed black line in Fig. 6.4(a)], the IRT mechanism may require more time to proceed.

We briefly discuss each mechanism in more detail. Regarding $G^{\rm PH}$, one expects that, for $d < 6$ Å, MgO grows in islands [130] or exhibits pinholes [241]. The pinholes are filled with Pt of the subsequently grown Pt layer and, thus, provide a conductive channel between the CoFeB and Pt layer [Fig. 6.1(b)]. $G_d^{\rm PH}$ depends on the in-plane areal fraction $f_d^{\rm PH}$ of pinholes according to $G_d^{\rm PH} \propto g^{\rm ref} f_d^{\rm PH}$. Thus, for $f_d^{\rm PH} = 1$, the reference situation ($d = 0$) is recovered. Because the PH contribution is instantaneous analogous to the reference sample, we obtain $G_d^{\rm PH}(t) = f_d^{\rm PH} g^{\rm ref} \delta(t)$.

CT [Fig. 6.1(b)] through the entire MgO barrier is instantaneous on the scale of our time resolution [139]. Therefore, $G_d^{\rm CT}(t) = g_d^{\rm CT}\left(1 - f_d^{\rm PH}\right)\delta(t)$, where the coefficient $g_d^{\rm CT}$ is the amplitude of the impulsive spin current in the absence of pinholes.

Regarding IRT, oxygen vacancies are known to provide localized electronic states within the MgO band gap and, thus, open up a resonant transport channel [123, 157, 167]. In the simplest IRT realization, an electron tunnels from F into a MgO vacancy and, subsequently,

into H [Fig. 6.1(b)], similar to resonant tunneling in quantum wells [73, 148, 157, 275]. One can quantify the resonant tunneling as $G_d^{\mathrm{IRT}}(t) = g_d^{\mathrm{IRT}}(t)(1 - f_d^{\mathrm{PH}})$, where $g_d^{\mathrm{IRT}}(t)$ is the IRT-related spin conductance of an MgO barrier without pinholes. Based on Fig. 6.1(b), we model $g_d^{\mathrm{IRT}}(t)$ by a single-sided exponential decay $g_{d,0}^{\mathrm{IRT}}\Theta(t)\,\mathrm{e}^{-t/\tau_d}$, where $\Theta(t)$ is the Heaviside step function and τ_d can be considered as the characteristic time of IRT.

With these specifications, Eq. (6.2) turns into

$$\frac{G_d(t)}{g^{\mathrm{ref}}} = A_d\delta(t) + B_d\Theta(t)\,\mathrm{e}^{-t/\tau_d}, \tag{6.3}$$

where

$$A_d = f_d^{\mathrm{PH}} + \left(1 - f_d^{\mathrm{PH}}\right)\frac{g_d^{\mathrm{CT}}}{g^{\mathrm{ref}}}, \quad B_d = \left(1 - f_d^{\mathrm{PH}}\right)\frac{g_{d,0}^{\mathrm{IRT}}}{g^{\mathrm{ref}}}. \tag{6.4}$$

We fit the convolution of G_d [Eq. (6.3)] and our time resolution δ_{exp} to the time-domain data of Fig. 6.4(a), where τ_d, A_d, B_d and possible deviations t_0 from time zero [i.e., $t \to t - t_0$ in Eq. (6.3)] due to substrate thickness variations [224] are fit parameters.

The model fits [Fig. 6.4(a)] describe our data excellently. The resulting amplitude A_d of the $\delta(t)$-like contribution [Fig. 6.4(b)] decreases monotonically with MgO thickness d. One can show that $A_d \approx f_d^{\mathrm{PH}}$ (see [208]). This assignment and Fig. 6.4(b) are consistent with previous work in which f_d^{PH} was found to decrease with increasing MgO thickness d on a scale of 2 Å [241]. According to calculations [256], MgO layers close to the CoFeB and Pt interface are slightly metallic. They have a total thickness of about 4 Å and can be understood to have a large PH fraction. This effect may explain the pronounced drop of A_d from $d = 3.0$ Å to 4.0 Å [Fig. 6.4(b)].

Using $A_d \approx f_d^{\mathrm{PH}}$, we can now determine $g_{d,0}^{\mathrm{IRT}}/g^{\mathrm{ref}} \approx B_d/(1 - A_d)$, i.e., the peak amplitude of the IRT contribution [Eq. (6.3)], which is found to decrease strongly with increasing d [Fig. 6.4(c)]. Remarkably, the characteristic IRT time τ_d is found to grow with d [Fig. 6.4(d)], consistent with the increase of the slope of $\arg \tilde{G}_d(\omega)$ vs ω [Fig. 6.3(b)].

6.8 Model of dynamic IRT

Qualitatively, we suggest the following dynamic scenario for the IRT conductance $g_d^{\mathrm{IRT}}(t) = g_{d,0}^{\mathrm{IRT}}\Theta(t)\,\mathrm{e}^{-t/\tau_d}$. At time $t = 0$, a $\delta(t)$-like spin voltage in CoFeB drives instantaneous tunneling of spin-polarized electrons from CoFeB to MgO defect states. Simultaneously, spin-unpolarized electrons from Pt are transferred to maintain local charge neutrality.

The subsequent tunneling events from occupied defect states to CoFeB or Pt are stochastic. Their rate $\partial_t N^\sigma$ is proportional to the number N^σ of spins $\sigma = \uparrow$ or $\downarrow$ occupying the defect state. Accordingly, we obtain a (i) simple temporal exponential decay of N^σ and, thus, the σ-current from defects to Pt. (ii) The characteristic time of this process increases with increasing d because the tunneling from defects to Pt becomes less likely as d and, thus, the average distance of defect and Pt grow. Finally, as two tunneling events over distance d are involved, (iii) the spin current from CoFeB to Pt decreases with increasing d. The implications (i), (ii), (iii) of our model are fully consistent with the experimental results

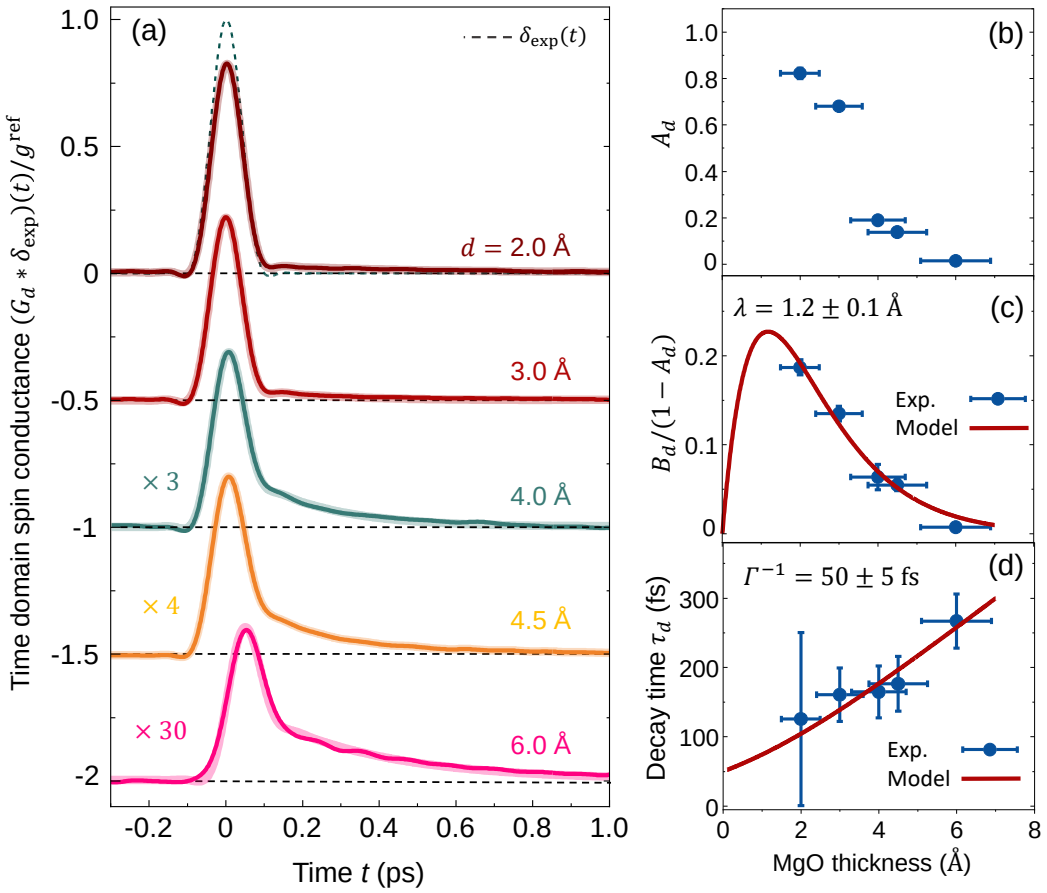

Figure 6.4. | THz spin transport through MgO layers. **(a)** Measured time-domain THz spin conductance of MgO films for various thicknesses d (thin solid lines). The spin conductance $G_d(t)$ can be understood as the current that is driven through the MgO layer by a $\delta(t)$-like spin voltage in the CoFeB layer. Due to the finite time resolution, the δ-function is broadened to the fictitious impulsive spin voltage $\delta_{exp}(t)$ (dashed black line). Accordingly, the extracted conductivity curves are also broadened and display $G_d * \delta_{exp}$. Thick solid lines are fits based on Eq. (6.3). **(b)** Amplitude $A_d \approx f_d^{PH}$ of the instantaneous, i.e., $\delta_{exp}(t)$-like component of $G_d(t)$ vs MgO thickness d (blue circles). **(c)** Amplitude $B_d/(1-A_d) \approx g_{d,0}^{IRT}/g^{ref}$ of the delayed current component vs MgO thickness (blue circles). The red solid line is a fit based on Eq. (6.5) with $\lambda = (1.2 \pm 0.1)$ Å. **(d)** Decay time τ_d of the IRT current component vs MgO thickness (blue circles). The red solid line is a fit based on Eq. (6.5) with $\Gamma^{-1} = (50 \pm 5)$ fs.

of Figs. 4(a), 4(c) and 4(d), respectively.

More quantitatively, a rate-equation treatment and the assumption of vanishing out-of-plane charge current (see Appendix A.5) reproduce the relationship $g_d^{IRT}(t) = g_{d,0}^{IRT}\Theta(t)\,e^{-t/\tau_d}$ with

$$g_{d,0}^{IRT} \propto d e^{-d/\lambda}, \quad \tau_d^{-1} = \Gamma \frac{1 - e^{-d/\lambda}}{d/\lambda}. \tag{6.5}$$

Here, Γ^{-1} quantifies the spin lifetime in a defect state for an infinitely thin MgO layer,

and λ is the spin decay length in a MgO barrier. Eq. (6.5) provides good fits to the data of Fig. 6.4(b), (c) and yields $\Gamma^{-1} = (50 \pm 5)$ fs and $\lambda = (1.2 \pm 0.1)$ Å in good agreement with theoretical predictions [33, 269] .

6.9 Discussion

Measurement of the THz spin conductance relies on the measurement of just two THz emission signals, without having to know any instrument response functions, in contrast to extraction of the charge source current. This approach can be extended to, in principle, any layer X other than MgO, if the following conditions are fulfilled: (1) The signal exclusively arises from the spin current j_S arriving in H. (2) j_S solely originates from the spin voltage μ_S. (3) The presence of the layers X and $H|X$ does not change the μ_S dynamics of F.

For our CoFeB|MgO(d)|Pt system, (1) is fulfilled for the reference sample ($d = 0$), but also for $d \neq 0$ because the ISHE of Pt dominates spin-to-charge conversion of the metal stack (see Appendix A.4 and [208]). (2) is fulfilled for the reference sample [205] and, thus, for $d \neq 0$, too. (3) is fulfilled because the presence of X in $F|H$ stacks was shown to leave the spin-voltage dynamics unchanged [205]. If X has a large optical and THz refractive index, the modified pump-propagation and current-to-THz-field conversion need to be accounted for [208].

In conclusion, we demonstrate THz conductance spectroscopy for the example of MgO barriers. In the time domain, we find ultrafast signatures of IRT, i.e., an exponentially decaying spin current with a relaxation time that increases with the MgO layer thickness. This behavior arises because the tunneling probability decreases with increasing thickness of the tunneling barrier. We anticipate that our method can be used to measure the spin conductance of a large set of materials, ranging from simple metals [164] to complex materials such as antiferromagnets [80, 140, 212], potentially also involving a transverse spin-current component.

7

Broadband spintronic terahertz source with peak electric fields exceeding 1.5 MV/cm

In this work, we improve the performance of an optically pumped spintronic terahertz emitter (STE) by a factor of up to 6 in field amplitude through an optimized photonic and thermal environment. Using high-energy pump pulses (5 mJ, >1 mJ/cm^2, 800 nm, ≈80 fs), we routinely generate terahertz pulses with focal peak electric fields above 1.5 MV/cm, fluences of the order of 1 mJ/cm^2 and a spectrum covering the range 0.1-11 THz. Remarkably, the field and fluence values are comparable to those obtained from a state-of-the-art terahertz table-top high-field source based on tilted-pulse-front optical rectification in $LiNbO_3$. The optimized STE inherits all attractive features of the standard STE design, for example, ease-of-use and the straightforward rotation of the terahertz polarization plane without the typical 75% power loss found in $LiNbO_3$ setups. It, thus, opens up a promising pathway to nonlinear terahertz spectroscopy. Using low-energy laser pulses (2 nJ, ∼0.2 mJ/cm^2, 800 nm, ≈10 fs), the emitted terahertz pulse has a focal peak electric field of 100 V/cm, which corresponds to a 2-fold improvement, and covers the spectrum 0.3-30 THz.

Publication information

This chapter was published as **Broadband spintronic terahertz source with peak electric fields exceeding 1.5 MV/cm** by R. Rouzegar, A. L. Chekhov, Y. Behovits, B. R. Serrano, M. A. Syskaki, C. H. Lambert, D. Engel, U. Martens, M. Münzenberg, M. Wolf, G. Jakob, M. Kläui, T. S. Seifert and T. Kampfrath, Phys. Rev. Applied 19, 034018 (2023) [207]. DOI: https://doi.org/10.1103/PhysRevApplied.19.034018.

Author contributions

RR and TK designed the Si-STE. RR performed the low-energy experiments, and AC performed the high-energy experiment with help from BS and YB. Samples were grown by MS, CL, DE, UM, MM, GJ, MK. RR, AC and TK wrote the manuscript with help from all coauthors.

7.1 Motivation

Terahertz (THz) radiation, which covers the range 0.1-30 THz, is a powerful tool to spectroscopically study fundamental modes of matter, for example, electronic intraband transport, magnons or phonons in solids [53, 278]. Thus, efficient broadband THz sources are of large interest for linear spectroscopy to extract the linear optical response over a large spectral range or the thickness of a known material with high precision [233]. On the other hand, high-amplitude THz sources are important, too, because they enable one to not only probe but drive numerous elementary excitations. This approach allows one to disentangle fundamental interactions between different subsystems or to push various degrees of freedom into highly nonlinear regimes [92, 102, 122, 178].

Laser-driven table-top THz emitters are typically based on 1) resonantly induced photocurrents and 2) off-resonant charge motion, also termed optical rectification. Examples of 1) include photoconductive antennas [22, 103, 230], shift-current emitters [162], laser-ionized gases [12, 62, 146, 160] and spintronic THz emitters (STEs) [31, 69, 218–220, 255]. Examples of 2) are inorganic crystals such as ZnTe, GaP and $LiNbO_3$ [54, 69, 91] and organic materials like BNA [199, 235, 280, 281].

Photoconductive antennas are commonly used sources for linear THz spectroscopy, and they can generate THz pulses with peak fields up to 200 kV/cm at kilohertz repetition rates with a spectral bandwidth that is typically limited to <6 THz at 10% of the amplitude maximum [103, 230]. More broadband THz pulses with fields up to 1 kV/cm at megahertz rates can be generated by ultrafast shift currents upon resonant interband photoexcitation of quantum-well emitters [162]. Organic crystals cover different THz frequency ranges at large field strengths of more than 2 MV/cm [199]. They are typically affected by gaps in the 1-10 THz window [235, 280, 281] and often require infrared wavelengths for pumping and, thus, optical parametric amplifiers for prior frequency conversion. Their long-term stability can be impacted by the applied pump laser fluence and power [202]. Air-plasma THz sources offer gap-less THz radiation over the range 1-40 THz [160] with the peak electric field reaching 0.4 MV/cm [12]. However, they require pump pulses with energies above ∼1 µJ and react sensitively to laser and setup fluctuations [31, 242].

In terms of high-field THz sources, $LiNbO_3$ is a workhorse of nonlinear THz spectroscopy and delivers peak fields beyond 1 MV/cm with a spectrum of 0.1-3.5 THz [54, 84, 91, 272, 277]. Rotation of the THz polarization plane often relies on projection operations by two wire-grid polarizers and is accompanied by an amplitude reduction of up to 50%. The THz-source alignment is challenging because it requires a tilted-pulse-front scheme for phase matching and a reflective telescope for tight THz-beam focusing [84].

Spintronic THz emitters (STEs) offer significant potential as THz sources, since they combine many benefits of other emitter types [2, 9, 31, 41, 66, 82, 98, 142, 186, 189, 216, 218, 220, 237, 243, 265–267, 270] . In particular, STEs permit generation of broadband and single-cycle THz pulses independent of the pump wavelength and pump polarization. The alignment is straightforward, and control of the THz polarization or even polarization landscape is easy by an external magnetic field [42, 89, 129, 180]. Although the approach is easily scalable with regard to the STE area and, thus, pump-pulse energy, peak fields

are, so far, limited to 0.3 MV/cm [219] . However, to drive nonlinear processes and achieve sufficient signal strengths, peak THz fields exceeding 1 MV/cm and fluences of the order of 1 mJ/cm^2 are highly desirable.

In this work, we significantly improve the performance of a STE by optimizing the management of light and heat flow. Our photonic and thermal modifications allow us to generate THz pulses with peak electric fields above 1.5 MV/cm and fluences above 1 mJ/cm^2 for 800 nm, 5 mJ pump pulses. The covered spectral range 0.1-11 THz is limited primarily by the pump-pulse duration. Remarkably, the field and fluence values are comparable to those obtained from a state-of-the-art THz table-top high-field source based on $LiNbO_3$. The optimized STE still has all attractive features of the standard STE, for instance, the straightforward rotation of the THz polarization plane, which is important for nonlinear spectroscopic applications. In particular, the THz field can be reversed easily without the typical 75% power loss found in $LiNbO_3$ setups. We demonstrate the power of the optimized STE in THz-pump optical-probe experiments.

7.2 Standard vs Si-STE design

7.2.1 Standard STE design

The conventional STE design is shown in Figure 7.1(a). It is based on a substrate such as glass or sapphire on top of which a spintronic trilayer stack W(2 nm)|$Co_{20}Fe_{60}B_{20}$(1.8 nm)|Pt(2 nm) is grown [Figure 7.1(b)]. The magnetization $\boldsymbol{M}$ of the ferromagnetic $Co_{20}Fe_{60}B_{20}$ (CoFeB) layer is set by an external magnetic field. An incident femtosecond laser pulse deposits excess energy in the electrons of CoFeB, resulting in a transient generalized spin voltage that drives a spin current from CoFeB into the Pt and W layers [23, 78, 109, 205]. The inverse spin Hall effect of Pt and W converts the spin current into an ultrafast in-plane charge current that emits an electromagnetic pulse with frequencies extending into the THz range. The THz waves from Pt and W add up constructively because Pt and W have spin Hall angles of opposite sign [218, 224].

Building on its success [63, 79, 174, 197, 218, 219, 256], the STE design of Figure 7.1(a) can be improved further. First, the transfer of excess energy into the substrate by heat flow is suboptimal for glass substrates as used previously [88, 219]. The energy deposited by the pump beam can lead to a stationary increase of the working temperature of the STE. As a consequence, a single pump pulse will more easily increase the transient electronic temperature above the Curie temperature of the magnetic layer, resulting in saturation of the STE THz output vs pump power [255].

Second, only 50-60% of the incident pump power is absorbed in the trilayer. This value can be increased to >90% by using dielectric cavities. The residual transmitted pump can be disturbing and is, thus, usually removed by subsequent filtering [219].

Finally, the THz-pulse outcoupling into the forward direction is not ideal because about 75% of the generated THz electromagnetic power is emitted into the backward direction, i.e., into the substrate. To illustrate this behavior, we calculate the THz electric-field

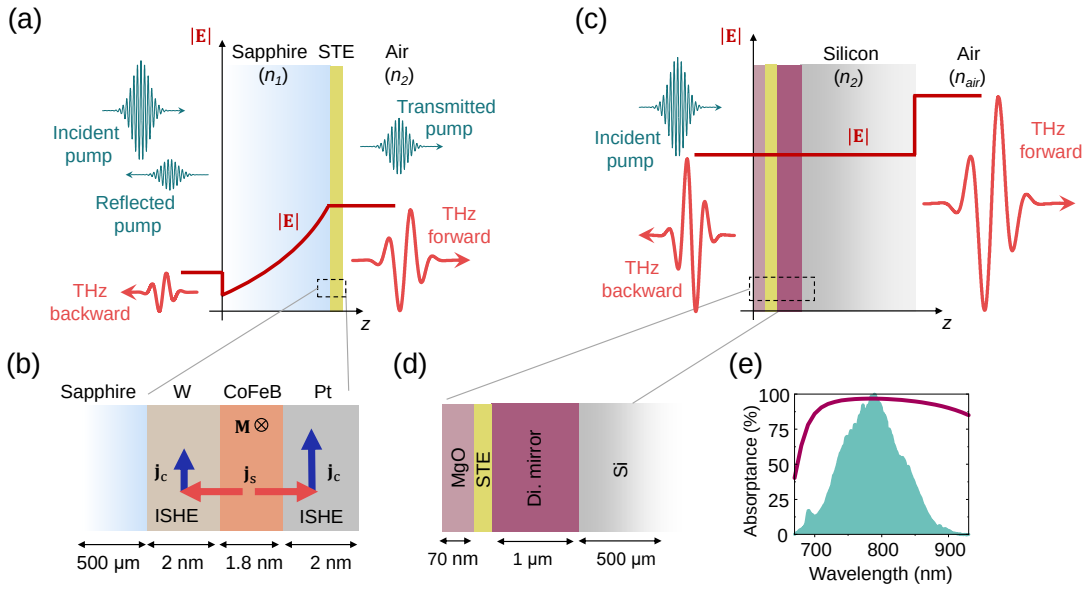

Figure 7.1. | Two photonic and thermal environments of the STE. (a) Standard STE configuration. An incident pump pulse (teal) deposits 50-60% of its energy in a metallic STE stack (yellow), resulting in the emission of a THz electromagnetic pulse (red). The red solid line indicates the calculated THz electric-field amplitude. The backward-propagating THz field is strongly attenuated in the sapphire substrate but increases abruptly when traversing the interface to air. **(b)** The STE stack is a metallic trilayer W(2 nm)|CoFeB(1.8 nm)|Pt(2 nm), in which the ferromagnetic CoFeB layer has in-plane magnetization **M**. Pump excitation induces a spin voltage that injects a spin current $\mathbf{j}_s$ into the adjacent Pt and W paramagnetic layers. In these layers, $\boldsymbol{j}_s$ is transformed into a transverse charge current $\boldsymbol{j}_c$ that acts as a source of THz electromagnetic pulses propagating forward and backward. **(c)** Si-based STE (Si-STE) design with a >2 larger forward-propagating electric field. The enhancement relies on >95% deposition of the pump pulse in the STE stack, negligible attenuation in the Si and the discontinuity of the forward-propagating THz electric field at the Si/air interface. **(d)** Si-STE design details. The STE is sandwiched between a dielectric mirror $[SiO_2(165\text{ nm})|TiO_2(94\text{ nm})]_5$ and a MgO layer, which minimize pump transmission into Si and reflection into air. **(e)** Calculated fraction A_p of the incident pump energy that is absorbed in the STE metal stack (purple curve) and measured pump-pulse intensity spectrum of the low-energy setup (green).

amplitude by a transfer-matrix approach [191], the result of which is shown by the red solid line in Figure 7.1(a).

7.2.2 Si-based STE design

To address the three challenges identified above, we introduce a Si-based STE [Si-STE, see Figure 7.1 (c)], which has an optimized photonic and thermal environment. First, to minimize the steady-state temperature increase of the metal films due to excess-energy accumulation, substrates with good thermal conductivity at 300 K are required. Therefore, Si (150 W/m K), diamond (1500 W/m K) and sapphire (30 W/m K) are very good candidate materials [105, 168, 226], but not glass (1.5 W/m K) [8]. As shown in the following, Si is the most suitable choice.

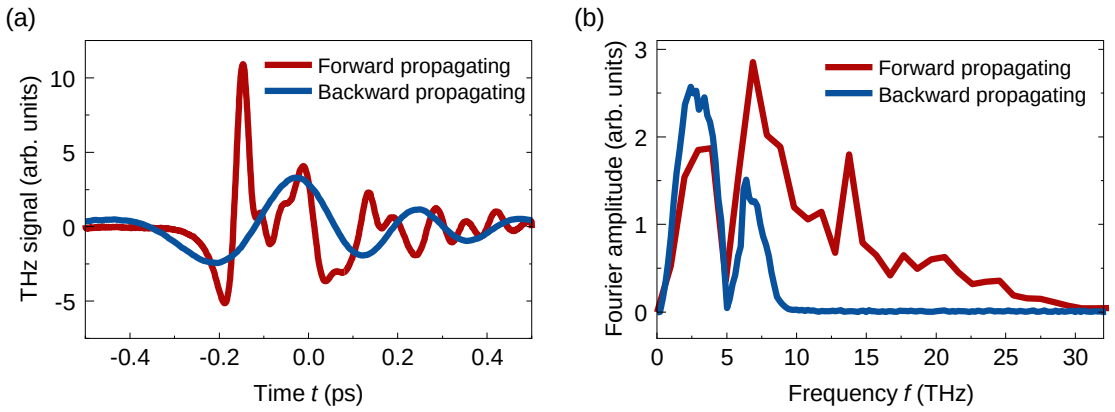

Figure 7.2. | Forward- and backward-propagating THz wave in standard STE. (a) THz electro-optic signal of forward- and backward-propagating THz wave in low-energy operation. **(b)** Fourier amplitude of the signals of panel (a).

Second, to optimize the photonic environment, we note that the THz electric field leaving the STE increases monotonically with the pump absorptance A_p of the spintronic trilayer and the impedance of the STE including any substrates, capping and buffer layers. The figure of merit (FOM) for the forward-propagating THz wave, which is the direction of interest, can, thus, be written as

$$\mathrm{FOM} = \left| \frac{Z_0}{n_1 + n_2 + Z_0/R_s} \mathrm{e}^{\mathrm{i}\omega n_2 d_2/c} \frac{2n_2}{n_2 + n_\mathrm{air}} \right| A_\mathrm{p}. \tag{7.1}$$

The first factor on the right-hand side of Eq. 7.1 is the impedance of the STE alone, i.e., as sandwiched between half-spaces with THz refractive index n_1 and n_2 [218]. The second factor accounts for the THz-pulse propagation through the window (refractive index n_2 and finite thickness d_2) behind the STE, while the third factor is a Fresnel coefficient that quantifies the transmission into air (refractive index $n_\mathrm{air} \approx 1$). Here, $Z_0 \approx 377\ \Omega$ and c are, respectively, the impedance and light velocity of free space, and $R_\square \approx 140\ \Omega$ is the sheet resistance of the STE metal trilayer measured with a 4-point probe. The last factor, A_p, is the fraction of the incident pump-pulse energy that is absorbed in the STE metal stack.

In the previous STE design [see Figure 7.1(a)] [88, 218, 219], the first window is the glass or sapphire substrate of the trilayer, and the second window is air ($n_2 = n_\mathrm{air}$, $d_2 = 0$). The resulting evolution of the THz field amplitude [red solid line in Figure 7.1(a)] shows that the backward-traveling wave is strongly attenuated by the sapphire window as shown in Figure 7.2. Because the refractive index of sapphire exhibits sharp features and shows up in the impedance [first factor in Eq.7.1], the spectrum of the forward-emitted wave is also frequency-dependent [79]. At a wavelength of 800 nm, the pump absorptance is $A_\mathrm{p} = 0.6$, as indicated by the reflected and transmitted pump pulses in Figure 7.1(a).

To enhance the forward-emitted THz amplitude, we propose a new Si-based STE (Si-STE) design, [see Figure 7.1(c)]. It relies on the idea that most of the THz electromagnetic energy

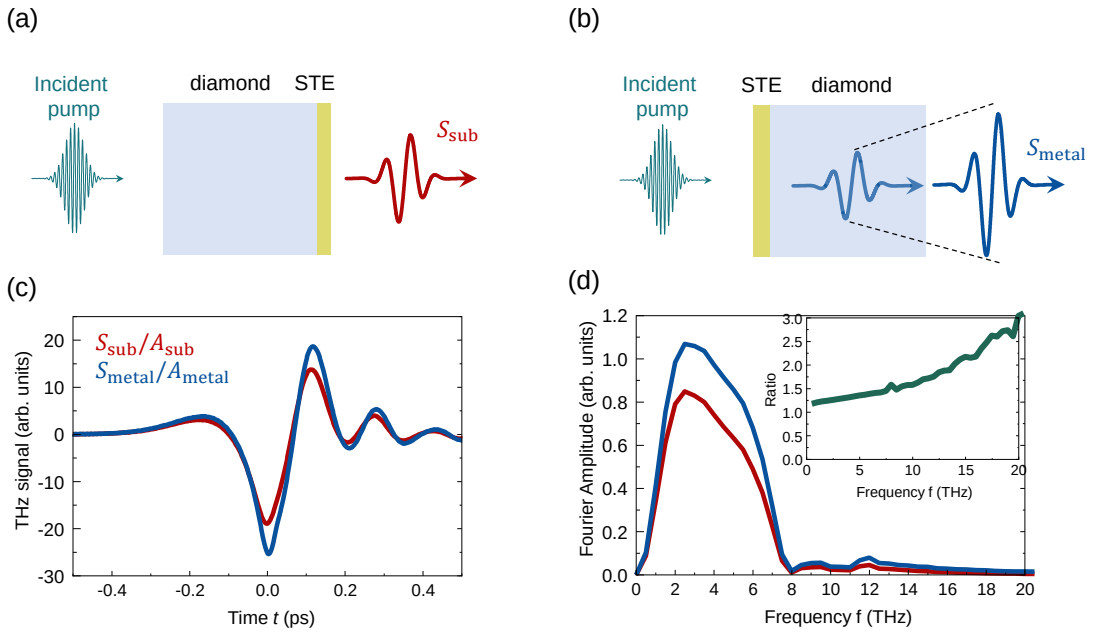

Figure 7.3. | Electric-field discontinuity of the forward-propagating THz pulse at the substrate/air interface. **(a,b)** Standard STE configuration on diamond substrate pumped through substrate [(a)] and metallic side [(b)]. **(c)** Forward-propagating THz time-domain signals normalized by the deposited power for the configurations of panels (a) and (b) as measured with a GaP(250 µm) crystal. **(d)** Fourier amplitude of the THz signals shown in panel (c). The inset shows the ratio of the two signals.

generated in the trilayer propagates into the adjacent window with the larger refractive index (see Figure 7.3). Consequently, we choose air ($n_1 \approx 1$) as the first half-space and high-resistivity Si ($n_2 \approx 3.4 \gg n_1$) as the second. These two media exhibit a spectrally flat refractive index with negligible attenuation throughout the range 0.3-30 THz. Diamond has similarly promising THz-optical properties as Si, but is not considered further because of its high cost for upscaling to 5-cm size. Sapphire is discarded, too, because of its significant THz-wave attenuation [see Figure 7.1(a) and Figure 7.2].

Note that the Si-STE configuration air||Pt|CoFeB|W||Si increases the product of the first three factors in Eq. (7.1) by 44% compared to the previous STE design based on glass or sapphire substrates [Figure 7.1(a)]. The major reason is the increased transmission from Si (n_2) to air (third factor), which amounts to 1.55. It still overcompensates the decreased trilayer impedance (first factor), which equals 57 Ω and 53 Ω in the standard STE and the Si-STE design, respectively. This effect is confirmed by the calculated spatial evolution of the THz field amplitude [red line in Figure 7.1(c)], which exhibits a significant amplitude increase at the Si/air interface.

Third and finally, we embed the trilayer between a dielectric mirror [SiO_2(165 nm)|TiO_2 (94 nm)]$_5$ and an impedance-matching layer MgO(70 nm) [see Figure 7.1(d) and Figure 7.4(a)] [88]. In this way, we push the pump absorptance from $A_p = 60\%$ in the sapphire-based STE [Figure 7.1(a)] to a calculated value >95% in the Si-STE in the range 740-840 nm [Figure 7.1(e) and Figure 7.4(c)]. The pump reflectance is reduced to <3%, as

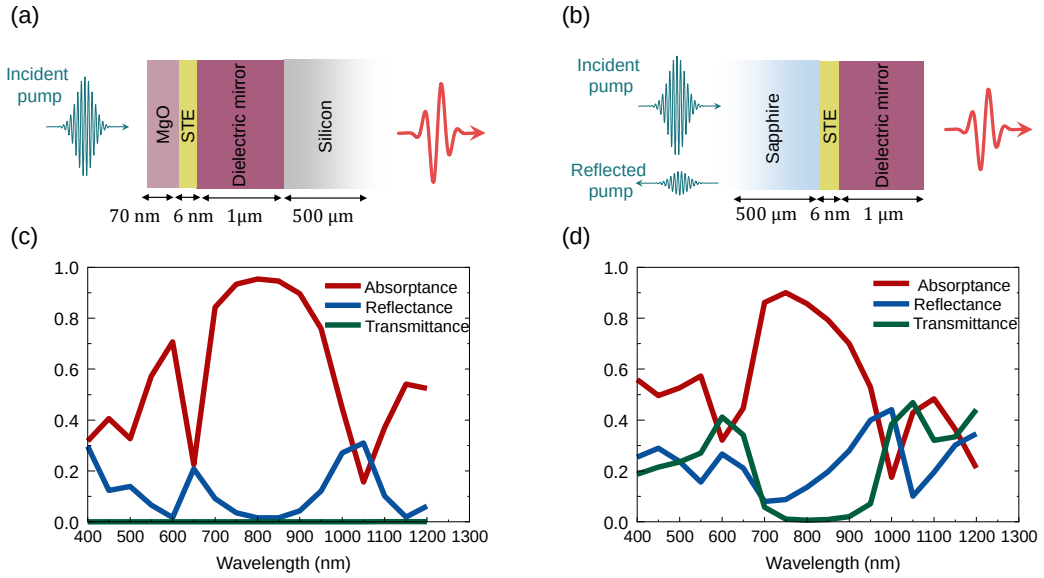

Figure 7.4. | Dielectric cavity design of Si-STE. (a) SiSTE design is same as Figure 7.1(d). Dielectric mirror is consist of $[SiO_2(165\ nm)|TiO_2(94\ nm)]_5$. **(b)** Dielectric cavity design introduced in [88]. **(c)** Reflectance, transmittance and absorptance of Si-STE design **(d)** same for the design shown in panel (b).

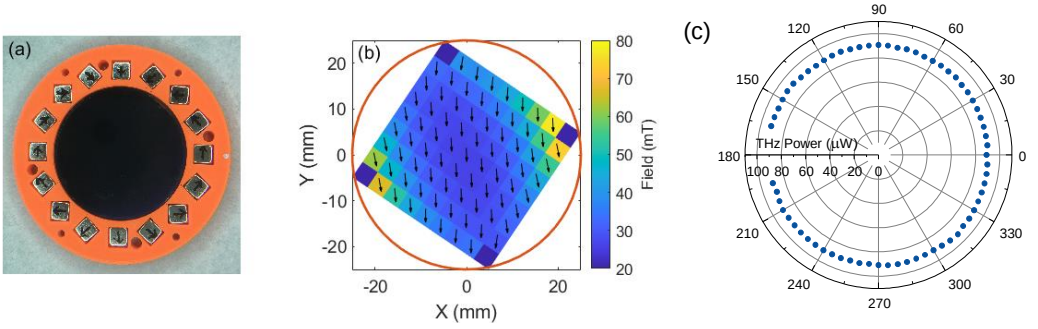

Figure 7.5. | Magnetic field distribution and THz polarization control. (a) Photograph of the large-area high-power Si-STE. It is mounted inside a Halbach array of permanent magnets. The emitter diameter is 5 cm. **(b)** Magnetic-field distribution inside the Halbach array as measured with a Hall probe. The field amplitude is color-coded, while the arrows indicate the direction of the field. **(c)** Emitted THz power measured at the maximum incident pump fluence of 1.1 mJ/cm2 vs the azimuthal rotation angle of the Si-STE.

indicated by the absence of reflected and transmitted pump pulses in Figure 7.1(c) and Figure 7.4(c). The dielectric mirror also reduces the amount of pump-induced free charge carriers in Si to <1%, which may otherwise attenuate and distort the THz pulse.

The THz amplitude evolution [red solid lines in Figure 7.1(a) and (c)] summarizes the benefits of the optimized STE [Figure 7.1(c)] relative to the previous design [Figure 7.1(a)]. In the standard STE, ≈25% of the emitted THz power propagates into the far-field in the forward direction, whereas it is ≈55% in the Si-STE design.

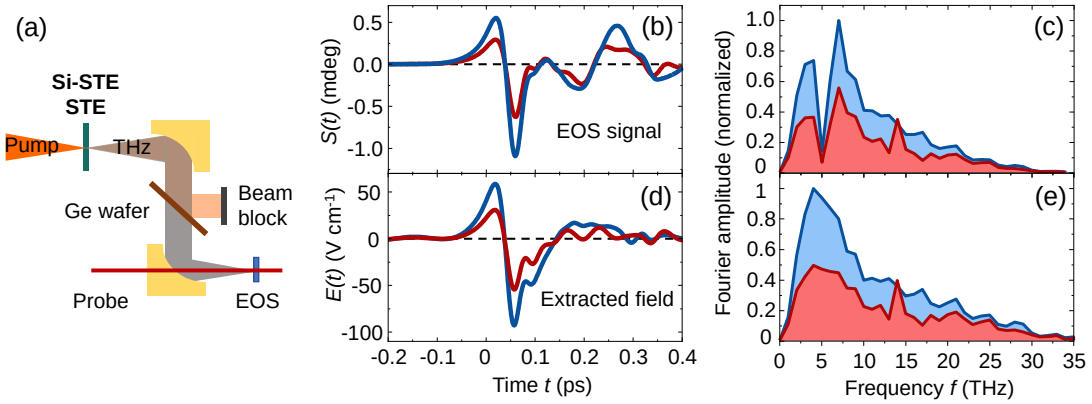

Figure 7.6. | Low-energy STE operation. **(a)** Schematic of the setup. A laser pulse [bandwidth-limited duration ≈10 fs, spectrum in Figure 7.1(e)] is focused into the STE (incident fluence ≈0.2 mJ/cm^2). The resulting THz pulse is collimated with a parabolic mirror and focused into a ZnTe(110) crystal (thickness 10 µm) for EOS by the probe pulse. **(b)** THz electro-optic signal waveforms (probe ellipticity) obtained from a standard STE and a Si-STE [Figure 7.1(a) and (c)]. **(c)** Fourier amplitude of the THz signals shown in panel (b). **(d)** Extracted electric field from the signals shown in panel (b). **(e)** Fourier amplitude of the extracted electric field.

7.3 Experimental details

7.3.1 STE fabrication and characterization

STE trilayers W(2 nm)|$Co_{20}Fe_{60}B_{20}$(1.8 nm)|Pt(2 nm) are deposited on top of Si||dielectric mirror or sapphire substrates using a Singulus Rotaris magnetron tool with a base pressure of 4×10^{-8} mbar by DC-magnetron sputtering. Radio-frequency sputtering is used for the MgO(70 nm) impedance-matching layer from a composite MgO target. The deposition rates for Pt, W, $Co_{20}Fe_{60}B_{20}$ and MgO are 0.91, 1.58, 0.66 and 0.09 Å s^{-1}, respectively, under pure Ar flow used as sputtering gas. The double-side-polished Si wafer has a resistivity >10 kΩ/cm. The dielectric mirror [SiO_2(165 nm)|TiO_2(94 nm)]$_5$ is grown on top of the Si (Siegert Wafer GmbH).

For STEs with pump-transparent substrate such as sapphire [Figure 7.1(a)], the pump absorptance A_p of the STE metal stack is experimentally determined by measuring the fractions of the reflected (R) and transmitted (T) pump power through $A_p = 1 - R - T$.

For the Si-STE, we find zero reflectance and transmittance into air within the accuracy of our measurement of ∼1%. Therefore, 100% of the pump power is absorbed in the Si-STE metal stack and the Si substrate. To estimate the pump power entering the Si substrate, we separately measure the reflectance of the dielectric-mirror stack on top of the Si slab and find >95%. We, thus, expect a pump transmittance $T < 5\%$ into the Si substrate for the Si-STE, resulting in $A_p = 1 - R - T > 95\%$. This result is consistent with our calculations in the range of the pump-pulse spectrum [Figure 7.1(e) and Figure 7.4(c)].

7.3.2 Low- and high-energy THz setups

To put our expectations to test, standard and Si-STEs (TeraSpinTec GmbH) are excited with femtosecond laser pulses, and their THz emission is measured in a low-energy (2 nJ, ∼0.2 mJ/cm^2) and high-energy (5 mJ, ∼1 mJ/cm^2) regime.

In the experiment, a homogeneous distribution of the in-plane magnetization $\boldsymbol{M}$ of the STE's CoFeB layer is achieved by an external magnetic field of approximately 10 mT, which is provided by a Halbach array of permanent magnets [183] (see Figure 7.5). As the array is rigidly connected to the STE, rotation of the STE allows us to rotate the CoFeB magnetization $\boldsymbol{M}$ in the plane.

For low-energy operation [Figure 7.6(a)], laser pulses [bandwidth-limited duration ≈10 fs full width at half maximum (FWHM) of intensity, center wavelength 800 nm, repetition rate 80 MHz, pulse energy up to 2 nJ, intensity spectrum in Figure 7.1(e)] are focused onto the STE surface with a spot size of 30 µm, resulting in a maximum incident fluence of 0.2 mJ/cm^2. By using two 90° off-axis parabolic mirrors, the generated THz pulse is focused into a ZnTe(110) crystal (thickness 10 µm) glued to a ZnTe(100) substrate [141], where its electric field is monitored by electro-optic sampling (EOS) with laser pulses from the same laser.

The resulting signal $S(t)$ vs time t and the THz electric field $\boldsymbol{E}(t)$ incident onto the detection crystal are in the frequency domain connected by [121, 141]

$$\tilde{S}(\omega) = \tilde{H}_{\mathrm{EOS}}(\omega)\,\tilde{E}(\omega)\,. \tag{7.2}$$

Here, the tilde denotes Fourier transformation, $\omega/2\pi$ is frequency, and $\tilde{H}_{\mathrm{EOS}}(\omega)$ is the transfer function of the EOS process. We note that EOS acts akin to a polarizer that projects the THz electric-field vector $\boldsymbol{E}$ onto a direction $\boldsymbol{v}$ with $|\boldsymbol{v}| = 1$. Therefore,

$$E(t) = \boldsymbol{v}\cdot\boldsymbol{E}(t)\,, \tag{7.3}$$

where $\boldsymbol{v}$ is given by the azimuthal angle of the ZnTe crystal and the direction of the probe polarization [250].

For high-energy operation [Figure 7.7(a) and (b)], pump pulses (≈35 fs if bandwidth-limited, 800 nm, 1 kHz, up to 5 mJ) are derived from an amplified Ti:sapphire laser system. The collimated pump beam is enlarged to a width of 2 cm (FWHM of intensity) using a telescope, resulting in an incident fluence of up to 1.1 mJ/cm^2. The generated THz beam is focused into a ZnTe(110) crystal (thickness 10 µm) for electro-optic sampling using pulses (≈20 fs if bandwidth-limited, 800 nm, 80 MHz, <1 nJ) from the seed laser oscillator [38, 151]. The THz power is measured by a power-meter (GenTec THZ9B-BL-DZ-D0). The approximate intensity distribution of the beam cross section in the THz focus is obtained by placing a microbolometer array (Xenics Gobi+ 640) at the position of the electro-optic crystal [Figure 7.7(c)].

In both setups, the standard STE is pumped from the substrate side. The pump radiation traversing the STE is filtered out by a Ge wafer (low-power setup) or a combination of an

ITO dichroic mirror and a Si window in Brewster angle (high-power setup). In contrast, the Si-STE is excited from the air side. As no pump radiation traverses the Si-STE, no further filtering of the beam is required.

Finally, as a reference of the STE under high-fluence operation, we employ a state-of-the-art THz source based on tilted-pulse-front excitation of a $LiNbO_3$ prism. It is driven by pump pulses analogous to the STE, but time-stretched and with slightly less energy (400 fs, 4.2 mJ) to avoid crystal damage [69, 91, 92, 210].

7.4 Results

7.4.1 Low-energy megahertz operation

Figure 7.6(b) shows THz signal waveforms $S(t)$ from a standard STE and a Si-STE. We find that the Si-STE delivers an amplitude that is a factor of 2 larger than that from the standard STE. This value reaches almost the ideal enhancement factor of 2.3 [see Figure 7.1(a) and (c)]. We ascribe the minor discrepancy to the astigmatism that arises as the strongly divergent THz beam traverses the Si window of the Si-STE (see the inset of Figure 7.3(d)).

The amplitude spectrum $|\tilde{S}(\omega)|$ of the THz signal is shown in Figure 7.6(c). The dip at frequency $\omega/2\pi \approx 5$ THz arises from a zero of the EOS transfer function $\tilde{H}_{\mathrm{EOS}}(\omega)$ of the ZnTe crystal [Eq. (7.2)] [141]. It results in temporal oscillations of $S(t)$, as seen in Figure 7.6(a) [207].

To extract the transient THz electric field $E(t)$ in the beam focus right in front of the electro-optic detection crystal, we make use of Eq. (7.2) and deconvolute the calculated $\tilde{H}_{\mathrm{EOS}}(\omega)$ [121] from the measured THz signal waveform [21, 104, 117] (see Fig. S4 in [207]). The resulting field $E(t)$ is shown in Figure 7.6(d). We find a peak field of 100 V/cm.

For both emitters, the spectrum of the electric field covers the range 0.3-30 THz at the 10% level of the peak amplitude [Figure 7.6(e)]. The Si-STE spectrum is smoother compared to the standard STE since the frequency dependence of the Si refractive index is substantially smoother than that of sapphire, in particular in the range 12-14 THz [79].

To summarize, under low-energy operation, the Si-STE design provides a factor of 2 higher amplitude of the emitted THz field compared to the standard STE. This increase is only slightly smaller than our expectation of the 1.4-fold higher THz outcoupling and the 1.6-fold higher pump absorptance. According to the photocurrent generation mechanism of the STE, the amplitude fluctuations of the THz pulses scale with the energy fluctuations of the pump pulses and, thus, the stability of the pump laser. The fluctuations of the measured THz signal waveforms depend, in addition, on the stability of the whole THz time-domain spectrometer [207].

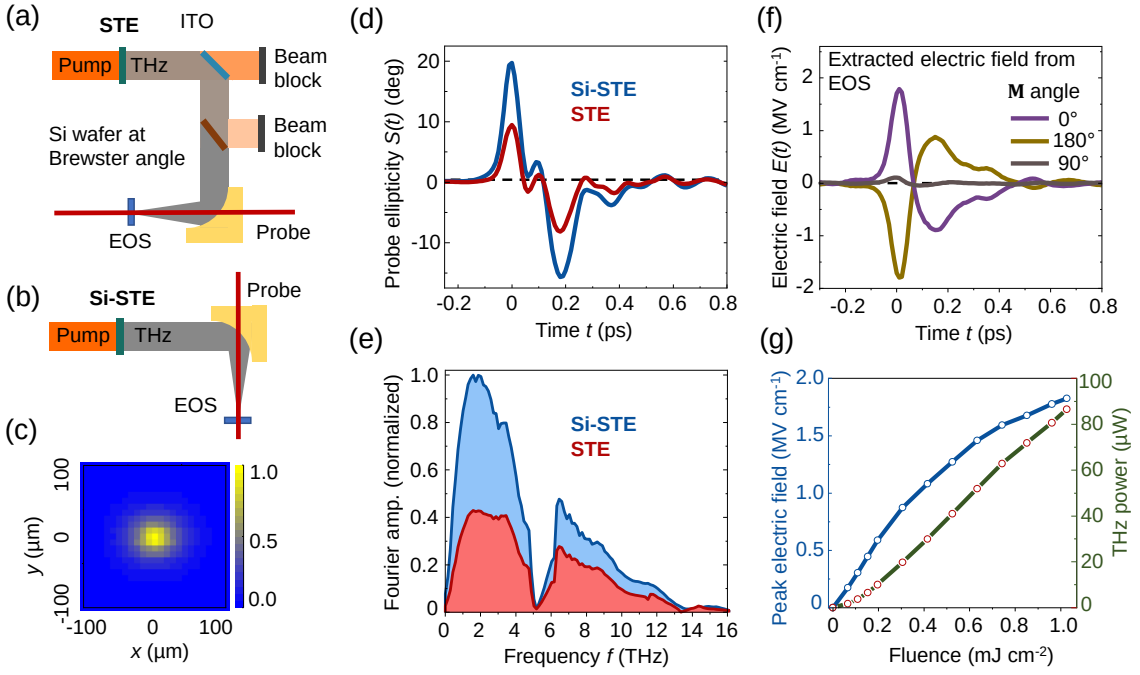

Figure 7.7. | High-energy STE operation. **(a,b)** Schematics of the setups. The collimated pump-pulse beam (≈35 fs if bandwidth-limited, 800 nm, 5 mJ, 1.1 mJ/cm^2) is partially transmitted by the STE on sapphire [panel (a)] and removed by an ITO dichroic mirror and Si wafer. In contrast, the Si-STE [panel (b)] fully absorbs the pump beam. The generated THz beam is focused into a ZnTe(110) crystal (thickness 10 µm) for electro-optic sampling by the probe pulse. **(c)** Intensity distribution of the Si-STE THz-beam focus as measured with a microbolometer array. **(d)** Electro-optic signal of STE and Si-STE THz pulses and **(e)** their amplitude spectra. **(f)** Focal THz electric field of Si-STE extracted from the electro-optic signals for 3 magnetization directions of the Si-STE. The detector is insensitive to the THz electric field emitted at 90° magnetization orientation. **(g)** Measured THz power and peak electric field vs incident and, thus, absorbed pump fluence for the Si-STE.

7.4.2 High-energy kilohertz operation

Figure 7.7(c) shows the spatially resolved intensity of the focused THz beam from the large-area Si-STE as measured by the microbolometer array. The THz spot has a circular shape and a width of about 100 µm (FWHM of the intensity). At the highest excitation fluence (1.1 mJ/cm^2), we measure a THz pulse energy of 90 nJ. Remarkably, this value is more than one order of magnitude larger than reported previously using a large-area STE design on a glass substrate [219].

Electro-optic signal waveforms $S(t)$ of the emitted THz pulses and their amplitude spectra $|\tilde{S}(\omega)|$ are shown in Figure 7.7(d) and (e). As in the low-energy case, the Si-STE is found to outperform the standard STE on sapphire and provides even a factor >2 larger THz signal strength. At the same time, the temporal [Figure 7.7(d)] and spectral [Figure 7.7(e)] shapes of the two STE designs remain approximately the same.

The extracted electric field $E(t)$ in the beam focus is shown in Figure 7.7(f). We find a peak electric field of 1.7±0.2 MV/cm, which implies a peak magnetic field of 0.6±0.1 T.

Time-integration over $E^2(t)/Z_0$ yields an incident fluence of 0.7 ± 0.1 mJ/cm^2 in the beam center. This value is fully consistent with the measured spot size (100 µm) and energy (90 nJ) of the THz pulse, which imply a fluence of 0.8 mJ/cm^2 [207]. Note that both the microbolometer array and the power-meter most likely have a frequency-dependent response over the large STE bandwidth, implying some uncertainty of the measured THz power and spot size.

The THz field can be perfectly reversed by a 180º rotation of the emitter. If we rotate the emitter by 90º, the extracted field approaches zero [Figure 7.7(f)]. As the electro-optic detector is polarization-sensitive [Eq. (7.3)], this finding indicates that the emitted THz pulse is indeed linearly polarized. The polarization direction can be directly controlled by the emitter rotation. Power measurements confirm that the emitted THz power is independent of the polarization of the emitted THz radiation (see Figure 7.5).

The THz peak field and pulse energy as a function of the incident and, thus, absorbed pump fluence are shown by Figure 7.7(g). The fluence scaling of the THz pulse energy changes from quadratic to linear at a fluence of ≈0.2 mJ/cm^2. Note that this value is more than a factor of 3 larger than in previous work in which a glass substrate was used [219], as expected from the significantly higher heat conductivity of the Si-STE's Si substrate. Therefore, to operate the Si-STE in the field-linear-with-fluence regime, the pump fluence should be kept at ≈0.2 mJ/cm^2 or below. Interestingly, in this mode, the THz field in the center of the THz beam focus is independent of the pump-beam diameter because an increased pump diameter implies a smaller THz focus size that compensates the decreased fluence [174, 219].

We summarize that, under high-energy operation, the Si-STE design provides a factor of 2.1 larger amplitude of the emitted THz field compared to the standard STE on sapphire. This performance improvement agrees well with our results from low-energy operation. It follows our expectations of a 1.4-fold higher THz outcoupling and a $1.6^{0.5}$-fold higher pump absorptance, where the exponent 0.5 arises from the fluence dependence [Figure 7.7(g)]. The remaining amplitude enhancement of 1.2 is ascribed to the higher heat conductivity of Si as compared to sapphire. The 6-fold amplitude enhancement relative to the previously demonstrated glass-based large-area STE [219] is even more dramatic. We primarily assign it to the much higher heat conductivity of Si relative to glass.

7.4.3 THz waveform shape

To understand the shape of the THz electric-field waveform $E(t)$ [Figure 7.7(f) and Figure 7.8], we note that the instantaneous THz electric field behind the STE metal stack is proportional to the instantaneous sheet charge current $I_c(t)$ in the STE [218, 224]. The latter can be described by the convolution [205]

$$I_c(t) \propto \left(H_{STE} * \boldsymbol{E}_p^2\right)(t) \tag{7.4}$$

of the squared pump electric field $\boldsymbol{E}_p^2(t)$ and the STE response function

$$H_{STE}(t) = \Theta(t)\left(A_{es}e^{-\Gamma_{es}t} - A_{ep}e^{-\Gamma_{ep}t}\right). \tag{7.5}$$

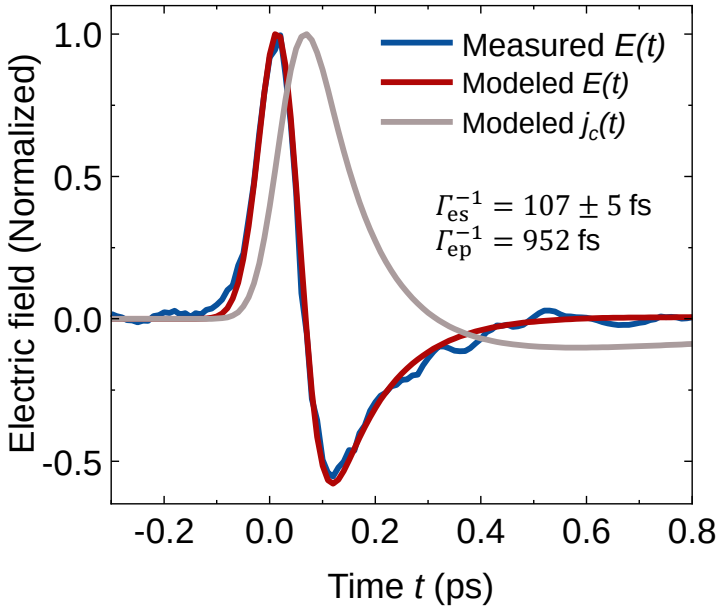

Figure 7.8. | Measured and modeled dynamics of the focal electric field from the Si-STE. The blue curve shows the electric field $E(t)$ extracted from the electro-optical signal $S(t)$. The red curve is a fit according to Eqs. (7.4) and (7.6) with $\Gamma_{es}^{-1} = 107 \pm 5$ fs and the pump-pulse duration of 84 fs (FWHM intensity) as fit parameters. The gray curve shows the resulting charge current inside the Si-STE metal stack.

Here, $\Theta(t)$ is the Heaviside step function, $A_{es} = (\Gamma_{es} - r\Gamma_{ep})/(\Gamma_{es} - \Gamma_{ep})$, $A_{ep} = (1 - r)\Gamma_{ep}/(\Gamma_{es} - \Gamma_{ep})$, Γ_{es}^{-1} and Γ_{ep}^{-1} are material-dependent time constants of electron-spin and electron-phonon relaxation, and r is the ratio of electronic and total heat capacity of the metal stack. The THz field $E(t)$ in the focus is approximately proportional to the time-derivative of $I_c(t)$ [219], i.e.,

$$E\,(t) \propto \partial_t I_c\,(t)\,. \tag{7.6}$$

We calculate Γ_{ep}^{-1} and r according to ref. [205] and obtain $\Gamma_{ep}^{-1} = 950$ fs and $r = 0.15$ for the fluence of 1 mJ/cm^2 used in our experiment. We fit the extracted THz field $E(t)$ by Eqs. (7.4) and (7.6), where Γ_{es} and the duration of the Gaussian pump intensity profile $\boldsymbol{E}_p^2\,(t)$ are fit parameters.

An excellent fit is obtained for $\Gamma_{es}^{-1} = 107 \pm 5$ fs and a pump-pulse duration of 84 ± 3 fs (FWHM of the intensity) as shown in Figure 7.8. The pump duration is a factor >2 longer than that of a bandwidth-limited pump pulse (35 fs) and likely arises from chromatic dispersion of the telescope lenses before the STE, which cannot be compensated entirely.

To summarize, in the dynamics $E\,(t)$ of the focal electric field of Figure 7.8, the width of the first (positive) peak and of the leading edge of the second (negative) peak is predominantly determined by the pump duration. The width of the relaxation tail of the second peak is given by both the pump duration and the electron-spin relaxation time Γ_{es}^{-1} of the STE.

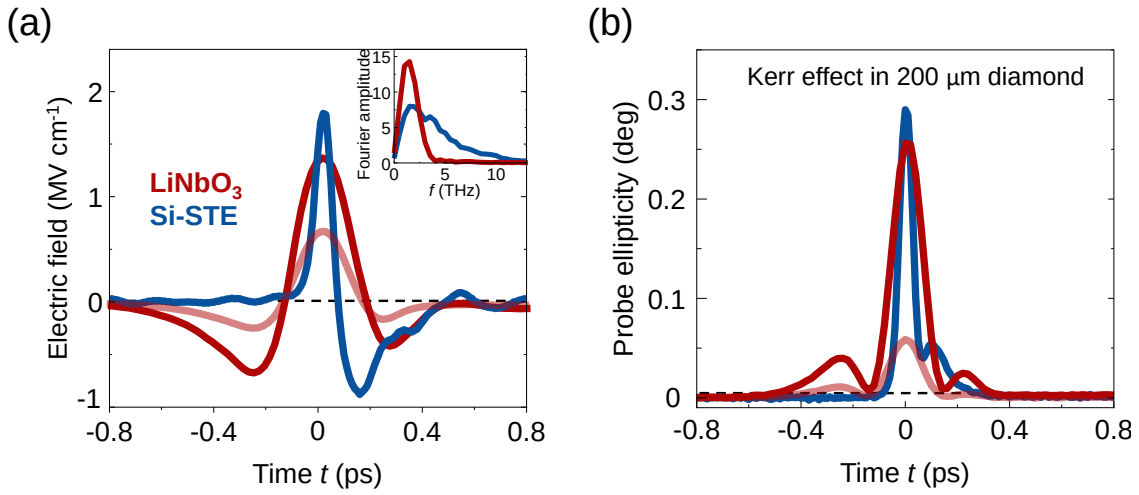

Figure 7.9. | Si-STE vs $LiNbO_3$. Quantitative back-to-back comparison of nonlinear THz spectroscopy with THz pulses from an Si-STE (blue solid lines) vs a $LiNbO_3$ source without (red solid lines) and with polarizers (light-red solid lines) enabling THz field reversal from $\boldsymbol{E}(t)$ to $-\boldsymbol{E}(t)$. **(a)** Electric fields obtained with a ZnTe(110) detector (thickness 10 µm). The inset shows the Fourier amplitude of the electric fields. **(b)** Signal of THz Kerr effect $\propto \boldsymbol{E}^2$ in a diamond window (thickness 200 µm). The resulting optical birefringence is probed by a pulse polarized 45° with respect to the direction of $\boldsymbol{E}$.

7.4.4 Comparison to $LiNbO_3$ source

To evaluate the Si-STE performance, we compare it to the gold standard of laser-driven table-top high-power THz sources: a state-of-the-art $LiNbO_3$ source. Figure 7.9(a) shows the transient THz electric field generated by the Si-STE and the $LiNbO_3$ source. We find similar THz peak fields above 1 MV/cm for $LiNbO_3$ [81, 91] and 1.5 MV/cm for the Si-STE.

However, the two sources are complementary in terms of spectral content as they cover the different spectral ranges 0.1-3.5 THz ($LiNbO_3$) and 0.1-11 THz (Si-STE) at the 10% amplitude level. Accordingly, the pulses have durations of 500 fs ($LiNbO_3$) and 200 fs (Si-STE) FWHM of the field envelope [207]. The THz fluences are comparable, too, and amount to 1.1 mJ/cm^2 ($LiNbO_3$) and 0.7 mJ/cm^2 (Si-STE).

As a further check, we use the THz pulses from the Si-STE and $LiNbO_3$ sources as pump pulses to induce a transient birefringence that scales quadratically rather than linearly with the instantaneous off-resonant THz pump field: the THz Kerr effect in a diamond window (thickness 200 µm) [50, 210]. The probe is polarized at 45° relative to the THz field, and we measure the induced linear birefringence by the ellipticity the optical probe acquires upon propagation through the sample.

Typical signals are displayed in Figure 7.9(b). As expected, they are unipolar and approximately proportional to the squared THz electric fields [Figure 7.9(a)], resulting in substantially faster dynamics for the Si-STE than the $LiNbO_3$ pulse. Deviations from the instantaneous scaling $\propto E^2(t)$ are ascribed to a mismatch of the propagation velocities of

pump and probe pulses [207] and, possibly, a noninstantaneous THz Kerr effect of diamond [179]. Consistent with Figure 7.9(a), the responses are of similar amplitude.

We emphasize that, in a substantial number of nonlinear THz experiments, signal contributions odd and even in the driving THz field occur. To separate them, one needs to measure the sample response to both the THz field $\boldsymbol{E}(t)$ and its reversed version $-\boldsymbol{E}(t)$. Examples are studies in ultrafast magnetism [38, 97] and THz scanning tunneling microscopy [1, 48].

The THz electric field from the Si-STE can be reversed without loss in THz power by rotating the external magnetic field by 180°. In contrast, to reverse the THz waveform from the $LiNbO_3$ source, we make use of two wire-grid polarizers at angles of, respectively, $\pm 45°$ and 90° relative to the polarization of the incident THz beam. We note that this commonly used projection approach leads to THz amplitude losses $\geqslant 50\%$.

To demonstrate the implications of such field reversal, we measure the electro-optic signal and THz-Kerr effect again for THz pulses from $LiNbO_3$ after the two polarizers for field reversal. The result is shown by the pink solid lines in Figure 7.9(a) and Figure 7.9(b): The THz electric field is reduced by about 50% [Figure 7.9(a)], while the THz-Kerr-effect amplitude reduces to $<25\%$ [Figure 7.9(b)], consistent with the expectations. Such signal reduction does not occur for the STE setup.

7.5 Conclusion

Our results demonstrate a significant performance improvement of STEs, which is a direct consequence of the improved thermal and photonic configuration. For high-energy and large-area operation, the Si-STE design exhibits a 4-fold and even 36-fold enhancement in terms of THz power compared to a standard STE on sapphire and glass, respectively [219]. The broadband THz fields from this easy-to-use source are highly interesting for spectroscopic studies of the linear and nonlinear response of fundamental modes of all phases of matter over a broad range of frequencies and pump fluences.

8

Summary

In this work, ultrafast spin transport in magnetic heterostructures has been investigated at THz frequencies. THz emission spectroscopy was employed to reveal the underlying microscopic transport dynamics. The objectives of this thesis were threefold: i) finding the driving force of ultrafast spin currents, ii) to explore and characterize spin transport within various material systems, and iii) enhance the terahertz emission of STEs. First, we found a striking connection between terahertz spin transport (TST) and ultrafast demagnetization (UDM) in magnetic heterostructures, revealing both arising from the same driving force. Subsequently, we studied spin transport through paramagnetic Cu layer, and we identified the spin current dispersion and separated ballistic and diffusive mode of transport. We also introduced the spin-conductance-spectroscopy technique for characterizing ultrafast spin transport across various materials. Applying this method to spin transport through MgO, we unveiled distinct mechanisms governing spin transport and tunneling. Concluding our investigation, we optimized terahertz radiation from STEs by optimizing THz outcoupling and maximizing the heat transport out of the STE. Below, the key findings of this thesis are summarized:

1) Spin voltage is the driving force of UDM and TST

Ultrafast demagnetization (UDM) and Terahertz spin transport (TST) are both driven by a common force, referred to as a generalized spin voltage, indicating the surplus spin polarization in relation to the equilibrium magnetization. This work proposes the term "pyrospintronic effect" for the heat-induced spin voltage, drawing an analogy to the pyroelectric effect observed in pyroelectric materials, where electric polarization follows instantaneous temperature changes. The pyrospintronic effect is predominantly ultrafast due to the limited relaxation time of the spin voltage governed by electron-spin relaxation, especially in metallic ferromagnets. It's important to emphasize that the observed spin current does not stem from a spin-dependent Seebeck effect [15]. Temperature gradients are found to be relevant either on longer timescales when the spin voltage has decayed, or in scenarios where the ferromagnetic layer is not excited, implying no change in spin voltage [96, 124, 166].

Upon excitation of a ferromagnet with a fs laser pulse, the spin voltage jumps to a nonzero value and subsequently relax through electron-spin equilibration, while electron-phonon equilibration has a minor influence since it is significantly slower. Our results also strongly indicate that the impact of TST on spin voltage dynamics is negligible in our experiments. This insight suggests that the decay of photoinduced spin voltage is primarily driven by spin-flip processes in F, even in the F|N stack. Consequently, only a small portion of the

excess spin angular momentum transfers to N. We thus anticipate that the TST amplitude can be increased significantly by using more transparent F|N interfaces and F materials with larger electron-spin relaxation time.

Regarding speed and bandwidth, it is noteworthy that the initiation of TST is genuinely ultrafast and mainly limited by the pump pulse's duration depositing energy into the electrons of F. This contrasts significantly with the interfacial spin Seebeck effect, where carrier multiplication is necessary to reach peak spin current [222].

This study bridges the understanding of UDM in F samples to TST from F to an adjoining N layer, offering potential enhancement avenues for spin-current amplitudes in various applications like spin torque [3, 137, 200], spintronic terahertz emitters [218, 243, 268, 270], and energy harvesting [125] [13]. Furthermore, these findings establish a direct link between femtomagnetism and spintronics. In particular, terahertz emission spectroscopy holds great promise to be an excellent ultrafast monitor of the evolution of the spin voltage.

2) Accessing ultrafast spin-transport regimes in copper

Chapter 5 addressed the spin current propagation through a Cu intermediate layer. We employed broadband time-domain terahertz (THz) spectroscopy to reconstruct optically generated spin current pulses in a trilayer of F|Cu|N, where F=CoFeB and N=Pt are thin ferromagnetic and nonmagnetic films and Cu is a wedge-shaped spacer. We resolved the spatiotemporal evolution of the spin current $j_s(d,t)$, while it is propagating through an increased travel distance in a Cu layer. We observed the spin current pulse undergoes a gradual temporal shifts and a significant dispersion. The propagation velocity of the leading edge of $j_s(d,t)$ reaches (0.6 ± 0.1) nm/fs, almost reaching the Fermi velocity of electrons in Cu. We could explain the peculiar spatiotemporal evolution of the spin current by a simple dynamical diffusion model and assuming realistic values of electron velocity of $v_F = 1.1 \pm 0.2$ nm and velocity relaxation time of $\tau = 4 \pm 2$ fs.

Further, by a thorough analysis of the resulting spatiotemporal dynamics of the spin current in terms of its temporal shifts and broadening, combined with a dynamical diffusion model, led us to the following conclusions: i) The maximal propagation speed of the initial parts of the spin-current profile is ballistic-like and reaching values close to Fermi velocity, even over traveled distances of 8 nm, i. e., larger than the mean free path in Cu. ii) The broadening and attenuation observed in the spin current pulse can be attributed to the direct influence of electron-scattering events on ultrafast spin transport. iii) For the majority of spin-polarized electrons propagating within copper, the dominant mode of transport is diffusion, particularly at distances exceeding 2 nm.

3) Ultrafast spin conductance spectroscopy in MgO tunnel junctions

We presented a novel technique in Chapter 6 that allows one to measure the complex-valued spin conductance of any given layer across a broad bandwidth covering the terahertz

(THz) range. In the time (t) domain, the spin conductance $G_d(t)$ has a very intuitive interpretation: It can be considered as the spin current through a given layer that is induced by an impulsive, i.e., $\delta(t)$-like spin voltage. Therefore, $G_d(t)$ contains important information on spin transport on microscopic (i.e., femtosecond) time scales, free from the impact of instrument response functions.

To demonstrate our approach, we used broadband THz emission spectroscopy and measured the spin conductance of an important model system, MgO tunnel junctions, over a wide frequency range (0.5-8 THz). We observed time-domain signatures of various spin transport mechanism in MgO tunnel barriers: (i) transport through metallic pinholes, (ii) coherent tunneling, and (iii) incoherent resonant tunneling. While (i) and (ii) proceed instantaneous within the time resolution of our experiment, (iii) shows delayed spin transport due to trapping and subsequent release of spins in MgO defects.

The simple example of MgO indicates that our approach can be used to measure the THz spin conductance of a large set of materials, ranging from simple metals [164] (conduction-electron spin transport) to complex materials such as antiferromagnets (magnon spin transport) [80, 140, 212]. Importantly, our method is easy to use because THz spin conductance can be measured without knowledge of any instrument transfer functions. This accessibility makes it viable for research groups equipped with a terahertz time-domain spectroscopy system or a femtosecond laser.

4) Broadband spintronic terahertz source with peak electric fields exceeding 1.5 MV/cm

In Chapter 5, we significantly improved the performance of an optically driven spintronic terahertz emitter (STE) by optimizing the management of light and heat flow. Our new Si-based STE (Si-STE) design features almost 100% pump absorptance, enhanced terahertz outcoupling and maximized heat-transport into the substrate.

For large-area emitters driven by 5 mJ, 50 fs, 800 nm femtosecond laser pulses, we accordingly increased the amplitude of the emitted terahertz electric field by a factor of 6 compared to the state of the art [219], resulting in peak fields of 1.5 MV/cm, a fluence of the order of 1 mJ/cm2, with a gapless spectrum covering the range 1-11 THz. In the low-energy operation mode driven by 1 nJ, 10 fs, 800 nm pump pulses, we could improve the emitted THz field by a factor >2 and achieved electric fields up to 100 V/cm and a gapless bandwidth of 0.3-30 THz.

We compared our new Si-STE design to $LiNbO_3$, which is the gold standard of table-top high-power terahertz sources. In the high-energy mode, we find comparable peak fields (1.5 vs 1 MV/cm for STE vs $LiNbO_3$) and fluences (0.7 vs 1.1 mJ/cm2). As a first test with respect to nonlinear terahertz material responses, we used the emitted terahertz electric field from both sources (Si-STE and $LiNbO_3$) to induce the THz Kerr effect in a 200 µm thick diamond window. While a terahertz Kerr signal of comparable magnitude was found for both the Si-STE and LiNbO3, the signal dynamics are substantially faster for the Si-STE-generated THz pulse owing to its significantly shorter THz pulse duration (200 fs vs

500 fs).

The optimized STE (Si-STE) still has all attractive features of the standard STE, e.g., straightforward rotation of the terahertz polarization plane by an external magnetic field, ease-of-use and independence of the pump wavelength. Thus, we believe that the Si-STE is a highly interesting alternative to terahertz sources such as LiNbO3 and nonlinear organic crystals and will, thus, find widespread application in linear and nonlinear terahertz spectroscopies.

A

Appendix

A.1 Spin dynamics model

The model presented here was developed by P. W. Brouwer and T. Kampfrath, both affiliated with the Department of Physics at Freie Universität Berlin, Germany. The numerical implementation was carried out by R. Rouzegar and D. Reiß.

This Appendix belongs to the paper [205] and the same publication information reported in Chapter 4, page 41, also applies here.

The goal of this Appendix is to model the spin dynamics of a single thin ferromagnetic metal layer F and an F|N stack where F is in contact with a thin normal-metal layer N. We assume that each layer X (F or N) can be treated as homogeneous.

A.1.1 Electronic structure

We describe the electronic structure of F and N by the Stoner model [181] in which a given electron feels the exchange coupling to other electrons through the mean magnetization $\boldsymbol{M} = M\boldsymbol{u}_y$ (Fig. 4.1). Transverse spin fluctuations perpendicular to $\boldsymbol{M}$ due to magnons are summarized by the reduced magnitude of $\boldsymbol{M}$. The Stoner model provides a good phenomenological description of various magnetism phenomena [15, 24, 56, 169, 238], but its microscopic parameters should not be overinterpreted [56].

The state of the electronic system in a given layer X is fully characterized by the occupation numbers $n_k^{\mathrm{X}\sigma}$ of a Bloch state (k, σ). Here, $\sigma = \uparrow, \downarrow$ refers to the electron spin, and k summarizes the band index and wavevector. We define the magnetic moment $\boldsymbol{m} = m\boldsymbol{u}_y$ of F such that $\left(g^F/2\right)\mu_B m = MV^F$ where $\boldsymbol{M} = M\boldsymbol{u}_y$ is the magnetization [Fig. 4.1(a)], $g^F \approx 2$ is the electron g-factor, μ_B is the Bohr magneton, and V^F is the volume of F. Similarly, we define the spin current through the interface as $J_s = j_s A^{F|N}$ where $(\hbar/2)\, j_s$ is the spin-current density, and $A^{\mathrm{F|N}}$ is the area of the F|N stack.

We adopt a simplified description in which the occupation of each Bloch state (k, σ) is fully given by its energy $\epsilon_k^\sigma(t)$, that is,

$$n_k^{X\sigma}(t) = n^{X\sigma}\left(\epsilon_k^{X\sigma}(t), t\right). \tag{A.1}$$

To model magnetic order, we make use of the Stoner model, in which the Bloch energy

depends on the pump-induced change Δm in the magnetic moment according to

$$\epsilon_k^{X\sigma}(t) = \epsilon_{k0}^{X\sigma} + I^{X\sigma}\Delta m(t) + e\,\Phi^X(t). \tag{A.2}$$

Here, $\epsilon_{k0}^{X\sigma}$ is the Bloch energy before arrival of the pump pulse, and $I^{X\sigma} = I^{X\uparrow,\downarrow} = \pm I^X/2$ quantifies the strength of the effective electron-electron Coulomb interaction for X =F only. The electrostatic potential Φ^X accounts for a possible charging of a given layer X due to transport, where $-e$ is the electron charge.

A.1.2 Rate equations

Before arrival of the pump pulse, the $n^{X\sigma}(\epsilon, t)$ are given by one and the same Fermi-Dirac function $n_0(\epsilon)$ at temperature T_0. We now focus on the rate of change $\dot{n}^{\mathrm{F}\sigma} = \partial_t n^{\mathrm{F}\sigma} = \partial n^{\mathrm{F}\sigma}/\partial t$ of the electron occupation numbers $n^{\mathrm{F}\sigma}$ in F. As detailed in the following, it is determined by four contributions,

$$\dot{n}^{\mathrm{F}\sigma} = \dot{n}^{\mathrm{F}\sigma}\big|_{\mathrm{sc}} + \dot{n}^{\mathrm{F}\sigma}\big|_{\mathrm{sf}} + \dot{n}^{\mathrm{F}\sigma}\big|_{\mathrm{tr}} + \dot{n}^{\mathrm{F}\sigma}\big|_{I}. \tag{A.3}$$

The first term on the right-hand side of Eq. (A.3) captures spin-conserving (sc) scattering events and the excitation by the pump pulse. It, thus, fulfills

$$0 = \int \mathrm{d}\epsilon D^{\mathrm{F}\sigma}\,\dot{n}^{\mathrm{F}\sigma}\big|_{\mathrm{sc}}, \tag{A.4}$$

where $D^{X\sigma}(\epsilon, t) = \sum_k \delta\left(\epsilon - \epsilon_k^{X\sigma}(t)\right)$ is the instantaneous density of Bloch states with spin σ.

Impurity- or phonon-mediated spin-flip (sf) events are captured by the second term of Eq. (A.3) and assumed to be quasi-elastic following Refs. [132, 171] and. They are not restricted to so-called Stoner excitations, in which the electron wavevector is conserved [181]. As indicated by Fig. 4.10(a), the rate of change of the electron occupation $n^{\mathrm{F}\uparrow}$ due to elastic spin-flip scattering is proportional to $n^{\mathrm{F}\uparrow}$ and the number $\left(1 - n^{\mathrm{F}\downarrow}\right) D^{\mathrm{F}\downarrow}$ of available unoccupied spin-down states at the same energy ϵ plus an analogous term for the reverse process,

$$\dot{n}^{\mathrm{F}\uparrow}\big|_{\mathrm{sf}} = -P_{\mathrm{sf}}^{\mathrm{F}} n^{\mathrm{F}\uparrow}\left(1 - n^{\mathrm{F}\downarrow}\right) D^{\mathrm{F}\downarrow} + P_{\mathrm{sf}}^{\mathrm{F}} n^{\mathrm{F}\downarrow} D^{\mathrm{F}\downarrow}\left(1 - n^{\mathrm{F}\uparrow}\right) = -\left(n^{\mathrm{F}\uparrow} - n^{\mathrm{F}\downarrow}\right)\frac{g_{\mathrm{sf}}}{D^{\mathrm{F}\uparrow}}. \tag{A.5}$$

Here, $g_{\mathrm{sf}}(\epsilon) = \left(P_{\mathrm{sf}}^{\mathrm{F}} D^{\mathrm{F}\uparrow} D^{\mathrm{F}\downarrow}\right)(\epsilon)$, and the factor $P_{\mathrm{sf}}(\epsilon)$ is proportional to the square of the matrix element for a spin-flip scattering event. The analogous equation for the rate of change of $n^{\downarrow}(\epsilon)$ is obtained by simply swapping $\uparrow$ and $\downarrow$.

The third term of Eq. (A.3) captures spin transport (tr) across the $F|N$ interface [see Fig. 4.10(b)]. We assume the transmission events to be spin-conserving and elastic. Consequently, we can consider spin-up (σ =$\uparrow$) and spin-down (σ =$\downarrow$) electrons separately.

By counting transmission events analogous to Eq. (A.5), we obtain

$$\dot{n}^{\mathrm{F}\sigma}\big|_{\mathrm{tr}} = -\left(n^{\mathrm{F}\sigma} - n^{\mathrm{N}\sigma}\right)\frac{g^{\sigma}_{\mathrm{tr}}}{D^{\mathrm{F}\sigma}}, \tag{A.6}$$

where $g^{\sigma}_{\mathrm{tr}}(\epsilon) = \left(T^{\sigma}_{\mathrm{tr}} D^{\mathrm{F}\sigma} D^{\mathrm{N}\sigma}\right)(\epsilon)$, and $T^{\sigma}_{\mathrm{tr}}(\epsilon)$ is a spin-dependent interface transmittance. The last term of Eq. (A.3) arises because n is evaluated at a fixed ϵ while the Bloch energy changes according to Eq. (A.2). We obtain

$$\dot{n}^{\mathrm{F}\sigma}\big|_{I} = n^{\mathrm{F}\sigma\prime} I^{\mathrm{F}\sigma} \dot{m} = I^{\mathrm{F}\sigma}\left(\partial_{\epsilon} n^{\mathrm{F}\sigma}\right)\left(\dot{m}|_{\mathrm{sf}} + \dot{m}|_{\mathrm{tr}}\right), \tag{A.7}$$

where $n^{\mathrm{F}\sigma\prime} = \partial_{\epsilon} n^{\mathrm{F}\sigma} = \partial n^{\mathrm{F}\sigma}/\partial\epsilon$. In the last step of Eq. (A.7), we split the rate of change of the magnetization into the contributions of spin flips and spin transport. As the electronic band structure depends on the magnetic moment m [see Eq. (A.2)], $D^{\mathrm{F}\sigma}(\epsilon)$, $g_{\mathrm{sf}}(\epsilon)$ and $g^{\sigma}_{\mathrm{tr}}(\epsilon)$ are also time-dependent. This time dependence is left implicit in our discussion.

A.1.3 Spin transfer rates

We are interested in the dynamics of the F magnetic moment

$$m = \int \mathrm{d}\epsilon \left(D^{\mathrm{F}\uparrow} n^{\mathrm{F}\uparrow} - D^{\mathrm{F}\downarrow} n^{\mathrm{F}\downarrow}\right). \tag{A.8}$$

Using Eq.(A.5), its rate of change due to spin-flip events is given by

$$\dot{m}|_{\mathrm{sf}} = -2\int \mathrm{d}\epsilon \left(n^{\mathrm{F}\uparrow} - n^{\mathrm{F}\downarrow}\right) g^{\mathrm{F}}_{\mathrm{sf}}. \tag{A.9}$$

Using Eq.(A.6), the spin-resolved electron current through the F|N interface can be calculated by

$$J^{\sigma} = \int \mathrm{d}\epsilon \left(n^{\mathrm{F}\sigma} - n^{\mathrm{N}\sigma}\right) g^{\sigma}_{\mathrm{tr}}. \tag{A.10}$$

We note that Eqs. (A.9) and (A.10) yield zero spin transfer before the pump pulse arrives because in this case, all distribution functions $n^{F\sigma}$ and $n^{N\sigma}$ equal the same Fermi-Dirac distribution n_0 with chemical potential μ_0 and temperature T_0.

A.1.4 Moment expansion

As the relevant observables $\dot{m}|_{\mathrm{sf}}$ and J^{σ} involve differences of distribution functions only, we focus our discussion on the difference

$$\Delta n^{X\sigma} = n^{X\sigma} - n_0 \tag{A.11}$$

of the distribution function $n^{X\sigma}(\epsilon, t)$ and the equilibrium distribution n_0. We assume that $\Delta n^{X\sigma}$ is significantly nonzero only in a relatively narrow energy window around the chem-

ical potential μ_0 of the unperturbed system and that the energy-dependent weight factors $D^{\mathrm{F}\sigma}(\epsilon)$, $g_{\mathrm{sf}}(\epsilon)$ and $g_{\mathrm{tr}}^{\sigma}(\epsilon)$ can be well approximated by the Sommerfeld approximation [38]

$$W(\epsilon) \approx W(\mu_0) + W'(\mu_0)(\epsilon - \mu_0), \tag{A.12}$$

where W stands for $D^{\mathrm{F}\sigma}$, g_{sf} or g_{tr}^{σ}. Integrals involving these functions, such as Eqs. (A.9) and (A.10) , then turn into

$$\int \mathrm{d}\epsilon W(\epsilon)\,\Delta n^{X\sigma}(\epsilon) = W(\mu_0)\,\Delta P^{X\sigma} + W'(\mu_0)\,\Delta A^{X\sigma}, \tag{A.13}$$

which is just a linear combination of the zeroth and first moment of Δn^{σ}, that is,

$$\Delta P^{X\sigma} = \int \mathrm{d}\epsilon \Delta n^{X\sigma} \quad \text{and} \quad \Delta A^{X\sigma} = \int \mathrm{d}\epsilon\,(\epsilon - \mu_0)\,\Delta n^{X\sigma}. \tag{A.14}$$

In the case that $n^{X\sigma} = n_0 + \Delta n^{X\sigma}$ is a Fermi-Dirac distribution with chemical potential $\mu^{X\sigma}$ and temperature $T^{X\sigma}$, the $\Delta P^{X\sigma}$ and $\Delta A^{X\sigma}$ become Fermi-Dirac integrals and reduce to

$$\Delta P^{X\sigma} = \mu^{X\sigma} - \mu_0 \quad \text{and} \quad \Delta A^{X\sigma} = \frac{\pi^2 k_{\mathrm{B}}^2}{6}\left[\left(T^{X\sigma}\right)^2 - T_0^2\right] + \frac{1}{2}\left(\mu^{X\sigma} - \mu_0\right)^2. \tag{A.15}$$

Because $\left(\mu^{X\sigma} - \mu_0\right)^2$ is typically small, one can interpret ΔP^{σ} and ΔA^{σ}, respectively, as changes in a generalized chemical potential and a squared generalized temperature. We emphasize, however, that the definition of the moments $\Delta P^{X\sigma}$ and $\Delta A^{X\sigma}$ [Eq. (A.14)] also applies to nonthermal electron distributions $n_0 + \Delta n^{X\sigma}$.

In Ref.[30], the difference $\Delta\mu_s = \Delta\mu^{F\uparrow} - \Delta\mu^{F\downarrow}$ is termed spin voltage. We accordingly term

$$\Delta P_s = \Delta P^{F\uparrow} - \Delta P^{F\downarrow} \tag{A.16}$$

generalized spin voltage. In the main text, ΔP_{s} is written as $\Delta\tilde{\mu}_{\mathrm{s}}$, and further below [Eq. (A.35)], we will express $\Delta A^{X\sigma}$ by the generalized excess temperature $\Delta\tilde{T}^{X\sigma}$ of the $X\sigma$ electrons.

As the pump-induced variation of the electron distribution functions $n^{X\sigma}$ and, thus, the transient state of the electronic system is fully characterized by the moments $\Delta P^{X\sigma}$ and $\Delta A^{X\sigma}$, it is sufficient to determine the dynamics of $\Delta P^{X\sigma}$ and $\Delta A^{X\sigma}$. This conclusion is consistent with a recent thermodynamic treatment of ultrafast spin dynamics [170]. In the following, we will connect the phenomenological coupling coefficients of Ref. [170] with the parameters of our simplified microscopic description.

A.1.5 Relevant observables

We apply Eq.(A.13) to the rate of change of the magnetic moment [Eq.(A.9)]. We find

$$\dot{m}|_{\mathrm{sf}} = -2g_{\mathrm{sf}}(\mu_0)\,\Delta P_s - 2g'_{\mathrm{sf}}(\mu_0)\left(\Delta A^{\mathrm{F}\uparrow} - \Delta A^{\mathrm{F}\downarrow}\right), \tag{A.17}$$

where the first term on the right-hand side describes magnetization relaxation driven by the generalized spin voltage [Eq. (A.16)]. The term proportional to $\Delta A^{\mathrm{F}\uparrow} - \Delta A^{\mathrm{F}\downarrow}$ is a term analogous to the Seebeck effect, which contributes as long as the generalized temperatures of spin-up and spin-down electrons are different.

The magnetic moment of F is also modified by spin transport through the F|N interface, $-\dot{m}|_{\mathrm{tr}} = J_s = J^{\uparrow} - J^{\downarrow}$. We assume vanishing charge transport, $J^{\uparrow} + J^{\downarrow} = 0$, and the same chemical potential for spin-up and spin-down electrons in N, $\Delta P^{N\uparrow} = \Delta P^{N\downarrow} = \Delta P^{N}$. These assumptions allow us to eliminate $\Phi^{\mathrm{N}} - \Phi^{\mathrm{F}}$ [205]. Along with Eqs. (A.10), (A.13) and (A.14), we find

$$-\dot{m}|_{\mathrm{tr}} = J_s = g_{\mathrm{tr}}(\mu_0)\,\Delta P_s + s_{\mathrm{tr}}^{\uparrow}(\mu_0)\left(\Delta A^{\mathrm{F}\uparrow} - \Delta A^{\mathrm{N}\uparrow}\right) - s_{\mathrm{tr}}^{\downarrow}(\mu_0)\left(\Delta A^{\mathrm{F}\downarrow} - \Delta A^{\mathrm{N}\downarrow}\right), \quad \text{(A.18)}$$

where $2g_{\mathrm{tr}}^{-1} = \left(g_{\mathrm{tr}}^{\uparrow}\right)^{-1} + \left(g_{\mathrm{tr}}^{\downarrow}\right)^{-1}$ and $s_{\mathrm{tr}}^{\sigma} = g_{\mathrm{tr}} g_{\mathrm{tr}}^{\sigma\prime}/g_{\mathrm{tr}}^{\sigma}$. The two final terms in Eq. (A.18) are again of Seebeck type and vanish once the temperatures of F and N have equilibrated. In this regime, the driving force of both $\dot{m}^{\mathrm{F}}\big|_{\mathrm{sf}}$ and $\dot{m}^{\mathrm{F}}\big|_{\mathrm{tr}}$ is given solely by the spin voltage ΔP_s of F.

The total energy of the F electrons including their spins is in the Stoner model given by

$$E^{\mathrm{F}} = \sum_{\sigma} \int \mathrm{d}\epsilon\,(\epsilon - \mu_0)\, D^{\mathrm{F}\sigma} n^{\mathrm{F}\sigma} + \frac{1}{4} I^{\mathrm{F}} m^2. \quad \text{(A.19)}$$

By using $\dot{D}^{\mathrm{F}\sigma}(\epsilon) = D^{\mathrm{F}\sigma\prime}(\epsilon)\, I^{\mathrm{F}\sigma}\dot{m}$ and Eq.(A.8), we find that the rate of change obeys

$$\dot{E}^{\mathrm{F}} = \sum_{\sigma} \int d\epsilon\,(\epsilon - \mu_0)\, D^{\mathrm{F}\sigma}\left(\dot{n}^{\mathrm{F}\sigma} - \dot{n}^{\mathrm{F}\sigma}\big|_{I}\right), \quad \text{(A.20)}$$

where the term $\dot{n}^{\mathrm{F}\sigma}\big|_{I}$ [Eq. (A.7)] takes the time-dependence of the Bloch energies into account.

A.1.6 Time evolution of ΔP_s

To determine the dynamics of the system and, thus, the magnetization, it is sufficient to determine the dynamics of the moments, that is, the generalized spin voltage ΔP_s and temperatures $\Delta A^{X\sigma}$. According to Eqs. (A.3) and (A.7), we need to consider contributions of spin flips, spin transport and spin-conserving processes,

$$\Delta\dot{P}_s = \Delta\dot{P}_s\Big|_{\mathrm{sf}} + \Delta\dot{P}_s\Big|_{\mathrm{tr}} + \Delta\dot{P}_s\Big|_{\mathrm{sc}}. \quad \text{(A.21)}$$

By taking the time derivative of Eq.(A.14), considering Eqs. (A.5) and (A.7), performing the moment expansion of Eq. (A.13), and using Eq. (A.17), we obtain [205]

$$\Delta\dot{P}_s\Big|_{\mathrm{sf}} = -\frac{2}{\chi^{\mathrm{F}}(\mu_0)}\left[g_{\mathrm{sf}}(\mu_0)\,\Delta P_s + s_{\mathrm{sf}}(\mu_0)\left(\Delta A^{\mathrm{F}\uparrow} - \Delta A^{\mathrm{F}\downarrow}\right)\right]. \quad \text{(A.22)}$$

Here,

$$\frac{1}{\chi^{\mathrm{F}}(\mu_0)} = \frac{1}{2}\left(\frac{1}{D^{\mathrm{F}\uparrow}} + \frac{1}{D^{\mathrm{F}\downarrow}}\right)(\mu_0) - I^{\mathrm{F}} \tag{A.23}$$

is the inverse of the Pauli susceptibility $\chi^{\mathrm{F}} = \partial m/\partial \mu_s$ of F, which depends on the electron distribution only implicitly through the sample magnetization m, i.e., $\chi^{\mathrm{F}}(\mu_0) = \chi^{\mathrm{F}}(m)$. The reason is that m fully determines the variations of $D^{\mathrm{F}\uparrow}$ and $D^{F\downarrow}$. The coefficient $s_{\mathrm{sf}} = g'_{\mathrm{sf}} - \chi^{\mathrm{F}} g_{\mathrm{sf}} \left[D^{\mathrm{F}\uparrow\prime}/(D^{F\uparrow})^2 + D^{\mathrm{F}\downarrow\prime}/(D^{\mathrm{F}\downarrow})^2\right]/2$ quantifies the Seebeck-type response of the spin voltage to a temperature difference between majority and minority electrons.

To determine the contribution of spin transport, we take the time derivative of Eq. (A.14), consider Eqs. (A.6) and (A.7), perform the moment expansion of Eq. (A.13) and use Eq. (A.18). Making the same assumptions as in the derivation of Eq. (A.18), we obtain

$$\Delta\dot{P}_s\Big|_{\mathrm{tr}} = -\frac{1}{\chi^{\mathrm{F}}(\mu_0)}\left[g_{\mathrm{tr}}(\mu_0)\,\Delta P_s + \tilde{s}^{\uparrow}_{\mathrm{tr}}(\mu_0)\left(\Delta A^{\mathrm{F}\uparrow} - \Delta A^{\mathrm{N}\uparrow}\right) - \tilde{s}^{\downarrow}_{\mathrm{tr}}(\mu_0)\left(\Delta A^{\mathrm{F}\downarrow} - \Delta A^{\mathrm{N}\downarrow}\right)\right], \tag{A.24}$$

where $\tilde{s}^{\sigma}_{\mathrm{tr}} = s^{\sigma}_{\mathrm{tr}} - g^{\sigma\prime}_{\mathrm{tr}}\chi^{\mathrm{F}}/D^{\mathrm{F}\sigma}$ [205].

Excitation by the pump pulse and subsequent spin-conserving electron-electron and electron-lattice interactions also affect the occupation numbers $n^{X\sigma}$. By applying the moment expansion of Eq. (A.13) to Eq. (A.4), we find that spin-conserving scattering processes couple the spin voltage and the generalized temperature through

$$\Delta\dot{P}_s\Big|_{\mathrm{sc}} = -\frac{D^{\mathrm{F}\uparrow\prime}}{D^{\mathrm{F}\uparrow}}(\mu_0)\,\Delta\dot{A}^{\mathrm{F}\uparrow}\Big|_{\mathrm{sc}} + \frac{D^{\mathrm{F}\downarrow\prime}}{D^{\mathrm{F}\downarrow}}(\mu_0)\,\Delta\dot{A}^{\mathrm{F}\downarrow}\Big|_{\mathrm{sc}}. \tag{A.25}$$

Equation (A.21) along with Eqs. (A.22), (A.24) and (A.25) determine the dynamics of the spin voltage, provided the dynamics of the squared generalized temperatures $\Delta A^{X\sigma}$ are given. In these equations, the prefactors of $\Delta A^{X\sigma}$ and ΔP_s depend on the instantaneous state of the system and, thus, on the time-dependent occupation numbers $n^{X\sigma} = n_0 + \Delta n^{X\sigma}$.

A.1.7 Example: uniform electron temperature

It is instructive to summarize the preceding considerations for the example of a uniform electron temperature ΔA. This situation is realized in our experiments because no indication of Seebeck-type contributions is observed. Therefore, the total rate of change in the magnetic moment of F can be written as

$$\dot{m} = -g_{\mathrm{tot}}(\mu_0)\,\Delta P_s, \tag{A.26}$$

where $g_{\mathrm{tot}} = 2g_{\mathrm{sf}} + g_{\mathrm{tr}}$ summarizes the contribution of spin flips [Eq. (A.17)] and spin transport [Eq. (A.18)]. For a uniform electron temperature, the state variables ΔP_{s} and ΔA fully determine the pump-induced changes in the electron distributions of F and N

and, thus, in all other observables. Indeed, combination of Eqs. (A.21)-(A.26) yields

$$\dot{m} = a\Delta\dot{P}_s + b\Delta\dot{A}. \tag{A.27}$$

The prefactors $a(t) = a(m(t)) = \chi^{\mathrm{F}}(\mu_0)$ and $b(t) = \chi^{\mathrm{F}}(\mu_0)\left(D^{\mathrm{F}\uparrow\prime}/D^{\mathrm{F}\uparrow} - D^{\mathrm{F}\downarrow\prime}/D^{\mathrm{F}\downarrow}\right)(\mu_0)$ depend on time t only through $m(t)$ because, in the Stoner model, changes in the electronic band structure are mediated solely by m. Note that, in standard thermodynamics of a system with state variables μ_s and T, Eq. (A.27) corresponds to the total differential

$$\mathrm{d}m = \frac{\partial m}{\partial \mu_s}\mathrm{d}\mu_s + \frac{\partial m}{\partial T}\mathrm{d}T. \tag{A.28}$$

To connect $b(m)$ in Eq. (A.27) to macroscopic observables, we consider an infinitesimal quasi-static process $P_{\mathrm{s}}\rightarrow P_{\mathrm{s}}+\mathrm{d}P_{\mathrm{s}}$ and $A\rightarrow A+\mathrm{d}A$. Because the system is in equilibrium at the start and the end of this process, we have $\mathrm{d}P_{\mathrm{s}} = 0$. Eq. (A.27) leads to $\mathrm{d}m = b\mathrm{d}A$ and, thus,

$$b(m) = m'_{\mathrm{eq}}(A) = \chi^{\mathrm{F}}(\mu_0)\left(\frac{D^{\mathrm{F}\uparrow\prime}}{D^{\mathrm{F}\uparrow}} - \frac{D^{\mathrm{F}\downarrow\prime}}{D^{\mathrm{F}\downarrow}}\right)(\mu_0) \tag{A.29}$$

with $m = m_{\mathrm{eq}}(A)$. In other words, $b(m)$ equals the slope of the equilibrium magnetization curve $m_{\mathrm{eq}}(A)$. Combination of Eqs. (A.27) and (A.29) yields the remarkable result

$$\Delta\dot{P}_s(t) = \frac{1}{\chi^{\mathrm{F}}(\mu_0)}\frac{\partial}{\partial t}\left[m(t) - m_{\mathrm{eq}}(A(t))\right]. \tag{A.30}$$

It shows that, in the limit of uniform electron temperature, a change in the spin voltage is directly proportional to a change in the difference between the instantaneous magnetization $m(t)$ and the equilibrium magnetization $m_{\mathrm{eq}}(A(t))$ at the instantaneous electron temperature $A(t)$. In the limit of small magnetization changes with $m(t) \approx m_0$, the susceptibility $\chi^{\mathrm{F}}(\mu_0) = \chi^{\mathrm{F}}(m(t))$ [Eq. (A.23)] becomes time-independent, and Eq. (A.30) turns into Eq. (4.20) and Fig. 4.10 (c) of the Chapter 4.

We emphasize that, in the relevant Eqs. (A.17), (A.18) and (A.30), all microscopic Stoner-model parameters, such as electronic densities of states and the Coulomb-interaction parameter, are replaced by macroscopic observables: the temperature-dependent equilibrium magnetization m_{eq}, the generalized electron temperature A, the magnetic spin susceptibility χ^{F} and the coefficients g_{sf} and g_{tr}. All preceding considerations also apply to nonthermal electron distributions.

A.1.8 Linear excitation limit

From now on, we focus on the limit of weak optical excitation of the F and F|N samples. In fact, in our experiments, all terahertz emission signals were found to scale linearly with the incident pump-pulse energy up to the maximum available incident fluence of 0.2 mJ/cm^2. Therefore, $\dot{m}$ and J_s and, through Eqs. (A.17) and (A.18), ΔP_{s} and $\Delta A^{\mathrm{X}\sigma}$, and, by Eq. (A.14), the changes in the occupation numbers $\Delta n^{X\sigma}$ are also directly proportional

to the deposited pump power. It follows that the prefactors in Eqs. (A.22), (A.24) and (A.25) are independent of the pump-induced changes $\Delta n^{X\sigma}$ in the occupation numbers and can, thus, be evaluated for the unperturbed system. This simplification has important consequences.

Dynamics.—First, we can solve Eq. (A.21) along with Eqs. (A.22), (A.24) and (A.25) for the spin voltage ΔP_s. We find that ΔP_s is a convolution

$$\Delta P_s\left(t\right) = -\left(H_\mathrm{es} * \Delta F\right)\left(t\right) = -\int \mathrm{d}\tau\ H_\mathrm{es}\left(t-\tau\right)\Delta O(\tau) \tag{A.31}$$

of a driving force ΔO with a response function

$$H_\mathrm{es}\left(t\right) = \Theta\left(t\right)\mathrm{e}^{-\Gamma_\mathrm{es}t}, \tag{A.32}$$

where $\Theta(t)$ is the Heaviside step function. The exponential decay rate equals

$$\Gamma_\mathrm{es} = \frac{2g_\mathrm{sf}+g_\mathrm{tr}}{\chi^\mathrm{F}}\left(\mu_0\right) \tag{A.33}$$

for the F|N stack. By setting $g_\mathrm{tr}=0$, Γ_es for the F sample is obtained. The expression for the driving force ΔO is

$$\begin{aligned}\Delta O = \frac{D^{\mathrm{F}\uparrow\prime}}{D^{\mathrm{F}\uparrow}}\Delta\dot{A}^{\mathrm{F}\uparrow}\Big|_\mathrm{sc} - \frac{D^{\mathrm{F}\downarrow\prime}}{D^{\mathrm{F}\downarrow}}\Delta\dot{A}^{\mathrm{F}\downarrow}\Big|_\mathrm{sc} + \frac{s_\mathrm{sf}}{\chi^\mathrm{F}}\left(\Delta A^{\mathrm{F}\uparrow}-\Delta A^{\mathrm{F}\downarrow}\right) + \\ \frac{\tilde{s}_\mathrm{tr}^{\uparrow}}{\chi^\mathrm{F}}\left(\Delta A^{\mathrm{F}\uparrow}-\Delta A^{\mathrm{N}\uparrow}\right) - \frac{\tilde{s}_\mathrm{tr}^{\downarrow}}{\chi^\mathrm{F}}\left(\Delta A^{\mathrm{F}\downarrow}-\Delta A^{\mathrm{N}\downarrow}\right).\end{aligned} \tag{A.34}$$

Here, all prefactors should be evaluated at $\epsilon=\mu_0$ and for the unperturbed system, thereby making them time-independent. The first two terms of ΔO cause a change in the spin voltage, and they scale with the time derivative of the pump-induced excess energy of spin-up and spin-down electrons. The remaining terms are Seebeck-type terms that disappear when the generalized temperatures of all electron subsystems $X\sigma$ have the same value. The last two terms in Eq. (A.34) are omitted for the case of an F sample.

Temperature and energy.—Second, the pump-induced change in the squared generalized temperature [Eq. (A.15)] of electron system $X\sigma$ simplifies to

$$\Delta A^{X\sigma} = \frac{\pi^2 k_\mathrm{B}^2}{3} T_0 \Delta\tilde{T}^{X\sigma}, \tag{A.35}$$

where $T_0+\Delta\tilde{T}^{X\sigma}$ can be interpreted as generalized temperature of the $X\sigma$ electrons. The expression for the generalized chemical potential $\mu_0+\Delta P^{X\sigma}=\mu_0+\Delta\tilde{\mu}^{X\sigma}$ remains unchanged.

Third, the rate of change of the energy of the X electrons [see Eq. (A.20)] simplifies to

$$\dot{E}^\mathrm{F} = \sum_\sigma \int \mathrm{d}\epsilon\left(\epsilon-\mu_0\right) D_0^{\mathrm{F}\sigma}\dot{n}^{\mathrm{F}\sigma} = \sum_\sigma C_e^{\mathrm{F}\sigma}\partial_t\Delta\tilde{T}^{\mathrm{F}\sigma}, \tag{A.36}$$

where $C_e^{X\sigma} = \left(\pi^2 k_B^2/3\right) T_0 D_0^{X\sigma}(\mu_0)$, and $C_e^X = C_e^{X\uparrow} + C_e^{X\downarrow}$ is the heat capacity of the X electrons. Here, we neglected terms of order $(\epsilon - \mu_0)^2$ in the spirit of the moment expansion of Eq. (A.13). Therefore, the excess energy of the F electrons is

$$\Delta E^{\mathrm{F}} = \sum_{\sigma} C_e^{X\sigma} \Delta\tilde{T}^{X\sigma}, \tag{A.37}$$

which underscores the interpretation of $T_0 + \Delta\tilde{T}^{X\sigma}$ as generalized temperature.

A.1.9 Dynamics for uniform electron temperature

Owing to Eqs. (A.17), (A.18), (A.31) and (A.34), the dynamics of UDM and TST are fully determined by a linear combination of the $\Delta A^{X\sigma}$ and, because of Eq. (A.35), the generalized excess temperatures $\Delta\tilde{T}^{X\sigma}$ of all electron subsystems $X\sigma$.

To develop a simple model for the time dependence of the generalized temperature, we briefly review the processes following photoexcitation of metal thin films [95]. At time $t = 0$, the δ-like pump pulse excites the sample, thereby causing a step-like increase of the electronic excess energy and, thus, of all $\Delta\tilde{T}^{X\sigma}$.

Due to electron-electron interactions, all electronic subsystems $X\sigma$ quickly reach thermal equilibrium with each other, resulting in approximately equal generalized electronic temperatures, $\Delta\tilde{T}^{X\sigma} = \Delta\tilde{T}_e$. In this limit, the Seebeck-type contributions to the magnetization dynamics [Eqs. (A.17) and (A.18)] and to the driving force ΔO [Eq. (A.34)] are absent. Because we do not observe any signature of Seebeck-type terms in our experiment (4), we assume one uniform electron temperature,

$$\Delta\tilde{T}^{X\sigma} = \Delta\tilde{T}_e, \tag{A.38}$$

at all times.

Spin dynamics.—As a consequence, Eqs. (A.34), (A.35) and (A.29) turn the driving force for the spin voltage into

$$\Delta O = \frac{m'_{\mathrm{eq}}(T_0)}{\chi^{\mathrm{F}}(\mu_0)} \Delta\dot{\tilde{T}}_e, \tag{A.39}$$

where $\chi^{\mathrm{F}}(\mu_0)$ should be evaluated for the unperturbed system. Eqs. (A.39) and (A.31) result in

$$\Delta P_s = -\frac{m'_{\mathrm{eq}}(T_0)}{\chi^{\mathrm{F}}(\mu_0)} \dot{H}_{\mathrm{es}} * \Delta\tilde{T}_e, \tag{A.40}$$

which is equivalent to Eq. (4.21) of the Chapter 4. The resulting magnetization dynamics due to spin flips and transport follows from Eq. (A.40) and, respectively, $\dot{m}|_{\mathrm{sf}} = -2g_{\mathrm{sf}}(\mu_0)\Delta P_{\mathrm{s}}$ [Eq. (A.17)] and $J_s = g_{\mathrm{tr}}(\mu_0)\Delta P_s$ [Eq. (A.18)]. In particular, integration of $\dot{m}|_{\mathrm{sf}}$ and taking advantage of $\Gamma_{\mathrm{es}} = 2g_{\mathrm{sf}}/\chi^{\mathrm{F}}$ yields

$$\Delta m|_{\mathrm{sf}} = m'_{\mathrm{eq}}(T_0)\, \Gamma_{\mathrm{es}} H_{\mathrm{es}} * \Delta\tilde{T}_e. \tag{A.41}$$

Relaxation of $\Delta\tilde{T}_e(t)$.—To model the dynamics $\Delta\tilde{T}_e(t)$ of the generalized electron temperature, we note that electron-electron scattering and, thus, carrier multiplication is not relevant for modifying the excess energy and, therefore, $\Delta\tilde{T}_e$ [see Eq. (A.37)]. Electron-phonon interaction, on the other hand, causes heat transfer from the electrons to the crystal lattice with time constant $\Gamma_{\mathrm{ep}}^{-1}$. On a much longer time scale, which is not considered here, heat is transferred into the sample environment. Consequently, and as derived in Appendix A.2, we model the time dependence of the generalized temperature by the ansatz

$$\Delta\tilde{T}_e(t) = \Theta(t)\left[\Delta\tilde{T}_\infty + \left(\Delta\tilde{T}_{e0} - \Delta\tilde{T}_\infty\right)\mathrm{e}^{-\Gamma_{\mathrm{ep}}t}\right]. \tag{A.42}$$

Here, $\Delta\tilde{T}_{e0}$ is the increase of the uniform generalized temperature after absorption of the δ-like pump pulse and the fast equilibration between all electron subsystems $X\sigma$. The term $\Delta\tilde{T}_\infty = R\Delta\tilde{T}_{e0}$ is the generalized excess temperature at which the combined electron and lattice system equilibrate, with R being the ratio of electronic and total heat capacity.

With $\dot{\Delta\tilde{T}}_e = \Delta\tilde{T}_{e0}\left[\delta(t) - (1-R)\Gamma_{\mathrm{ep}}\Theta(t)\,\mathrm{e}^{-\Gamma_{\mathrm{ep}}t}\right]$ and Eq. (A.40), one immediately finds that

$$\Delta P_s(t) = -\frac{m'_{\mathrm{eq}}(T_0)}{\chi^{\mathrm{F}}(\mu_0)}\Delta\tilde{T}_{e0}\Theta(t)\left[\frac{\Gamma_{\mathrm{es}} - R\Gamma_{\mathrm{ep}}}{\Gamma_{\mathrm{es}} - \Gamma_{\mathrm{ep}}}\mathrm{e}^{-\Gamma_{\mathrm{es}}t} - \frac{(1-R)\Gamma_{\mathrm{ep}}}{\Gamma_{\mathrm{es}} - \Gamma_{\mathrm{ep}}}\mathrm{e}^{-\Gamma_{\mathrm{ep}}t}\right]. \tag{A.43}$$

Without the Seebeck-type contributions, $\dot{m}|_{\mathrm{sf}}$ [Eq. (A.17)] and $\dot{m}|_{\mathrm{tr}} = -j_{\mathrm{s}}$ [Eq. (A.18)] are both directly proportional to $\Delta P_s(t)$, and Eq. (A.43) turns into Eq. (4.23) of the main text. To account for the time resolution of our experiment, we convolute Eq. (A.43) with a Gaussian of 40 fs full width at half maximum.

To fit our data with Eq. (A.43), we obtain Γ_{ep} and R from previous works and Eqs. (A.53) and (A.54) in Appendix A.2. Prior to fitting, all measured curves are shifted to the same time zero. The only fit parameters are Γ_{es} and an overall scaling factor. As seen in Fig. (4.10), we obtain excellent agreement with our measurements. All parameters and references are summarized in Table S1 in [205].

A.1.10 Spin-current characteristics

Because of its relevance for applications, we here estimate the major characteristics of the spin current $J_s = g_{\mathrm{tr}}(\mu_0)\,\Delta P_s$ [Eq. (A.18)]. According to Eq. (A.43), the maximum value is reached directly after excitation by the δ-like pump. In this early stage ($t = 0^+$), the magnetization is approximately unchanged ($m(t) \approx m_0$), and Eq. (A.30) can be time-integrated to yield

$$J_s\left(t = 0^+\right) = \left[m_0 - m_{\mathrm{eq}}\left(T_0 + \Delta\tilde{T}_{e0}\right)\right]\frac{g_{\mathrm{tr}}}{\chi^{\mathrm{F}}}(\mu_0). \tag{A.44}$$

We emphasize that this relationship is valid beyond the linear excitation limit. On the other hand, when the optical excitation is sufficiently weak, we use Eqs. (A.37) and (A.38), the definition of $g_{\mathrm{tr}}(\mu_0)$ and assume $D^{\mathrm{F}\uparrow}(\mu_0) \ll D^{\mathrm{F}\downarrow}(\mu_0)$ to find that $J_s(0^+)$ scales according

to

$$J_s\left(t=0^+\right) \propto -m'_{\mathrm{eq}}\left(T_0\right) T_{\mathrm{tr}}^{\uparrow} \frac{D^{\mathrm{N}\uparrow} D^{\mathrm{F}\uparrow}}{\chi^{\mathrm{F}} D^{\mathrm{F}\downarrow}}\left(\mu_0\right), \tag{A.45}$$

for a given amount of deposited pump-pulse energy. After attaining its maximum, ΔP_s [Eq. (A.43)] and, thus, the spin current decay with the inverse time constant $\Gamma_{\mathrm{es}}+\Gamma_{\mathrm{ep}} \approx \Gamma_{\mathrm{es}}$, since electron-phonon relaxation is substantially slower than electron-spin relaxation (see Section 4.3). Because in our experiment, the presence of N does not noticeably change the dynamics of F, Eq. (A.33) becomes $\Gamma_{\mathrm{es}} \approx 2g_{\mathrm{sf}}/\chi^{\mathrm{F}}$. Using the definition of $g_{\mathrm{sf}}\left(\mu_0\right)$, we obtain

$$\Gamma_{\mathrm{es}} \approx 2P_{\mathrm{sf}} \frac{D^{\mathrm{F}\uparrow} D^{\mathrm{F}\downarrow}}{\chi^{\mathrm{F}}}\left(\mu_0\right), \tag{A.46}$$

in the linear excitation regime. Eqs. (A.44)-(A.46) are potentially useful for optimizing the height $J_{\mathrm{s}}\left(0^+\right)$ and width $1/\Gamma_{\mathrm{es}}$ of the ultrashort spin-current pulse $J_s\left(t\right)$ in future studies. While Eq. (A.44) is given by macroscopic observables, we note that Eqs. (A.45) and (A.46) strongly depend on microscopic parameters of the Stoner model, which should be considered as phenomenological parameters.

A.2 Two-temperature model for nonthermal states

The model presented in this section was developed by T. Kampfrath and P. W. Brouwer, both affiliated with the Department of Physics at Freie Universität Berlin, Germany. The two temperature model for F|N case is developed by R. Rouzegar and T. Kampfrath.

This Appendix is associated with the paper [205] and the same publication information reported in Chapter 4, page 41, also applies here.

To determine Γ_{ep} and R [see Eq. (A.42)] for an F sample, we extend the standard two-temperature model [4, 95] (2TM) to nonthermal electron and phonon distributions and, subsequently, to a two-layer stack F|N.

A.2.1 2TM for F

To model the decay of the electronic excess heat in the F sample, we follow the argumentation of Appendix A.9 and assume that all electron baths $X\sigma$ can be described by one common generalized excess temperature $\Delta\tilde{T}_e{=}\Delta\tilde{T}^{X\sigma}$.

Energy balance.—Changes in the total electron energy of F arise from excitation by the pump laser and by energy transfer to the phonons. Using Eq. (A.36), the rate of change of the electron excess energy can, thus, be written as

$$\Delta\dot{E}^{\mathrm{F}} = C_e^{\mathrm{F}}\Delta\dot{\tilde{T}}_e = \Delta\dot{E}^{\mathrm{F}}\Big|_{\mathrm{ep}} + \Delta\dot{E}^{\mathrm{F}}\Big|_{\mathrm{pump}}, \tag{A.47}$$

where $C_e^{\mathrm{F}} = C_e^{\mathrm{F}\uparrow} + C_e^{\mathrm{F}\downarrow}$ is the total electronic heat capacity of F. The pump action is modeled as $\Delta\dot{E}^{\mathrm{F}}\Big|_{\mathrm{pump}}{=}C_e^{\mathrm{F}}\Delta\tilde{T}_{e0}\delta(t)$. To describe electron-phonon relaxation, we neglect spin flips and use [4]

$$\Delta\dot{E}^{\mathrm{F}}\Big|_{\mathrm{ep}} \propto \sum_{\sigma}\int \mathrm{d}\delta\left(\alpha^2\mathrm{F}\right)^{\mathrm{F}\sigma}(\delta)\int \mathrm{d}\epsilon\left\{\left[n^{\mathrm{F}\sigma}(\epsilon) - n^{\mathrm{F}\sigma}(\epsilon+\delta)\right]p^{\mathrm{F}}(\delta) - \left[1-n^{\mathrm{F}\sigma}(\epsilon)\right]n^{\mathrm{F}\sigma}(\epsilon+\delta)\right\}. \tag{A.48}$$

Here, $\left(\alpha^2\mathrm{F}\right)^{\mathrm{F}\sigma}(\delta)$ denotes the Eliashberg function that describes the coupling of phonons of energy δ with two electronic states of the same spin σ and energy ϵ and $\epsilon+\delta$. The occupation number of the phonons is given by $p(\delta)$. Note that the term under the ϵ-integral becomes zero for all δ and ϵ, provided $n^{\mathrm{F}\sigma}$ is a Fermi-Dirac distribution and p is a Bose-Einstein distribution with the same temperature.

Linear regime.—We follow Ref. [38] and linearize Eq. (A.48) with respect to $\Delta n^{\mathrm{F}\sigma} = n^{\mathrm{F}\sigma} - n_0$ and $\Delta p^{\mathrm{F}} = p^{\mathrm{F}} - p_0$ to obtain

$$\begin{aligned}\Delta\dot{E}^{\mathrm{F}}\Big|_{\mathrm{ep}} \propto \sum_{\sigma}\int \mathrm{d}\delta\left(\alpha^2\mathrm{F}\right)^{\mathrm{F}\sigma}(\delta)\,\delta\Delta p^{\mathrm{F}}(\delta)\\ -\sum_{\sigma}\int \mathrm{d}\epsilon\Delta n^{\mathrm{F}\sigma}(\epsilon)\int \mathrm{d}\delta\left(\alpha^2\mathrm{F}\right)^{\mathrm{F}\sigma}\left[1-n_0(\epsilon-\delta)-n_0(\epsilon+\delta)\right].\end{aligned} \tag{A.49}$$

Because the weight factor of $\Delta n^{\mathrm{F}\sigma}(\epsilon)$ in Eq. (A.49) is sufficiently smooth, it is legitimate to apply the moment expansion of Eq. (A.13), resulting in [38]

$$\Delta\dot{E}^{\mathrm{F}}\Big|_{\mathrm{ep}} \propto \sum_{\sigma}\int \mathrm{d}\delta\left(\alpha^2\mathrm{F}\right)^{\mathrm{F}\sigma}(\delta)\,\delta\Delta p^{\mathrm{F}}(\delta) - \Delta A^{\mathrm{F}}\sum_{\sigma}\int \mathrm{d}\delta\left(\alpha^2\mathrm{F}\right)^{\mathrm{F}\sigma}(\delta)\left[-2n_0'(\mu_0-\delta)\right]. \tag{A.50}$$

The first integral approximately scales with the pump-induced phonon excess energy because $\left(\alpha^2\mathrm{F}\right)^{\mathrm{F}\sigma}(\delta)$ is approximately proportional to the phonon density of states [4]. Owing to Eq. (A.37), the second integral approximately scales with the excess energy of the F electrons. The generalized chemical potential does not show up in Eq. (A.50) as the weight factor of $\Delta n^{\sigma}(\epsilon)$ in Eq. (A.49) is antisymmetric with respect to $\epsilon-\mu_0$.

When we finally assume that the phonon distribution $p_0+\Delta p$ is thermal and obeys Bose-Einstein statistics at temperature $T_0+\Delta T_p^{\mathrm{F}}$, Eq. (A.50) leads to the familiar result [38]

$$\Delta\dot{E}^{\mathrm{F}}\Big|_{\mathrm{ep}} = -G_{\mathrm{ep}}^{\mathrm{F}}\cdot\left(\Delta\tilde{T}_e^{\mathrm{F}} - \Delta T_p^{\mathrm{F}}\right). \tag{A.51}$$

Here, the coupling strength G_{ep}^{F} is proportional to $\sum_{\sigma}\int \mathrm{d}\delta\left(\alpha^2\mathrm{F}\right)^{\mathrm{F}\sigma}(\delta)\left[-2n_0'(\mu_0-\delta)\right]$. In the last step to Eq. (A.51), we took advantage of the fact that $\Delta\dot{E}^{\mathrm{F}}\Big|_{\mathrm{ep}} = 0$ when $\Delta\tilde{T}_e^{\mathrm{F}} = \Delta T_p^{\mathrm{F}}$. Equation (A.51) is the generalization of the 2TM to nonthermal electron distributions in the linear excitation limit.

To close the system of equations, an equation of motion for the phonon temperature analogous to Eqs. (A.47) and (A.51) is given by

$$C_p^{\mathrm{F}}\Delta\dot{T}_p^{\mathrm{F}} = +G_{\mathrm{ep}}^{\mathrm{F}}\cdot\left(\Delta\tilde{T}_e^{\mathrm{F}} - \Delta T_p^{\mathrm{F}}\right), \tag{A.52}$$

where C_p^{F} is the phonon heat capacity of F.

A.2.2 2TM for F|N stack

To model the decay of the electronic excess heat in the F|N stack, we assume that equilibration between electron baths of different spins and in different layers is much faster than electron-phonon equilibration. Therefore, all electron baths $X\sigma$ can be described by one common generalized excess temperature $\Delta\tilde{T}_e = \Delta\tilde{T}^{X\sigma}$. The phonon bath of each layer couples to the electrons of the same layer. Direct coupling of phonons between F and N is neglected. The energy-flow diagram, the differential equations [analogous to Eqs. (A.47), (A.51) and (A.52)] and their solution are detailed in Supplemental Note 2 in Ref. [205].

We find that, for the time scales relevant to our experiment, the dynamics of the generalized electron excess temperature is given by Eq. (A.42) with

$$\Gamma_{\mathrm{ep}} = \frac{G_{\mathrm{ep}}^{\mathrm{F}} + G_{\mathrm{ep}}^{\mathrm{N}}}{C_{\mathrm{e}}^{\mathrm{F}} + C_{\mathrm{e}}^{\mathrm{N}}}, \tag{A.53}$$

and

$$R = \frac{C_e^{\mathrm{F}} + C_e^{\mathrm{N}}}{C_e^{\mathrm{F}} + C_e^{\mathrm{N}} + C_p^{\mathrm{F}} + C_p^{\mathrm{N}}}. \tag{A.54}$$

Here, C_e^X and C_p^X are the heat capacities of electrons and phonons in X, respectively, and G_{ep}^X quantifies electron-phonon coupling in X. For an F sample, the parameters Γ_{ep} and R are obtained by setting $C_e^{\mathrm{N}} = 0$ and $G_{\mathrm{ep}}^{\mathrm{N}} = 0$ in Eqs. (A.53) and (A.54).

Note that the C_e^X, C_p^X and G_{ep}^X are extensive quantities because they refer to the F and N volumes that are effectively coupled to each other in terms of ultrafast energy exchange. For our stack geometry, we assume equal coupling lengths into the depth of F and N. Therefore, we can replace the extrinsic quantities C_e^X, C_p^X and G_{ep}^X by their specific (volume-normalized) counterparts, which can be obtained from literature (see Table S1 in Ref. [205]).

A.3 Wave-diffusion spin transport

This Appendix is associated with the paper [208] and the same publication information reported in Chapter 5, page 67, also applies here.

The aim of this Section is to present a derivation of the spin transport model used in Chapter 5. First, we derive the dynamical diffusion equation starting from Boltzmann transport equations. Subsequently, we provide a phenomenological model for spin transport, combining ballistic and diffusive modes of transport.

A.3.1 Dynamical diffusion

In the absence of an external force and under the relaxation-time approximation, the occupation function of electrons is described by the Boltzmann transport equation [249, 283]

$$\frac{\partial n_k\left(z,t\right)}{\partial t}+v_z\frac{\partial n_k\left(z,t\right)}{\partial z}=-\frac{\left(n_k-n_0\right)}{\tau}, \tag{A.55}$$

where $v_z = v_{\mathrm{F}}\cos(\theta)$ is the projection of electron velocity into the z-direction, n_0 is the equilibrium Fermi-Dirac function, $n_k = n_0 + \Delta n_k$ is the non-equilibrium distribution and τ is the electron scattering time and k is the wavevector. The electron-current density is given by

$$j=-e\int\frac{d^3\boldsymbol{k}}{\left(2\pi\right)^3}v_z n_k, \tag{A.56}$$

Using the diffusion approximations $\Delta n_k \ll n_0$ and $\frac{\partial}{\partial z}\Delta n_k \ll n_0$, we can insert Eq. (A.56) into Eq. (A.55) in the Fourier domain, which results in

$$j=-\frac{D_0}{1-\mathrm{i}\omega\tau}\frac{\partial N}{\partial z}, \tag{A.57}$$

where N is the electron density. This is the time-dependent dynamical Fick's law where the static diffusion coefficient $D_0 = \frac{v_{\mathrm{F}}^2\tau}{3}$ is replaced by the frequency-dependent diffusion coefficient $D\left(\omega\right) = \frac{D_0}{1-\mathrm{i}\omega\tau}$. Notably, $D\left(\omega\right)$ has the same form of the Drude conductivity.

A.3.2 Wave-diffusion transport

Here, we derive phenomenologically the full dispersion relation given in the 5.5. However, a rigorous derivation is given in refs. [116, 283].

We combine dynamical Fick's law in Eq. (A.57) and the continuity equation for the spin transport $\partial_z j_s \propto -\partial_t\mu_s - 2\mu_s/\tau_{\mathrm{sf}}$ [116, 249, 283] in the Fourier domain, yielding

$$j_s\left(z,\omega\right)=-D\left(\omega\right)\partial_z\mu_s(z,\omega), \tag{A.58}$$

$$-\mathrm{i}\omega\mu_s\left(z,\omega\right)+\partial_z j_s\left(z,\omega\right)+\frac{2\mu_s}{\tau_{\mathrm{sf}}}=0, \tag{A.59}$$

where μ_s is the spin voltage as introduced in the main text, and τ_{sf} is the spin-flip time constant. Combining Eq. (A.58) and (A.58), one finds the dispersion relation

$$\overline{c}^2k^2=\omega^2+\mathrm{i}\omega\left(\frac{1}{\tau}+\frac{2}{\tau_{\mathrm{sf}}}\right)-\frac{2}{\tau\tau_{\mathrm{sf}}}, \tag{A.60}$$

where $\overline{c}^2=v_{\mathrm{F}}^2/3$ is the mean propagation velocity and k the wavevector. The spin current is given according to

$$j_{\mathrm{s}}\left(z,t\right)=\int \mathrm{d}t'\mu_{\mathrm{s}}\left(t'\right)P\left(z,t-t'\right), \tag{A.61}$$

where the propagator is

$$P\left(z,t\right)=\int \mathrm{d}\omega e^{\mathrm{i}(\omega t-kz)}. \tag{A.62}$$

The $P\left(z,t\right)$ captures the spin current propagation in Cu layer and $\mu_{\mathrm{s}}\left(t\right)$ is the initial condition, i.e., the spin voltage generated in the ferromagnet after the optical pump excitation.

A.4 Spin conductance spectroscopy

The model presented here was developed with significant help of T. Kampfrath. This Appendix is associated with the paper [208] and the same publication information reported in Chapter 6, page 77, also applies here.

The aim of this section is derivation of the Eq. (6.1) presented in Chapter 6.

A.4.1 Spin conductance of X layer in F|X|N sample

The emitted THz electric field for $F|X|H$ sample is given by

$$\tilde{E}^d(\omega) = e\tilde{Z}^d(\omega)\int \mathrm{d}z\ \tilde{\theta}_{\mathrm{SH}}(\omega)\,\tilde{j}_S^d(z,\omega) = e\tilde{Z}^d(\omega)\,\tilde{\theta}_{\mathrm{SH}}(\omega)\,\tilde{\lambda}_{\mathrm{rel}}(\omega)\ \tilde{j}_S^d(\omega)\,, \tag{A.63}$$

where $-e$ is the electron charge, $\tilde{Z}^d(\omega)$ is the impedance of the $F|H$ reference sample, $\tilde{\theta}_{\mathrm{SH}} = \tilde{j}_C/\tilde{j}_S$ is the spin Hall angle of H = Pt and $\tilde{\lambda}_{\mathrm{rel}}$ is the spin relaxation length in H = Pt. The spin current in the reference sample $j_S^d\ (\omega)$ is simply given by

$$\tilde{j}_S^d(\omega) = \tilde{G}_d(\omega)\,\tilde{\mu}_S(\omega)\,, \tag{A.64}$$

where $\tilde{\mu}_S(\omega)$ is the spin voltage generated in layer F, and $\tilde{G}^d(\omega)$ is the spin conductance of layer X. Finally, the measured THz signal $\tilde{S}^d(t)$ at the detector position is connected to the emitted THz electric field through

$$\tilde{S}^d(\omega) = \tilde{H}(\omega)\,\tilde{E}^d(\omega)\,, \tag{A.65}$$

where $\tilde{H}(\omega)$ is the setup transfer function that captures THz propagation to the detector and the electro-optic sampling process. Note that the case for $d = 0$ coincides with the $F|H$ reference sample with $\tilde{G}_{d=0}(\omega) = g^{\mathrm{ref}}(\omega)$, $\tilde{Z}^{d=0}(\omega) = \tilde{Z}^{\mathrm{ref}}(\omega)$ and $\tilde{j}_S^{d=0}(\omega) = \tilde{j}_S^{\mathrm{ref}}(\omega)$. The interface spin conductance of the reference sample $g^{\mathrm{ref}}(\omega) = g^{\mathrm{ref}}$ was shown to be frequency-independent [205, 208]. Therefore, one can find the X-layer spin conductance as

$$\frac{\tilde{G}_d(\omega)}{g^{\mathrm{ref}}} = \frac{\tilde{j}_S^d(\omega)}{\tilde{j}_S^{\mathrm{ref}}(\omega)}. \tag{A.66}$$

Here, we assumed that the spin-voltage dynamics $\tilde{\mu}_s(\omega)$ in F does not change between $F|H$ and $F|X|H$ samples [205]. Because $\tilde{\theta}_{\mathrm{SH}}(\omega)$, $\tilde{\lambda}_{\mathrm{rel}}(\omega)$ and $\tilde{H}(\omega)$ do not change between $F|H$ and $F|X|H$ samples, one can find

$$\frac{\tilde{G}_d(\omega)}{g^{\mathrm{ref}}} = \frac{\tilde{j}_S^d(\omega)}{\tilde{j}_S^{\mathrm{ref}}(\omega)} = \frac{\tilde{S}(\omega)}{\tilde{S}^{\mathrm{ref}}(\omega)}\frac{\tilde{Z}^{\mathrm{ref}}(\omega)}{\tilde{Z}^d(\omega)}. \tag{A.67}$$

In Eq. (A.67), all unknowns such as $\tilde{\theta}_{\mathrm{SH}}(\omega)$, $\tilde{\lambda}_{\mathrm{rel}}(\omega)$ and $\tilde{H}(\omega)$ cancel. In other words,

one can measure the THz spin conductance of a layer X without knowledge of the setup transfer function and the difficult-to-measure $\tilde{\theta}_{\mathrm{SH}}(\omega)$ and $\tilde{\lambda}_{\mathrm{rel}}(\omega)$.

The impedance for $F|X|H$ is measured by THz transmission spectroscopy, and we find $\tilde{Z}^{d}(\omega) = \tilde{Z}^{\mathrm{ref}}(\omega) = 80\ \Omega$ for all d (see Fig. S4 in [256]). Therefore, Eq. (A.67) simplifies to Eq. (6.1) in Chapter 6

A.4.2 Spin conductance of CoFeB|Pt interface

To determine the conductance of the CoFeB|Pt interface of the CoFeB|Pt reference stack, we directly interrogate the spin-voltage dynamics $\mu_S(t)$ by measuring the rate of change $\partial_t M$ of the magnetization of a single F = CoFeB film, which fulfills $\partial_t M \propto \mu_S(t)$ [205]. The emitted THz field antisymmetric with respect to sample turning by 180° about the magnetization is dominated by magnetic-dipole radiation emitted by $\partial_t M$. In the frequency domain, the THz field amplitude directly behind the sample is

$$\tilde{E}_M(\omega) = -\frac{\tilde{Z}_F(\omega)\ \tilde{n}(\omega)\, d_F}{c}\ \mathrm{i}\omega\tilde{M}(\omega)\,, \tag{A.68}$$

where $\tilde{n}(\omega)$ is the refractive index of the substrate, d_F is the F thickness, $\tilde{Z}_F(\omega)$ is the impedance of the F sample and c is the speed of light [205]. On the other hand, the rate of magnetization change $\mathrm{i}\omega\tilde{M}(\omega)$ is given by

$$\mathrm{i}\omega\tilde{M}(\omega) = 2g_{\mathrm{sf}}\ \tilde{\mu}_S(\omega)\,, \tag{A.69}$$

Where the coefficient g_{sf} quantifies the spin-flip strength of F. Analogous to Eq. (A.65), the measured THz signal $\tilde{S}_M(\omega)$ is given by $\tilde{S}_M(\omega) = \tilde{H}(\omega)\,\tilde{E}_M(\omega)$. Combining all relationships (A.63)-(A.69), we find that

$$\frac{\tilde{G}^{\mathrm{ref}}(\omega)}{g_{\mathrm{sf}}} = \frac{\tilde{j}_S^{\mathrm{ref}}(\omega)}{\mathrm{i}\omega\ \tilde{M}(\omega)} = \frac{\tilde{S}^{\mathrm{ref}}(\omega)}{\tilde{S}_M(\omega)} \cdot \frac{2\tilde{Z}_F(\omega)\ d_F\tilde{n}(\omega)}{\tilde{Z}^{\mathrm{ref}}(\omega)\,\tilde{\theta}_{\mathrm{SH}}(\omega)\,\tilde{\lambda}_{\mathrm{rel}}(\omega)c}. \tag{A.70}$$

As the second factor in Eq. (A.71) is constant in the frequency range considered here [10,18] Eq. (A.71) becomes

$$\frac{\tilde{G}^{\mathrm{ref}}(\omega)}{g_{\mathrm{sf}}} \propto \frac{\tilde{S}^{\mathrm{ref}}(\omega)}{\tilde{S}_M(\omega)}. \tag{A.71}$$

Note that $\tilde{S}_M(\omega)$ and $\tilde{S}^{\mathrm{ref}}(\omega)$ are measured under identical experimental conditions, implying an identical setup transfer function $\tilde{H}(\omega)$. Fig. S2(a) and S2(b) in Ref. [208] display the amplitude and phase of $\tilde{S}^{\mathrm{ref}}(\omega)/\tilde{S}_M(\omega)$, which is constant to very good approximation in the frequency range shown. Therefore, $\tilde{G}^{\mathrm{ref}}(\omega) = g^{\mathrm{ref}} = \mathrm{const}_\omega$. Accordingly, in the time domain, we find $G^{\mathrm{ref}}(t) \propto \delta_{\mathrm{exp}}(t)$ [Fig. S2(c) in [208]].

A.5 Rate equation model for incoherent resonant tunneling

The model presented here was developed with significant help of T. Kampfrath and P. W. Brouwer, both affiliated with the Department of Physics at Freie Universität Berlin, Germany. This Appendix is associated with the paper [208] and the same publication information reported in Chapter 6, page 77, also applies here.

The aim of this section is derivation of the Eq. (6.1) presented in Chapter 6.

To model the incoherent resonant spin tunneling (IRT) dynamics of the $F|X|H$ stack, we assume that (i) only one defect located at, say z, is involved in the IRT process of an electron tunneling from F to H. (ii) Spin transport does not change the spin voltage dynamics of F because transport is only small perturbation [205].

To determine the time-domain spin conductance $g_z^\sigma(t)$ of the IRT process of an electron with spin direction $\sigma =\uparrow$ or $\downarrow$, we consider an impulsive chemical potential $\mu^\sigma(t) = a\delta(t)$ for each sort σ in F. More precisely, to avoid infinitely high electron energies, we assume that $a\delta(t)$ is a peak of finite height and area a, yet a nonzero width that is still shorter than the time scale of all relevant processes of the system.

Current by one defect. The quasi-impulsive $\mu^\sigma(t)$ instantaneously populates a defect at z by tunneling, resulting in a defect occupation of $N_0(z)$. Subsequently, N decays due to tunneling from z to F or H with a rate proportional to the instantaneous occupation, i.e.,

$$\partial_t N^\sigma(z,t) = -\Gamma^\sigma(z) N^\sigma(z,t) \tag{A.72}$$

with $\Gamma^\sigma(z) = \Gamma_F^\sigma(z) + \Gamma_H^\sigma(z)$. Eq. (A.72) yields

$$N^\sigma(z,t) = N_0^\sigma(z) \mathrm{e}^{-\Gamma^\sigma(z)t}\Theta(t), \tag{A.73}$$

where $\Theta(t)$ is the Heaviside step function. The sheet current density of σ electrons from z to H is $J_{zH}^\sigma = -\partial_t N^\sigma|_H = \Gamma_H^\sigma(z) N^\sigma$ and becomes

$$J_{zH}^\sigma(t) = g_z^\sigma(t) = N_0^\sigma(z)\Gamma_H^\sigma(z)\mathrm{e}^{-\Gamma^\sigma(z)t}\Theta(t), \tag{A.74}$$

which equals the time-domain spin conductance $g_z^\sigma(t)$ for ITR through MgO by a defect at z.

Summation over defects. To obtain the total spin current, we sum over all defects by integration

$$g^\sigma(t) = \int \mathrm{d}z\ D_{\mathrm{def}}(z)\, g_z^\sigma(t) := \langle g_z^\sigma(t)\rangle \int \mathrm{d}z\ D_{\mathrm{def}}(z), \tag{A.75}$$

where $D_{\mathrm{def}}(z)$ is the defect density, and $\langle g_z^\sigma(t)\rangle$ is the average over all defects. We assume

a homogeneous defect density and that the $N_0^\sigma(z)$ and $\Gamma_H^\sigma(z)$ depend exponentially on the distance of the defect at z from F and H, i.e.,

$$N_0^\sigma(z) \propto \gamma_{FX}^\sigma \mathrm{e}^{-z/\lambda}\ , \quad \Gamma_H^\sigma(z) = \gamma_{XH}^\sigma \mathrm{e}^{-(d-z)/\lambda}, \tag{A.76}$$

where γ_F and γ_H can be interpreted as attempt rates. We find

$$g^\sigma(t) = D_{\mathrm{def}} \gamma_{FX}^\sigma \gamma_{XH}^\sigma d \mathrm{e}^{-d/\lambda^\sigma} e^{-\langle \Gamma^\sigma(z)\rangle t} \tag{A.77}$$

with

$$\langle \Gamma^\sigma(z)\rangle = (\gamma_{FX}^\sigma + \gamma_{XH}^\sigma) \frac{1-\mathrm{e}^{-d/\lambda^\sigma}}{d/\lambda^\sigma} \tag{A.78}$$

Here, we assumed short enough times $|t| \ll 1/\Gamma^\sigma(z)$ at which $\mathrm{e}^{-\Gamma^\sigma(z)t}$ can be linearized;

Spin current. To determine the spin current, we assume charge neutrality on the time scales relevant to our experiment. In frequency space, the response equations $\tilde{J}_H^\sigma = \tilde{g}^\sigma \Delta\tilde{\mu}^\sigma$ and the neutrality condition $\tilde{J}_N^\uparrow + \tilde{J}_N^\downarrow = 0$ imply a spin current $\tilde{J}_s = \tilde{g}_d^{\mathrm{IRT}} \Delta\tilde{\mu}_s$ with the IRT spin conductance [205]

$$\frac{1}{\tilde{g}_d^{\mathrm{IRT}}} = \frac{1}{2}\left(\frac{1}{\tilde{g}^\uparrow} + \frac{1}{\tilde{g}^\downarrow}\right). \tag{A.79}$$

Eq. (A.79) shows that $\tilde{g}_d^{\mathrm{IRT}}$ is dominated by the lower of the two conductances $\tilde{g}^\uparrow$ and $\tilde{g}^\downarrow$. This result is plausible: If the initial spin transport is dominated by the more conductive $\uparrow$ channel, charge backflow without spin backflow must proceed over the $\downarrow$ channel. Due to this causality chain, $\tilde{g}^\uparrow$ and $\tilde{g}^\downarrow$ are effectively connected in series, consistent with Eq. (A.79), and the total conductance is dominated by the bottleneck of the small $\tilde{g}^\downarrow$, i.e., $\tilde{g}_d^{\mathrm{IRT}} \approx \tilde{g}^\downarrow$.

One may argue that the summation over defects [Eq. (A.75)] should not be performed before Eq. (A.79). However, summation before applying the charge neutrality condition is justified for the following reason. Transfer of a spin from F to H causes transient charging and, thus, a transient electric field between F and H. This field acts on many defects and enables charge backflow through them, not just the one defect through which the initial tunneling event happened.

Bibliography

[1] M. Abdo, S. Sheng, S. Rolf-Pissarczyk, L. Arnhold, J. A. J. Burgess, M. Isobe, L. Malavolti, and S. Loth, *Variable repetition rate THz source for ultrafast scanning tunneling microscopy*, ACS Photonics, 8 (2021), pp. 702–708.

[2] R. Adam, G. Chen, D. E. Bürgler, T. Shou, I. Komissarov, S. Heidtfeld, H. Hardtdegen, M. Mikulics, C. M. Schneider, and R. Sobolewski, *Magnetically and optically tunable terahertz radiation from ta/nife/pt spintronic nanolayers generated by femtosecond laser pulses*, Applied Physics Letters, 114 (2019).

[3] A. Alekhin, I. Razdolski, N. Ilin, J. P. Meyburg, D. Diesing, V. Roddatis, I. Rungger, M. Stamenova, S. Sanvito, U. Bovensiepen, and A. Melnikov, *Femtosecond spin current pulses generated by the nonthermal spin-dependent seebeck effect and interacting with ferromagnets in spin valves*, Physical Review Letters, 119 (2017), pp. 17202–17202.

[4] P. B. Allen, *Theory of thermal relaxation of electrons in metals*, Physical Review Letters, 59 (1987), pp. 1460–1463.

[5] D. Apalkov, B. Dieny, and J. M. Slaughter, *Magnetoresistive random access memory*, Proceedings of the IEEE, 104 (2016), pp. 1796–1830.

[6] M. Asada and S. Suzuki, *Terahertz emitter using resonant-tunneling diode and applications*, Sensors, 21 (2021), p. 1384.

[7] N. W. Ashcroft and N. D. Mermin, *Solid State Physics*, Harcourt College Publishers, 1976.

[8] M. J. Assael, K. D. Antoniadis, and J. Wu, *New measurements of the thermal conductivity of PMMA, BK7, and pyrex 7740 up to 450k*, International Journal of Thermophysics, 29 (2008), pp. 1257–1266.

[9] N. Awari, S. Kovalev, C. Fowley, K. Rode, R. A. Gallardo, Y. C. Lau, D. Betto, N. Thiyagarajah, B. Green, O. Yildirim, J. Lindner, J. Fassbender, J. M. D. Coey, A. M. Deac, and M. Gensch, *Narrow-band tunable terahertz emission from ferrimagnetic mn3-xga thin films*, Applied Physics Letters, 109 (2016).

[10] V. Balos, P. Müller, G. Jakob, M. Kläui, and M. Sajadi, *Imprinting the complex dielectric permittivity of liquids into the spintronic terahertz emission*, Applied Physics Letters, 119 (2021).

[11] P. Barla, V. K. Joshi, and S. Bhat, *Spintronic devices: a promising alternative to cmos devices*, Journal of Computational Electronics, 20 (2021), pp. 805–837.

[12] T. Bartel, P. Gaal, K. Reimann, M. Woerner, and T. Elsaesser, *Generation of single-cycle THz transients with high electric-field amplitudes*, Optics Letters, 30 (2005), p. 2805.

[13] J. Bass and W. P. Pratt, *Spin-diffusion lengths in metals and alloys, and spin-flipping at metal/metal interfaces: an experimentalist's critical review*, Journal of Physics: Condensed Matter, 19 (2007), p. 183201.

[14] M. Battiato, K. Carva, and P. M. Oppeneer, *Superdiffusive spin transport as a mechanism of ultrafast demagnetization*, Physical Review Letters, 105 (2010).

[15] G. E. W. Bauer, E. Saitoh, B. J. V. Wees, and P. St, *Spin caloritronics*, Nature Publishing Group, 11 (2012), pp. 391–399.

[16] E. Beaurepaire, J.-C. Merle, A. Daunois, and J.-Y. Bigot, *Ultrafast spin dynamics in ferromagnetic nickel*, Physical Review Letters, 76 (1996), pp. 4250–4253.

[17] E. Beaurepaire, G. M. Turner, S. M. Harrel, M. C. Beard, J.-Y. Bigot, and C. A. Schmuttenmaer, *Coherent terahertz emission from ferromagnetic films excited by femtosecond laser pulses*, Applied Physics Letters, 84 (2004), pp. 3465–3467.

[18] M. Beens, R. A. Duine, and B. Koopmans, *s-d model for local and nonlocal spin dynamics in laser-excited magnetic heterostructures*, Physical Review B, 102 (2020), p. 054442.

[19] M. Beens, R. A. Duine, and B. Koopmans, *Modeling ultrafast demagnetization and spin transport: The interplay of spin-polarized electrons and thermal magnons*, Physical Review B, 105 (2022).

[20] Y. Behovits, A. L. Chekhov, S. Y. Bodnar, O. Gueckstock, S. Reimers, Y. Lytvynenko, Y. Skourski, M. Wolf, T. S. Seifert, O. Gomonay, M. Kläui, M. Jourdan, and T. Kampfrath, *Terahertz néel spin-orbit torques drive nonlinear magnon dynamics in antiferromagnetic mn2au*, Nature Communications, 14 (2023).

[21] Y. Berozashvili, S. Machavariani, A. Natsvlishvili, and A. Chirakadze, *Dispersion of the linear electro-optic coefficients and the non-linear susceptibility in GaP*, Journal of Physics D: Applied Physics, 22 (1989), pp. 682–686.

[22] C. Berry, N. Wang, M. Hashemi, M. Unlu, and M. Jarrahi, *Significant performance enhancement in photoconductive terahertz optoelectronics by incorporating plasmonic contact electrodes*, Nature Communications, 4 (2013).

[23] G. Bierhance, A. Markou, O. Gueckstock, R. Rouzegar, Y. Behovits, A. L. Chekhov, M. Wolf, T. S. Seifert, C. Felser, and T. Kampfrath, *Spin-voltage-driven efficient terahertz spin currents from the magnetic weyl semimetals co2mnga and co2mnal*, Applied Physics Letters, 120 (2022), p. 082401.

[24] S. R. Boona, R. C. Myers, and J. P. Heremans, *Spin caloritronics*, Energy Environ. Sci., 7 (2014), pp. 885–910.

[25] R. W. Boyd, *Nonlinear Optics*, Academic Press, Burlington, third ed., 2008.

[26] L. Brandt, U. Ritzmann, N. Liebing, M. Ribow, I. Razdolski, P. Brouwer, A. Melnikov, and G. Woltersdorf, *Effective exchange interaction for terahertz spin waves in iron layers*, Physical Review B, 104 (2021).

[27] L. Braun, G. Mussler, A. Hruban, M. Konczykowski, T. Schumann, M. Wolf, M. Munzenberg, L. Perfetti, and T. Kampfrath, *Ultrafast photocurrents at the surface of the three-dimensional topological insulator bi2se3*, Nat Commun, 7 (2016), p. 13259.

[28] L. Z. Braun, *Electron and Phonon Dynamics in Topological Insulators at THz Frequencies*, PhD thesis, Freie Universität Berlin, Berlin, 2016.

[29] E. Bründermann, H.-W. Hübers, and M. FitzGerald Kimmitt, *Terahertz Techniques*, Springer, Berlin, 2012.

[30] K. Bühlmann, G. Saerens, A. Vaterlaus, and Y. Acremann, *Detection of femtosecond spin voltage pulses in a thin iron film*, Structural Dynamics, 7 (2020), p. 065101.

[31] C. Bull, S. M. Hewett, R. Ji, C.-H. Lin, T. Thomson, D. M. Graham, and P. W. Nutter, *Spintronic terahertz emitters: Status and prospects from a materials perspective*, APL Materials, 9 (2021).

[32] W. H. Butler, *Tunneling magnetoresistance from a symmetry filtering effect*, Science and Technology of Advanced Materials, 9 (2008), p. 014106.

[33] W. H. Butler, X.-G. Zhang, T. C. Schulthess, and J. M. MacLaren, *Spin-dependent tunneling conductance of fe|mgo|fe*, Physical Review B, 63 (2001).

[34] J. L. Cabellos, B. S. Mendoza, and A. I. Shkrebtii, *Optical coherent current control at surfaces: Theory of injection current*, Physical Review B, 84 (2011).

[35] K. Carva, M. Battiato, and P. M. Oppeneer, *Ab initio investigation of the elliott-yafet electron-phonon mechanism in laser-induced ultrafast demagnetization*, Physical Review Letters, 107 (2011).

[36] J. J. Cha, J. C. Read, R. A. Buhrman, and D. A. Muller, *Spatially resolved electron energy-loss spectroscopy of electron-beam grown and sputtered cofeb/mgo/cofeb magnetic tunnel junctions*, Applied Physics Letters, 91 (2007).

[37] A. Chekhov, Y. Behovits, U. Martens, B. Serrano, M. Wolf, T. Seifert, M. Münzenberg, and T. Kampfrath, *Broadband spintronic detection of the absolute field strength of terahertz electromagnetic pulses*, Physical Review Applied, 20 (2023).

[38] A. L. Chekhov, Y. Behovits, J. J. F. Heitz, C. Denker, D. A. Reiss, M. Wolf, M. Weinelt, P. W. Brouwer, M. Munzenberg, and T. Kampfrath, *Ultrafast demagnetization of iron induced by optical versus terahertz pulses*, Phys. Rev. X, 11 (2021), p. 041055.

[39] G. Chen, *Nanoscale energy transport and conversion: a parallel treatment of electrons, molecules, phonons, and photons*, Oxford university press, 2005.

[40] J. Chen, U. Bovensiepen, A. Eschenlohr, T. Mueller, P. Elliott, E. Gross, J. Dewhurst, and S. Sharma, *Competing spin transfer and dissipation at co/cu(001)interfaces on femtosecond timescales*, Physical Review Letters, 122 (2019).

[41] M. Chen, Y. Wu, Y. Liu, K. Lee, X. Qiu, P. He, J. Yu, and H. Yang, *Current-enhanced broadband THz emission from spintronic devices*, Advanced Optical Materials, (2018), p. 1801608.

[42] X. Chen, X. Wu, S. Shan, F. Guo, D. Kong, C. Wang, T. Nie, C. Pandey, L. Wen, W. Zhao, C. Ruan, J. Miao, Y. Li, and L. Wang, *Generation and manipulation of chiral broadband terahertz waves from cascade spintronic terahertz emitters*, Applied Physics Letters, 115 (2019).

[43] G.-M. Choi, B.-C. Min, K.-J. Lee, and D. G. Cahill, *Spin current generated by thermally driven ultrafast demagnetization*, Nature Communications, 5 (2014), pp. 4334–4334.

[44] G.-M. Choi, C.-H. Moon, B.-C. Min, K.-J. Lee, and D. G. Cahill, *Thermal spin-transfer torque driven by the spin-dependent seebeck effect in metallic spin-valves*, Nature Physics, 11 (2015), pp. 576–581.

[45] A. V. Chumak, V. I. Vasyuchka, A. A. Serga, and B. Hillebrands, *Magnon spintronics*, Nature Physics, 11 (2015), pp. 453–461.

[46] S. Clark and H. Durrant-Whyte, *Autonomous land vehicle navigation using millimeter wave radar*, in Proceedings. 1998 IEEE International Conference on Robotics and Automation (Cat. No.98CH36146), IEEE.

[47] T. L. Cocker, V. Jelic, M. Gupta, S. J. Molesky, J. A. J. Burgess, G. D. L. Reyes, L. V. Titova, Y. Y. Tsui, M. R. Freeman, and F. A. Hegmann, *An ultrafast terahertz scanning tunnelling microscope*, Nature Photonics, 7 (2013), pp. 620–625.

[48] T. L. Cocker, D. Peller, P. Yu, J. Repp, and R. Huber, *Tracking the ultrafast motion of a single molecule by femtosecond orbital imaging*, Nature, 539 (2016), pp. 263–267.

[49] J. M. D. Coey, *Magnetism and Magnetic Materials*, Cambridge University Press, 2010.

[50] M. Cornet, J. Degert, E. Abraham, and E. Freysz, *Terahertz kerr effect in gallium phosphide crystal*, Journal of the Optical Society of America B, 31 (2014), p. 1648.

[51] J. A. del Alamo, *Nanometre-scale electronics with III–v compound semiconductors*, Nature, 479 (2011), pp. 317–323.

[52] J. K. Dewhurst, P. Elliott, S. Shallcross, E. K. U. Gross, and S. Sharma, *Laser-induced intersite spin transfer*, Nano Letters, 18 (2018), pp. 1842–1848.

[53] S. L. Dexheimer, *Terahertz Spectroscopy: Principles and Applications*, CRC Press, 2017.

[54] S. S. Dhillon, M. S. Vitiello, E. H. Linfield, A. G. Davies, M. C. Hoffmann, J. Booske, C. Paoloni, M. Gensch, P. Weightman, and W. et al., *The 2017 terahertz science and technology roadmap*, Journal of Physics D: Applied Physics, 50 (2017), p. 043001.

[55] C. Dornes, Y. Acremann, M. Savoini, M. Kubli, M. J. Neugebauer, E. Abreu, L. Huber, G. Lantz, C. A. F. Vaz, H. Lemke, E. M. Bothschafter, M. Porer, V. Esposito, L. Rettig, M. Buzzi, A. Alberca, Y. W. Windsor, P. Beaud, U. Staub, D. Zhu, S. Song, J. M. Glownia, and S. L. Johnson, *The ultrafast einstein–de haas effect*, Nature, 565 (2019), pp. 209–212.

[56] S. Eich, M. Plötzing, M. Rollinger, S. Emmerich, R. Adam, C. Chen, H. C. Kapteyn, M. M. Murnane, L. Plucinski, D. Steil, B. Stadtmüller, M. Cinchetti, M. Aeschlimann, C. M. Schneider, and S. Mathias, *Band structure evolution during the ultrafast ferromagnetic-paramagnetic phase transition in cobalt*, Science Advances, 3 (2017).

[57] A. El-Ghazaly, J. Gorchon, R. B. Wilson, A. Pattabi, and J. Bokor, *Progress towards ultrafast spintronics applications*, Journal of Magnetism and Magnetic Materials, 502 (2020), p. 166478.

[58] H. Elayan, O. Amin, R. M. Shubair, and M.-S. Alouini, *Terahertz communication: The opportunities of wireless technology beyond 5g*, in 2018 International Conference on Advanced Communication Technologies and Networking (CommNet), IEEE, 2018, pp. 1–5.

[59] F. Ellrich, M. Bauer, N. Schreiner, A. Keil, T. Pfeiffer, J. Klier, S. Weber, J. Jonuscheit, F. Friederich, and D. Molter, *Terahertz quality inspection for automotive and aviation industries*, Journal of Infrared, Millimeter, and Terahertz Waves, 41 (2019), pp. 470–489.

[60] A. Eschenlohr, *Spin dynamics at interfaces on femtosecond timescales*, Journal of Physics: Condensed Matter, 33 (2020), p. 013001.

[61] A. Eschenlohr, M. Battiato, P. Maldonado, N. Pontius, T. Kachel, K. Holldack, R. Mitzner, A. Föhlisch, P. M. Oppeneer, and C. Stamm, *Ultrafast spin transport as key to femtosecond demagnetization*, Nature Materials, 12 (2013), pp. 332–336.

[62] V. Y. Fedorov and S. Tzortzakis, *Extreme THz fields from two-color filamentation of midinfrared laser pulses*, Physical Review A, 97 (2018).

[63] Z. Feng, H. Qiu, D. Wang, C. Zhang, S. Sun, B. Jin, and W. Tan, *Spintronic terahertz emitter*, Journal of Applied Physics, 129 (2021).

[64] Z. Feng, W. Tan, Z. Jin, Y.-J. Chen, Z. Zhong, L. Zhang, S. Sun, J. Tang, Y. Jiang, P.-H. Wu, J. Cheng, B. Miao, H. Ding, D. Wang, Y. Zhu, L. Guo, S. Shin, G.-H. Ma, D. Hou, and S.-Y. Huang, *Anomalous nernst effect induced terahertz emission in a single ferromagnetic film*, Nano Letters, (2023).

[65] M. E. Fermann, A. Galvanauskas, and G. Sucha, *Ultrafast lasers: Technology and applications*, CRC Press, 2002.

[66] M. Fix, R. Schneider, J. Bensmann, S. Michaelis de Vasconcellos, R. Bratschitsch, and M. Albrecht, *Thermomagnetic control of spintronic thz emission enabled by ferrimagnets*, Applied Physics Letters, 116 (2020).

[67] A. Fognini, T. U. Michlmayr, A. Vaterlaus, and Y. Acremann, *Laser-induced ultrafast spin current pulses: a thermodynamic approach*, Journal of Physics: Condensed Matter, 29 (2017), p. 214002.

[68] R. Freeman, A. Zholud, Z. Dun, H. Zhou, and S. Urazhdin, *Evidence for dyakonov-perel-like spin relaxation in pt*, Physical Review Letters, 120 (2018).

[69] Fülöp, S. Tzortzakis, and T. Kampfrath, *Laser-driven strong-field terahertz sources*, Advanced Optical Materials, 8 (2019), p. 1900681.

[70] J. W. Gadzuk, *Resonance tunneling through impurity states in metal-insulator-metal junctions*, Journal of Applied Physics, 41 (1970), pp. 286–291.

[71] D. Gall, *Electron mean free path in elemental metals*, Journal of Applied Physics, 119 (2016).

[72] E. G. Gamaly, *Femtosecond Laser-Matter Interaction*, Jenny Stanford Publishing, Oct. 2011.

[73] M. M. Glazov, P. S. Alekseev, M. A. Odnoblyudov, V. M. Chistyakov, S. A. Tarasenko, and I. N. Yassievich, *Spin-dependent resonant tunneling in symmetrical double-barrier structures*, Physical Review B, 71 (2005).

[74] R. E. Glover and M. Tinkham, *Conductivity of superconducting films for photon energies between 0.3 and* $40kT_c$, Phys. Rev., 108 (1957), pp. 243–256.

[75] J. Gorchon, S. Mangin, M. Hehn, and G. Malinowski, *Is terahertz emission a good probe of the spin current attenuation length?*, Applied Physics Letters, 121 (2022).

[76] A. Grechnev, I. D. Marco, M. I. Katsnelson, A. I. Lichtenstein, J. Wills, and O. Eriksson, *Theory of bulk and surface quasiparticle spectra for fe, co, and ni*, Physical Review B, 76 (2007).

[77] O. P. Gückstock, *Spintronic terahertz emission: insights and applications*, PhD thesis, Freie Universität Berlin, 2023.

[78] O. Gueckstock, L. Nadvornik, M. Gradhand, T. S. Seifert, G. Bierhance, R. Rouzegar, M. Wolf, M. Vafaee, J. Cramer, M. A. Syskaki, G. Woltersdorf, I. Mertig, G. Jakob, M. Klaui, and T. Kampfrath, *Terahertz spin-to-charge conversion by interfacial skew scattering in metallic bilayers*, Adv Mater, 33 (2021), p. e2006281.

[79] O. Gueckstock, L. Nádvorník, T. S. Seifert, M. Borchert, G. Jakob, G. Schmidt, G. Woltersdorf, M. Kläui, M. Wolf, and T. Kampfrath, *Modulating the polarization of broadband terahertz pulses from a spintronic emitter at rates up to 10 khz*, Optica, 8 (2021).

[80] O. Gueckstock, R. L. Seeger, T. S. Seifert, S. Auffret, S. Gambarelli, J. N. Kirchhof, K. I. Bolotin, V. Baltz, T. Kampfrath, and L. Nádvorník, *Impact of gigahertz and terahertz transport regimes on spin propagation and conversion in the antiferromagnet irmn*, Applied Physics Letters, 120 (2022).

[81] L. Guiramand, J. E. Nkeck, X. Ropagnol, T. Ozaki, and F. Blanchard, *Near-optimal intense and powerful terahertz source by optical rectification in lithium niobate crystal*, Photonics Research, 10 (2022), p. 340.

[82] J. Hawecker, T. Dang, E. Rongione, J. Boust, S. Collin, J. George, H. Drouhin, Y. Laplace, R. Grasset, J. Dong, J. Mangeney, J. Tignon, H. Jaffrès, L. Perfetti, and S. Dhillon, *Spin injection efficiency at metallic interfaces probed by thz emission spectroscopy*, Advanced Optical Materials, 9 (2021).

[83] W. He, T. Zhu, X.-Q. Zhang, H.-T. Yang, and Z.-H. Cheng, *Ultrafast demagnetization enhancement in CoFeB/MgO/CoFeB magnetic tunneling junction driven by spin tunneling current*, Scientific Reports, 3 (2013).

[84] J. Hebling, G. Almasi, I. Kozma, and J. Kuhl, *Velocity matching by pulse front tilting for large area THz-pulse generation*, Optics Express, 10 (2002), p. 1161.

[85] E. Heinz, T. May, D. Born, G. Zieger, S. Anders, V. Zakosarenko, H.-G. Meyer, and C. Schäffel, *Passive 350 GHz video imaging systems for security applications*, Journal of Infrared, Millimeter, and Terahertz Waves, 36 (2015), pp. 879–895.

[86] J. J. F. Heitz, *Spintronic Operations Driven by Terahertz Electromagnetic Pulses*, PhD thesis, Freie Universität Berlin, 2023.

[87] T. Helgaker, S. Coriani, P. Jørgensen, K. Kristensen, J. Olsen, and K. Ruud, *Recent advances in wave function-based methods of molecular-property calculations*, Chemical Reviews, 112 (2012), pp. 543–631.

[88] R. I. Herapath, S. M. Hornett, T. S. Seifert, G. Jakob, M. Kläui, J. Bertolotti, T. Kampfrath, and E. Hendry, *Impact of pump wavelength on terahertz emission of a cavity-enhanced spintronic trilayer*, Applied Physics Letters, 114 (2019).

[89] M. T. Hibberd, D. S. Lake, N. A. B. Johansson, T. Thomson, S. P. Jamison, and D. M. Graham, *Magnetic-field tailoring of the terahertz polarization emitted from a spintronic source*, Applied Physics Letters, 114 (2019), p. 031101.

[90] D. Hillerkuss, R. Schmogrow, T. Schellinger, M. Jordan, M. Winter, G. Huber, T. Vallaitis, R. Bonk, P. Kleinow, F. Frey, M. Roeger, S. Koenig, A. Ludwig, A. Marculescu, J. Li, M. Hoh, M. Dreschmann, J. Meyer, S. B. Ezra, N. Narkiss, B. Nebendahl, F. Parmigiani, P. Petropoulos, B. Resan, A. Oehler, K. Weingarten, T. Ellermeyer, J. Lutz, M. Moeller, M. Huebner, J. Becker, C. Koos, W. Freude, and J. Leuthold, *26 tbit s-1 line-rate super-channel transmission utilizing all-optical fast fourier transform processing*, Nature Photonics, 5 (2011), pp. 364–371.

[91] H. Hirori, A. Doi, F. Blanchard, and K. Tanaka, *Single-cycle terahertz pulses with amplitudes exceeding 1 mv/cm generated by optical rectification in linbo3*, Applied Physics Letters, 98 (2011), p. 091106.

[92] M. C. Hoffmann and J. A. Fülöp, *Intense ultrashort terahertz pulses: generation and applications*, Journal of Physics D: Applied Physics, 44 (2011), p. 083001.

[93] M. Hofherr, S. Häuser, J. K. Dewhurst, P. Tengdin, S. Sakshath, H. T. Nembach, S. T. Weber, J. M. Shaw, T. J. Silva, H. C. Kapteyn, M. Cinchetti, B. Rethfeld, M. M. Murnane, D. Steil, B. Stadtmüller, S. Sharma, M. Aeschlimann, and S. Mathias, *Ultrafast optically induced spin transfer in ferromagnetic alloys*, Science Advances, 6 (2020).

[94] J. Hohlfeld, E. Matthias, R. Knorren, and K. H. Bennemann, *Nonequilibrium magnetization dynamics of nickel*, Physical Review Letters, 78 (1997), pp. 4861–4864.

[95] J. Hohlfeld, S.-S. Wellershoff, J. Güdde, U. Conrad, V. Jähnke, and E. Matthias, *Electron and lattice dynamics following optical excitation of metals*, Chemical Physics, 251 (2000), pp. 237–258.

[96] W. Hoppe, J. Weber, S. Tirpanci, O. Gueckstock, T. Kampfrath, and G. Woltersdorf, *On-chip generation of ultrafast current pulses by nanolayered spintronic terahertz emitters*, ACS Applied Nano Materials, 4 (2021), pp. 7454–7460.

[97] M. Hudl, M. d'Aquino, M. Pancaldi, S. H. Yang, M. G. Samant, S. S. P. Parkin, H. A. Durr, C. Serpico, M. C. Hoffmann, and S. Bonetti, *Nonlinear magnetization dynamics driven by strong terahertz fields*, Phys Rev Lett, 123 (2019), p. 197204.

[98] T. J. Huisman, R. V. Mikhaylovskiy, J. D. Costa, F. Freimuth, E. Paz, J. Ventura, P. P. Freitas, S. Blugel, Y. Mokrousov, T. Rasing, and A. V. Kimel, *Femtosecond control of electric currents in metallic ferromagnetic heterostructures*, Nat Nanotechnol, 11 (2016), pp. 455–8.

[99] T. J. Huisman, R. V. Mikhaylovskiy, T. Rasing, A. V. Kimel, A. Tsukamoto, B. de Ronde, L. Ma, W. J. Fan, and S. M. Zhou, *Sub-100-ps dynamics of the anomalous hall effect at terahertz frequencies*, Physical Review B, 95 (2017).

[100] T. J. Huisman, R. V. Mikhaylovskiy, A. Tsukamoto, T. Rasing, and A. V. Kimel, *Simultaneous measurements of terahertz emission and magneto-optical kerr effect for resolving ultrafast laser-induced demagnetization dynamics*, Physical Review B, 92 (2015), p. 104419.

[101] J. Hurst, P.-A. Hervieux, and G. Manfredi, *Spin current generation by ultrafast laser pulses in ferromagnetic nickel films*, Physical Review B, 97 (2018).

[102] H. Y. Hwang, S. Fleischer, N. C. Brandt, B. G. Perkins, M. Liu, K. Fan, A. Sternbach, X. Zhang, R. D. Averitt, and K. A. Nelson, *A review of non-*

linear terahertz spectroscopy with ultrashort tabletop-laser pulses, Journal of Modern Optics, 62 (2015), pp. 1447–1479.

[103] E. Isgandarov, X. Ropagnol, M. Singh, and T. Ozaki, *Intense terahertz generation from photoconductive antennas*, Frontiers of Optoelectronics, 14 (2021), pp. 64–93.

[104] F. T. J. Worlock, Arecchi and E. O. Schulz-Dubois, *Laser handbook. volume 1*, (1972).

[105] H. Jang, J. Kimling, and D. G. Cahill, *Nonequilibrium heat transport in pt and ru probed by an ultrathin co thermometer*, Physical Review B, 101 (2020).

[106] J. Jechumtal, R. Rouzegar, O. Gueckstock, C. Denker, W. Hoppe, Q. Remy, T. S. Seifert, P. Kubaščík, G. Woltersdorf, P. W. Brouwer, M. Münzenberg, T. Kampfrath, and L. Nádvorník, *Accessing ultrafast spin-transport dynamics in copper using broadband terahertz spectroscopy*, (2023).

[107] P. U. Jepsen, D. G. Cooke, and M. Koch, *Terahertz spectroscopy and imaging - modern techniques and applications*, Laser and Photonics Reviews, 5 (2011), pp. 124–166.

[108] K. Jhuria, J. Hohlfeld, A. Pattabi, E. Martin, A. Y. A. Córdova, X. Shi, R. L. Conte, S. Petit-Watelot, J. C. Rojas-Sanchez, G. Malinowski, S. Mangin, A. Lemaître, M. Hehn, J. Bokor, R. B. Wilson, and J. Gorchon, *Spin–orbit torque switching of a ferromagnet with picosecond electrical pulses*, Nature Electronics, 3 (2020), pp. 680–686.

[109] P. Jiménez-Cavero, O. Gueckstock, L. Nádvorník, I. Lucas, T. S. Seifert, M. Wolf, R. Rouzegar, P. W. Brouwer, S. Becker, G. Jakob, M. Kläui, C. Guo, C. Wan, X. Han, Z. Jin, H. Zhao, D. Wu, L. Morellón, and T. Kampfrath, *Transition of laser-induced terahertz spin currents from torque- to conduction-electron-mediated transport*, Phys. Rev. B, 105 (2022), p. 184408.

[110] Z. Jin, J. Li, W. Zhang, C. Guo, C. Wan, X. Han, Z. Cheng, C. Zhang, A. V. Balakin, A. P. Shkurinov, Y. Peng, G. Ma, Y. Zhu, J. Yao, and S. Zhuang, *Magnetic modulation of terahertz waves via spin-polarized electron tunneling based on magnetic tunnel junctions*, Physical Review Applied, 14 (2020).

[111] Z. Jin, A. Tkach, F. Casper, V. Spetter, H. Grimm, A. Thomas, T. Kampfrath, M. Bonn, M. Kläui, and D. Turchinovich, *Accessing the fundamentals of magnetotransport in metals with terahertz probes*, Nature Physics, 11 (2015), pp. 761–766.

[112] S. Jung, H. Lee, S. Myung, H. Kim, S. K. Yoon, S. W. Kwon, Y. Ju, M. Kim, W. Yi, S. Han, B. Kwon, B. Seo, K. Lee, G. H. Koh, K. Lee,

Y. Song, C. Choi, D. Ham, and S. J. Kim, *A crossbar array of magnetoresistive memory devices for in-memory computing*, Nature, 601 (2022), pp. 211–216.

[113] M. B. Jungfleisch, Q. Zhang, W. Zhang, J. E. Pearson, R. D. Schaller, H. Wen, and A. Hoffmann, *Control of terahertz emission by ultrafast spin-charge current conversion at rashba interfaces*, Phys Rev Lett, 120 (2018), p. 207207.

[114] M. B. Jungfleisch, W. Zhang, and A. Hoffmann, *Perspectives of antiferromagnetic spintronics*, Physics Letters A, 382 (2018), pp. 865–871.

[115] T. Jungwirth, X. Marti, P. Wadley, and J. Wunderlich, *Antiferromagnetic spintronics*, Nat Nanotechnol, 11 (2016), pp. 231–41. Jungwirth, T Marti, X Wadley, P Wunderlich, J eng Research Support, Non-U.S. Gov't Review England Nat Nanotechnol. 2016 Mar;11(3):231-41. doi: 10.1038/nnano.2016.18.

[116] S. Kaltenborn, Y.-H. Zhu, and H. C. Schneider, *Wave-diffusion theory of spin transport in metals after ultrashort-pulse excitation*, Physical Review B, 85 (2012).

[117] I. P. Kaminow and E. H. Turner, *"linear electrooptical materials," in handbook of lasers*, (1971), pp. 447–459.

[118] T. Kampfrath, *Charge-Carrier Dynamics in Solids and Gases Observed by Time-Resolved Terahertz Spectroscopy*, PhD thesis, 2006.

[119] T. Kampfrath, M. Battiato, P. Maldonado, G. Eilers, J. Notzold, S. Mahrlein, V. Zbarsky, F. Freimuth, Y. Mokrousov, S. Blugel, M. Wolf, I. Radu, P. M. Oppeneer, and M. Munzenberg, *Terahertz spin current pulses controlled by magnetic heterostructures*, Nat Nanotechnol, 8 (2013), pp. 256–60.

[120] T. Kampfrath, A. Kirilyuk, S. Mangin, S. Sharma, and M. Weinelt, *Ultrafast and terahertz spintronics: Guest editorial*, Applied Physics Letters, 123 (2023), p. 050401.

[121] T. Kampfrath, J. Nötzold, and M. Wolf, *Sampling of broadband terahertz pulses with thick electro-optic crystals*, Applied Physics Letters, 90 (2007).

[122] T. Kampfrath, K. Tanaka, and K. A. Nelson, *Resonant and nonresonant control over matter and light by intense terahertz transients*, Nature Photonics, 7 (2013), pp. 680–690.

[123] Y. Ke, K. Xia, and H. Guo, *Oxygen-vacancy-induced diffusive scattering in fe/mgo/fe magnetic tunnel junctions*, Physical Review Letters, 105 (2010).

[124] F. N. Kholid, D. Hamara, M. Terschanski, F. Mertens, D. Bossini, M. Cinchetti, L. McKenzie-Sell, J. Patchett, D. Petit, R. Cowburn,

J. Robinson, J. Barker, and C. Ciccarelli, *Temperature dependence of the picosecond spin seebeck effect*, Applied Physics Letters, 119 (2021).

[125] A. Kirihara, K. ichi Uchida, Y. Kajiwara, M. Ishida, Y. Nakamura, T. Manako, E. Saitoh, and S. Yorozu, *Spin-current-driven thermoelectric coating*, Nature Materials, 11 (2012), pp. 686–689.

[126] A. Kirilyuk, A. V. Kimel, and T. Rasing, *Ultrafast optical manipulation of magnetic order*, Reviews of Modern Physics, 82 (2010), pp. 2731–2784.

[127] A. Kirilyuk, A. V. Kimel, and T. Rasing, *Laser-induced magnetization dynamics and reversal in ferrimagnetic alloys*, Reports on Progress in Physics, 76 (2013), p. 026501.

[128] P. Koleják, K. Postava, M. Mičica, P. Kužel, F. Kadlec, and J. Pištora, *Experimental gouy phase shift compensation in terahertz time-domain spectroscopy*, Photonics and Nanostructures - Fundamentals and Applications, 31 (2018), pp. 129–133.

[129] D. Kong, X. Wu, B. Wang, T. Nie, M. Xiao, C. Pandey, Y. Gao, L. Wen, W. Zhao, C. Ruan, J. Miao, Y. Li, and L. Wang, *Broadband spintronic terahertz emitter with magnetic-field manipulated polarizations*, Advanced Optical Materials, 7 (2019).

[130] T. König, G. H. Simon, H.-P. Rust, and M. Heyde, *Work function measurements of thin oxide films on metals—MgO on ag(001)*, The Journal of Physical Chemistry C, 113 (2009), pp. 11301–11305.

[131] T. König, G. H. Simon, H.-P. Rust, G. Pacchioni, M. Heyde, and H.-J. Freund, *Measuring the charge state of point defects on MgO/ag(001)*, Journal of the American Chemical Society, 131 (2009), pp. 17544–17545.

[132] B. Koopmans, G. Malinowski, F. D. Longa, D. Steiauf, M. Fähnle, T. Roth, M. Cinchetti, and M. Aeschlimann, *Explaining the paradoxical diversity of ultrafast laser-induced demagnetization*, Nature Materials, 9 (2010), pp. 259–265.

[133] K. Krieger, J. K. Dewhurst, P. Elliott, S. Sharma, and E. K. U. Gross, *Laser-induced demagnetization at ultrashort time scales: Predictions of TDDFT*, Journal of Chemical Theory and Computation, 11 (2015), pp. 4870–4874.

[134] P. Kubaščík, A. Farkaš, K. Olejník, T. Troha, M. Hývl, F. Krizek, D. C. Joshi, T. Ostatnický, J. Jechumtál, E. Schmoranzerová, R. P. Campion, J. Zázvorka, V. Novák, P. Kužel, T. Jungwirth, P. Němec, and L. Nádvorník, *Terahertz probing of anisotropic conductivity and morphology of cumnas epitaxial thin films*, (2023).

[135] T. Kürner and S. Priebe, *Towards THz communications - status in research, standardization and regulation*, Journal of Infrared, Millimeter, and Terahertz Waves, 35 (2013), pp. 53–62.

[136] B. Laikhtman and S. Luryi, *Landauer formula for transmission across an interface*, Physical Review B, 49 (1994), pp. 17177–17184.

[137] M. L. M. Lalieu, R. Lavrijsen, R. A. Duine, and B. Koopmans, *Investigating optically excited terahertz standing spin waves using noncollinear magnetic bilayers*, Physical Review B, 99 (2019), p. 184439.

[138] N. Laman, M. Bieler, and H. M. van Driel, *Ultrafast shift and injection currents observed in wurtzite semiconductors via emitted terahertz radiation*, Journal of Applied Physics, 98 (2005), p. 103507.

[139] A. S. Landsman, M. Weger, J. Maurer, R. Boge, A. Ludwig, S. Heuser, C. Cirelli, L. Gallmann, and U. Keller, *Ultrafast resolution of tunneling delay time*, Optica, 1 (2014), p. 343.

[140] K. Lee, D.-K. Lee, D. Yang, R. Mishra, D.-J. Kim, S. Liu, Q. Xiong, S. K. Kim, K.-J. Lee, and H. Yang, *Superluminal-like magnon propagation in antiferromagnetic NiO at nanoscale distances*, Nature Nanotechnology, 16 (2021), pp. 1337–1341.

[141] A. Leitenstorfer, S. Hunsche, J. Shah, M. C. Nuss, and W. H. Knox, *Detectors and sources for ultrabroadband electro-optic sampling: Experiment and theory*, Applied Physics Letters, 74 (1999), pp. 1516–1518.

[142] G. Li, R. Medapalli, R. V. Mikhaylovskiy, F. E. Spada, T. Rasing, E. E. Fullerton, and A. V. Kimel, *Thz emission from co/pt bilayers with varied roughness, crystal structure, and interface intermixing*, Physical Review Materials, 3 (2019).

[143] T. Lichtenberg, M. Beens, M. H. Jansen, B. Koopmans, and R. A. Duine, *Probing optically induced spin currents using terahertz spin waves in noncollinear magnetic bilayers*, Physical Review B, 105 (2022), p. 144416.

[144] F. Lindner, G. G. Paulus, H. Walther, A. Baltuška, E. Goulielmakis, M. Lezius, and F. Krausz, *Gouy phase shift for few-cycle laser pulses*, Physical Review Letters, 92 (2004).

[145] L. Liu, O. J. Lee, T. J. Gudmundsen, D. C. Ralph, and R. A. Buhrman, *Current-induced switching of perpendicularly magnetized magnetic layers using spin torque from the spin hall effect*, Phys Rev Lett, 109 (2012), p. 096602.

[146] S. Liu, C. Lu, Z. Fan, S. Wang, P. Li, X. Chen, J. Pan, Y. Xu, Y. Liu, and X. Wu, *Modulated terahertz generation in femtosecond laser plasma filaments by high-field spintronic terahertz pulses*, Applied Physics Letters, 120 (2022), p. 172404.

[147] W.-T. Lu, Y. Zhao, M. Battiato, Y. Wu, and Z. Yuan, *Interface reflectivity of a superdiffusive spin current in ultrafast demagnetization and terahertz emission*, Physical Review B, 101 (2020).

[148] Z.-Y. Lu, X.-G. Zhang, and S. T. Pantelides, *Spin-dependent resonant tunneling through quantum-well states in magnetic metallic thin films*, Physical Review Letters, 94 (2005).

[149] O. Madelung, *Introduction to Solid-State Theory*, Springer Berlin Heidelberg, 1978.

[150] S. F. Maehrlein, *Nonlinear Terahertz Phononics: A Novel Route to Controlling Matter*, PhD thesis, Freie Universität Berlin, Berlin, 2016.

[151] S. F. Maehrlein, I. Radu, P. Maldonado, A. Paarmann, M. Gensch, A. M. Kalashnikova, R. V. Pisarev, M. Wolf, P. M. Oppeneer, J. Barker, and T. Kampfrath, *Dissecting spin-phonon equilibration in ferrimagnetic insulators by ultrafast lattice excitation*, Science Advances, 4 (2018).

[152] S. Maekawa, T. Kikkawa, H. Chudo, J. Ieda, and E. Saitoh, *Spin and spin current—From fundamentals to recent progress*, Journal of Applied Physics, 133 (2023), p. 020902.

[153] G. Malinowski, N. Bergeard, M. Hehn, and S. Mangin, *Hot-electron transport and ultrafast magnetization dynamics in magnetic multilayers and nanostructures following femtosecond laser pulse excitation*, The European Physical Journal B, 91 (2018).

[154] G. Malinowski, F. Dalla Longa, J. H. H. Rietjens, P. V. Paluskar, R. Huijink, H. J. M. Swagten, and B. Koopmans, *Control of speed and efficiency of ultrafast demagnetization by direct transfer of spin angular momentum*, Nature Physics, 4 (2008), pp. 855–858.

[155] A. Manchon, Q. Li, L. Xu, and S. Zhang, *Theory of laser-induced demagnetization at high temperatures*, Physical Review B, 85 (2012).

[156] A. Manchon, J. Zelezny, I. M. Miron, T. Jungwirth, J. Sinova, A. Thiaville, K. Garello, and P. Gambardella, *Current-induced spin-orbit torques in ferromagnetic and antiferromagnetic systems*, Rev. Mod. Phys., 91 (2019), p. 035004.

[157] P. G. Mather, J. C. Read, and R. A. Buhrman, *Disorder, defects, and band gaps in ultrathin (001) MgO tunnel barrier layers*, Physical Review B, 73 (2006).

[158] S. Mathias, C. La-O-Vorakiat, P. Grychtol, P. Granitzka, E. Turgut, J. M. Shaw, R. Adam, H. T. Nembach, M. E. Siemens, S. Eich, C. M. Schneider, T. J. Silva, M. Aeschlimann, M. M. Murnane, and H. C. Kapteyn, *Probing the timescale of the exchange interaction in a ferromagnetic alloy*, Proceedings of the National Academy of Sciences, 109 (2012), pp. 4792–4797.

[159] J. Mathon and A. Umerski, *Theory of tunneling magnetoresistance of an epitaxial fe/MgO/fe(001) junction*, Physical Review B, 63 (2001).

[160] E. Matsubara, M. Nagai, and M. Ashida, *Ultrabroadband coherent electric field from far infrared to 200 thz using air plasma induced by 10 fs pulses*, Applied Physics Letters, 101 (2012), p. 011105.

[161] N. Matthews, M. J. Hagmann, and A. Mayer, *Comment: Generalized formula for the electric tunnel effect between similar electrodes separated by a thin insulating film*, Journal of Applied Physics, 123 (2018).

[162] C. Meineke, M. Prager, J. Hayes, Q. Wen, L. Z. Kastner, D. Schuh, K. Fritsch, O. Pronin, M. Stein, F. Schafer, S. Chatterjee, M. Kira, R. Huber, and D. Bougeard, *Scalable high-repetition-rate sub-half-cycle terahertz pulses from spatially indirect interband transitions*, Light: Science and Applications, 11 (2022).

[163] M. Meinert, B. Gliniors, O. Gueckstock, T. S. Seifert, L. Liensberger, M. Weiler, S. Wimmer, H. Ebert, and T. Kampfrath, *High-throughput techniques for measuring the spin hall effect*, Physical Review Applied, 14 (2020), p. 064011.

[164] A. Melnikov, L. Brandt, N. Liebing, M. Ribow, I. Mertig, and G. Woltersdorf, *Ultrafast spin transport and control of spin current pulse shape in metallic multilayers*, Physical Review B, 106 (2022).

[165] A. Melnikov, I. Razdolski, T. O. Wehling, E. T. Papaioannou, V. Roddatis, P. Fumagalli, O. Aktsipetrov, A. I. Lichtenstein, and U. Bovensiepen, *Ultrafast transport of laser-excited spin-polarized carriers in au|fe|mgo(001)*, Physical Review Letters, 107 (2011), pp. 76601–76601.

[166] B. F. Miao, S. Y. Huang, D. Qu, and C. L. Chien, *Inverse spin hall effect in a ferromagnetic metal*, Phys Rev Lett, 111 (2013), p. 066602.

[167] G. X. Miao, Y. J. Park, J. S. Moodera, M. Seibt, G. Eilers, and M. Münzenberg, *Disturbance of tunneling coherence by oxygen vacancy in epitaxial fe/mgo/fe magnetic tunnel junctions*, Physical Review Letters, 100 (2008).

[168] D. T. Morelli, C. P. Beetz, and T. A. Perry, *Thermal conductivity of synthetic diamond films*, Journal of Applied Physics, 64 (1988), pp. 3063–3066.

[169] B. Y. Mueller, A. Baral, S. Vollmar, M. Cinchetti, M. Aeschlimann, H. C. Schneider, and B. Rethfeld, *Feedback effect during ultrafast demagnetization dynamics in ferromagnets*, Physical Review Letters, 111 (2013).

[170] B. Y. Mueller and B. Rethfeld, *Thermodynamic μt model of ultrafast magnetization dynamics*, Physical Review B, 90 (2014), p. 144420.

[171] B. Y. Mueller, T. Roth, M. Cinchetti, M. Aeschlimann, and B. Rethfeld, *Driving force of ultrafast magnetization dynamics*, New Journal of Physics, 13 (2011), p. 123010.

[172] Naftaly, Vieweg, and Deninger, *Industrial applications of terahertz sensing: State of play*, Sensors, 19 (2019), p. 4203.

[173] N. Nagaosa, J. Sinova, S. Onoda, A. H. MacDonald, and N. P. Ong, *Anomalous hall effect*, Reviews of Modern Physics, 82 (2010), pp. 1539–1592.

[174] U. Nandi, M. S. Abdelaziz, S. Jaiswal, G. Jakob, O. Gueckstock, S. M. Rouzegar, T. S. Seifert, M. Kläui, T. Kampfrath, and S. Preu, *Antenna-coupled spintronic terahertz emitters driven by a 1550 nm femtosecond laser oscillator*, Applied Physics Letters, 115 (2019).

[175] F. Nastos and J. E. Sipe, *Optical rectification and shift currents in GaAs and GaP response: Below and above the band gap*, Physical Review B, 74 (2006).

[176] F. Nastos and J. E. Sipe, *Optical rectification and current injection in unbiased semiconductors*, Physical Review B, 82 (2010).

[177] D. M. Nenno, S. Kaltenborn, and H. C. Schneider, *Boltzmann transport calculation of collinear spin transport on short timescales*, Physical Review B, 94 (2016).

[178] D. Nicoletti and A. Cavalleri, *Nonlinear light–matter interaction at terahertz frequencies*, Advances in Optics and Photonics, 8 (2016), p. 401.

[179] M. F. Nielson, E. S.-H. Ho, C. D. Moss, J. Dominguez, and J. A. Johnson, *Analysis of the frequency dependence of the kerr effect in diamond using two-dimensional spectroscopy*, (2022).

[180] H. Niwa, N. Yoshikawa, M. Kawaguchi, M. Hayashi, and R. Shimano, *Switchable generation of azimuthally- and radially-polarized terahertz beams from a spintronic terahertz emitter*, Optics Express, 29 (2021), p. 13331.

[181] W. Nolting and A. Ramakanth, *Quantum Theory of Magnetism*, Springer, 2009.

[182] L. Novotny and B. Hecht, *Principles of Nano-Optics*, Cambridge University Press, Sept. 2012.

[183] L. Nádvorník, M. Borchert, L. Brandt, R. Schlitz, K. A. de Mare, K. Vyborny, I. Mertig, G. Jakob, M. Kläui, S. T. B. Goennenwein, M. Wolf, G. Woltersdorf, and T. Kampfrath, *Broadband terahertz probes of anisotropic magnetoresistance disentangle extrinsic and intrinsic contributions*, Physical Review X, 11 (2021), p. 021030.

[184] L. Nádvorník, O. Gueckstock, L. Braun, C. Niu, J. Gräfe, G. Richter, G. Schütz, H. Takagi, T. S. Seifert, P. Kubaščík, A. K. Pandeya, A. Anane, H. Yang, A. Bedoya-Pinto, S. S. P. Parkin, M. Wolf, Y. Mokrousov, H. Nakamura, and T. Kampfrath, *Terahertz spin-to-charge current conversion in stacks of ferromagnets and the transition-metal dichalcogenide* $nbse_2$, arXiv, 2208.00846 (2022).

[185] P. Němec, M. Fiebig, T. Kampfrath, and A. V. Kimel, *Antiferromagnetic opto-spintronics*, Nature Physics, 14 (2018), pp. 229–241.

[186] Y. Ogasawara, Y. Sasaki, S. Iihama, A. Kamimaki, K. Z. Suzuki, and S. Mizukami, *Laser-induced terahertz emission from layered synthetic magnets*, Applied Physics Express, 13 (2020), p. 063001.

[187] N. Ong and W. Lee, *Geometry and the anomalous hall effect in ferromagnets*, Proceedings of the 8th International Symposium on Foundations of Quantum Mechanics in the Light of New Technology, ISQM-Tokyo 2005, World Scientific Publishing Co. Pte Ltd, 2006, pp. 121–126.

[188] P. M. Oppeneer, *Handbook of Magnetic Materials Vol. 13*, Elsevier, 2001, book Magneto-Optical Kerr Spectra.

[189] E. T. Papaioannou and R. Beigang, *THz spintronic emitters: a review on achievements and future challenges*, Nanophotonics, 10 (2021), pp. 1243–1257.

[190] S. S. P. Parkin, C. Kaiser, A. Panchula, P. M. Rice, B. Hughes, M. Samant, and S.-H. Yang, *Giant tunnelling magnetoresistance at room temperature with MgO (100) tunnel barriers*, Nature Materials, 3 (2004), pp. 862–867.

[191] N. C. Passler, M. Jeannin, and A. Paarmann, *Layer-resolved absorption of light in arbitrarily anisotropic heterostructures*, Physical Review B, 101 (2020).

[192] K.-E. Peiponen, A. Zeitler, and M. Kuwata-Gonokami, *Terahertz spectroscopy and imaging*, Springer, 2012.

[193] M. Porer, J.-M. Ménard, and R. Huber, *Shot noise reduced terahertz detection via spectrally postfiltered electro-optic sampling*, Optics Letters, 39 (2014), p. 2435.

[194] G. Prenat, K. Jabeur, G. D. Pendina, O. Boulle, and G. Gaudin, *Beyond STT-MRAM, spin orbit torque RAM SOT-MRAM for high speed and high reliability applications*, Springer, 2015.

[195] G. A. Prinz, *Spin-polarized transport*, Physics Today, 48 (1995), pp. 58–63.

[196] H. Qiu, L. Zhou, C. Zhang, J. Wu, Y. Tian, S. Cheng, S. Mi, H. Zhao, Q. Zhang, D. Wu, B. Jin, J. Chen, and P. Wu, *Ultrafast spin current generated from an antiferromagnet*, Nature Physics, 17 (2020), pp. 388–394.

[197] H. S. Qiu, K. Kato, K. Hirota, N. Sarukura, M. Yoshimura, and M. Nakajima, *Layer thickness dependence of the terahertz emission based on spin current in ferromagnetic heterostructures*, Opt Express, 26 (2018), pp. 15247–15254.

[198] Z. Q. Qiu and S. D. Bader, *Surface magneto-optic kerr effect*, Review of Scientific Instruments, 71 (2000), pp. 1243–1255.

[199] C. Rader, Z. B. Zaccardi, S.-H. E. Ho, K. G. Harrell, P. K. Petersen, M. F. Nielson, H. Stephan, N. K. Green, D. J. H. Ludlow, M. J. Lutz, S. J. Smith, D. J. Michaelis, and J. A. Johnson, *A new standard in high-field terahertz generation: the organic nonlinear optical crystal PNPA*, ACS Photonics, 9 (2022), pp. 3720–3726.

[200] I. Razdolski, A. Alekhin, N. Ilin, J. P. Meyburg, V. Roddatis, D. Diesing, U. Bovensiepen, and A. Melnikov, *Nanoscale interface confinement of ultrafast spin transfer torque driving non-uniform spin dynamics*, Nat Commun, 8 (2017), p. 15007.

[201] J. Reimann, S. Schlauderer, C. P. Schmid, F. Langer, S. Baierl, K. A. Kokh, O. E. Tereshchenko, A. Kimura, C. Lange, J. Güdde, U. Höfer, and R. Huber, *Subcycle observation of lightwave-driven dirac currents in a topological surface band*, Nature, 562 (2018), pp. 396–400.

[202] F. Roeder, M. Shalaby, B. Beleites, F. Ronneberger, and A. Gopal, *THz generation by optical rectification of intense near-infrared pulses in organic crystal BNA*, Optics Express, 28 (2020), p. 36274.

[203] E. Rongione, O. Gueckstock, M. Mattern, O. Gomonay, H. Meer, C. Schmitt, R. Ramos, T. Kikkawa, M. Mičica, E. Saitoh, J. Sinova, H. Jaffrès, J. Mangeney, S. T. B. Goennenwein, S. Geprägs, T. Kampfrath, M. Kläui, M. Bargheer, T. S. Seifert, S. Dhillon, and R. Lebrun, *Emission of coherent THz magnons in an antiferromagnetic insulator triggered by ultrafast spin–phonon interactions*, Nature Communications, 14 (2023).

[204] T. Roth, A. J. Schellekens, S. Alebrand, O. Schmitt, D. Steil, B. Koopmans, M. Cinchetti, and M. Aeschlimann, *Temperature dependence of laser-*

induced demagnetization in ni: A key for identifying the underlying mechanism, Physical Review X, 2 (2012).

[205] R. Rouzegar, L. Brandt, L. Nádvorník, D. A. Reiss, A. L. Chekhov, O. Gueckstock, C. In, M. Wolf, T. S. Seifert, P. W. Brouwer, G. Woltersdorf, and T. Kampfrath, *Laser-induced terahertz spin transport in magnetic nanostructures arises from the same force as ultrafast demagnetization*, Physical Review B, 106 (2022).

[206] R. Rouzegar, L. Brandt, L. Nádvorník, D. A. Reiss, A. L. Chekhov, O. Gueckstock, C. In, M. Wolf, T. S. Seifert, P. W. Brouwer, G. Woltersdorf, and T. Kampfrath, *Spin voltage gradient is the driving force for ultrafast demagnetization and terahertz spin transport*, in 2023 IEEE International Magnetic Conference - Short Papers (INTERMAG Short Papers), 2023, pp. 1–2.

[207] R. Rouzegar, M. Wahada, A. Chekhov, W. Hoppe, J. Jechumtal, L. Nadvornik, M. Wolf, T. Seifert, S. Parkin, G. Woltersdorf, et al., *Terahertz spin conductance probes of coherent and incoherent spin tunneling through mgo tunnel junctions*, arXiv preprint arXiv:2305.09074, (2023).

[208] R. Rouzegar, M. A. Wahada, A. L. Chekhov, W. Hoppe, J. Jechumtal, L. Nadvornik, M. Wolf, T. S. Seifert, S. S. P. Parkin, G. Woltersdorf, P. W. Brouwer, and T. Kampfrath, *Terahertz spin conductance probes of coherent and incoherent spin tunneling through mgo tunnel junctions*, (2023).

[209] D. Rudolf, C. La-O-Vorakiat, M. Battiato, R. Adam, J. M. Shaw, E. Turgut, P. Maldonado, S. Mathias, P. Grychtol, H. T. Nembach, T. J. Silva, M. Aeschlimann, H. C. Kapteyn, M. M. Murnane, C. M. Schneider, and P. M. Oppeneer, *Ultrafast magnetization enhancement in metallic multilayers driven by superdiffusive spin current*, Nature Communications, 3 (2012), pp. 1037–1037.

[210] M. Sajadi, M. Wolf, and T. Kampfrath, *Terahertz-field-induced optical birefringence in common window and substrate materials*, Optics Express, 23 (2015), p. 28985.

[211] D. Sander, S. O. Valenzuela, D. Makarov, C. H. Marrows, E. E. Fullerton, P. Fischer, J. McCord, P. Vavassori, S. Mangin, P. Pirro, B. Hillebrands, A. D. Kent, T. Jungwirth, O. Gutfleisch, C. G. Kim, and A. Berger, *The 2017 magnetism roadmap*, Journal of Physics D: Applied Physics, 50 (2017), p. 363001.

[212] Y. Sasaki, G. Li, T. Moriyama, T. Ono, R. V. Mikhaylovskiy, A. V. Kimel, and S. Mizukami, *Laser stimulated thz emission from pt/coo/fecob*, Applied Physics

Letters, 117 (2020).

[213] K. Sato and E. Saitoh, *Spintronics for Next Generation Innovative Devices*, John Wiley & Sons, Ltd, 2015.

[214] A. J. Schellekens, K. C. Kuiper, R. R. J. C. de Wit, and B. Koopmans, *Ultrafast spin-transfer torque driven by femtosecond pulsed-laser excitation*, Nature Communications, 5 (2014), pp. 4333–4333.

[215] J. M. Schleicher, S. M. Harrel, C. A. Schmuttenmaer, E. Beaurepaire, and J.-Y. Bigot, *Characterization of magnetization dynamics using terahertz emission spectroscopy*, in 15th International Conference on Ultrafast Phenomena, OSA, 2006.

[216] R. Schneider, M. Fix, J. Bensmann, S. Michaelis de Vasconcellos, M. Albrecht, and R. Bratschitsch, *Spintronic gdfe/pt thz emitters*, Applied Physics Letters, 115 (2019).

[217] R. Schneider, M. Fix, R. Heming, S. M. de Vasconcellos, M. Albrecht, and R. Bratschitsch, *Magnetic-field-dependent THz emission of spintronic TbFe/pt layers*, ACS Photonics, 5 (2018), pp. 3936–3942.

[218] T. Seifert, S. Jaiswal, U. Martens, J. Hannegan, L. Braun, P. Maldonado, F. Freimuth, A. Kronenberg, J. Henrizi, I. Radu, E. Beaurepaire, Y. Mokrousov, P. M. Oppeneer, M. Jourdan, G. Jakob, D. Turchinovich, L. M. Hayden, M. Wolf, M. Münzenberg, M. Kläui, and T. Kampfrath, *Efficient metallic spintronic emitters of ultrabroadband terahertz radiation*, Nature Photonics, 10 (2016), pp. 483–488.

[219] T. Seifert, S. Jaiswal, M. Sajadi, G. Jakob, S. Winnerl, M. Wolf, M. Kläui, and T. Kampfrath, *Ultrabroadband single-cycle terahertz pulses with peak fields of 300 kv cm^{-1} from a metallic spintronic emitter*, Applied Physics Letters, 110 (2017).

[220] T. S. Seifert, L. Cheng, Z. Wei, T. Kampfrath, and J. Qi, *Spintronic sources of ultrashort terahertz electromagnetic pulses*, Applied Physics Letters, 120 (2022), p. 180401.

[221] T. S. Seifert, D. Go, H. Hayashi, R. Rouzegar, F. Freimuth, K. Ando, Y. Mokrousov, and T. Kampfrath, *Time-domain observation of ballistic orbital-angular-momentum currents with giant relaxation length in tungsten*, Nature Nanotechnology, 18 (2023), pp. 1132–1138.

[222] T. S. Seifert, S. Jaiswal, J. Barker, S. T. Weber, I. Razdolski, J. Cramer, O. Gueckstock, S. F. Maehrlein, L. Nadvornik, S. Watanabe, C. Ciccarelli, A. Melnikov, G. Jakob, M. Munzenberg, S. T. B. Goennen-

wein, G. Woltersdorf, B. Rethfeld, P. W. Brouwer, M. Wolf, M. Klaui, and T. Kampfrath, *Femtosecond formation dynamics of the spin seebeck effect revealed by terahertz spectroscopy*, Nature Communications, 9 (2018), p. 2899.

[223] T. S. Seifert, U. Martens, F. Radu, M. Ribow, M. Berritta, L. Nadvornik, R. Starke, T. Jungwirth, M. Wolf, I. Radu, M. Munzenberg, P. M. Oppeneer, G. Woltersdorf, and T. Kampfrath, *Frequency-independent terahertz anomalous hall effect in dyco5 , co32 fe68 , and gd27 fe73 thin films from dc to 40 thz*, Adv Mater, 33 (2021), p. e2007398.

[224] T. S. Seifert, N. M. Tran, O. Gueckstock, S. M. Rouzegar, L. Nadvornik, S. Jaiswal, G. Jakob, V. V. Temnov, M. Münzenberg, M. Wolf, M. Kläui, and T. Kampfrath, *Terahertz spectroscopy for all-optical spintronic characterization of the spin-hall-effect metals pt, w and cu80ir20*, Journal of Physics D: Applied Physics, 51 (2018), p. 364003.

[225] A. Shafie, N. Yang, C. Han, J. M. Jornet, M. Juntti, and T. Kürner, *Terahertz communications for 6g and beyond wireless networks: Challenges, key advancements, and opportunities*, IEEE Network, 37 (2023), pp. 162–169.

[226] H. R. Shanks, P. D. Maycock, P. H. Sidles, and G. C. Danielson, *Thermal conductivity of silicon from 300 to 1400°k*, Physical Review, 130 (1963), pp. 1743–1748.

[227] X. Shen, Y. Cai, Y. Wu, and Y. Ji, *Tuning of spin relaxation and the kondo effect in copper thin films by ionic gating*, Physical Review B, 106 (2022).

[228] F. Siegrist, J. A. Gessner, M. Ossiander, C. Denker, Y. P. Chang, M. C. Schroder, A. Guggenmos, Y. Cui, J. Walowski, U. Martens, J. K. Dewhurst, U. Kleineberg, M. Munzenberg, S. Sharma, and M. Schultze, *Light-wave dynamic control of magnetism*, Nature, 571 (2019), pp. 240–244.

[229] J. G. Simmons, *Generalized formula for the electric tunnel effect between similar electrodes separated by a thin insulating film*, Journal of Applied Physics, 34 (1963), pp. 1793–1803.

[230] A. Singh, A. Pashkin, S. Winnerl, M. Helm, and H. Schneider, *Gapless broadband terahertz emission from a germanium photoconductive emitter*, ACS Photonics, 5 (2018), pp. 2718–2723.

[231] J. Sinova, S. O. Valenzuela, J. Wunderlich, C. H. Back, and T. Jungwirth, *Spin hall effects*, Rev. Mod. Phys., 87 (2015), pp. 1213–1260.

[232] A. Slachter, F. L. Bakker, J. P. Adam, and B. J. Van Wees, *Thermally driven spin injection from a ferromagnet into a non-magnetic metal*, Nature Physics, 6 (2010), pp. 879–882.

[233] H.-J. Song and T. Nagatsuma, *Handbook of terahertz technologies*, (2015).

[234] D. Steil, J. Walowski, F. Gerhard, T. Kiessling, D. Ebke, A. Thomas, T. Kubota, M. Oogane, Y. Ando, J. Otto, A. Mann, M. Hofherr, P. Elliott, J. K. Dewhurst, G. Reiss, L. Molenkamp, M. Aeschlimann, M. Cinchetti, M. Münzenberg, S. Sharma, and S. Mathias, *Efficiency of ultrafast optically induced spin transfer in heusler compounds*, Physical Review Research, 2 (2020).

[235] A. G. Stepanov, C. Ruchert, J. Levallois, C. Erny, and C. P. Hauri, *Generation of broadband THz pulses in organic crystal OH1 at room temperature and 10 k*, Optical Materials Express, 4 (2014), p. 870.

[236] M. Stiehl, M. Weber, C. Seibel, J. Hoefer, S. T. Weber, D. M. Nenno, H. C. Schneider, B. Rethfeld, B. Stadtmüller, and M. Aeschlimann, *Role of primary and secondary processes in the ultrafast spin dynamics of nickel*, Applied Physics Letters, 120 (2022), p. 062410.

[237] F.-F. Stiewe, T. Winkel, Y. Sasaki, T. Tubandt, T. Kleinke, C. Denker, U. Martens, N. Meyer, T. S. Parvini, S. Mizukami, J. Walowski, and M. Münzenberg, *Spintronic emitters for super-resolution in thz-spectral imaging*, Applied Physics Letters, 120 (2022), p. 032406.

[238] J. Stöhr and H. C. Siegmann, *Magnetism: From Fundamentals to Nanoscale Dynamics*, Springer Series in Solid-State Sciences, Springer, 2006.

[239] S. R. Tauchert, M. Volkov, D. Ehberger, D. Kazenwadel, M. Evers, H. Lange, A. Donges, A. Book, W. Kreuzpaintner, U. Nowak, and P. Baum, *Polarized phonons carry angular momentum in ultrafast demagnetization*, Nature, 602 (2022), pp. 73–77.

[240] J. M. Teixeira, J. Ventura, J. P. Araujo, J. B. Sousa, P. Wisniowski, S. Cardoso, and P. P. Freitas, *Resonant tunneling through electronic trapping states in thin MgO magnetic junctions*, Physical Review Letters, 106 (2011).

[241] J. M. Teixeira, J. Ventura, F. Carpinteiro, J. P. Araujo, J. B. Sousa, P. Wisniowski, and P. P. Freitas, *The effect of pinhole formation/growth on the tunnel magnetoresistance of MgO-based magnetic tunnel junctions*, Journal of Applied Physics, 106 (2009), p. 073707.

[242] M. D. Thomson, V. Blank, and H. G. Roskos, *Terahertz white-light pulses from an air plasma photo-induced by incommensurate two-color optical fields*, Optics Express, 18 (2010), p. 23173.

[243] G. Torosyan, S. Keller, L. Scheuer, R. Beigang, and E. T. Papaioannou, *Optimized spintronic terahertz emitters based on epitaxial grown fe/pt layer struc-*

tures, Sci Rep, 8 (2018), p. 1311. Torosyan, Garik Keller, Sascha Scheuer, Laura Beigang, Rene Papaioannou, Evangelos Th eng Research Support, Non-U.S. Gov't England Sci Rep. 2018 Jan 22;8(1):1311. doi: 10.1038/s41598-018-19432-9.

[244] W. Töws and G. Pastor, *Many-body theory of ultrafast demagnetization and angular momentum transfer in ferromagnetic transition metals*, Physical Review Letters, 115 (2015).

[245] E. Y. Tsymbal and D. G. Pettifor, *Local impurity-assisted conductance in magnetic tunnel junctions*, Physical Review B, 64 (2001).

[246] E. Turgut, C. La-o vorakiat, J. M. Shaw, P. Grychtol, H. T. Nembach, D. Rudolf, R. Adam, M. Aeschlimann, C. M. Schneider, T. J. Silva, M. M. Murnane, H. C. Kapteyn, and S. Mathias, *Controlling the competition between optically induced ultrafast spin-flip scattering and spin transport in magnetic multilayers*, Physical Review Letters, 110 (2013), pp. 197201–197201.

[247] E. G. Tveten, A. Brataas, and Y. Tserkovnyak, *Electron-magnon scattering in magnetic heterostructures far out of equilibrium*, Physical Review B, 92 (2015).

[248] K. I. Uchida, H. Adachi, T. Ota, H. Nakayama, S. Maekawa, and E. Saitoh, *Observation of longitudinal spin-seebeck effect in magnetic insulators*, Applied Physics Letters, 97 (2010), p. 172505.

[249] T. Valet and A. Fert, *Theory of the perpendicular magnetoresistance in magnetic multilayers*, Physical Review B, 48 (1993), pp. 7099–7113.

[250] N. C. J. van der Valk, T. Wenckebach, and P. C. M. Planken, *Full mathematical description of electro-optic detection in optically isotropic crystals*, Journal of the Optical Society of America B, 21 (2004), p. 622.

[251] E. Y. Vedmedenko, R. K. Kawakami, D. D. Sheka, P. Gambardella, A. Kirilyuk, A. Hirohata, C. Binek, O. Chubykalo-Fesenko, S. Sanvito, B. J. Kirby, J. Grollier, K. Everschor-Sitte, T. Kampfrath, C. Y. You, and A. Berger, *The 2020 magnetism roadmap*, Journal of Physics D: Applied Physics, 53 (2020).

[252] J. P. Velev, K. D. Belashchenko, S. S. Jaswal, and E. Y. Tsymbal, *Effect of oxygen vacancies on spin-dependent tunneling in fe/mgo/fe magnetic tunnel junctions*, Applied Physics Letters, 90 (2007), p. 072502.

[253] J. P. Velev, M. Y. Zhuravlev, K. D. Belashchenko, S. S. Jaswal, E. Y. Tsymbal, T. Katayama, and S. Yuasa, *Defect-mediated properties of magnetic tunnel junctions*, IEEE Transactions on Magnetics, 43 (2007), pp. 2770–2775.

[254] E. Villamor, M. Isasa, L. E. Hueso, and F. Casanova, *Contribution of defects to the spin relaxation in copper nanowires*, Physical Review B, 87 (2013).

[255] T. Vogel, A. Omar, S. Mansourzadeh, F. Wulf, N. M. Sabanés, M. Müller, T. S. Seifert, A. Weigel, G. Jakob, M. Kläui, I. Pupeza, T. Kampfrath, and C. J. Saraceno, *Average power scaling of THz spintronic emitters efficiently cooled in reflection geometry*, Optics Express, 30 (2022), p. 20451.

[256] M. A. Wahada, E. Şaşioğlu, W. Hoppe, X. Zhou, H. Deniz, R. Rouzegar, T. Kampfrath, I. Mertig, S. S. P. Parkin, and G. Woltersdorf, *Atomic scale control of spin current transmission at interfaces*, Nano Letters, 22 (2022), pp. 3539–3544.

[257] J. Walowski and M. Münzenberg, *Perspective: Ultrafast magnetism and thz spintronics*, Journal of Applied Physics, 120 (2016).

[258] L. Wang, H. Cheng, P. Li, Y. L. W. van Hees, Y. Liu, K. Cao, R. Lavrijsen, X. Lin, B. Koopmans, and W. Zhao, *Picosecond optospintronic tunnel junctions*, Proceedings of the National Academy of Sciences, 119 (2022).

[259] J. Weischenberg, F. Freimuth, J. Sinova, S. Blügel, and Y. Mokrousov, *Ab initio theory of the scattering-independent anomalous hall effect*, Phys. Rev. Lett., 107 (2011), p. 106601.

[260] R. M. White, *Quantum Theory of Magnetism*, Springer, 2007.

[261] F. Willems, C. T. L. Smeenk, N. Zhavoronkov, O. Kornilov, I. Radu, M. Schmidbauer, M. Hanke, C. von Korff Schmising, M. J. J. Vrakking, and S. Eisebitt, *Probing ultrafast spin dynamics with high-harmonic magnetic circular dichroism spectroscopy*, Physical Review B, 92 (2015).

[262] R. B. Wilson, Y. Yang, J. Gorchon, C.-H. Lambert, S. Salahuddin, and J. Bokor, *Electric current induced ultrafast demagnetization*, Physical Review B, 96 (2017).

[263] S. A. Wolf, D. D. Awschalom, R. A. Buhrman, J. M. Daughton, S. Von Molnár, M. L. Roukes, A. Y. Chtchelkanova, and D. M. Treger, *Spintronics: A spin-based electronics vision for the future*, Science, 294 (2001), pp. 1488–1495.

[264] Q. Wu and X.-C. Zhang, *Free-space electro-optics sampling of mid-infrared pulses*, Applied Physics Letters, 71 (1997), pp. 1285–1286.

[265] W. Wu, S. Lendinez, M. Taghipour Kaffash, R. D. Schaller, H. Wen, and M. B. Jungfleisch, *Modification of terahertz emission spectrum using microfabricated spintronic emitters*, Journal of Applied Physics, 128 (2020).

[266] W. Wu, C. Yaw Ameyaw, M. F. Doty, and M. B. Jungfleisch, *Principles of spintronic thz emitters*, Journal of Applied Physics, 130 (2021).

[267] Y. Wu, M. Elyasi, X. Qiu, M. Chen, Y. Liu, L. Ke, and H. Yang, *High-performance thz emitters based on ferromagnetic/nonmagnetic heterostructures*, Advanced Materials, 29 (2016), p. 1603031.

[268] Y. Wu, M. Elyasi, X. Qiu, M. Chen, Y. Liu, L. Ke, and H. Yang, *High-performance thz emitters based on ferromagnetic/nonmagnetic heterostructures*, Adv Mater, 29 (2017).

[269] Y. Xu, D. Ephron, and M. R. Beasley, *Directed inelastic hopping of electrons through metal-insulator-metal tunnel junctions*, Physical Review B, 52 (1995), pp. 2843–2859.

[270] D. Yang, J. Liang, C. Zhou, L. Sun, R. Zheng, S. Luo, Y. Wu, and J. Qi, *Powerful and tunable thz emitters based on the fe/pt magnetic heterostructure*, Advanced Optical Materials, 4 (2016), pp. 1944–1949.

[271] G. Yao and Y. Pi, *Terahertz active imaging radar: preprocessing and experiment results*, EURASIP Journal on Wireless Communications and Networking, 2014 (2014).

[272] K.-L. Yeh, M. C. Hoffmann, J. Hebling, and K. A. Nelson, *Generation of 10μj ultrashort terahertz pulses by optical rectification*, Applied Physics Letters, 90 (2007), p. 171121.

[273] S. Yoshida, Y. Arashida, H. Hirori, T. Tachizaki, A. Taninaka, H. Ueno, O. Takeuchi, and H. Shigekawa, *Terahertz scanning tunneling microscopy for visualizing ultrafast electron motion in nanoscale potential variations*, ACS Photonics, 8 (2021), pp. 315–323.

[274] S. Yuasa and D. D. Djayaprawira, *Giant tunnel magnetoresistance in magnetic tunnel junctions with a crystalline (001) barrier*, Journal of Physics D: Applied Physics, 40 (2007), pp. R337–R354.

[275] S. Yuasa, T. Nagahama, and Y. Suzuki, *Spin-polarized resonant tunneling in magnetic tunnel junctions*, Science, 297 (2002), pp. 234–237.

[276] H. Zhang, Z. Feng, J. Zhang, H. Bai, H. Yang, J. Cai, W. Zhao, W. Tan, F. Hu, B. Shen, and J. Sun, *Laser pulse induced efficient terahertz emission from co/al heterostructures*, Physical Review B, 102 (2020).

[277] Q. Zhang, Z. Chen, H. Shi, X. Chen, A. Talapatra, X. Zhang, and Y. Wu, *Terahertz emission from cofeb/cr/pt trilayers: The role of cr as both a spin current transporter and generator*, Applied Physics Letters, 118 (2021).

[278] W. Zhang, P. Maldonado, Z. Jin, T. S. Seifert, J. Arabski, G. Schmerber, E. Beaurepaire, M. Bonn, T. Kampfrath, P. M. Oppeneer, and D. Turchinovich, *Ultrafast terahertz magnetometry*, Nat Commun, 11 (2020), p. 4247.

[279] X.-C. Zhang, J. Xu, et al., *Introduction to THz wave photonics*, vol. 29, Springer, 2010.

[280] Y. Zhang, X. Zhang, S. Li, J. Gu, Y. Li, Z. Tian, C. Ouyang, M. He, J. Han, and W. Zhang, *A broadband thz-tds system based on dstms emitter and ltg ingaas/inalas photoconductive antenna detector*, Scientific Reports, 6 (2016).

[281] H. Zhao, Y. Tan, T. Wu, G. Steinfeld, Y. Zhang, C. Zhang, L. Zhang, and M. Shalaby, *Efficient broadband terahertz generation from organic crystal BNA using near infrared pump*, Applied Physics Letters, 114 (2019), p. 241101.

[282] C. Zhou, Y. P. Liu, Z. Wang, S. J. Ma, M. W. Jia, R. Q. Wu, L. Zhou, W. Zhang, M. K. Liu, Y. Z. Wu, and J. Qi, *Broadband terahertz generation via the interface inverse rashba-edelstein effect*, Phys Rev Lett, 121 (2018), p. 086801.

[283] Y.-H. Zhu, B. Hillebrands, and H. C. Schneider, *Signal propagation in time-dependent spin transport*, Physical Review B, 78 (2008).

[284] W. Zouaghi, M. D. Thomson, K. Rabia, R. Hahn, V. Blank, and H. G. Roskos, *Broadband terahertz spectroscopy: principles, fundamental research and potential for industrial applications*, European Journal of Physics, 34 (2013), pp. S179–S199.

[285] I. Zutic, J. Fabian, and S. Das Sarma, *Spintronics: Fundamentals and applications*, Reviews of Modern Physics, 76 (2004), pp. 323–410.

List of Publications

Publications within this thesis

R. Rouzegar, L. Brandt, L. Nádvorník, D. A. Reiss, A. L. Chekhov, O. Gueckstock, C. In, M. Wolf, T. S. Seifert, P. W. Brouwer, G. Woltersdorf, T. Kampfrath. *Laser-induced terahertz spin transport in magnetic nanostructures arises from the same force as ultrafast demagnetization.* Phys. Rev. B **106**, 144427 (2022).

R. Rouzegar, A.L. Chekhov, Y. Behovits, B.R. Serrano, M.A. Syskaki, C.H. Lambert, D. Engel, U. Martens, M. Münzenberg, M. Wolf, G. Jakob, M. Kläui, T.S. Seifert, and T. Kampfrath. *Broadband Spintronic Terahertz Source with Peak Electric Fields Exceeding 1.5 MV/cm.* Phys. Rev. Applied **19**, 034018 (2023).

R. Rouzegar, M. Wahada, A. Chekhov, W. Hoppe, J. Jechumtal, L. Nadvornik, M. Wolf, T. Seifert, S. Parkin, G. Woltersdorf, P. W. Brouwer, T. Kampfrath. *Terahertz spin conductance probes of coherent and incoherent spin tunneling through mgo tunnel junctions.* arXiv preprint arXiv:2305.09074, (2023) (shared 1st authorship).

J. Jechumtal, **R. Rouzegar**, O. Gueckstock, C. Denker, W. Hoppe,Q. Remy, T. S. Seifert, P. Kubascik, G. Woltersdorf, P. W. Brouwer, M. Münzenberg, T. Kampfrath, and L. Nadvornik. *Accessing ultrafast spintransport dynamics in copper using broadband terahertz spectroscopy.* Accepted in Phys. Rev. Letter (2024) (shared 1st authorship).

Publications concerning other topics

R. Rouzegar, A. Alighanbari, O. M. Ramahi. *Wideband uniplanar artificial magnetic conductors based on curved coupled microstrip line resonators.* IEEE Microwave and Wireless Components Letters **27.4** 326-328 (2017).

R. Rouzegar, and U. Spagnolini. *Channel estimation for diffusive MIMO molecular communications.* European Conference on Networks and Communications (EuCNC). IEEE, 2017.

T. S. Seifert, N.M. Tranh, O. Gueckstock, **R. Rouzegar**, L. Nádvorník, S. Jaiswal, G. Jakob, V. Temnov, M. Münzenberg, M. Wolf, M. Kläui, T. Kampfrath. *Terahertz spectroscopy for all-optical spintronic characterization of the spin-Hall-effect metals Pt, W and* $Cu_{80}Ir_{20}$. J. Phys. D: Appl. Phys. **51**, 364003 (2018).

R. Rouzegar, and U. Spagnolini. *Diffusive MIMO molecular communications: Channel*

estimation, equalization, and detection. IEEE Transactions on Communications **67.7** 4872-4884 (2019).

U. Nandi, M.S. Abdelaziz, S. Jaiswal, G. Jakob, O. Gueckstock, **R. Rouzegar**, T.S. Seifert, M. Kläui, T. Kampfrath, and S. Preu. *Antenna-coupled spintronic terahertz emitters driven by a 1550 nm pulsed laser.* Appl. Phys. Lett. **115**, 022405 (2019).

U. Nandi, M.S. Abdelaziz, S. Jaiswal, G. Jakob, O. Gueckstock, **R. Rouzegar**, T.S. Seifert, M. Kläui, T. Kampfrath, S. Preu. *Effect of DC Electric Field on the Emitted THz Signal of Antenna-Coupled Spintronic Emitters.* 2019 44$^{\text{th}}$ International Conference on Infrared, Millimeter, and Terahertz Waves (IRMMW-THz), IEEE (2019).

O. Gueckstock, L. Nádvorník, M. Gradhand, T. S. Seifert, G. Bierhance, **R. Rouzegar**, M. Wolf, M. Vafaee, J. Cramer, M. A. Syskaki, G. Woltersdorf, I. Mertig, G. Jakob, M. Kläui, T. Kampfrath. *Terahertz spin-to-charge conversion by interfacial skew scattering in metallic bilayers.* Adv. Mater. **33**, 2006281 (2021).

G. Bierhance, A. Markou, O. Gueckstock, **R. Rouzegar**, Y. Behovits, A. L. Chekhov, M. Wolf, T. S. Seifert, C. Felser, T. Kampfrath. *Spin-voltage-driven efficient terahertz spin currents from the magnetic Weyl semimetals Co_2MnGa and Co_2MnAl.* Appl. Phys. Lett. **120**, 082401 (2022).

M.A. Wahada, E. Sasıoglu, W. Hoppe, X. Zhou, H. Deniz, , **R. Rouzegar**, T. Kampfrath, I. Mertig, S.S. Parkin, G. Woltersdorf. *Atomic scale control of spin current transmission at interfaces.* Nano Letters, 22, **9** , pp.3539-3544 (2022).

P. Jimenez-Cavero, O. Gueckstock, L. Nádvorník, I. Lucas, T. S. Seifert, M. Wolf, **R. Rouzegar**, P. W. Brouwer, S. Becker, G. Jakob, M. Kläui, C. Guo, C. Wan, X. Han, Z. Jin, H. Zhao, D. Wu, L. Morellon, T. Kampfrath. *Transition of laser-induced terahertz spin currents from torque- to conduction-electron-mediated transport.* Phys. Rev. B **105**, 184408 (2022).

R. Rouzegar, L. Brandt, L. Nádvorník, D. A. Reiss, A. L. Chekhov, O. Gueckstock, C. In, M. Wolf, T. S. Seifert, P. W. Brouwer, G. Woltersdorf, T. Kampfrath. *Spin voltage gradient is the driving force for ultrafast demagnetization and Terahertz spin transport.* 2023 IEEE International Magnetic Conference (INTERMAG Short Papers)(2023).

T.S. Seifert, D. Go, H. Hayashi, **R. Rouzegar**, F. Freimuth, K. Ando, Y. Mokrousov, T. Kampfrath. *Time-domain observation of ballistic orbital-angular-momentum currents with giant relaxation length in tungsten.* Nat. Nanotechnol. **18**, 1132–1138 (2023).

B. Das-Mohapatra, **R. Rouzegar**, E. T. Papaioannou, T. Kampfrath, G. Schmidt. *Shap-*

ing THz emission spectra by using sub-wavelength nanopatterned spintronic THz emitters. arXiv preprint arXiv:2308.07159 (2023).

Academic curriculum vitae

Reza Rouzegar
10969 Berlin

For reasons of data protection, the curriculum vitae is not published in the electronic version.

Acknowledgments

This thesis would not have been possible without the great teamwork of many individuals and institutions. I would like to express my gratitude to all those who contributed to this work.

First, I am profoundly grateful to my supervisor, Prof. Dr. Tobias Kampfrath, whose guidance and mentorship were instrumental in the completion of this thesis. Tobias, I have learned immeasurable lessons from you, and I am forever thankful for the privilege of working alongside you.

My sincere appreciation extends to my second supervisor, Prof. Dr. Martin Wolf, not only for his second review of this thesis but also for his exceptional hospitality within the THz physics group at FHI, which provided a vital environment for our research.

A special note of gratitude is reserved for Tom Seifert. Thanks for your valuable guidance through these years and the many proofreadings of this thesis. I'm looking forward to our future projects together.

Lukáš Nádvorník, I am immensely grateful for the privilege of working with you and, more importantly, for the cherished friendship we've cultivated. Our adventure in Spain is unforgettable, and I am looking forward to repeating it.

I would like to express my gratitude to Prof. Dr. Piet Brouwer for the numerous projects and discussions we've had. It's such an honor to work with you.

Oliver Gückstock and Genaro Bierhance, I can't imagine going through my PhD journey without you. Thank you for your incredible support over the years and proofreading of this thesis. We have shared many fun and memorable moments, from Spain to Dresden and all Halloween parties. I'm looking forward to working and traveling more with you.

Quentin Remy, thank you for your numerous proofreadings and engaging scientific discussions. Your presence in Berlin has been a great blessing, both as a colleague and a friend.

Alex, Bruno, Amon, Yannic, and Julius, you are the coolest. I believe that a primary requirement to join the KHz table is to embody this level of coolness. It's always fun to spend time with all of you.

My heartfelt thanks go out to the rest of the THz physics group, former and current members, including Afnan, Zdeněk, Chihun, Martin, Junwei, Aditya, Hongsong, Pilar, Clara, and Ilie Radu, whose collective efforts contributed to the achievements of this research.

I extend my thanks to my colleagues and friends at FHI, including Marcel, Mohsen, Vasili, Sebastian, Selene, Max, Leona, and many more, for their unwavering support and friendship.

I am grateful for the assistance and support provided by the TRR 227 office team: Christian Frischkorn, Britta Anstötz, and Julia Walter.

I extend my appreciation to the IMPRS research school and its current and former mem-

bers. Particularly, I would like to thank Alexander Paarmann and Ines Bressel for their support and guidance. You are amazing people!

I acknowledge the invaluable assistance of the secretaries at FU and FHI, including Manuel Krüger, Daria Haberland, Marietta Wissmann, and Bolle Selke-Fölster, in navigating bureaucratic matters.

To the FHI cool kids—Marie, Ivana, Stefano, and Ali—thank you for the wonderful times we shared. You are the best.

I would like to recognize the incredible friendships of Mehrdad, Leon, Alex, Jimena, Elahe, Graziana, Chiara, and Sudi. Your friendship and the wonderful moments we shared have brought me immense joy.

Rahil and Quentin, we had so many fun memories together, from Brno, to many nights in Berlin and even in Sendai. Let's always stick together.

Hossein and Vahid, you're not just cousins but also close friends. Our shared memories from childhood to now hold a special place in my heart.

Shahin, you are my life companion, Kako. From bus rides in Iran, to crazy nights in Berlin and Amsterdam, I enjoyed every moment with you. I wish for a life-long friendship with you.

Reza, my quasi-brother, we have been through the highs and the lows together, from Mofatteh to Milano. Here's to a long-lasting friendship.

Amir and Amjad, having your friendship is one of my biggest achievements. You are my chosen family. Cheers to all our memories we made and will continue to make.

Jafar, you are not only a great uncle to me, but also a valuable friend. Thanks for always being there for me. It means a lot.

Louisa, your unwavering love and support have been the lighthouse that guided me through the challenges, and for that, I am deeply thankful.

Lastly, I extend my immense gratitude to my family. Thank you, Dad, for teaching me how to enjoy life. Thank you, Mom, for teaching me how to be kind and open. Maryam, your love has been a constant source of strength. Thank you, Aria, for being the best "Bro" ever. And thank you, Majid, for entering our family and bringing new light and color to it. Thank you for always believing in me.

I sincerely thank each and every one who contributed to this journey, even though I could not mention all of you.

Selbstständigkeitserklärung

Ich erkläre gegenüber der Freien Universität Berlin, dass ich die vorliegende Dissertation selbstständig und ohne Benutzung anderer als der angegebenen Quellen und Hilfsmittel angefertigt habe. Die vorliegende Arbeit ist frei von Plagiaten. Alle Ausführungen, die wörtlich oder inhaltlich aus anderen Schriften entnommen sind, habe ich als solche kenntlich gemacht. Diese Dissertation wurde in gleicher oder ähnlicher Form noch in keinem früheren Promotionsverfahren eingereicht.

Mit einer Prüfung meiner Arbeit durch ein Plagiatsprüfungsprogramm erkläre ich mich einverstanden.

Berlin, den

Mohammadreza Rouzegar